

**PONTIFICIA UNIVERSIDAD CATÓLICA DEL PERÚ**

**FACULTAD DE CIENCIAS E INGENIERÍA**



**MINERALOGY OF THE LITHIUM-RICH TUFF IN THE MACUSANI  
VOLCANIC FIELD, CORDILLERA ORIENTAL, SOUTHERN PERU**

**Tesis para obtener el título profesional de Ingeniera Geóloga**

**AUTORA:**

MARIANA KELLY SEGOVIA MORE

**ASESOR:**

Dr. LISARD TORRÓ I ABAT

**CO-ASESORA:**

Dra. CRISTINA VILLANOVA-DE-BENAVENT

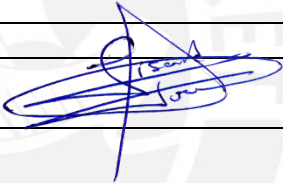
**Lima, enero de 2024**

## Informe de Similitud

Yo, Lisard Torró i Abat,  
docente de la Facultad de Ciencias e Ingeniería de la Pontificia Universidad Católica del Perú,  
asesor de la tesis titulada “Mineralogy of the Lithium-rich Tuff in the Macusani Volcanic Field,  
Cordillera Oriental, southern Peru”, de la autora Mariana Kelly Segovia More de constancia  
de lo siguiente:

- El mencionado documento tiene un índice de puntuación de similitud de 15 %. Así lo consigna el reporte de similitud emitido por el software *Turnitin* el 29/01/2024.
- He revisado con detalle dicho reporte y la Tesis y no se advierten indicios de plagio.
- Las citas a otros autores y sus respectivas referencias cumplen con las pautas académicas.

Lugar y fecha: Lima a 29 de enero de 2024

Apellidos y nombres del asesor:	
DNI: Torró i Abat, Lisard	Firma 
ORCID: 0000-0002-3557-8334	

## RESUMEN

El litio es un metal de gran importancia económica y una materia prima clave para la transición energética desde una generación de energía basada en combustibles fósiles hacia una basada en fuentes renovables. En este sentido, el descubrimiento de nuevos yacimientos de litio es fundamental para abastecer la creciente demanda de este metal.

La compañía Macusani Yellowcake, subsidiaria de American Lithium, anunció un importante recurso que asciende a 0,9 Mt Li en el Proyecto de Litio Falchani, en el Campo Volcánico de Macusani, Puno, SE Perú. El recurso está alojado en tobas volcánicas y brechas neógenas pertenecientes a la Formación Macusani. Con contenidos de Li que oscilan entre ~2000 y 4000 ppm, la unidad denominada Lithium-rich Tuff contiene el principal recurso. En esta tesis se ha realizado una caracterización mineralógica general y de alta resolución de muestras de Lithium-rich Tuff utilizando difracción de rayos X (XRD), microscopía electrónica de barrido con espectroscopía de rayos X de energía dispersiva (SEM-EDS) y microscopía electrónica de transmisión (TEM).

Las muestras estudiadas están compuestas por cuarzo, plagioclasa, feldespato potásico, micas trioctaédricas (zinnwaldita y lepidolita), minerales del subgrupo de la caolinita y esmectitas (montmorillonita - beidellita), además de zeolitas (mordenita y mutinaita) y cristobalita en algunas muestras. Los contenidos más altos de Li (3000-4200 ppm Li) se encuentran en la porción central de la secuencia del Lithium-rich Tuff, que se caracteriza por contener micas + caolinita ± mordenita. En los dominios superior e inferior de la secuencia, los contenidos de Li alcanzan valores de 2000 ppm y la mineralogía está dominada por mica + esmectita dioctaédrica ± caolinita ± halloysita.

La integración de estos datos con resultados de ensayos metalúrgicos proporcionados por Macusani Yellowcake respalda que, además de en micas trioctaédricas primarias, parte del Li en el Proyecto de Litio Falchani puede estar adsorbido o en posiciones interlaminares de minerales arcillosos secundarios. Se descarta la existencia de arcillas con Li tipo hectorita. Estos datos permiten una clasificación tentativa del proyecto de litio de Falchani como un depósito volcanogénico ‘mixto’ mica primaria – minerales secundarios de arcilla.

## ABSTRACT

Lithium is a metal with high economic importance and a key raw material to the energetic transition from carbon fuels to renewable energy sources. In this sense, exploring and discovering new lithium deposits is essential to supply the growing demand for this element.

A major lithium resource amounting to 0.9 Mt was announced by Macusani Yellowcake – American Lithium in the Falchani Lithium Project, Macusani Volcanic Field, Puno, SE Peru. The resource is hosted by Neogene volcanic tuff and breccia of the Macusani Formation. With Li contents ranging between ~2,000 to 4,000 ppm, the so-called Lithium-rich Tuff hosts the main resource. In this thesis, a general and high-resolution mineralogical characterization of samples from the Lithium-rich Tuff has been performed using X-Ray diffraction (XRD), scanning electron microscopy with energy dispersive X-ray spectroscopy (SEM–EDS), and transmission electron microscopy (TEM).

The studied samples comprise quartz, plagioclase, K-feldspar, trioctahedral micas (zinnwaldite and lepidolite), kaolinite-subgroup minerals, and smectites (montmorillonite – beidellite), in addition to zeolites (mordenite, and mutinaite) and cristobalite in a few samples. The highest Li contents (3,000-4,200 ppm Li) are found in the central portion of the Lithium-rich Tuff sequence, which is characterized by micas + kaolinite subgroup minerals ± mordenite. In the upper and lower domains of the tuff sequence, Li contents reach values of 2,000 ppm, and the mineralogy is dominated by mica + dioctahedral smectite ± kaolinite ± halloysite.

The integration of these data with metallurgical assay results reported by Macusani Yellowcake supports that, in addition to magmatic trioctahedral micas, Li in the Falchani Lithium Project may be in part adsorbed onto and/or occupy interlaminal positions in secondary clay minerals. The occurrence of clays with Li such as hectorite is discarded. These data allow a tentative classification of the Falchani Lithium Project as a ‘mixed’ primary mica– secondary clay volcanogenic deposit.

## AGRADECIMIENTOS

Quiero expresar mi profundo agradecimiento a las personas que han sido fundamentales en el proceso de desarrollo de esta tesis.

Dedico este proyecto a mi familia. A mis queridos abuelos Frida y Pedro, agradezco su apoyo incondicional a lo largo de mi vida. De igual manera, agradezco a mis padres Ana y Edward, a mis tíos Katia y Julio, y a mi compañero de vida Sergio, por sus innumerables palabras de aliento y confianza en mí.

Un agradecimiento especial a mi asesor, Dr. Lisard Torró, por la confianza, paciencia y palabras de motivación, así como su invaluable contribución y orientación a lo largo del desarrollo del proyecto. A mi co-asesora, Dra. Cristina Villanova (Universidad de Barcelona) por sus comentarios y conocimientos que han enriquecido cada aspecto del proyecto de tesis. Debo agradecer la detallada revisión del documento de tesis por el Dr. César Muñoz y el Dr. Diego Benites. También, quiero agradecer al Dr. Patrice Baby y el Dr. Jean Vallance por su participación en la campaña de campo en la que se muestrearon las rocas analizadas en esta tesis y al Dr. Joaquín A. Proenza (Universidad de Barcelona) y al Dr. Fernando Nieto (Universidad de Granada) por su colaboración durante la obtención de los datos de TEM y la discusión de los resultados.

Extiendo mi gratitud a los técnicos-especialistas encargados de la preparación y análisis de las muestras, especialmente a Pablo Valverde (Laboratorio de Geología, PUCP) y a Cecilia de la Prada y a María del Mar Abad (TEM, Universidad de Granada). Finalmente, también debo mi agradecimiento a Rolf Griesler por brindarme entrenamiento en el uso del equipo de DRX en el Centro de Caracterización de Materiales (CAM-PUCP).

Esta tesis no hubiera sido posible sin el apoyo de Macusani Yellowcake – American Lithium, quienes brindaron acceso a información técnica así como a afloramientos y sondajes y apoyaron logísticamente durante las tareas de muestreo en sus concesiones. Agradezco al Dr. Ulises Solís y a los geólogos de la compañía, en particular a Gregorio Tasayco y Miguel Cavani, por el apoyo constante.

Asimismo, agradezco al equipo de trabajo, especialmente a Johan Ramirez y Mercy Sanandres, y a mis mejores amigos Isabel Salazar y Jhon Amasifuen, por su grata compañía durante los últimos años de carrera.

**This thesis was economically supported by the Peruvian PROCENCIA-CONCYTEC project 122-2020 E041-2020-01-01.**

## Table of contents

1.	INTRODUCTION	9
1.1.	Lithium: a critical raw material for the global economy	9
1.2.	Geochemistry and mineralogy of lithium	13
1.3.	Overview of lithium deposits	16
1.3.1.	Pegmatite deposits	18
1.3.2.	Hydromorphic deposits	19
1.3.3.	Volcanogenic deposits	21
1.3.4.	Manganese deposits	22
1.3.5.	Bauxite deposits	22
1.4.	The discovery of a major lithium resource at Falchani	22
1.5.	Conundrum	25
1.6.	Objectives	26
1.7.	Hypothesis	26
1.8.	Justification	26
2.	METHODOLOGY	27
2.1.	Sampling	27
2.2.	X-Ray Diffraction	28
2.3.	SEM-EDS	30
2.4.	TEM	31
3.	GEOLOGICAL SETTING	31
3.1.	Geology of the Central Andes of southern Peru: the Cordillera Oriental	31
3.2.	Regional geology of the Cordillera de Carabaya	33
3.3.	Geology of the Macusani Basin and the Macusani Volcanic Field	37
3.3.1.	Picotani Group	37
3.3.2.	Quenamari Group	38
3.3.3.	Quenamari and Picotani Intrusive Suites	42
4.	RESULTS	43
4.1.	XRD	43
4.2.	SEM-EDS	52
4.3.	TEM	56
5.	DISCUSSION	59
5.1.	Mineralogical expression of lithium in the Lithium-rich Tuff	59
5.2.	Classification of the Falchani Lithium Project	62
6.	CONCLUSIONS	64
7.	REFERENCES	66

## List of figures

- Figure 1.** Critical Raw Materials for the European Commission (2023) based on their supply risk and economic importance, including lithium \_\_\_\_\_ 10
- Figure 2.** Bar chart of forecasts (f) of lithium over the decade 2018-2028, expressed in thousands of metric tonnes of LCEs. Major uses of lithium are indicated. The dotted green line indicates predicted maximum demand of LCEs, and the red one indicates predicted minimum demand of LCEs. Note that lithium demand in 2018 was about 300,000 tonnes of LCE, whereas it is expected that by 2028 it will reach 1.0-1.3 Mt of LCE. Modified from Bibienne et al. (2020) \_\_\_\_\_ 12
- Figure 3.** Variation of the prices of lithium carbonate in yuan/t during the last 5 years. The red point indicates the maximum price of lithium carbonate (approx. 6,000 dollars/t). Modified from Trading Economics (2023) \_\_\_\_\_ 13
- Figure 4.** Lithium resources distribution in the world according to type of deposit. Adapted from Bradley and Jaskula (2014) \_\_\_\_\_ 17
- Figure 5.** Major lithium deposits in the world. Modified from Howell et al. (2020) \_\_\_\_\_ 17
- Figure 6.** Location of the Macusani Volcanic Field to the north of the Lithium Triangle of the Andes, which is delimited by Salar Uyuni (Bolivia), Salar de Atacama (Chile), and Salar del Hombre Muerto (Argentina) \_\_\_\_\_ 20
- Figure 7.** Exploration concessions in the Macusani Basin between the coordinates 280,000 and 360,000 East and 8,420,000 and 8,480,000 North. The Falchani Project covers an area of 1,700 ha (SIDEMCAT 2022) \_\_\_\_\_ 25
- Figure 8.** Location of the studied rock samples and exploration concessions owned by Macusani Yellowcake (SIDEMCAT 2022) in the Macusani Volcanic Field \_\_\_\_\_ 28
- Figure 9.** A) Diamond saw and B) jaw crusher available at the QEMSCAN laboratory (PUCP) used in this study \_\_\_\_\_ 29
- Figure 10.** A, B) Rotary splitters used in this study at the QEMSCAN laboratory (PUCP) \_\_\_\_\_ 29
- Figure 11.** A) Agate mortar. B) Bruker D8 Discover diffractometer, available at CAM-PUCP \_\_\_\_\_ 30
- Figure 12.** Geomorphotectonic structures of the Central Andes including the location of the Macusani Volcanic Field. The dotted-line box around Macusani Volcanic Field indicate the area covered in Fig. 13. Modified from Kontak et al. (1990) \_\_\_\_\_ 32
- Figure 13.** Simplified geology of the tectonic/structural domains: Cordillera de Carabaya, Precordillera de Carabaya (a.k.a. Macusani Tectonic Zone), and Central Andean Backthrust Belt. The locations of the Macusani, Crucero, and Ananea-Ancocalla intermontane depressions are also shown. Modified from Kontak et al. (1990) and Sandeman et al. (1997) \_\_\_\_\_ 36
- Figure 14.** Geological map of the SW quadrant of the Quenamari Meseta, where the Quenamari Volcanic Field is located. Modified from Sandeman et al. (1997) \_\_\_\_\_ 38
- Figure 15.** Comparative stratigraphic columns after Sandeman et al. (1996) and Lopez (1996). Sandeman et al (1996) presented a stratigraphic column of the Quenamari Group (Macusani Formation) and Picotani Group (Cerro Sumpiruni, Pucalacaya, Lago Perhuacarca Formations) exposed in the Macusani Field. Lopez et al (1996) described the Chacacuniza, Sapanuta and Yapamayo Members of the Quenamari Formation (in full synonymy with Macusani Formation) \_\_\_\_\_ 41
- Figure 16.** Powder XRD patterns (left) and oriented aggregate mount XRD patterns (right) of samples 2021-MAC-008B, 2021-MAC-011A, 2021-MAC-038, 2021-MAC-039, and 2021-MAC-040. Major mineralogy includes plagioclase (Pl), quartz (Qz), K-feldspar (Kfs), and mica (Mca). In all diffractograms (except for sample 2021-MAC-

011A), the  $d_{001}$  of 7.1 Å ( $2\theta \sim 12.5^\circ$ ) is interpreted to correspond to kaolinite subgroup minerals (Kln) \_\_\_\_\_ 45

**Figure 17.** Powder XRD patterns (left) and oriented aggregate mount XRD patterns (right) of samples 2021-MAC-048, 2021-MAC-052, 2021-MAC-065A, and 2021-MAC-066. Common minerals include mica (Mca), plagioclase (Pl), quartz (Qz), and K-feldspar (Kfs). The  $d_{001}$  of 7 to 7.1 Å ( $2\theta \sim 12.5^\circ$ ) is interpreted as kaolinite subgroup minerals (Kln). In the oriented aggregate mounts of sample 2021-MAC-052, the XRD pattern presents a peak at  $2\theta \sim 7.1^\circ$  ( $d_{001}$  of 12.2 Å) corresponding to smectite (Sme). In the oriented aggregate mounts of samples 2021-MAC-065A and 2021-MAC-066, smectite peaks were not detected \_\_\_\_\_ 46

**Figure 18.** Powder XRD patterns (left) and oriented aggregate mount XRD patterns (right) of samples 2021-MAC-035, 2021-MAC-042, 2021-MAC-049, 2021-MAC-050, and 2021-MAC-051. The  $d_{001}$  of 12.5 to 15.1 Å ( $2\theta \sim 5.8 - 7^\circ$ ) are interpreted as smectite (Sme). Also, the  $d_{001}$  of 7 to 7.1 Å ( $2\theta \sim 12.5^\circ$ ) are interpreted as kaolinite (Kln). Other identified phases include mica (Mca), plagioclase (Pl), and cristobalite (Crs) \_\_\_\_\_ 47

**Figure 19.** Powder XRD patterns of (left) and oriented aggregate mount XRD patterns (right) of samples 2021-MAC-026 and 2021-MAC-053. The  $d_{001}$  of 9.8 Å ( $2\theta \sim 8.9^\circ$ ) corresponds to mica (Mca). The  $d_{110}$  of 13.5 to 13.7 Å ( $2\theta \sim 6.5^\circ$ ) are interpreted as mordenite (Mor). Other mineral phases identified include plagioclase (Pl), quartz (Qz), and K-feldspar (Kfs) \_\_\_\_\_ 48

**Figure 20.** Powder XRD patterns showing the interpreted major peaks as black vertical lines with the corresponding mineral labels. Samples are classified according to their prevalent mineralogy. Abbreviations: plagioclase (Pl), mica (Mca), quartz (Qz), K-feldspar (Kfs), kaolinite subgroup minerals (Kln), smectite (Sme), cristobalite (Crs), mordenite (Mor), and mutinaite (Mut) \_\_\_\_\_ 49

**Figure 21.** Powder XRD patterns of samples from the drill core PCHAC-01-TSW sorted by increasing depth. Lithium values provided by Macusani Yellowcake-American Lithium. Color code as in Fig. 20. Abbreviations: plagioclase (Pl), mica (Mca), quartz (Qz), K-feldspar (Kfs), kaolinite (Kln), and smectite (Sme) \_\_\_\_\_ 50

**Figure 22** Powder XRD patterns of samples from the drill core PCHAC-04-TV sorted by increasing depth. Lithium values provided by Macusani Yellowcake-American Lithium. Color code as in Fig. 20. Abbreviations: plagioclase (Pl), mica (Mca), quartz (Qz), K-feldspar (Kfs), kaolinite (Kln), smectite (Sme), and cristobalite (Crs) \_\_\_\_\_ 51

**Figure 23** XRD patterns of samples from the drill core PCHAC-32 sorted by depth. Lithium values provided by Macusani Yellowcake-American Lithium. Color code as in Fig. 20. Abbreviations: albite (Ab), plagioclase (Pl), mica (Mca), quartz (Qz), K-feldspar (Kfs), kaolinite (Kln), smectite (Sme), cristobalite (Crs), mordenite (Mor), and mutinaite (Mut) \_\_\_\_\_ 51

**Figure 24.** Powder XRD patterns of drill core samples (2021-MAC-035 to 2021-MAC-053) classified according to their mineralogy and sorted by increasing depth. Color code as in Fig. 20. Abbreviations: plagioclase (Pl), mica (Mca), quartz (Qz), K-feldspar (Kfs), kaolinite subgroup minerals (Kln), smectite (Sme), cristobalite (Crs), and mordenite (Mor) \_\_\_\_\_ 52

**Figure 25.** Secondary-electron SEM images of sample 2021-MAC-026 (“zeolite with mica” type). A) Subhedral, sheet-like crystal aggregates, probably of mordenite. B) Pseudohexagonal plates of kaolinite with different thicknesses. C-D) Feldspar crystals with rugged and altered surfaces \_\_\_\_\_ 53

**Figure 26.** Secondary-electron SEM images of smectite in sample 2021-MAC-035 (“smectite with mica” type). A-B) Wavy, flaky masses of smectite (Sme) with curved



edges. C) Tightly interwoven, elongated flakes of smectite. D) Wavy flakes with curved edges (left), and irregular and sharp masses (right) of smectite \_\_\_\_\_ 54

**Figure 27.** Secondary-electron SEM images of sample 2021-MAC-050 (“smectite with mica” type). A-B) Angular fragments of feldspar (Fsp) altered to smectite (Sme). C) Tabular mica (Mca) crystal (~750  $\mu\text{m}$ ) surrounded by crystal fragments of feldspar altered to clay minerals. D) Close up of C), showing the tabular mica crystal (upper right) in a fragmentary matrix composed of feldspar and cemented by smectite \_\_\_\_\_ 55

**Figure 28.** Secondary-electron SEM images of sample 2021-MAC-039 (“mica with kaolinite subgroup minerals” type). A) Tabular crystals of feldspar (Fsp) and euhedral grains of quartz (Qz) embedded in a mass of kaolinite (Kln). B) Detail of a mica (Mca) tabular crystals with an irregular surface. C) Small (<5  $\mu\text{m}$ ), subhedral feldspar crystal, partially altered to and embedded in a mass of kaolinite. D) Flaky, undulated grains of mica embedded in a mass of kaolinite \_\_\_\_\_ 56

**Figure 29.** TEM data of sample 2021-MAC-038 (“mica with kaolinite subgroup minerals” type). A-B) Bright-field images of pseudo-hexagonal-shaped platelets of kaolinite (Kln). C) Electron diffraction of kaolinite showing crystal parameters  $a=5.11 \text{ \AA}$  ( $2*2.55 \text{ \AA}$ ) and  $b=8.88 \text{ \AA}$  ( $2*4.44 \text{ \AA}$ ). D) TEM-AEM spectrum of kaolinite. E) Halloysite (Hly) crystals with a tubular morphology and basal sections, with lengths >200 nm \_ 57

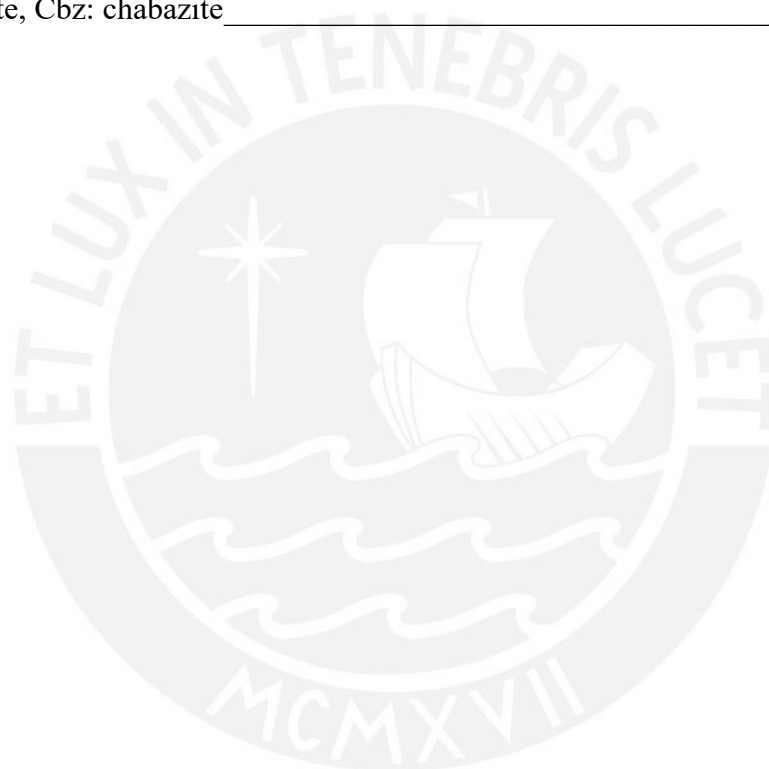
**Figure 30.** TEM data of sample 2021-MAC-049 (“smectite with mica” type). A) Bright-field image of smectite (Sme) particles (bright and dark) and B) its representative TEM-AEM spectrum. C) High resolution TEM image of the frame area in A showing  $d_{001}$  of 10.23  $\text{\AA}$  and 10.26  $\text{\AA}$  in smectite. D) Electron diffraction pattern of smectite aggregates from which crystal parameters  $a = 5.1 \text{ \AA}$  and  $b = 8.9 \text{ \AA}$  were calculated. E) Bright-field image, F) electron diffraction with crystal parameters ( $a = 5.14 \text{ \AA}$  and  $b = 8.88 \text{ \AA}$ ), and G) TEM-AEM spectrum of kaolinite (Kln) \_\_\_\_\_ 58

**Figure 31.** TEM data of sample 2021-MAC-050 (“smectite with mica” type). A) Bright-field image of a feldspar (Fsp) particle with scaly particles of smectite (Sme) forming rose-shaped aggregates on its edges. B) Detail of an isolated rose-shaped smectite aggregate. C) High-resolution TEM image of smectite with a  $d_{001}$  11.05  $\text{\AA}$ . D) Smooth ring electron diffraction pattern with spacing of 10.96  $\text{\AA}$ , and E) TEM-AEM spectrum of a smectite particle \_\_\_\_\_ 59

**Figure 32.** Classification of lithium deposits mostly based on *Bowell et al. (2020)*, highlighting the proposed “mixed” primary mica – secondary clay/zeolite volcanogenic deposit type for the Falchani deposit. The zeolite\* and primary-mica\* endmembers within volcanogenic lithium deposits are merely indicative since they have not been described

## List of Tables

<b>Table 1.</b> Main lithium minerals _____	16
<b>Table 2.</b> Lithium mine production, reserves, and resources in the world in 2021. Extracted from United States Geological Survey 2023. _____	18
<b>Table 3.</b> Lithium Resources in Falchani Project. LRT: Lithium Rich-Tuff; BX: Breccia (Upper and Lower Breccia); Li Conversion Factors as follows: Li: $\text{Li}_2\text{CO}_3=5.323$ ; $\text{Li}_2\text{O}:\text{Li}_2\text{CO}_3=2.473$ . Modified from The Mineral Corporation (2019) _____	24
<b>Table 4.</b> Comparative data of major element whole rock compositions of the three members of the Quenamari Formation (Chacacuniza, Sapanuta and Yapamayo; López 1996) _____	41
<b>Table 5.</b> Minerals identified in samples of Lithium-rich Tuff from the Macusani Volcanic Field using XRD. Pl: plagioclase, Mca: mica, Qz: quartz, Kfs: K-feldspar, Kln: kaolinite subgroup minerals, Sme: smectite, Crs: cristobalite, Mor: mordenite, Mut: mutinaite, Cbz: chabazite _____	44



## 1. INTRODUCTION

### 1.1. Lithium: a critical raw material for the global economy

The growing awareness of anthropogenic global warming has generated international convergence upon the objective of an energy transition from fossil fuels to renewable energy sources to reach carbon neutrality (Jowitt and McNulty 2021; European Commission 2023). This global purpose affects not only the energy sector but also our society and economy (IRENA 2019). This shift requires the development of clean and renewable energies, increasing the demand for raw materials and the associated concern over their supply (Lee et al. 2020; Jowitt and McNulty 2021). Unfortunately, if the demand for key raw materials exceeds its supply, the long-awaited transition might slow down (IRENA 2019).

Raw materials of mineral origin are essential not only for the production of domestic services but also developing eco-efficient energy technologies (e.g., wind turbines, solar panels, electric vehicles, among others; Bauer et al. 2011; European Commission 2023). According to the European Commission (2023), a *critical raw material (CRM)* is one that has a high economic importance and a high risk of supply disruptions (Fig. 1). Similarly, the United States Geological Survey defines as critical those nonfuel mineral materials that are essential to the economic and national security of the United States whose supply chain is vulnerable to disruption, and that is essential in the manufacturing of products that are crucial for the national economy or security (Fortier et al. 2018). Both institutions list lithium as critical.

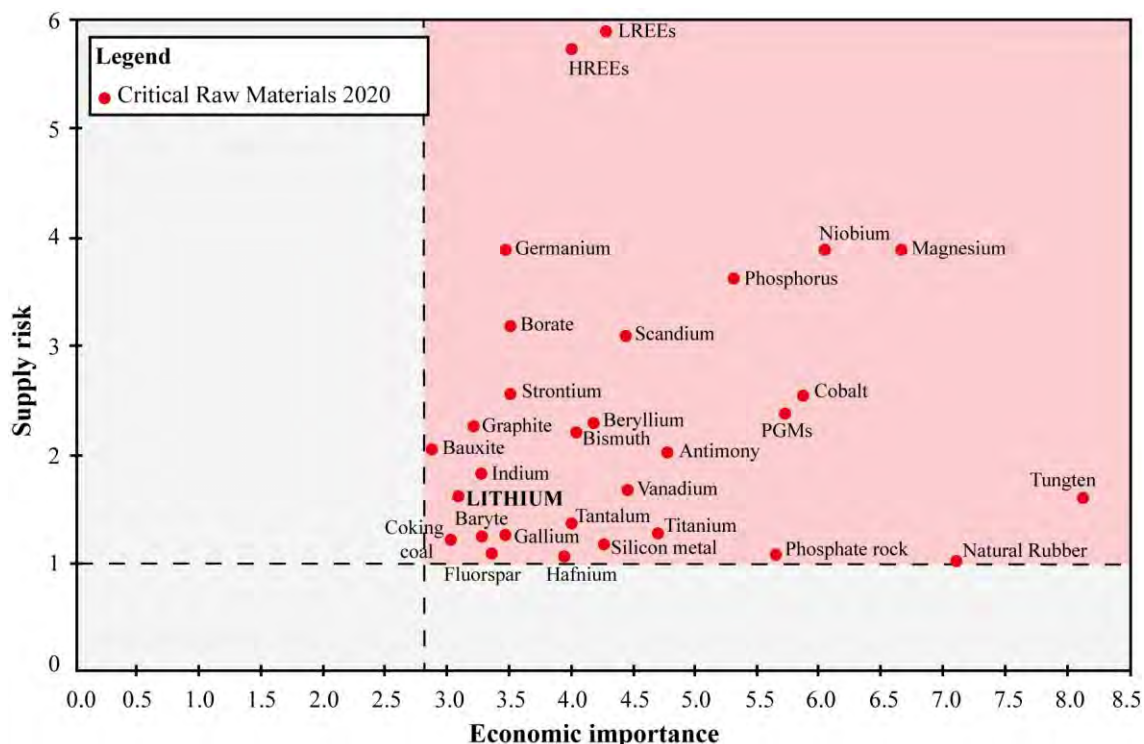


**Figure 1.** Critical Raw Materials for the European Commission (2023) based on their supply risk and economic importance, including lithium

Lithium is mainly traded as i) mineral concentrates extracted from lithium minerals such as spodumene, petalite, and lepidolite; ii) lithium chemicals or mineral compounds, chiefly lithium carbonate ( $\text{Li}_2\text{CO}_3$ ) and chloride ( $\text{LiCl}$ ), and to a lesser extent as lithium bromide ( $\text{LiBr}$ ) and hydroxide monohydrate ( $\text{LiOH}\cdot\text{H}_2\text{O}$ ); and iii) lithium metal, which is obtained by electrolysis from lithium chloride (Evans 2014; Bradley et al. 2017a; Bibienne et al. 2020). Lithium production is expressed in tonnes of lithium carbonate equivalents (LCEs) considering that Li-carbonate is the major chemical compound (Evans 2014; Bradley et al. 2017a). In that way, lithium carbonate, with 0.188 wt.% Li corresponds to one LCEs, lithium metal products are 5.32 LCEs, and lithium bromides are 0.425 LCEs (Evans 2014).

The principal applications of lithium are divided according to its chemical or non-chemical demand (Evans 2014). Non-chemical lithium (i.e., mineral concentrates) are used in ceramics and glass fabrication (Evans 2014). For example, the addition of lithia ( $\text{Li}_2\text{O}$ ) in ceramics or glass production reduces the melting temperature and increases density, thus lowering production costs (Evans 2014; Bibienne et al. 2020). As an example of comparison, a glass containing 15 wt.%  $\text{Li}_2\text{O}$  will have a melting point temperature of 500 °C, while the same glass containing 15 wt.%  $\text{K}_2\text{O}$  will have a melting

point of 850 °C (Garrett 2004). Chemical lithium is also used in glasses, ceramics, enamels, and glass ceramics for cookware and telescopic lenses (Evans 2014). The most important use of lithium carbonate is to produce cathode for Li-ion batteries, although it has been largely replaced by lithium hydroxide in such use (Sterba et al. 2019). Also, lithium carbonate is used in mental disorder medications such as bipolar disorder and is one of the few proven drugs that has an anti-suicidal effect, hence its classification as essential in medicine by the World Health Organization (Bradley and Jaskula 2014; Bibienne et al. 2020). Lithium hydroxide monohydrate is required in advanced rechargeable Li-ion batteries in plug-in electric-hybrid vehicles (PHEVs; Evans 2014), and also its  $^6\text{Li}$  content has been used in the production of tritium ( $^3\text{H}$ ) for nuclear weapons (Garrett 2004). Moreover, lithium hydroxides are used in greases, lubricants, and air conditioning systems as dehumidifiers (Kesler et al. 2012). In its anhydrous form, it is used as a  $\text{CO}_2$  absorbent in submarines and spaceships (Evans 2014; Bibienne et al. 2020). Lithium chloride is used in food processing for controlling humidity and in hospitals as a solution with a sanitizing effect (Evans 2014). Lithium bromide is used in absorption-refrigeration systems (Evans 2014). Lithium metal is used in primary non-rechargeable Li-batteries in calculators, cameras, and watches, providing a high electrochemical potential and a long operating life (Evans 2014; Bradley et al. 2017a). Finally, a lithium-aluminum-copper alloy is applied in the aerospace industry to reduce the weight of aircraft structures (Garrett 2004; Bradley et al. 2017a).

The future demand for lithium will depend on several factors including the growth of the population and the requirement of this critical raw material to hold back anthropogenic global warming through the development of clean energies (Kesler et al. 2012). Inevitably, it will boost the development of new rechargeable batteries, which at the same time will lead to an increase in lithium demand (Fig. 2; Bibienne et al. 2020). Then, by 2028 to 2030, the manufacturing of lithium batteries for electric vehicles is expected to correspond to 95 percent of the lithium demand (Azevedo et al. 2022).

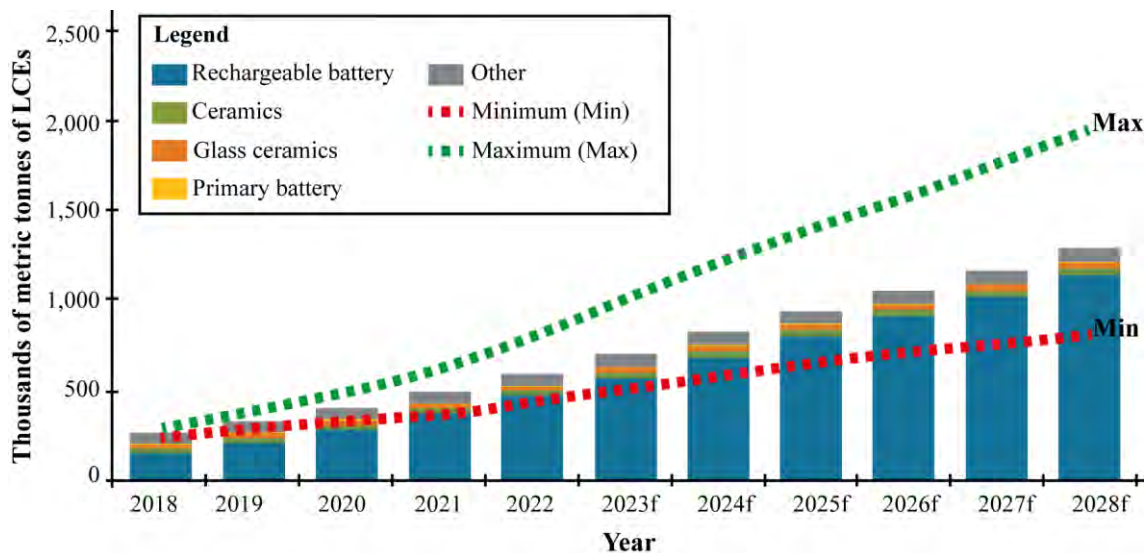


**Figure 2.** Bar chart of forecasts (f) of lithium over the decade 2018-2028, expressed in thousands of metric tonnes of LCEs. Major uses of lithium are indicated. The dotted green line indicates predicted maximum demand of LCEs, and the red one indicates predicted minimum demand of LCEs. Note that lithium demand in 2018 was about 300,000 tonnes of LCE, whereas it is expected that by 2028 it will reach 1.0-1.3 Mt of LCE. Modified from Bibienne et al. (2020)

Five factors have been identified to rule risk supply: i) geologic, with the study and identification of undiscovered lithium resources and evaluation of economic exploitation (reserves); ii) technical, since few countries are capable of extracting and processing the ore; iii) environmental and social; iv) political, taking into account the influence of governments; and v) economic, depending whether production and extraction costs of lithium can be paid by countries that require it or not (National Research Council 2008; European Commission 2023). In order to reduce the growing supply-demand gap, new technologies are under development to exploit unconventional lithium sources, including direct lithium extraction (DLE) and direct lithium to product (DLP), which not only hold the future supply of this material but also will allow to reduce the environmental and social footprint (Azevedo et al. 2022). Secondary supply, such as recycling Li-ion batteries, is also expected to increase in the following years and help cover part of the forecasted high demand for lithium (Azevedo et al. 2022).

According to Trading Economics (2023), the price of lithium has considerably increased in recent years as a consequence of its demand for the manufacture of batteries used in electric-hybrid vehicles (Fig. 3). For comparison purposes, at the end of the year 2020 the price of lithium carbonate dropped to a minimum value of 40,000 yuan/t (approx. 6,000 USD/t) while in November 2022 its price reached 600,000 yuan/t (approx. 83,500 USD/t; Trading Economics 2023).

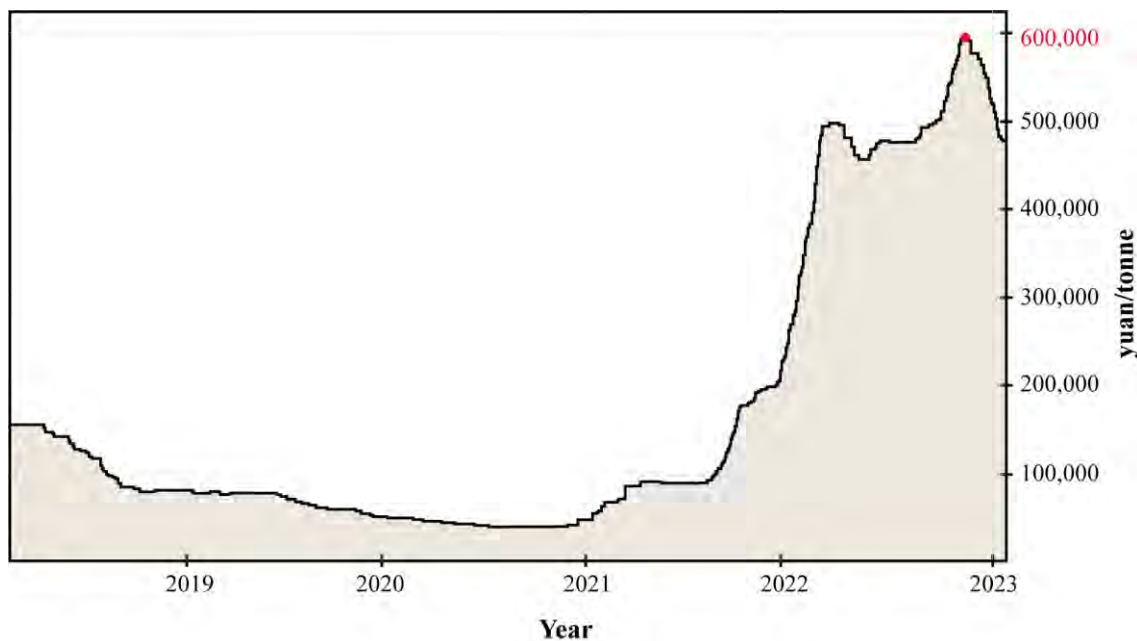


**Figure 3.** Variation of the prices of lithium carbonate in yuan/t during the last 5 years. The red point indicates the maximum price of lithium carbonate (approx. 6,000 dollars/t). Modified from Trading Economics (2023)

## 1.2. Geochemistry and mineralogy of lithium

Lithium, known by its chemical symbol Li, is the third chemical element in the periodic table and the lightest alkali metal. It is a soft and silvery-white metal with an atomic mass of 6.49 and a specific gravity of 0.534. Lithium has two stable isotopes in nature:  ${}^6\text{Li}$ , with an abundance of 92.1 – 92.6 %, and  ${}^7\text{Li}$ , with an abundance of 7.4 – 7.9 % (Pogge von Strandmann et al. 2020). Due to its high reactivity, lithium does not occur in its elemental form in nature but forms mineral compounds such as silicates and phosphates in rocks and chloride complexes in brines (Bradley and Jaskula 2014; Evans 2014).

Although lithium was the only metal produced in the Big Bang, the abundance of this element in the universe is very low compared to other light elements produced in that event, namely H and He (Lodders 2020). Due to the low binding nuclear energy of lithium isotopes (5.3 MeV/n to  ${}^6\text{Li}$  and 5.6 MeV/n to  ${}^7\text{Li}$ ), both nuclides are fragile and can be destroyed in Sun-like stars, thus explaining their low abundance. Even so, lithium is still present in the universe due to production by spallation (i.e., the break-up of nuclei by a collision) of heavier elements through interaction with galactic cosmic rays and by nuclear reactions in some red giant Li-rich stars (Lodders 2020).

The average lithium concentration in the bulk silicate Earth (equivalent to the Primitive Mantle) is 1.39 ppm. Lithium average contents in the mantle and the oceanic crust are 1.6 ppm and 4.3 ppm, respectively (Bradley et al. 2017a; Lodders 2020). In the bulk continental crust, the average lithium content is 18 ppm; in the upper continental crust, it is 20-40 ppm (Bradley et al. 2017a; Pogge von Strandmann et al. 2020). Lithium contents may uncommonly reach values higher than 7,000 ppm in granitic LCT (lithium-cesium-tantalum) pegmatites (London 2017; Michaud et al. 2021).

During magmatic differentiation processes, lithium shows a positive correlation with SiO<sub>2</sub>, which indicates a moderately incompatible element behavior in basaltic magmas (Penniston-Dorland et al. 2017; Chen et al. 2020). Also, lithium is incompatible with quartz and feldspar, and its concentration increases in residual melts as the crystallization of magmas proceeds (Stewart 1978; London 2017). Then, minerals in which Li is an essential component could be used as indicators of the degree of differentiation of the granitic melt from which they were deposited (London 2017).

Due to its hydrophilic properties, lithium is highly soluble during weathering of silicate rocks and easily transported primarily in its ionic form (Aral and Vecchio-Sadus 2008; Bradley et al. 2017a). Once dissolved, lithium partitions into solution (e.g., rivers, groundwaters) and secondary weathering minerals (e.g., clays, oxides, and zeolites; Pogge von Strandmann et al. 2020). Whereas lithium is in trace concentrations in rivers (average value of 0.0015 ppm) and seawater (average value of 0.18 ppm), it may reach much higher contents in secondary minerals formed during weathering processes, commonly in the range of 70-500 ppm (Huh et al. 1998; Evans 2014; Pogge von Strandmann et al. 2020).

The isotopic composition of lithium is commonly expressed in the delta notation as  $\delta^7\text{Li}$  in per mil (‰), which is calculated using the following expression:

$$\delta^7\text{Li} = \left( \frac{{}^7\text{Li}/{}^6\text{Li}_{\text{sample}}}{{}^7\text{Li}/{}^6\text{Li}_{\text{standard}}} - 1 \right) * 10^3$$

The used standard is NIST-RM8545, which represents a Li<sub>2</sub>CO<sub>3</sub> with  ${}^7\text{Li}/{}^6\text{Li} = 12.019$  (Marschall and Tang 2020). The  $\delta^7\text{Li}$  values of the Earth's reservoirs are  $+1.7\text{‰} \pm 1.0\text{‰}$  for continental crust,  $+3.5\text{‰} \pm 1.0\text{‰}$  for mantle, and  $+31.2\text{‰} \pm 0.3\text{‰}$  for modern seawater (Marschall and Tang 2020). The relative variation in abundances of both



isotopes is particularly useful to trace surface processes that occur during weathering of rocks, in which Li isotopes strongly fractionate (Pogge von Strandmann et al. 2020). In contrast, the use of lithium isotopes to trace high-temperature processes has been mostly discarded due to the high diffusion of this element at igneous and metamorphic temperatures (Marschall and Tang 2020).

Regarding the mineralogy of lithium, the first described lithium mineral, petalite (Table 1), was identified in 1817 by the chemist Johan Arfvedson (Evans 2014). To date, the International Mineralogical Association has approved 112 minerals containing essential lithium (<https://www.mindat.org/element/Lithium>). However, it is noteworthy that some rare Li minerals are restricted to a single locality. Approximately 73% of the lithium minerals are silicates, 19% are phosphates, and 8% include other mineral types (carbonates, fluorides, oxides, hydroxides, borates, and arsenites; Grew 2020). In addition, lithium may occur in trace amounts, mostly substituting magnesium, in rock-forming minerals (Bradley et al. 2017a).

According to the lithium mineral classification of pegmatites by London (2017), the principal Li minerals include aluminosilicates, micas, tourmalines, and phosphates (Table 1). In granitic pegmatites, the most important Li-bearing mineral is the inosilicate spodumene, which is found along with the nesosilicate eucryptite and the phyllosilicate petalite (Table 1; London 2007; Brooks 2020). In LCT pegmatites, lithium micas belong to the lepidolite solid solution between trilithionite and polyolithionite endmember compositions. In non-LCT pegmatites, chiefly in those of the NYF (niobium-yttrium-fluorine) family, zinnwaldite occurs, which is a solid solution between siderophyllite and polyolithionite. Lithium end-members of the tourmaline group are elbaite, rossmanite, and fluor-liddicoatite, also commonly found in granitic pegmatites (London 2017; Grew 2020). Granitic Li-rich pegmatites may also show a variety of lithium phosphates, including the Li-Al amblygonite-montebbrasite solid solution and the Li-Mn-Fe triphylite-lithiophilite solid solution (London 2017; Grew 2020).

Lithiophorite and sugilite are Li-mineral species related to manganese deposits (Grew 2020). Hectorite – a sodium-magnesium-lithium clay mineral of the smectite family –, the phyllosilicates tainiolite and norrishite, and jadarite – a lithium-borosilicate that have been identified in sedimentary sequences in Serbia – are found in rhyolite caldera sequences (Bowell et al. 2020; Borojević Šoštarić and Brenko 2023). Lithium can also be

adsorbed in clay minerals such as illite, kaolinite, smectites, or in interstratified smectite-illite (Castor and Henry 2020; Tang et al. 2022).

**Table 1.** Main lithium minerals. Hectorite has been cataloged as questionable, which applies to poorly characterized minerals whose validity could be doubtful.

Mineral	Classification	Formula	Li <sub>2</sub> O wt.%
Amblygonite	Phosphate	LiAl(PO <sub>4</sub> )F	7.40
Bikitaite	Tectosilicate	LiAlSi <sub>2</sub> O <sub>6</sub> ·H <sub>2</sub> O	7.32
Cookeite	Phyllosilicate	(LiAl <sub>4</sub> □) [AlSi <sub>3</sub> O <sub>10</sub> ] (OH) <sub>8</sub>	2.86
Elbaite	Cyclosilicate	Na (Li <sub>1.5</sub> Al <sub>1.5</sub> ) Al <sub>6</sub> (Si <sub>6</sub> O <sub>18</sub> ) (BO <sub>3</sub> ) <sub>3</sub> (OH) <sub>3</sub> (OH)	4.07
Eucryptite	Nesosilicate	LiAlSiO <sub>4</sub>	9.7-11.86
Hectorite	Phyllosilicate	Na <sub>0.3</sub> (Mg,Li) <sub>3</sub> (Si <sub>4</sub> O <sub>10</sub> )(F,OH) <sub>2</sub>	1.17
Holmquistite	Inosilicate	□ {Li <sub>2</sub> } {Mg <sub>3</sub> Al <sub>2</sub> } (Si <sub>8</sub> O <sub>22</sub> ) (OH) <sub>2</sub>	3.98
Jadarite	Nesosilicate	LiNaSiB <sub>3</sub> O <sub>7</sub> (OH)	7.28
Fluor-liddicoatite	Cyclosilicate	Ca (Li <sub>2</sub> Al) Al <sub>6</sub> (Si <sub>6</sub> O <sub>18</sub> ) (BO <sub>3</sub> ) <sub>3</sub> (OH) <sub>3</sub> F	2.61
Lithiophilite	Phosphate	LiMn <sup>2+</sup> (PO <sub>4</sub> )	9.53
Lithiophorite	Hydroxide	(Al, Li) Mn <sup>4+</sup> O <sub>2</sub> (OH) <sub>2</sub>	3.16
Montebrasite	Phosphate	LiAl(PO <sub>4</sub> )(OH)	7.4-10.21
Norrishite	Phyllosilicate	KLiMn <sup>3+</sup> <sub>2</sub> (Si <sub>4</sub> O <sub>10</sub> ) O <sub>2</sub>	3.25
Petalite	Phyllosilicate	LiAl (Si <sub>4</sub> O <sub>10</sub> )	4.50-4.73
Polyolithionite	Phyllosilicate	KLi <sub>2</sub> Al (Si <sub>4</sub> O <sub>10</sub> ) (F, OH) <sub>2</sub>	6.46
Rossmannite	Cyclosilicate	□(Al <sub>2</sub> Li) Al <sub>6</sub> (Si <sub>6</sub> O <sub>18</sub> ) (BO <sub>3</sub> ) <sub>3</sub> (OH) <sub>3</sub> (OH)	1.62
Simmonsite	Halide	Na <sub>2</sub> LiAlF <sub>6</sub>	7.71
Spodumene	Inosilicate	LiAlSi <sub>2</sub> O <sub>6</sub>	6-9
Sugilite	Cyclosilicate	KNa <sub>2</sub> (Fe <sup>3+</sup> , Mn <sup>3+</sup> , Al) <sub>2</sub> Li <sub>3</sub> Si <sub>12</sub> O <sub>30</sub>	3.04
Tainiolite	Phyllosilicate	KLiMg <sub>2</sub> (Si <sub>4</sub> O <sub>10</sub> ) F <sub>2</sub>	3.69
Trilithionite	Phyllosilicate	K(Li <sub>1.5</sub> Al <sub>1.5</sub> ) (AlSi <sub>3</sub> O <sub>10</sub> ) (F, OH) <sub>2</sub>	5.61
Triphylite	Phosphate	LiFe <sup>2+</sup> PO <sub>4</sub>	9.47

### 1.3. Overview of lithium deposits

Lithium resources and reserves in the world are mainly hosted in 3 types of deposits: i) *granitic pegmatite*, mostly of the LCT family; ii) *hydromorphic*, including brines in which Li-ions are found in saline solutions; iii) *volcanogenic*, including clay and jadarite deposit. In addition, deposits that may contain lithium in lesser proportions are iv) *manganese deposits* with a Li-rich hydrothermal imprint; and v) *bauxite deposits* (Figs. 4-5; Bradley et al. 2017a, b; Gourcerol et al. 2019; Bowell et al. 2020). Although the most important lithium resources and with the lowest processing costs are found in continental brines (58%), lithium is mostly extracted from pegmatites with conventional methods due

to their relatively higher lithium contents (Bradley et al. 2017a; Sterba et al. 2019; Karrech et al. 2020).

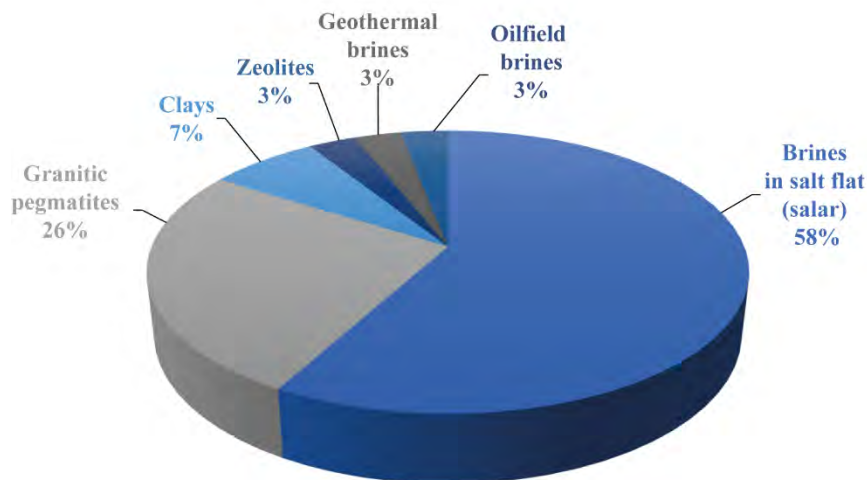


**Figure 4.** Lithium resources distribution in the world according to type of deposit. Adapted from Bradley and Jaskula (2014). Hydromorphic deposits include salt flat (salar), geothermal, and oilfield brines and volcanogenic deposits include clays and zeolites

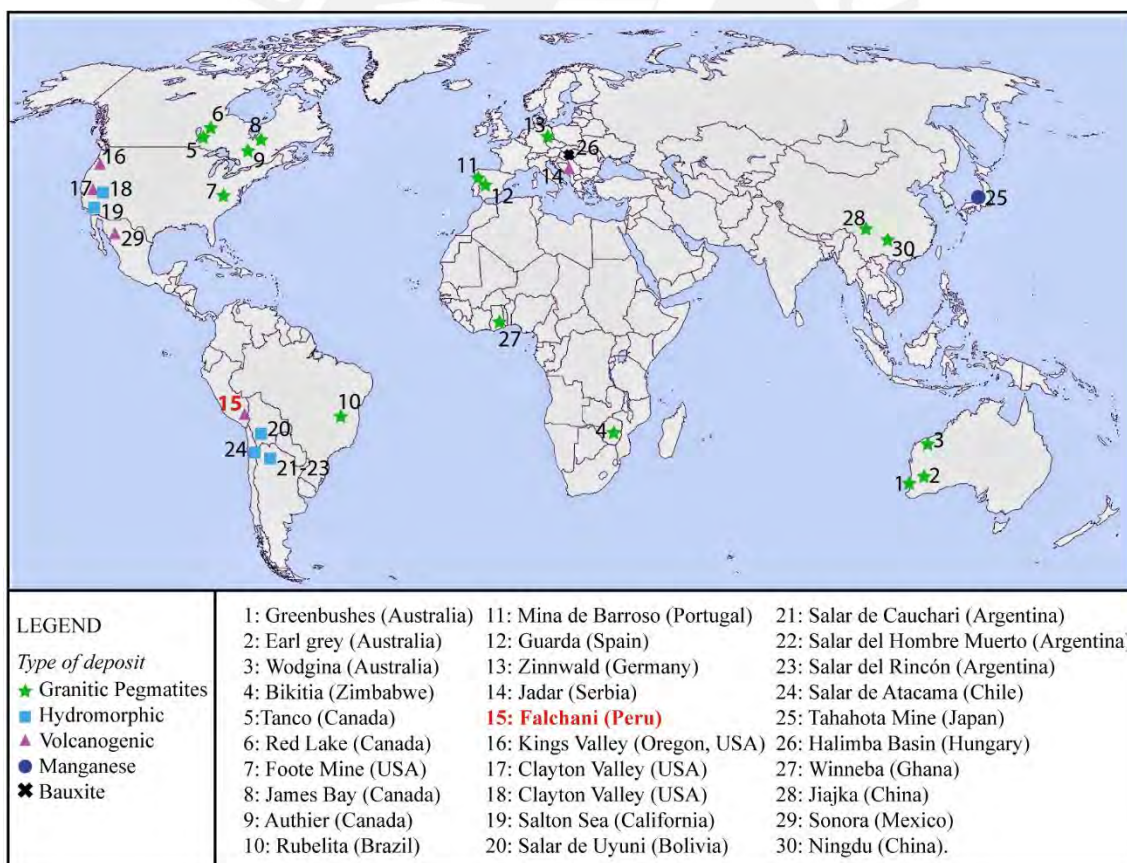


**Figure 5.** Major lithium deposits in the world. Modified from Bowell et al. (2020)

At the present, world lithium production is concentrated in Australia (spodumene operations), Latin America (brine operations), China (unknown origin), and smaller

productions in Russia, Portugal, the United States, and Zimbabwe (Table 2; United States Geological Survey 2023). Furthermore, new lithium sources to be developed in the future are found in Austria, Argentina, Bolivia, Chile, Peru, Portugal, Spain, and the United States, among others (Table 2, United States Geological Survey 2023).

**Table 2.** Lithium mine production, reserves, and resources in the world in 2021. Extracted from United States Geological Survey 2023.

	<b>Mine production*</b>	<b>Reserves*</b>	<b>Resources*</b>
<b>Bolivia</b>	-	-	21,000,000
<b>Argentina</b>	5,970	2,700,000	20,000,000
<b>United States</b>	-	1,000,000	12,000,000
<b>Chile</b>	28,300	9,300,000	11,000,000
<b>Australia</b>	55,300	6,200,000	7,900,000
<b>China</b>	14,000	2,000,000	6,800,000
<b>Germany</b>	-	-	3,200,000
<b>Congo</b>	-	-	3,000,000
<b>Canada</b>	-	930,000	2,900,000
<b>Mexico</b>	-	-	1,700,000
<b>Czechia</b>	-	-	1,300,000
<b>Serbia</b>	-	-	1,200,000
<b>Russia</b>	-	-	1,000,000
<b>Peru</b>	-	-	880,000
<b>Mali</b>	-	-	840,000
<b>Brazil</b>	1,700	250,000	730,000
<b>Zimbabwe</b>	710	310,000	690,000
<b>Spain</b>	-	-	320,000
<b>Portugal</b>	900	60,000	270,000
<b>Namibia</b>	-	-	230,000
<b>Ghana</b>	-	-	180,000
<b>Finland</b>	-	-	68,000
<b>Austria</b>	-	-	60,000
<b>Kazakhstan</b>	-	-	50,000
<b>Other</b>	-	3,300,000	-
<b>Total</b>	107,000	26,000,000	76,318,000

\*Note: Mine production in 2021, reserves, and resources in metric tonnes (t).

### 1.3.1. Pegmatite deposits

Rare element granitic pegmatites of both the LCT and NYF families stood out as the main Li source despite the high costs of its processing that are offset by its relatively high contents compared to brine deposits (Fig. 4; Karrech et al. 2020). Pegmatites of the LCT family are the main *hard-rock* source of lithium and are also enriched in other *high-tech* metals such as Cs, Ta, Be, Rb, Nb, and Sn (London 2017; Bowell et al. 2020). Pegmatites of the LCT family have a peraluminous nature (i.e., high alumina content) and

form by anatexis of Li-enriched sedimentary rocks and extreme differentiation of I-type granites (Stewart 1978; Bradley et al. 2017b; Grew 2020). Li-rich pegmatites get enriched in incompatible elements due to sequential crystallization of a single fluid, multiple fluids injections, or a late hydrothermal alteration (London 2008). The most abundant lithium mineral in LCT pegmatites is spodumene; other important lithium silicate minerals in LCT pegmatites include polyolithionite-trilithionite (lepidolite), amblygonite, petalite, elbaite, montebrasite, among others (Bowell et al. 2020). In NYF pegmatites, simmonsite is found (Grew 2020). In addition, metasomatic rocks associated with contact zones of pegmatites present holmquistite as a characteristic Li-bearing mineral (Grew 2020).

The pegmatitic deposits with the highest tonnages are found in Australia, including Greenbushes (Fig. 5; 118 Mt of spodumene ore with a grade of 2.4%  $\text{Li}_2\text{O}$  – i.e., 7.12 of LCE), Earl Grey (Fig. 5; 189 Mt of spodumene ore with a grade of 1.5%  $\text{Li}_2\text{O}$ ), and Wodgina (Fig. 5; 233 Mt of spodumene ore with 1.21%  $\text{Li}_2\text{O}$  grade; Karrech et al. 2020). Other important pegmatite deposits and advanced prospects include Tanco in Canada (Fig. 5; 7.3 Mt of spodumene ore with 2.76%  $\text{Li}_2\text{O}$ ), San José in Spain (112 Mt of spodumene ore with 0.61%  $\text{Li}_2\text{O}$ ), and Bikita in Zimbabwe (Fig. 5; 23 Mt of spodumene, lepidolite and petalite ore with 1.4%  $\text{Li}_2\text{O}$  grade; Bradley et al. 2017b).

### 1.3.2. Hydromorphic deposits

The most important hydromorphic Li deposits consist of continental brines, which nowadays stand out as the preferred source of lithium (Fig. 5; Bowell et al. 2020). Lithium brines are normally hypersaline (1.7 – 24 times more saline than seawater) solutions that are near saturation for many compounds and may contain high concentrations of dissolved lithium ions (Bowell et al. 2020).

Continental lithium brine deposits develop in endorheic basins containing a salar and/or salt lake, allowing its concentration in arid environments (Munk et al. 2016). These deposits are associated to surface- and ground-waters that contain important quantities of lithium derived from igneous and/or hydrothermal activity (Evans 2014; Munk et al. 2016; Bradley et al. 2017a).

South American brine deposits in the so-called *Lithium Triangle of the Andes* occur at shallow depths and are considered the largest brine deposits worldwide (Fig.6; Evans 2014; Vilca 2020). The Lithium Triangle of the Andes contains more than 50% of

the global resources of lithium and delimits a strategic zone for the exploration of this element in Chile, Argentina, and Bolivia (The Mineral Corporation 2019; Vilca 2020; United States Geological Survey 2023). In Chile, lithium-rich continental brines include Salar de Atacama (Fig. 5; 6300 Kt of Li with 0.184 wt.% Li) and Salar Maricunga (269 Kt Li with 0.117 wt.% Li). In Bolivia is the Salar de Uyuni (Fig. 5; 3600 Kt Li with 0.045 wt.% Li), and in Argentina are the Salar Centenario (921 Kt Li with 0.045 wt.% Li), Salar del Hombre Muerto (835 Kt Li with 0.071 wt.% Li), Salar Cauchari (282 Kt Li with 0.069 wt.% Li), and Salar del Rincón (203 Kt Li with 0.032 wt.% Li; *Bowell et al. 2020*).

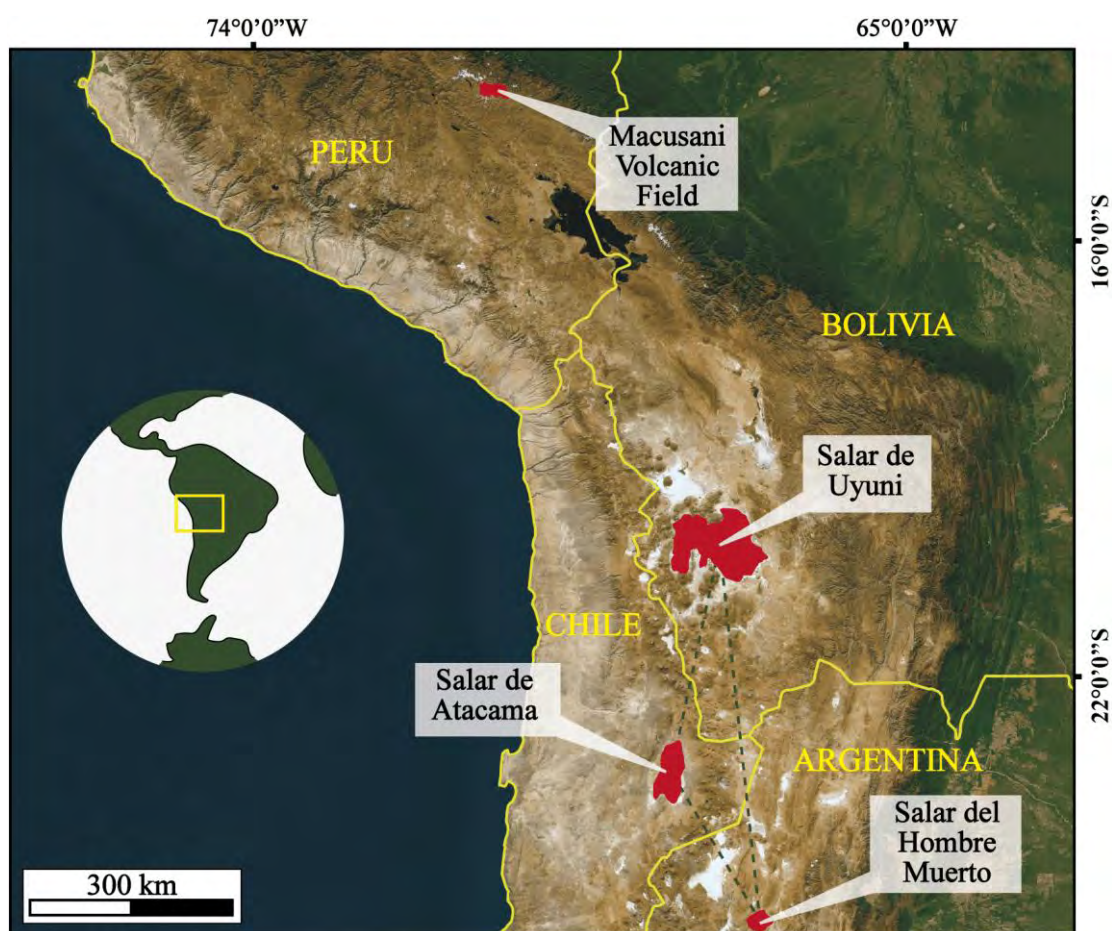


**Figure 6.** Location of the Macusani Volcanic Field to the north of the Lithium Triangle of the Andes, which is delimited by Salar Uyuni (Bolivia), Salar de Atacama (Chile), and Salar del Hombre Muerto (Argentina)

Significant salar lithium deposits are also found in the Clayton Valley basin in Nevada, USA (Fig. 4; 41 Kt Li with 0.012 wt.% Li), where lithium-rich brines and clays are described; the latter includes hectorite, which has been interpreted as the remaining of a former brine system (*Bradley et al. 2017a*).

Unconventional hydromorphic lithium sources include geothermal and oilfield brines. Lithium extraction as a by-product of geothermal brines may become a

fundamental source of lithium in the future (Brooks 2020; Toba et al. 2021). Although lithium concentration is relatively low, the ratio between Li and other dissolved elements is similar to continental brines with 100-200 ppm Li (Kesler et al. 2012). One of the most enriched geothermal brine sources is found in Salton Sea in the U.S. (Fig. 5; up to 286 mg/L Li; Thompson and Fournier 1988; Toba et al. 2021). Lithium concentration in oilfield brines may typically contain more than 50 mg/L Li as identified in the Jurassic Smackover formation (up to 112 mg/L; Howell et al. 2020) in Texas, in North Dakota (~400 to 118 mg/L), Wyoming (~90 to 93 mg/L), and Oklahoma (51 to 70 mg/L; Collins 1976).

### 1.3.3. Volcanogenic deposits

Volcanogenic lithium deposits are closely related to secondary minerals such as clays, zeolites, or jadarite, with a genetic-spatial relation to felsic volcanic rocks in calderas.

In clay deposits, lithium may occur either within clay minerals – mostly as hectorite or in illite-smectite mixed-layer clays – or as an adsorbed ion to clay minerals (Howell et al. 2020). Lithium-clay deposits result from the interaction of pre-existing volcanic rocks enriched in lithium with atmospheric or hydrothermal fluids, triggering the deposition of secondary clay minerals (Howell et al. 2020).

One of the best examples of lithium clay deposits occurs in the McDermitt caldera, on the Nevada-Oregon border in the US (Castor and Henry 2020). The 40 x 25-km McDermitt caldera, in which lithium resources are hosted by tuffaceous sediments, is the largest clay deposit in the world (Castor and Henry 2020). Lithium occurs as Li-illite (chemically similar to tainiolite), hectorite and in mixed clay layers with a range of 2,000-3,000 ppm Li (Castor and Henry 2020). Within the McDermitt caldera, Kings Valley (Fig. 5) has become one of the most illustrative and highest-grade clay deposits (27 Mt Li with 0.395 wt.% Li). In this deposit, illite-tainiolite is the main lithium ore, followed by hectorite (Howell et al. 2020). In the Falchani deposit in Peru (Fig. 5; 0.9 Mt Li and 0.296 wt.% Li), lithium occurs as an adsorbed ion to hydrothermal clays in lacustrine sedimentary and rhyolite tuffaceous rocks, according to Howell et al. (2020); however, a detailed mineralogical characterization of the Falchani deposit is not available.

A less common lithium-boron deposit type is related to jadarite in the Neogene Jadar volcano-sedimentary basin in Serbia (Fig. 5; Gourcerol et al. 2019; Howell et al. 2020; Borojević Šoštarić and Brenko 2023). This basin has an LCT pegmatites basement, which could represent a local Li endowment, followed by jadarite precipitation due to the interaction between geothermal-hydrothermal fluids and volcano-sedimentary sequences (Gourcerol et al. 2019; Howell et al. 2020). The high contents of Li in the Jadar deposit (~156 Mt @ 1.8% Li<sub>2</sub>O; Borojević Šoštarić and Brenko 2023) rank it as one of the largest lithium deposits in the world (Howell et al. 2020).

#### **1.3.4. Manganese deposits**

In manganese deposits, lithium mineralization is associated with hydrothermal fluid circulation, and Li-bearing minerals include sugilite, lithiophorite, and norrishite (Gourcerol et al. 2019; Grew 2020). The occurrence of these lithium minerals along veins and fractures and radiometric dating evidence that the Li mineralization is younger than the sedimentary host rock (Grew 2020). For that reason, Grew (2020) suggests that lithium minerals are products of hydrothermal alteration. For example, in the Tahohata mine in Japan (Fig. 5), the lithium mineralization occurred during the alteration of a Cretaceous granodiorite intrusive by the circulation of hydrothermal fluids (Grew 2020).

#### **1.3.5. Bauxite deposits**

Secondary minerals such as lithiophorite and cookeite predominate in karst bauxite deposits, in which stratiform bauxite horizons are related to karst bedrocks (Gourcerol et al. 2019). In the Halimba basin (Fig. 5; Hungary), bauxites contain lithiophorite, which deposited from hydrothermal fluids (Bárdossy 2013; Gourcerol et al. 2019). In the Xinmin bauxite deposit, Tang et al. (2022) proposed Li enrichment due to surface runoff.

### **1.4. The discovery of a major lithium resource at Falchani**

In November 2017, the discovery of a major lithium resource in the Falchani concession, located in Macusani Volcanic Field (Carabaya Province, Puno Department), was announced. The Falchani concession belongs to the Falchani Lithium Project and consists of lithium-uranium exploration properties owned by Macusani Yellowcake S.A.C., the Peruvian subsidiary of American Lithium (formerly Plateau Energy Metals; The Mineral Corporation 2019).



In 2018, different national media, such as *Gestión* and *Redacción RPP* reported that the Falchani Project had estimated resources of 2.2-2.5 Mt lithium carbonate equivalents, considering it as ‘white gold’ and 130-132 Mt  $U_3O_8$  (Redacción RPP 2018). Ulises Solís, manager of Macusani Yellowcake, declared to *Gestión* (2018) that Falchani contains sufficient resources, which would increase with exploration, to become “*the largest lithium mine in the world, with a higher production than Chile, Bolivia and Argentina together*”. In addition, *Gestión* (2018) highlighted that by then, only 8,000 of 92,000 hectares owned by Macusani had been explored and that production would begin at the end of 2020.

Recent news published in May 2022 by *RPP noticias* indicates that the Macusani Yellowcake company has postponed the lithium production until 2023 due to various factors, such as the coronavirus pandemic (Agencia Reuters 2020) and social-environmental issues. At first, Vilca (2020) refers to administrative-judicial issues, reporting that 32 of the 151 concessions of Macusani Yellowcake are in litigation with INGEMMET. Furthermore, the Ministerio de Energía y Minas (MINEM) went into a discrepancy with Macusani Yellowcake since MINEM indicates that the project would be more feasible if lithium was not related to uranium, as it would represent a radiation danger for the population at Corani (Saldarriaga 2021).

The Falchani Lithium Project (Fig. 7) includes two concessions: Falchani and Ocasaca 4 (The Mineral Corporation 2019), in which exploration started as a result of a radiometric anomaly and superficial sampling. Lithium and uranium occurrences in the Macusani area are associated with Tertiary tuffs and ignimbrites of the Macusani Formation (a.k.a. Quenamari Formation; The Mineral Corporation 2019). In April 2018, a sample of tuff yielded a grade close to 4,000 ppm; although no lithium minerals were identified, clay alteration was recognized in the groundmass of the rhyodacitic tuffs (The Mineral Corporation 2019).

In the technical report by The Mineral Corporation (2019), a local stratigraphy was delimited, including, top to bottom, the *Upper Rhyolite*, the *Upper Breccia (UBX)*, the *Lithium-rich Tuffs (LRT)*, and *Lower Breccia (LBX)* (Table 3; The Mineral Corporation 2019).

**Table 3.** Lithium Resources in Falchani Project. LRT: Lithium Rich-Tuff; BX: Breccia (Upper and Lower Breccia); Li Conversion Factors as follows: Li:  $\text{Li}_2\text{CO}_3=5.323$ ;  $\text{Li}_2\text{O}:\text{Li}_2\text{CO}_3=2.473$ . Modified from The Mineral Corporation (2019)

<b>Lithium resources in the Falchani project</b>					
<b>Category</b>	<b>Zone</b>	<b>Metric Tonnes (Mt)</b>	<b>Li (ppm)</b>	<b><math>\text{Li}_2\text{CO}_3</math> (Mt)</b>	<b><math>\text{Li}_2\text{O}</math> (%)</b>
<b>Indicated</b>	LRT	42.53	3566	0.8	2.3
	LRT+BX	60.92	2954	0.96	0.64
<b>Inferred</b>	LRT	123.55	3275	2.14	2.12
	LRT+BX	260.07	2706	3.75	0.58

A second company exploring uranium-lithium in Macusani at that time was Fission 3.0 Corp. According to SIDEMCAT (2022), Fission 3.0 Corp. owns the Llama Norte and Llama Sur concessions near the Falchani Lithium Project (Fission 3.0 Corp. 2022). This company reported in 2016 that 13 out of 16 drill holes cut high-grade uranium ( $>1.21\%$   $\text{U}_3\text{O}_8$ ) and superficial (i.e., over 0.5 m deep) anomalies of lithium ( $>533$  ppm).

In 2018, INGEMMET started a project under the title “*Evaluación del Potencial de Litio en el Sur del Perú*” in different regions of Perú, such as Arequipa, Cusco, Huancavelica, Ica, Moquegua, Puno, and Tacna (Ronquillo et al. 2019). The main objective was to identify the presence of lithium in economic quantities in volcanic and plutonic rocks (Ronquillo et al. 2019). According to the analyzed samples, the highest lithium values were found in the central segment of a lapilli tuff sequence belonging to the Sapanuta Member of the Quenamari Formation in Puno, with 2,815 to 3,070 ppm Li; in contrast, they reported much lower Li values in the range between 135 and 342 ppm in the Chacacuniza and Picotani Members of the Quenamari Formation.

In June 2022, American Lithium Corp. (2022) announced the production of sulphate of potash (SOP, also known as potash or potassium sulphate) as a by-product of lithium, which provides an additional potential for the Falchani Project and an alternative fertilizer supply for Peru.

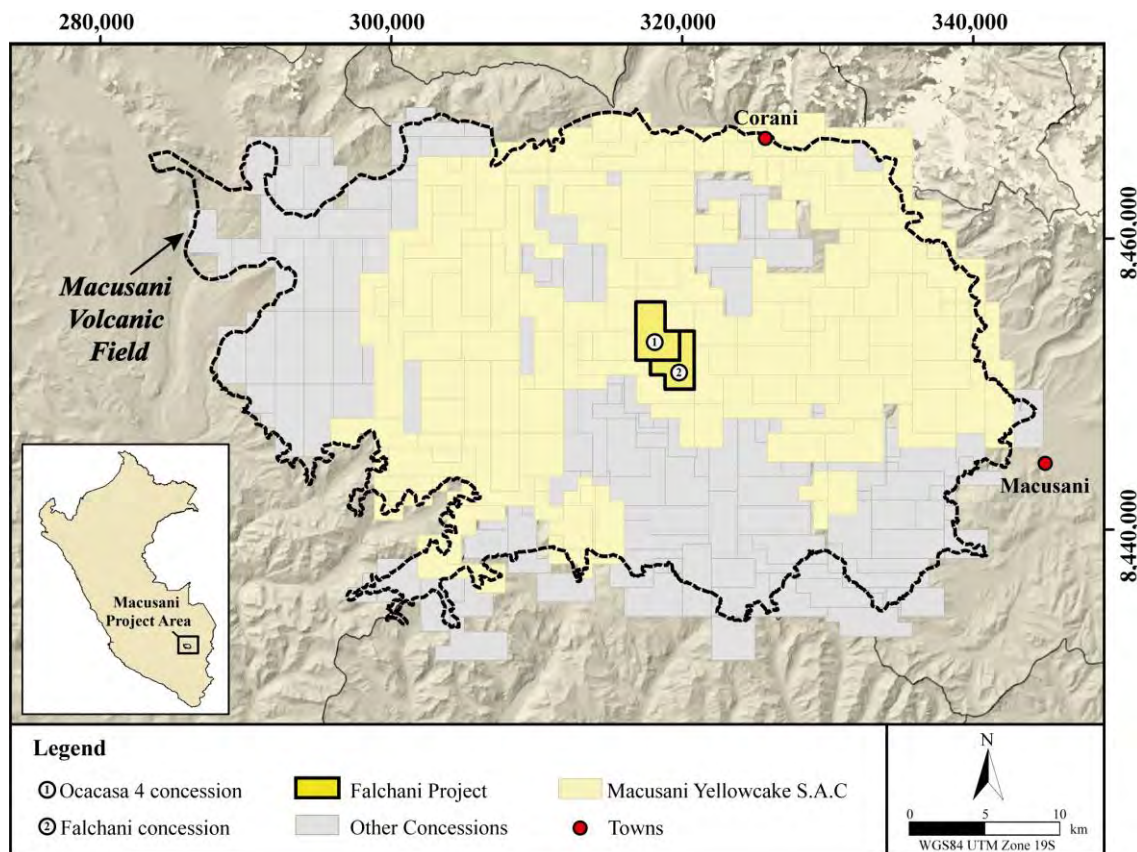


**Figure 7.** Exploration concessions in the Macusani Basin between the coordinates 280,000 and 360,000 East and 8,420,000 and 8,480,000 North. The Falchani Project covers an area of 1,700 ha (SIDEMCAT 2022)

### 1.5. Conundrum

In recent years, the demand for lithium has increased due to various factors, such as the energy transition, and is expected to continue to increase in the next years (IRENA 2019; European Commission 2023; Azevedo et al. 2022). Currently, the manufacture of rechargeable batteries is the sector with the highest demand for lithium (Bibienne et al. 2020), which has triggered an abrupt increase in its price from its minimum value of 5,400 USD/t in 2020 to the current (August 2023) 36,900 USD/t (Trading Economics 2023). The exploration for new – both conventional and non-conventional – lithium sources is necessary to secure its supply in the next decade.

Rhyolitic tuffs and ignimbrites from the Macusani Volcanic Field are known for their high lithium contents. This Lithium-rich Tuff is related to lacustrine sedimentary units in a volcanic field of important dimensions (the Falchani Lithium Project area alone comprises 93 hectares). The Falchani Lithium Project has indicated and inferred resources of 0.9 Mt Li and grades around 3,000 ppm Li (The Mineral Corporation 2019). The Li

resource is chiefly hosted by a tuff level, the so-called Lithium-rich Tuff, undocumented in previous studies of volcanic and volcanogenic rocks in the area (e.g., Pichavant and Montel 1988; Pichavant et al. 1988a, b; Cheilletz et al. 1992). Studies on the mineralogical expression of lithium in such rocks are still unavailable. In this sense, the discovery of the Falchani Lithium Project represents a favorable area to be surveyed through detailed mineralogical studies focused on the identification of clay minerals formed as a result of the circulation of meteoric and/or hydrothermal fluids that leached lithium from rhyolitic materials in a caldera basin (see Benson et al. 2017).

### **1.6. Objectives**

The main objective of this study is the assessment of the mineralogical expression of lithium in the Lithium-rich Tuff in the Macusani Volcanic Field.

Specific objectives include:

- To identify primary and secondary mineral phases in the Li-rich Tuff;
- To perform high-resolution mineralogy on the identified clay minerals;
- To ascertain the minerals that contribute to the lithium endowment; and
- To discuss the classification of the Falchani Lithium Project according to its environment of formation and mineralogy.

### **1.7. Hypothesis**

According to limited previous studies, it is expected that the Lithium-rich Tuff presents a homogeneous mineralogy composed of primary quartz, feldspar, and micas, as well as secondary clays and zeolites. It is expected that lithium is associated with secondary clay minerals either in their crystal lattice (i.e., lithium-clay phases) or as an adsorbed ion (ion-clay) due to the strong alteration/weathering undergone by the rhyolitic volcanic and volcanoclastic rocks within the Macusani Volcanic Field.

### **1.8. Justification**

Lithium is a critical element in growing demand mostly due to its use in the manufacture of electric vehicle batteries. The discovery and characterization of new sources of this element, including non-conventional ones, are crucial (Bibienne et al. 2020). Tuffs and ignimbrites in the Macusani Volcanic Field in south-eastern Peru, particularly those in the newly defined Lithium-rich Tuff unit, stand as non-conventional

volcanogenic lithium sources. On the other hand, reported resources for the Falchani Lithium Project rank it as one of the largest potential sources of lithium globally (Vilca 2020). Despite this, the mineralogy of ore-bearing rocks in the Falchani Lithium Project is largely unknown, notably that of clay minerals. The Falchani Lithium Project and surrounding areas represent an excellent opportunity to survey further the mineralogy of volcanogenic lithium deposits, including the high-resolution mineralogical characterization of clay minerals, potential bearers of Li in this type of deposits. The correct identification of clay minerals at the Lithium-rich Tuff from the Macusani Volcanic Field and their crystallochemical relation with lithium will also be relevant for the mineral and metallurgical processes for lithium recovery.

## **2. METHODOLOGY**

### **2.1. Sampling**

Seventy rock samples were collected during a fieldwork campaign developed in the Macusani Volcanic Field in October 2021. Out of these, thirty-one samples of Lithium-rich Tuff were selected for this thesis to investigate their mineralogy. A list of the analyzed samples and their respective sample code, description, and location (including coordinates of outcrop samples, collar drill cores, and concessions) is provided in Appendix A. The location of the studied samples is shown in Figure 8.

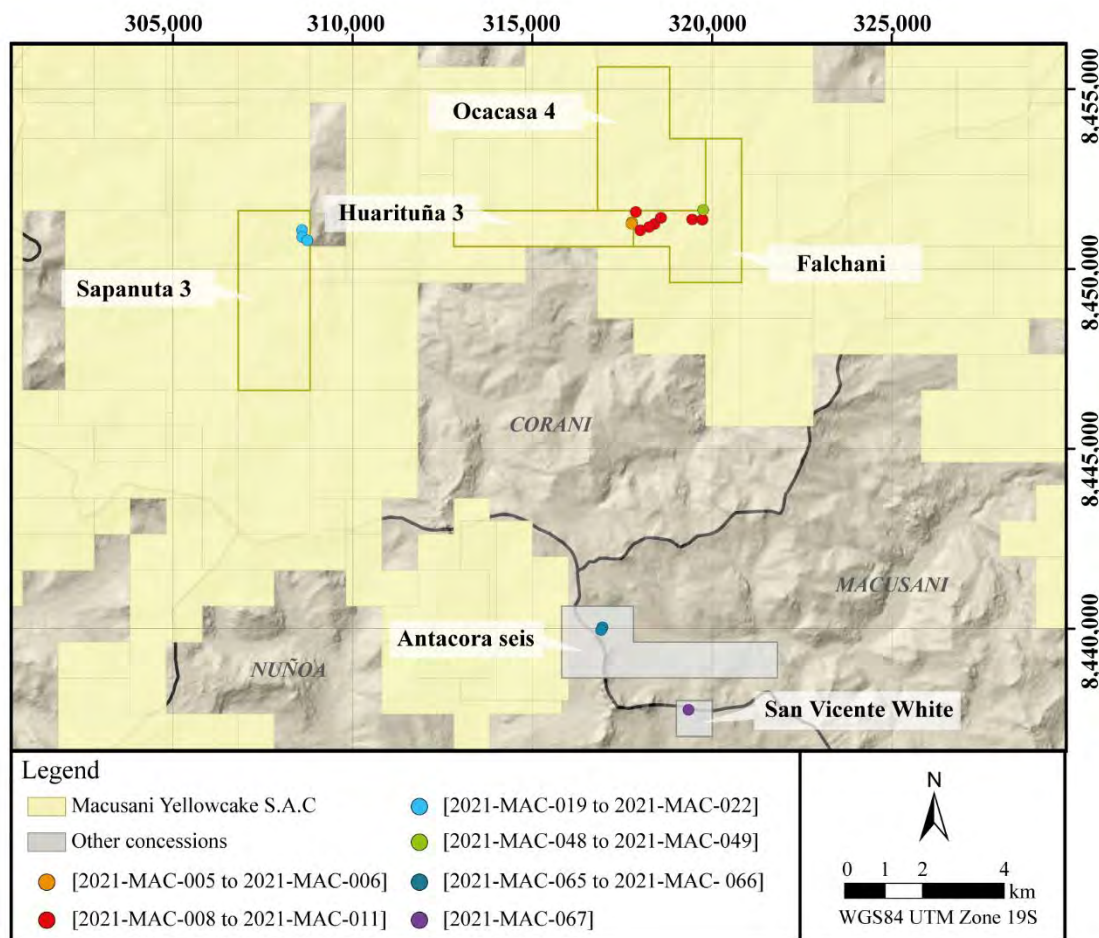


**Figure 8.** Location of the studied rock samples and exploration concessions owned by Macusani Yellowcake (SIDEMCAT 2022) in the Macusani Volcanic Field

## 2.2. X-Ray Diffraction

Previous to their analysis, weathered parts of the rock samples were removed by cutting with a diamond saw (Fig. 9A). The samples were then dried at 70°C for 24 hours and subsequently crushed with a jaw crusher (Fig. 9B) until a fine powder was obtained. A representative fraction of about 10 g of the crushed rock samples was obtained through rotary splitters (Figs.10A, B).

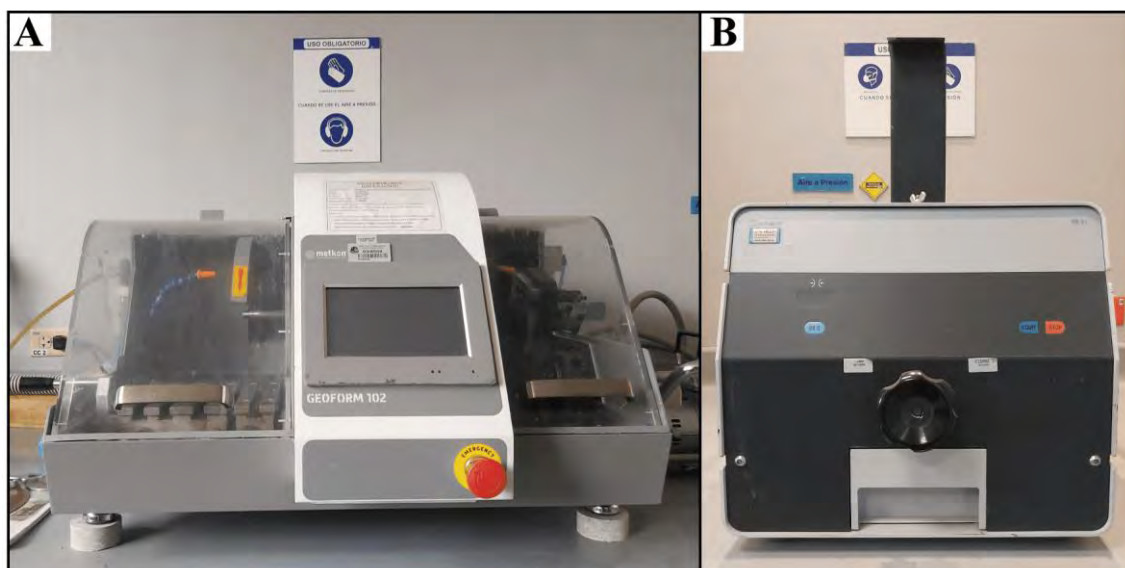


**Figure 9.** A) Diamond saw and B) jaw crusher available at the QEMSCAN laboratory (PUCP) used in this study

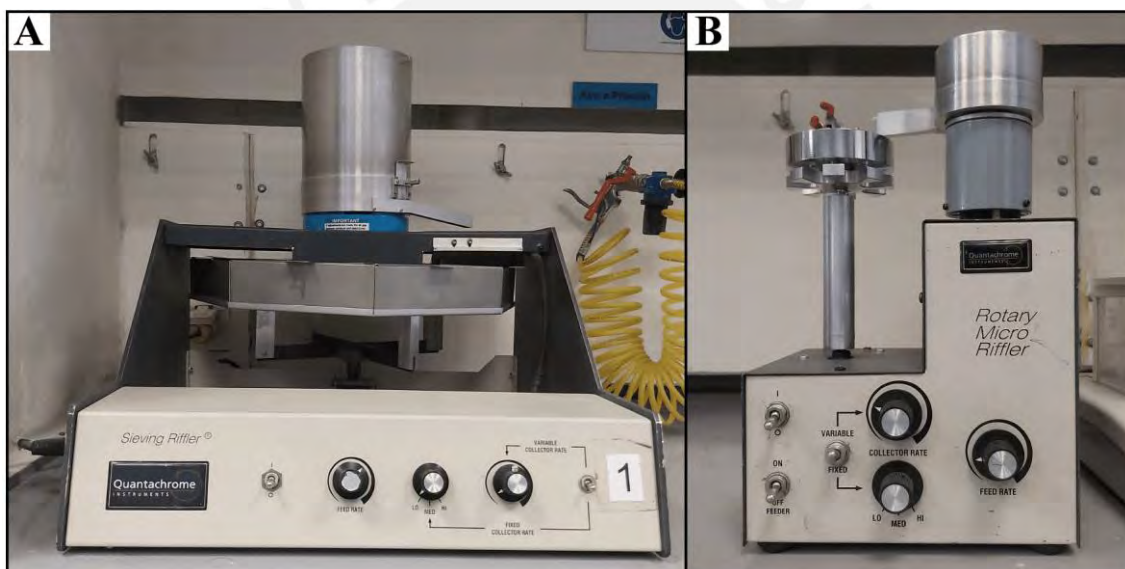


**Figure 10.** A, B) Rotary splitters used in this study at the QEMSCAN laboratory (PUCP)

The obtained representative fractions of the samples were ground in an agate mortar (Fig. 11A) and manually pressed using a glass plate to obtain a flat surface in cylindrical standard sample holders of 16 mm in diameter and 2.5 mm in height. Powder XRD data were collected with a Bruker D8 Discover diffractometer (Fig. 11B) in Bragg-Brentano  $\theta/2\theta$  geometry of 240 mm of radius at the Centro de Caracterización de Materiales of the Pontifical Catholic University of Peru (CAM-PUCP). Scanning from 4 to 70 ° ( $2\theta$ ) was performed at a step size of 0.017° and a scan time of 1 s per step. Nickel-filtered Cu  $K\alpha$  radiation ( $k = 1.5418 \text{ \AA}$ ) and 40 kV–40 mA conditions were used.

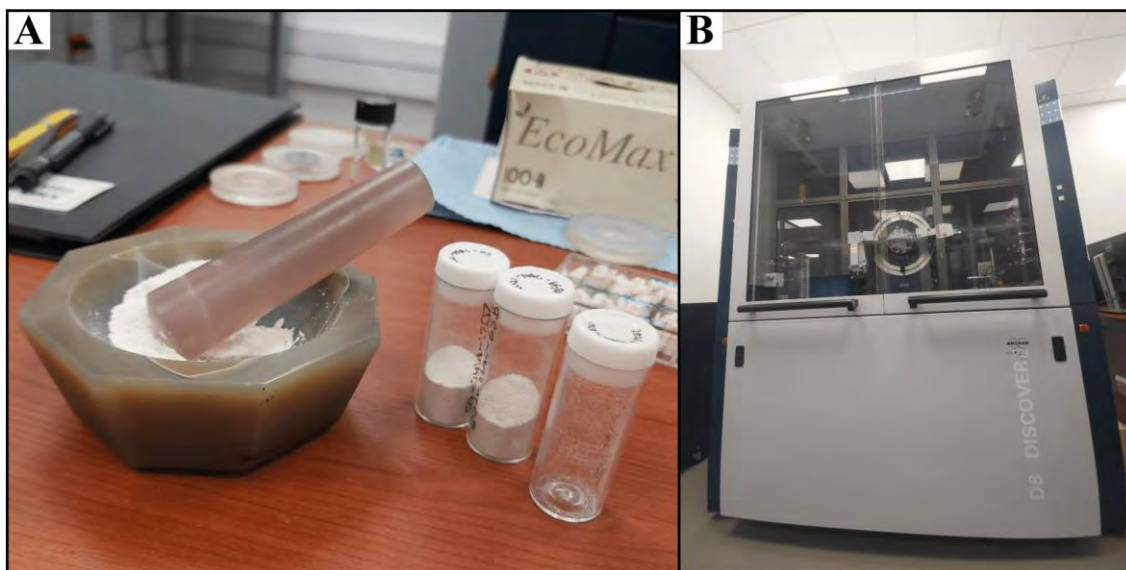


**Figure 11.** A) Agate mortar. B) Bruker D8 Discover diffractometer, available at CAM-PUCP

In addition, a total of seventeen clay-rich samples were selected for clay identification. For this purpose, the clay fraction was analyzed as oriented mounts (Moore and Reynolds 1989) at CAM-PUCP using the same equipment and setup as for powdered samples, although with variable scanning ranges as follows: (i) air dried, scanning from 2 to 50° (2 $\theta$ ); (ii) samples saturated with ethylene glycol, scanning from 2 to 30° (2 $\theta$ ); (iii) samples heated at 400°C, scanning from 2 to 30° (2 $\theta$ ); and (iv) samples heated to 550°C, scanning from 2 to 30° (2 $\theta$ ).

The software PANalytical X'Pert Highscore 2.0.1 was used to subtract the background of the diffractograms, detect the peaks, and assign mineral phases to each peak. To identify clay minerals, we followed the flow diagram proposed by the USGS, available at <https://pubs.usgs.gov/of/2001/of01-041/html/docs/flow/index.htm>. Results of XRD analyses are provided in Appendix B.

### 2.3. SEM-EDS

Four samples were studied using a Quanta 650 FEI scanning electron microscope (SEM) equipped with an EDAX-Octane Pro EDS microanalysis system at CAM-PUCP. The operating conditions for the analyses were 20 keV of accelerating voltage and a current of 5 nA. The images were obtained in secondary electron (SE) mode, and the composition of the imaged mineral phases was obtained using the EDS detector. Textures and morphologies of clay minerals, micas, and zeolites and their major element composition analyzed by SEM-EDS are presented in Appendix C.



## 2.4. TEM

A transmission electron microscopy (TEM) study was carried out on three samples (2021-MAC-38, 2021-MAC-49, and 2021-MAC-50). The samples were prepared as powders, dispersed in ethanol, sonicated, and deposited onto Formvar®-covered Cu grids. Mineral compositions were determined by analytical electron microscopy (AEM) in a HAADF Thermo Fisher Scientific TALOS F200X microscope at the Centro de Instrumentación Científica (CIC) of the Universidad de Granada. Operating conditions were 200 kV, with a point-to-point resolution of 1.2 Å in the TEM mode and 1.9 Å in the scanning (STEM) mode. The quantitative micro- to nano-chemical analyses in STEM mode were obtained by energy dispersive X-ray microscopy (AEM-EDX), using the Super-X system. Mineral standards were used to obtain K-factors according to the method proposed by Lorimer and Cliff (1976). High-resolution transmission electron microscopy (HRTEM) and selected-area electron diffraction (SAED) patterns were taken with a Titan instrument with an XFEG emission gun, spherical aberration corrector, and HAADF detector, operated at 300 kV at the CIC. The point-to-point resolution is 0.8 Å in the HRTEM mode and 2 Å in the STEM mode.

## 3. GEOLOGICAL SETTING

### 3.1. Geology of the Central Andes of southern Peru: The Cordillera Oriental

The Andes Cordillera is a mountain belt-shaped by the subduction of the oceanic Nazca plate beneath the South American continent (Kay and Mpodozis 2020; Ramos 1999; Wörner et al. 2018). The Andean mountain belt is geographically divided into the Northern (0-15°S), Central (15-33°S), and Southern Andes (33-56°S). The Central Andes, where the study area is located, is the largest of these segments (~4,000 km long). Major geomorphotectonic units in the Central Andes include the high-elevation Cordillera Occidental and Cordillera Oriental, the low-relief and high-elevation Altiplano-Puna Plateau, and the Subandean fold and thrust belt (Fig. 12; Kay and Mpodozis 2020). Sempere and Jacay (2008) divided the Central Andes into two domains: the *Western Magmatic Andes*, comprising the forearc, Cordillera Occidental, and SW Altiplano, which formed dominantly by magmatic accretion; and the *Eastern Tectonic Andes*, consisting of the NE Altiplano, Cordillera Oriental, and Subandean belt, where tectonic shortening was significant. In southern Peru, these two domains are separated by

a lithospheric boundary coinciding with the Urcos-Ayaviri-Copacabana-Coniri Fault System (Sempere and Jacay 2006).

In southern Peru, the Cordillera Oriental orogenic belt separates the Altiplano from the Sub-Andean thrust and fold belt. The so-called Inner Arc in the Cordillera Oriental is characterized by igneous rocks of peralkaline and peraluminous affinities in contrast with the calc-alkaline and alkaline affinities in the Main Arc domain stretching along the Cordillera de la Costa and Cordillera Occidental (Clark et al. 1990).

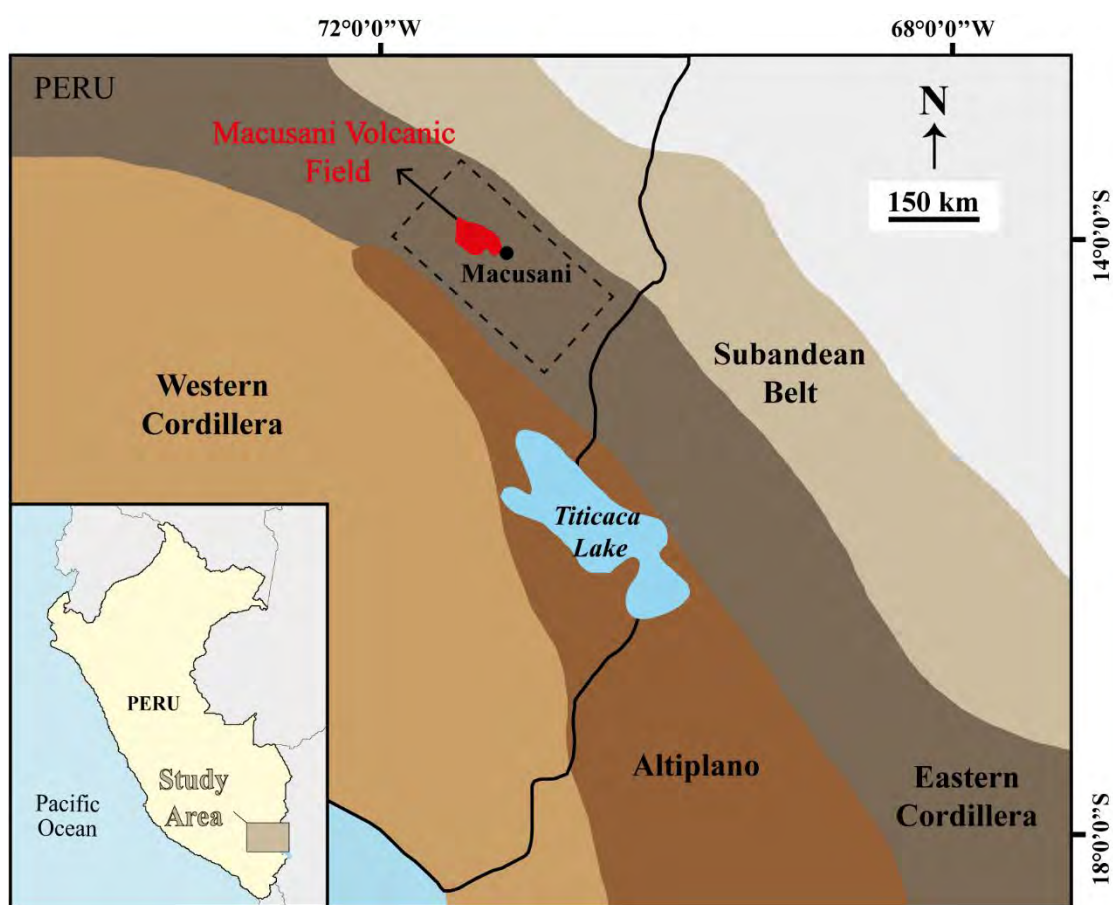


**Figure 12.** Geomorphotectonic structures of the Central Andes including the location of the Macusani Volcanic Field. The dotted-line box around Macusani Volcanic Field indicates the area covered in Fig. 13. Modified from Kontak et al. (1990)

The Triassic Mitu rifting in central Peru, which occurred in the context of the breakup of Pangea, roughly coincided with the present axis of *Cordillera Oriental* (Sempere et al. 2002; Spikings et al. 2016; Mišković et al. 2009). The termination of Triassic Mitu rifting due to the change in plate convergency in the latest Triassic and Early Jurassic (Spikings et al. 2016) was followed by Jurassic to the early Cretaceous establishment of subduction-related arc magmatism in the Central Andes and extensional back-arc basins formed in

southern Peru (Kay and Mpodozis 2020). In the late Cretaceous, there was a transition to compressional tectonism as a result of the westward shift of the South American plate (Mišković et al. 2009) and from the Late Oligocene to the present, high convergence rate plate dynamics, orogenic uplift, and strong magmatism have prevailed in the Central Andes (Cheilletz et al. 1992).

At the latitudes of southern Peru, Perez et al. (2016) subdivided the Cordillera Oriental into three tectonic/structural domains: i) the Central Andean Backthrust Belt, which is a SW-verging system of fold and thrust belt formed during the Andean orogeny by tectonic inversion of a Mesozoic back-arc basin; ii) the Precordillera de Carabaya, with high elevations separated by series of Tertiary intermontane basins, namely the Macusani, Crucero, and Ananea-Ancocala basins (Kontak et al. 1990; Sandeman et al. 1997), also known as the Macusani Structural Zone (Perez et al. 2016); and iii) the glaciated peaks of the Cordillera de Carabaya, also known as the Carabaya batholith, which is defined by a suite of Triassic plutons (Fig. 12; Kontak et al. 1990). Tertiary intermontane basins are spatially related to three major volcanic fields, represented geomorphologically by the Macusani (a.k.a. Quenamari), Cayconi, and Picotani mesetas (Fig. 13).

### **3.2. Regional geology of the Cordillera de Carabaya**

The Cordillera of Carabaya is a 195-km-long mountain range covering the southeastern segment of the Cordillera Oriental in Peru. Geographically, it extends between 13°07'S and 14°52'S and between 69°14'W and 70°16'W across the Cusco and Puno regions.

In the Cordillera de Carabaya, Neoproterozoic to Mesozoic volcanic, sedimentary, and metamorphic sequences, Triassic-Jurassic intrusive rocks, and Paleogene-Neogene volcanic and intrusive rocks are exposed (Kontak et al. 1990; Sandeman et al. 1996; Sánchez and Zapata 2003; Mišković et al. 2009). Rocks in Cordillera de Carabaya record three main periods of deformation: i) Eohercynian, during the Late Devonian-Early Carboniferous period, ii) Late Hercynian, during the late Permian, and iii) Andean, from Upper Cretaceous to Miocene (Laubacher 1978; Perez et al. 2016; Mišković et al. 2009).

The oldest rocks exposed in Cordillera de Carabaya are the gneisses, micaschists, and amphibolites of Neoproterozoic-Lower Cambrian age grouped under the name of Iscaybamba Complex (Sánchez and Zapata 2003). From the Ordovician to the Lower

Carboniferous, more than 15 km of (meta-)sedimentary strata comprising shales and sandstones were accumulated in the paleogeographic position that today encompasses the Cordillera de Carabaya (Sandeman and Clark 2004; Kontak et al. 1990). From the Lower Ordovician to the Upper Devonian, siliciclastic sedimentation took place in a large epicontinental marine basin covering part of the Brazilian shield and reached its maximum depths in the area covered by present-day Cordillera Oriental (Laubacher 1978). With a total thickness up to 7,000 m, the exposed Lower Paleozoic sequences consist mostly of the Middle Ordovician San José Formation and the Upper Ordovician Sandia Formation (Laubacher 1978). The San José Formation is characterized by a flyschoid sequence of fossiliferous black shales with small intercalations of sandstone levels. The Sandia Formation is a detrital sequence composed of quartzites interbedded with gray-black shales. Overlying this unit is the Ananea Formation, a >2,500-m-thick Silurian-Devonian sequence comprising black shales interbedded with quartzites in the uppermost part of this unit (Laubacher 1978).

The Upper Paleozoic lithologies exposed in this segment of the Cordillera Oriental are composed of carbonate and detrital facies that overlie unconformably on the Lower Paleozoic series and were folded during the Late Hercynian deformation phase (Laubacher 1978). They correspond to the Mississippian Ambo Group and the overlying Pennsylvanian Tarma Group. Materials belonging to both groups are composed of silico-calcareous marine deposits including sandstones, shales, and limestones (Laubacher 1978). In the earliest Permian, rocks of the Copacabana Group were deposited in an epicontinental sea. The Copacabana Group comprises fossiliferous limestones with intercalations of sandstones, and black shales, cherty limestones (Sempere et al. 2002).

The sedimentary continuity observed between the Early Permian Copacabana Group and the overlying Triassic Mitu Group is associated with the Middle Triassic continental rifting allowing the accumulation of the sedimentary and volcanic rocks (Laubacher 1978; Sempere et al. 2002; Rosas et al. 2007; Spikings et al. 2016). Spikings et al. (2016) indicating that the deposition of the Mitu Group started in the Middle Triassic (~240-245 Ma) and lasted until the Late Triassic (~220 Ma). It consists of a >2,000-m-thick succession of interbedded red siliciclastic (conglomerates, sandstones, and mudstones) and local carbonate and evaporite rocks with volcanic and volcanoclastic rocks, the assemblage intruded by hypabyssal to plutonic rocks (Sempere et al. 2002; Spikings et al. 2016). Volcanic rocks have a predominantly basaltic to andesitic composition and

alkaline intraplate signatures (Kontak et al. 1990). Most Triassic plutons exposed in the Cordillera de Carabaya were emplaced between  $236.3 \pm 0.9$  Ma and  $216.1 \pm 3.1$  Ma, coevally with the deposition of the Mitu Group, thus indicating that these events took place in the same tectonic environment (Spikings et al. 2016).

Younger Early Jurassic igneous complexes in the Cordillera de Carabaya include peralkaline volcanic and intrusive rocks of the Allincapac Complex ( $206 \pm 70.8$  Ma; Kontak et al. 1990) and Late Triassic-Early Jurassic peraluminous granitoids corresponding to the Carabaya granitoid batholith ( $190.3 \pm 2.5$  to  $216.1 \pm 3.1$  Ma; Kontak et al. 1990; Mišković et al. 2009).

The Cretaceous sequences in Cordillera de Carabaya belong to four units deposited in fluvial and eolian environments which, from bottom to top, include the Huancané, Viluyo, Ayabacas, and Vilquechico Formations (Laubacher 1978; Sandeman et al. 1996; Rodríguez et al. 2021). According to Rodríguez et al. (2021), the Huancané Formation consists of a sequence of massive white sandstones with a subordinate intercalation of shales deposited in a fluvial environment. The Viluyo Formation is composed of arkosic and/or quartz sandstones with the eventual presence of horizontal and crossed lamination. The Ayabacas Formation corresponds to grayish limestones deposited in an unstable shelf marine environment. Finally, the Vilquechico Formation is composed of greenish-gray shales deposited in a fluvial sedimentation environment with floodplains.

After a major uplift due to compressional tectonics during the Late Eocene, the emplacement of strongly peraluminous volcanic and intrusive rocks of the Crucero Supergroup and Crucero Intrusive Supersuite took place (Cheilletz et al. 1992; Sandeman et al. 1996, 1997). Oligocene-to-Miocene igneous and sedimentary rocks belonging to the Crucero Supergroup are exposed in and adjacent to the Macusani, Crucero, and Ananea-Ancocala intermontane depressions (Fig. 13), in which the igneous rocks represent the most recent manifestation of magmatic activity in the Inner Arc domain (Clark et al. 1990). Extrusive rocks of the Crucero Supergroup occur within four volcanic fields: Macusani (a.k.a. Quenamari), Cayconi, Picotani, and Antauta (Sandeman et al. 1996). The Crucero Supergroup encompasses two petrologically and temporally distinct assemblages: the older Picotani Group and the younger Quenamari Group (Sandeman et al. 1996, 1997).

The Picotani Group comprises a sequence that dominates in the Picotani Field and consists of an assemblage of rhyodacitic volcanic rocks intercalated with mafic flows of Late Oligocene – Early Miocene age (ca. 22-26 Ma; Sandeman et al. 1997, Sandeman and Clark 2003); in finer detail, volcanic rocks include S-type rhyodacites and rhyolites, lamprophyres, medium-to high-K calc-alkaline basalts, and shoshonites; subdivided into ten formations by Sandeman et al. (1997), namely Cerro Queuta, Cerro Huanchahuancane, Cerro Sumpiruni, Pucalacaya, Lago Perhuacarca, Cerro Moromoroni, Cerro Cancahuine, Pachachaca, Jama Jama, and Suratira. As for the Quenamari Group, it comprises a sequence of strongly peraluminous rhyolitic ash flows of Miocene age (ca. 6.5 - 17 Ma) that are prevalent in the Quenamari Field (Sandeman et al. 1997, Sandeman and Clark 2003). It was subdivided by Sandeman et al. (1997) into the Huacchane, Quebrada Escalera, and Macusani Formations. Whereas the Huacchane and Quebrada Escalera Formations occur in the Picotani Field, the Macusani Formation occurs in the Quenamari Field.

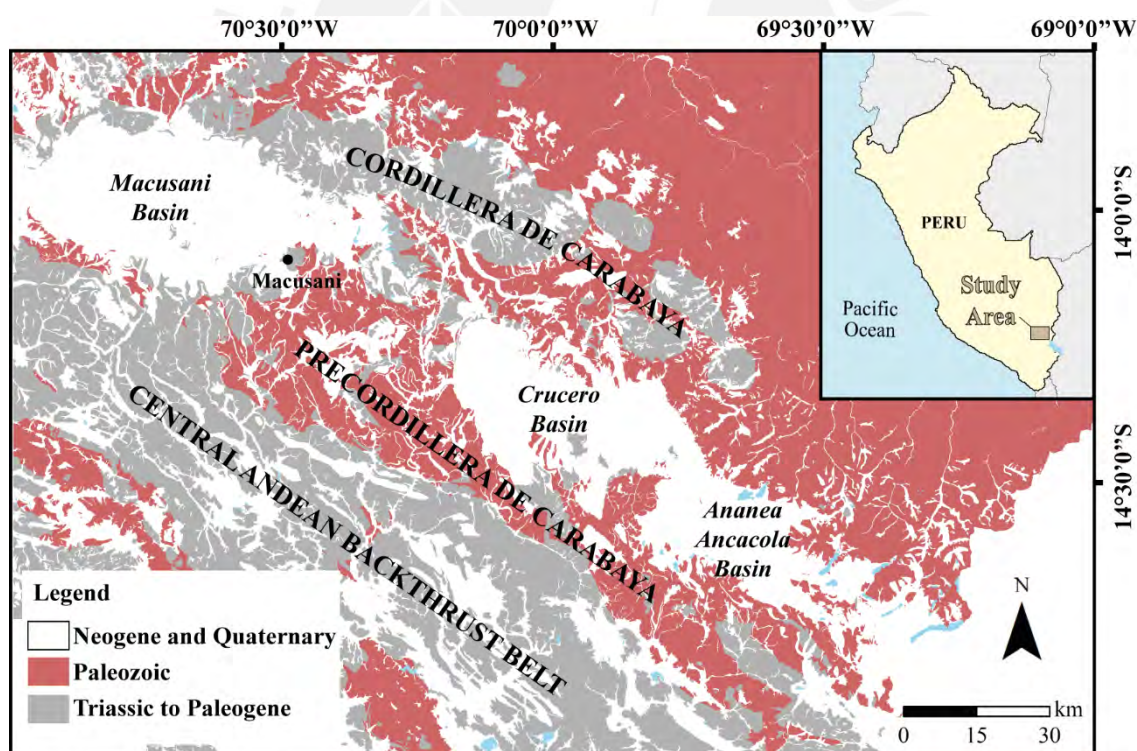


**Figure 13.** Simplified geology of the tectonic/structural domains: Cordillera de Carabaya, Precordillera de Carabaya (a.k.a. Macusani Tectonic Zone), and Central Andean Backthrust Belt. The locations of the Macusani, Crucero, and Ananea-Ancacola intermontane depressions are also shown. Modified from Kontak et al. (1990) and Sandeman et al. (1997)

### 3.3. Geology of the Macusani Basin and the Macusani Volcanic Field

The Macusani basin is located in the northern part of the Puno Department and is surrounded by the 4,500 to 5,500 m peaks of the Cordillera and Precordillera de Carabaya (Cheilletz et al. 1992; Sandeman et al. 1997). It lies between the Cordillera de Carabaya to the north and the Central Andean Backthrust Belt to the south (Fig. 13). The Macusani Basin encompasses part of the Macusani Volcanic Field.

According to Sandeman et al. (1997), the exposed Crucero Supergroup lithologies in the Macusani Volcanic Field include volumetrically dominant rhyolitic rocks of the Macusani Formation (Quenamari Group) and, in a lesser proportion, rhyodacitic sequences of the Lago Perhuacarca, Pucalacaya, and the Cerro Sumpiruni Formations (Picotani Group). The volcano-sedimentary sequence of the Macusani Volcanic Field is cut by hypabyssal units of the Quenamari and Picotani Intrusive Suites (Fig.14).

#### 3.3.1. Picotani Group

In the Quenamari Volcanic Field, the Picotani Group is represented by the Late Oligocene to Early Miocene Lago Perhuacarca, Pucalacaya, and Cerro Sumpiruni Formations. The descriptions and geochronological constraints provided in the following paragraphs are taken from Sandeman et al. (1997).

The Cerro Sumpiruni Formation is composed of a sequence of peraluminous, greyish-green, cordierite-biotite bearing rhyodacitic ash-flow tuffs unconformably overlying Paleozoic-Mesozoic rocks. Biotite crystals from the lowest and highest exposed rocks on Cerro Sumpiruni (Fig. 14) yielded  $^{40}\text{Ar}/^{39}\text{Ar}$  dates of  $24.13 \pm 0.11$  Ma and  $24.00 \pm 0.25$  Ma, respectively (Fig. 15).

The Pucalacaya Formation is composed of high-K calc-alkaline, basaltic andesite flows with calcite-filled amygdules and peraluminous, cordierite-biotite rhyodacitic ash-flow tuffs that crop out in the south of Hacienda Pucalacaya (Fig. 15). The latter is petrographically similar to the Cerro Sumpiruni Formation. This unit unconformably overlies pre-Cenozoic units and is locally covered by rhyolitic ash-flows of the Macusani Formation.  $^{40}\text{Ar}/^{39}\text{Ar}$  dating of a shoshonite from this locality yielded  $21.90 \pm 1.68$  Ma (Fig. 15).

The Lago Perhuacarca Formation is composed of flows of intermediate composition interlayered with rhyodacitic-rhyolitic ash-flow tuffs. Metaluminous to peraluminous intermediate lavas in this unit are interpreted as the result of incomplete

mixing between minette and cordierite + biotite-bearing, more silicic melts.  $^{40}\text{Ar}/^{39}\text{Ar}$  analyses in biotite from an andesite yielded a  $23.86 \pm 0.40$  Ma date.

### 3.3.2. Quenamari Group

In the Quenamari Field, the Quenamari Group is represented by the Macusani Formation, which is a 500-m-thick sequence that covers an area of 850 km<sup>2</sup> (Fig. 14).  $^{40}\text{Ar}/^{39}\text{Ar}$  analyses on rocks from the Macusani Formation yield dates between ca. 10.4 and 6.7 Ma (Cheilletz et al. 1992). This formation is mostly composed of whitish grey, poorly stratified, crystal-rich rhyolitic ash-flow tuffs containing ash- and lapilli-size pyroclastic fragments, juvenile pumice fragments and shards, and lithic fragments (Arribas and Figueroa 1985; Cheilletz et al. 1992; Sandeman et al. 1997). The ash-flow tuffs have a relatively uniform mineralogical composition comprising sanidine, sillimanite, andalusite, muscovite, biotite, and tourmaline (Pichavant et al. 1988a). Juvenile fragments include obsidian clasts interbedded within the ash-flow tuffs, and lithic fragments include pelites, quartzites, and limestones barely or not metamorphosed (Cheilletz et al. 1992). Other obsidian glasses of equivalent age, known as *macusanite* (or Macusani glasses), occur as pebbles scattered in stream gravels (Barnes et al. 1970; Pichavant et al. 1987).

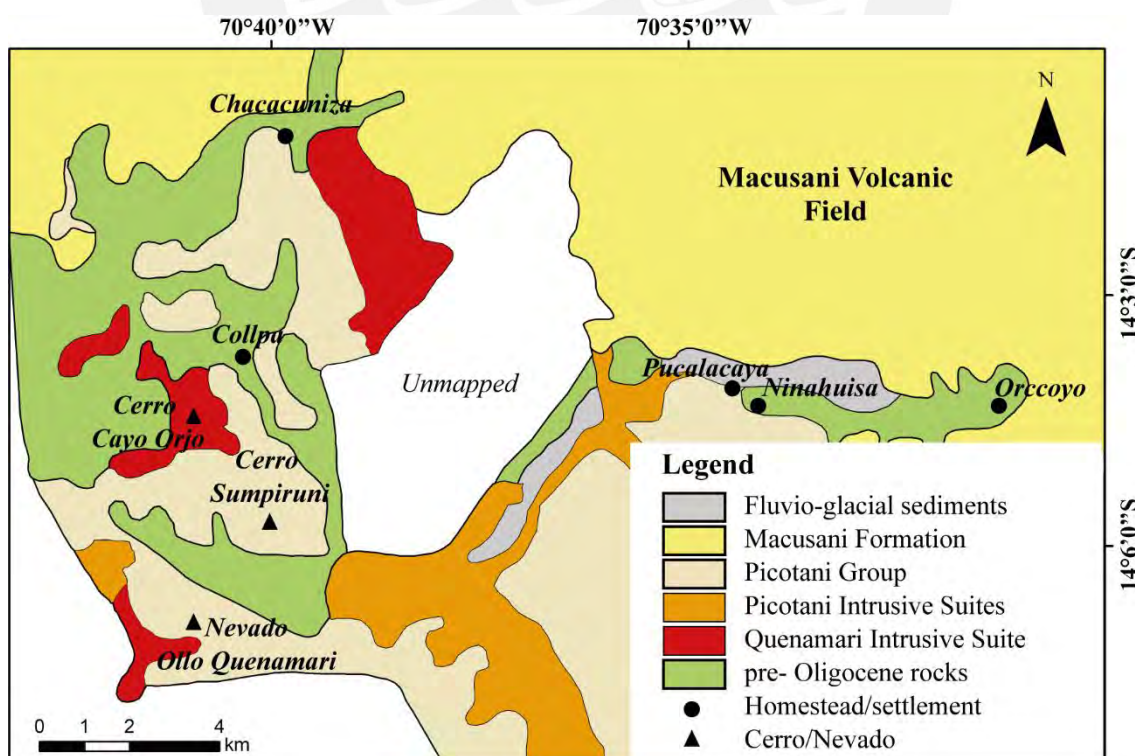


**Figure 14.** Geological map of the SW quadrant of the Quenamari Meseta, where the Quenamari Volcanic Field is located. Modified from Sandeman et al. (1997)



The ash-flow tuffs of the Macusani Formation are characterized by high silica (71.5-75 wt% SiO<sub>2</sub>) and highly peraluminous signatures with normative corundum >2%. Also, by high alkalis and a marked depletion in FeO<sub>t</sub>, MgO, CaO, and TiO<sub>2</sub> (Barnes et al. 1970; Pichavant et al. 1988b). The age-equivalent Macusanite glasses are enriched in Na<sub>2</sub>O and normative corundum, and depleted in K<sub>2</sub>O, MgO, CaO, FeO<sub>t</sub>, and TiO<sub>2</sub> relative to the ash-flow tuffs (Pichavant et al. 1988b). Although F, Li<sub>2</sub>O, B<sub>2</sub>O<sub>3</sub>, and P<sub>2</sub>O<sub>5</sub> contents are high in the tuffs, these are even higher in the Macusanite glasses (Pichavant and Montel 1988; Pichavant et al. 1987); both are also enriched in As, Cs, Rb, Sn, and Te (Barnes et al. 1970). Pichavant et al (1988b) concluded that the unusual, lithophile-enriched compositions of the ash-flow tuffs of the Macusani Formation and the macusanite glasses are compositionally equivalent to Himalayan or Hercynian two-mica leucogranites and peraluminous leucogranite series, respectively. According to Pichavant et al (1987), macusanite glasses and tuffs of the Macusani Formation shared a common magmatic evolution. Geochemical and mineralogical data indicates that magma was produced by direct melting of the crust, specifically by anatectic melting of metapelitic materials, and there is no evidence of mixing or assimilation by another meta- to sub-aluminous magma (Pichavant et al. 1988b).

Cheilletz et al. (1992) proposed a lithological subdivision of tuff layers from the Macusani Formation based on the size of their lapilli clasts into large-lapilli ash-flow tuffs (LLT) and lapilli ash-flow tuffs (LT). The LLT is the lower layer of the Formation and is less consolidated than the LT zone. It is porous and strongly altered. The base of the layer is enriched in >20 cm-diameter lapilli. The LT overlies the LLT, is consolidated, less porous than the former, and contains <5 cm-sized clastic fragments. It is characterized by columnar jointing.

INGEMMET used a different nomenclature for Neogene volcano-sedimentary rocks exposed in the Macusani Volcanic Field. The materials corresponding to the Macusani Formation of Sandeman et al. (1996) were grouped under the Quenamari Formation by INGEMMET, who proposed its subdivision into the Chacacuniza, Sapanuta, and Yapamayo Members (Fig. 16; López 1996, De la Cruz et al. 1996, Chávez et al. 1997). The Chacacuniza and Sapanuta Members would correspond to a first eruptive event in the Middle to Late Miocene (10 ± 0.5 Ma; Cheilletz et al. 1992), and the Yapamayo Member, to a Late Miocene-Pliocene volcanic event (6.7 ± 1.0 Ma; Cheilletz et al. 1992). The lithofacies, litho-geochemistry (Table 4), and mineralogy of the three

members summarized below are after De la Cruz et al. (1996), López (1996) and Chávez et al. (1997).

- ***Chacacuniza Member:*** Lower member of the Quenamari Formation. It is 10 to 15 meters thick and consists of compact and well-welded rhyolitic ignimbrite flows. This member is considered the first explosive event recorded in the Chacacuniza area, and it is found in angular unconformity over rocks of the Mitu Group. Its mineralogy includes quartz, plagioclase, biotite, sanidine, and zeolites embedded in a volcanic glassy matrix along with glass shards, pumice fragments, lithic material, and amygdules.
- ***Sapanuta Member:*** This member is a succession of three white tuffaceous rhyolitic-dacitic ignimbrite units and shows characteristic columnar jointing. Its uppermost unit corresponds to a flow of pumice and lithic fragments. The Sapanuta Member overlies in angular unconformity rocks of the Mitu Group and, in some sectors, concordantly overlies rocks of the Chacacuniza Member. The mineralogy consists of quartz, plagioclase (in some cases with acicular rutile inclusions), K-feldspar, biotite, apatite, and lithic fragments embedded in a cryptocrystalline matrix with chalcedony-filled amygdules.
- ***Yapamayo Member:*** Upper member of the Quenamari Formation. It consists of a succession of four rhyolitic ignimbrite flows with thicknesses that vary from 30 to 50 m. The ignimbrite flows have angles  $< 5^\circ$  to the NW, allowing the formation of plains that shape the Quenamari Meseta. It presents weakly welded ash-flows at the base and a white tuff to the top. Mineralogically, it is composed of quartz, plagioclase, biotite, K-feldspar, sericite, and clays. Volcanic glass was found as obsidian shards in a matrix with a vitroclastic texture. Uranium mineralization in this member comprises pitchblende (Arribas and Figueroa 1985).

**Table 4.** Comparative data of major element whole rock compositions of the three members of the Quenamari Formation (Chacacuniza, Sapanuta and Yapamayo; López 1996)

Member	Major elements (wt.%)					
	SiO <sub>2</sub>	Al <sub>2</sub> O <sub>3</sub>	Fe <sub>2</sub> O <sub>3</sub>	MgO	CaO	TiO <sub>2</sub>
Chacacuniza	69.53 - 72.20%	14.29 - 15.48%	1.49 - 1.97%	0.37 - 0.8%	0.43 - 1.12%	-
Sapanuta	70.21%	15.23 - 15.48%	2.02%	0.30%	0.82%	0.23%
Yapamayo	70.25 - 73.54%	14.3 - 15.8%	0.37 - 1.47%	0.05 - 0.37%	0.5 - 0.81%	0.08 - 0.28%

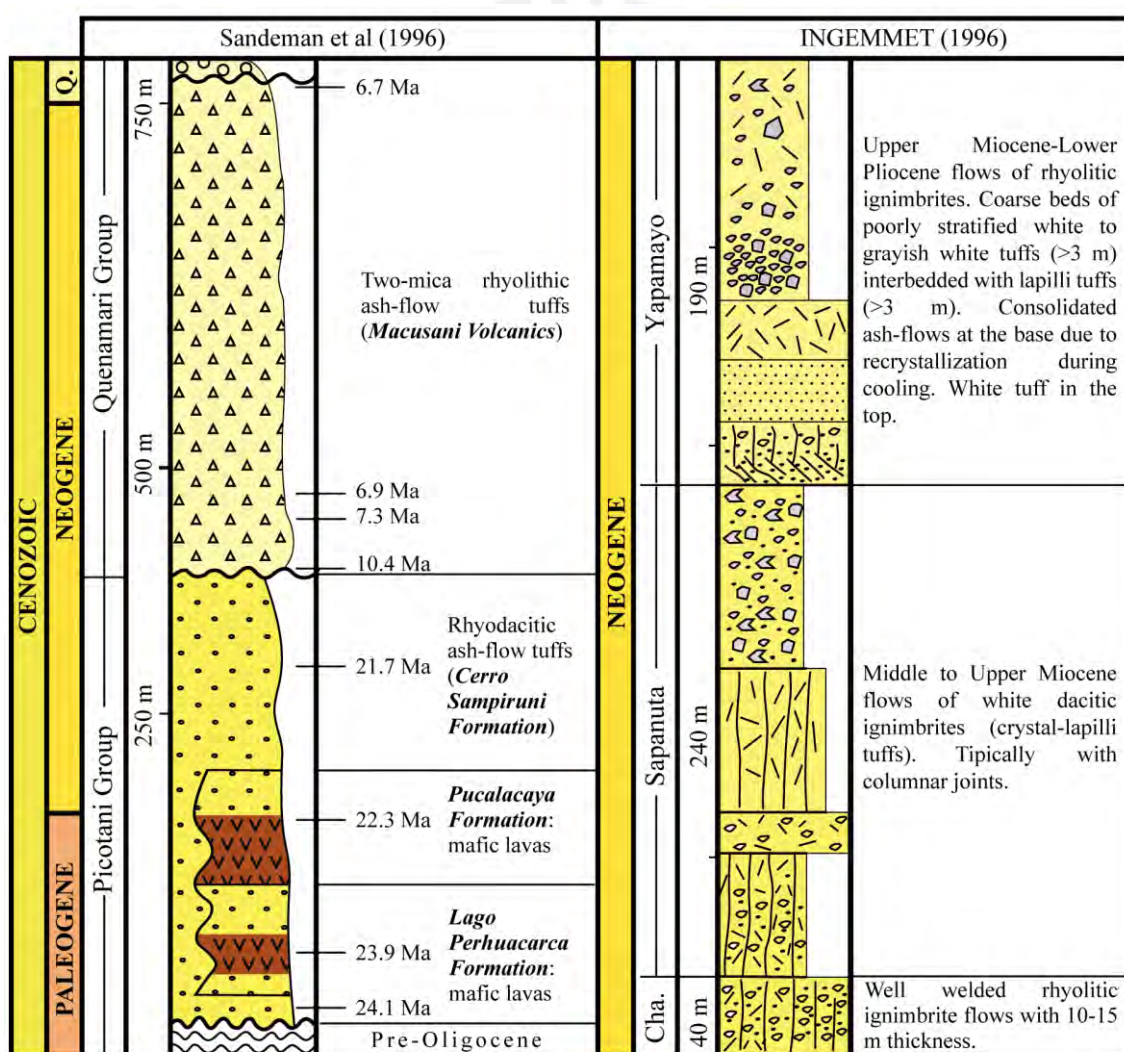


**Figure 15.** Comparative stratigraphic columns after Sandeman et al. (1996) and Lopez (1996). Sandeman et al (1996) presented a stratigraphic column of the Quenamari Group (Macusani Formation) and Picotani Group (Cerro Sumpiruni, Pucalacaya, Lago Perhuacarca Formations) exposed in the Macusani Field. Lopez et al (1996) described the Chacacuniza, Sapanuta and Yapamayo Members of the Quenamari Formation (in full synonymy with Macusani Formation)

### 3.3.3. Quenamari and Picotani Intrusive Suites

Many of the peaks around the southern margin of the Quenamari Meseta are underlain by the Crucero Intrusive Supersuite, which consists of hypabyssal silicic intrusions such as the Quebrada Centilla Stock, Ninahuisa Stock, Revancha Dyke, Chacacuniza Stock, and Nevado Ollo Quenamari plug (Sandeman et al. 1997).

The **Quebrada Centilla Stock** is a cordierite-biotite monzogranite intrusion exposed along the northern and northeastern flanks of Nevado Ollo Quenamari, apparently intruding Lago Perhuacarca and Cerro Sumpiruni Formations (Sandeman et al. 1997).  $^{40}\text{Ar}/^{39}\text{Ar}$  dates of  $24.09 \pm 0.18$  Ma and  $23.65 \pm 0.14$  Ma indicate a cogenetic relation with flows of the Lago Perhuacarca Formation (Sandeman et al. 1997).

The **Ninahuisa Stock** is a peraluminous, cordierite-biotite monzogranite exposed along the floor of the Ninahuisa Valley (Sandeman et al. 1997).  $^{40}\text{Ar}/^{39}\text{Ar}$  dating in biotite and sanidine yielded  $23.52 \pm 0.58$  Ma and  $23.15 \pm 0.20$  Ma, respectively (Sandeman et al. 1997).

The **Revancha Dyke** is a peraluminous, glass-rich cordierite-biotite rhyodacite dike that crops out on the southern slope of the Ninahuisa Valley (Sandeman et al. 1997). It cuts rhyodacitic ash-flows and monzogranitic intrusive rocks (Sandeman et al. 1997; Sandeman and Clark 2003).  $^{40}\text{Ar}/^{39}\text{Ar}$  dating in biotite yielded  $24.1 \pm 0.2$  Ma (Sandeman and Clark 2003).

The **Chacacuniza Stock** is one of the two Miocene, highly peraluminous intrusions that are exposed in the southern Quenamari Field (Sandeman et al. 1997). The total-fusion  $^{40}\text{Ar}/^{39}\text{Ar}$  muscovite date was of  $7.51 \pm 0.14$  Ma (Sandeman et al. 1997), which demonstrates that the Chacacuniza stock is coeval with the Yapamayo Member (Cheilletz et al. 1992).

Finally, the **Nevado Ollo Quenamari Plug** is a sanidine-quartz-biotite intrusion.  $^{40}\text{Ar}/^{39}\text{Ar}$  dating of sanidine yielded a plateau date of  $12.14 \pm 0.11$  Ma (Sandeman et al. 1997).

## 4. RESULTS

### 4.1. XRD

The results of powder XRD indicate that the studied samples of Lithium-rich Tuff from the Macusani Volcanic Field are mostly composed of quartz, plagioclase, K-feldspar, and micas (zinnwaldite and lepidolite, according to electron probe and Raman micro-analyses in Torr o et al. 2023; Table 5). In addition, variable proportions of kaolinite subgroup minerals, smectite, and mordenite were identified. Finally, the presence of other minerals, such as cristobalite and mutinaite, is plausible in a few samples, but the X-ray diffractograms were not conclusive, and therefore, their occurrence is not confirmed.

In all samples, the  $d_{001}$  of 9.8   (2  ~8.9 ) is consistent with mica group minerals (Figs. 16 to 19). On the other hand, the peaks at 2  ~12.5 , corresponding to  $d_{001}$  of 7.1 to 7.2  , for air-dried oriented mounts are interpreted as kaolinite subgroup minerals (samples 2021-MAC-008, 2021-MAC-011A, 2021-MAC-038, 2021-MAC-039, 2021-MAC-040, 2021-MAC-048, 2021-MAC-052, 2021-MAC-065A, 2021-MAC-066, 2021-MAC-042, and 2021-MAC-049). The diffractogram showed no change with ethylene glycol and oven-dried treatment at 400 C, while with the oven-dried treatment at 550 C, the  $d_{001}$  ~7.1 peak collapsed (Figs. 16 to 18).

**Table 5.** Minerals identified in samples of Lithium-rich Tuff from the Macusani Volcanic Field using XRD. Pl: plagioclase, Mca: mica, Qz: quartz, Kfs: K-feldspar, Kln: kaolinite subgroup minerals, Sme: smectite, Crs: cristobalite, Mor: mordenite, Mut: mutinaite, Cbz: chabazite

N°	Samples	Rock Forming Minerals				Clays		Other		
		Pl	Mca	Qz	Kfs	Kln	Sme	Mor	Crs	Mut
1	2021-MAC-005	X	X	X	X					
2	2021-MAC-006	X	X	X	X					
3	2021-MAC-008A	X	X	X	X	X				
4	2021-MAC-008B	X	X	X	X	X				
5	2021-MAC-011A	X	X	X	X	X				
6	2021-MAC-011B	X	X	X	X	X				
7	2021-MAC-019A		X	X	X					
8	2021-MAC-021		X	X	X	X				
9	2021-MAC-022A	X	X	X	X					
10	2021-MAC-022B		X	X						
11	2021-MAC-025	X	X	X	X	X				
12	2021-MAC-026	X	X	X				X		X
13	2021-MAC-031	X	X	X	X					
14	<b>2021-MAC-035</b>	X	X							
15	<b>2021-MAC-038</b>	X	X	X	X	X	X			
16	<b>2021-MAC-039</b>	X	X	X	X	X				
17	<b>2021-MAC-040</b>	X	X	X	X	X				
18	<b>2021-MAC-042</b>		X			X	X			
19	<b>2021-MAC-048</b>	X	X	X	X	X				
20	<b>2021-MAC-049</b>		X			X	X		X	
21	<b>2021-MAC-050</b>		X				X		X	
22	<b>2021-MAC-051</b>		X				X		X	
23	<b>2021-MAC-052</b>	X	X	X	X	X	X			
24	<b>2021-MAC-053</b>	X	X	X				X		X
25	2021-MAC-065A	X	X	X	X	X				
26	2021-MAC-065B	X	X	X	X	X				
27	2021-MAC-065C	X	X	X	X	X				
28	2021-MAC-066	X	X	X	X	X				
29	2021-MAC-067A	X	X	X	X	X				
30	2021-MAC-067B	X	X	X	X	X				
31	2021-MAC-067C	X	X	X	X					

Note: Labels in bold correspond to drill core samples

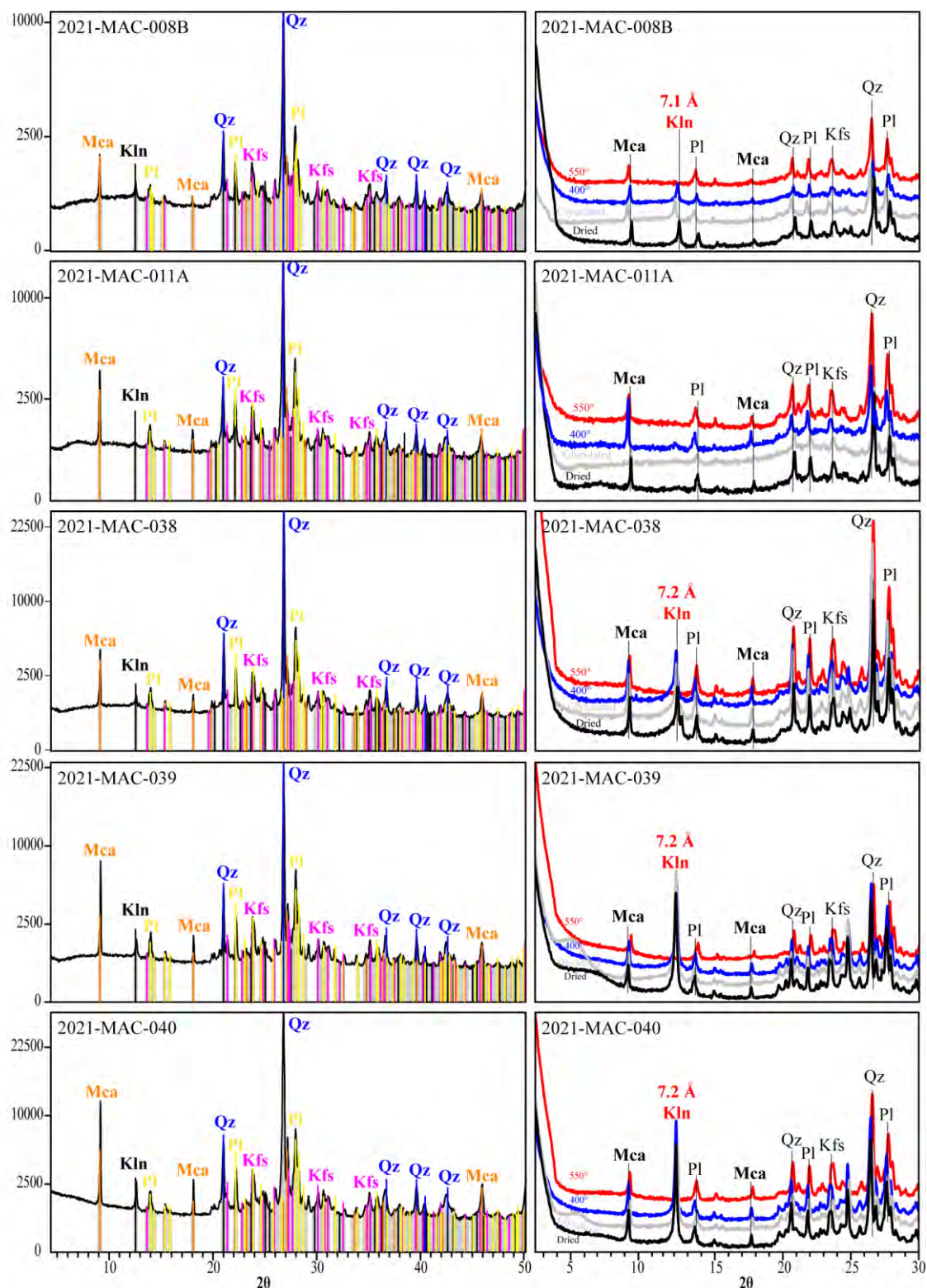


**Figure 16.** Powder XRD patterns (left) and oriented aggregate mount XRD patterns (right) of samples 2021-MAC-008B, 2021-MAC-011A, 2021-MAC-038, 2021-MAC-039, and 2021-MAC-040. Major mineralogy includes plagioclase (Pl), quartz (Qz), K-feldspar (Kfs), and mica (Mca). In all diffractograms (except for sample 2021-MAC-011A), the  $d_{001}$  of 7.1 Å ( $2\theta \sim 12.5^\circ$ ) is interpreted to correspond to kaolinite subgroup minerals (Kln)

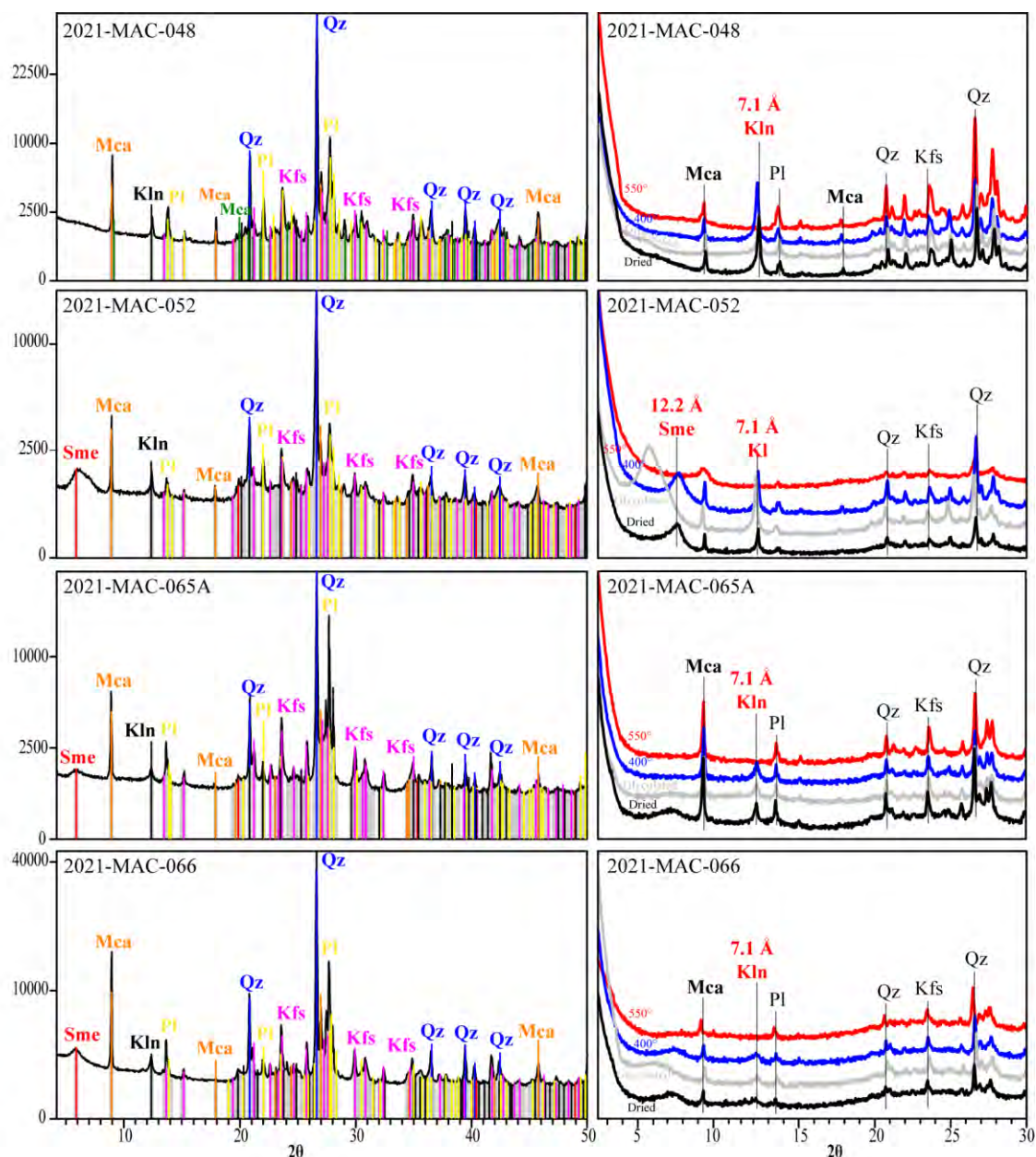


**Figure 17.** Powder XRD patterns (left) and oriented aggregate mount XRD patterns (right) of samples 2021-MAC-048, 2021-MAC-052, 2021-MAC-065A, and 2021-MAC-066. Common minerals include mica (Mca), plagioclase (Pl), quartz (Qz), and K-feldspar (Kfs). The  $d_{001}$  of 7 to 7.1 Å ( $2\theta \sim 12.5^\circ$ ) is interpreted as kaolinite subgroup minerals (Kln). In the oriented aggregate mounts of sample 2021-MAC-052, the XRD pattern presents a peak at  $2\theta \sim 7.1^\circ$  ( $d_{001}$  of 12.2 Å) corresponding to smectite (Sme). In the oriented aggregate mounts of samples 2021-MAC-065A and 2021-MAC-066, smectite peaks were not detected

In samples 2021-MAC-035, 2021-MAC-042, 2021-MAC-049, 2021-MAC-050, and 2021-MAC-051, smectite peaks at  $2\theta \sim 5.8-7^\circ$  for air-dried oriented aggregate mounts present a  $d_{001}$  of 12.4 to 15.1 Å (Fig. 18). With the ethylene glycol treatment, the  $d_{001}$  expands to 16.6-17 Å, and undergoes slight sharpening. Then, it contracts to  $\sim 10$  Å with the oven-dried treatments at 400°C and 550°C.



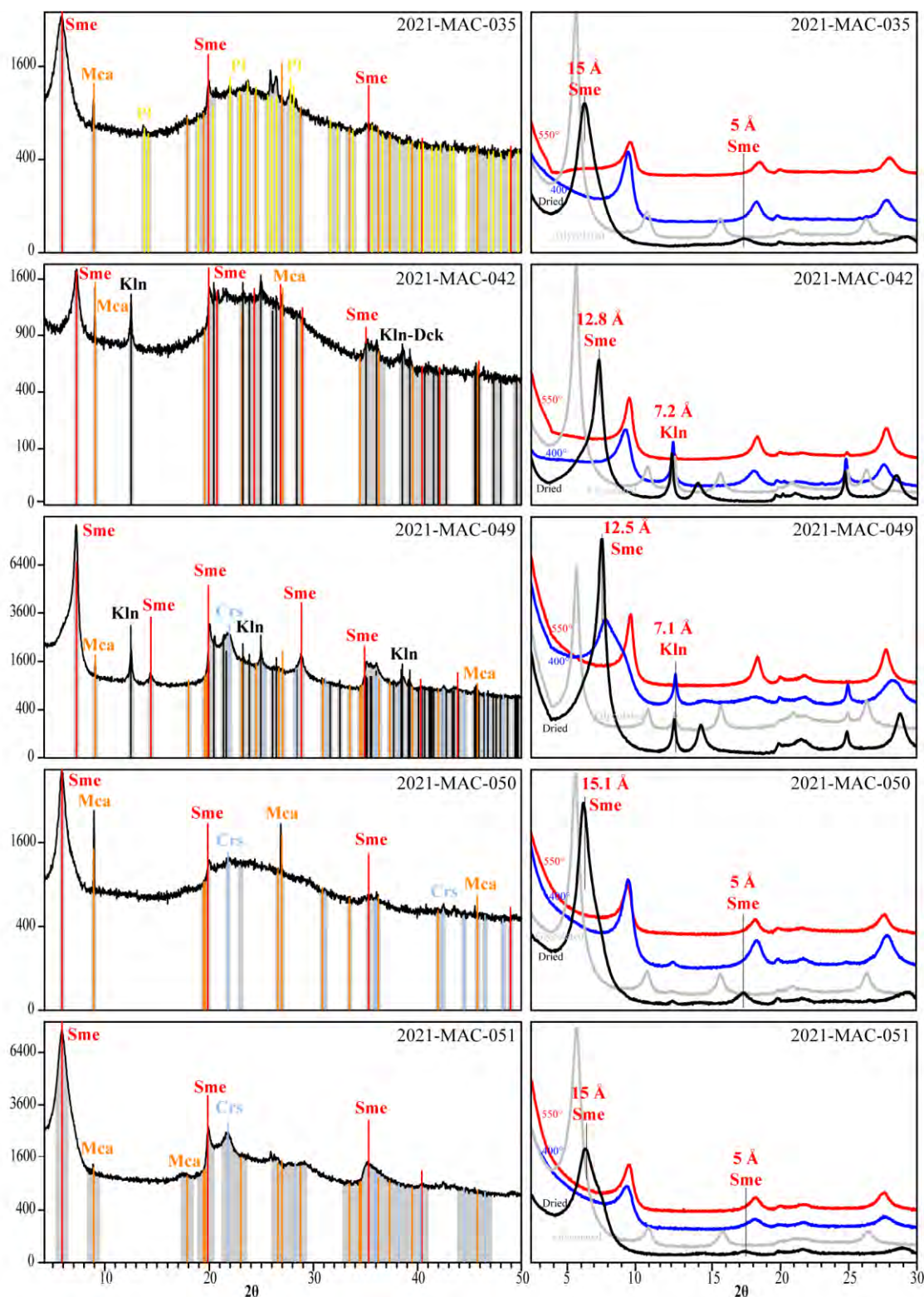


**Figure 18.** Powder XRD patterns (left) and oriented aggregate mount XRD patterns (right) of samples 2021-MAC-035, 2021-MAC-042, 2021-MAC-049, 2021-MAC-050, and 2021-MAC-051. The  $d_{001}$  of 12.5 to 15.1 Å ( $2\theta \sim 5.8 - 7^\circ$ ) are interpreted as smectite (Sme). Also, the  $d_{001}$  of 7 to 7.1 Å ( $2\theta \sim 12.5^\circ$ ) are interpreted as kaolinite (Kln). Other identified phases include mica (Mca), plagioclase (Pl), and cristobalite (Crs)

In samples 2021-MAC-026 and 2021-MAC-053, the peaks at  $2\theta \sim 6.5^\circ$ , are interpreted as the zeolite group mineral mordenite, and correspond to  $d_{110}$  of 13.5-13.7 Å. As

expected, no changes were observed for this peak in the diffractograms of ethylene glycol-treated and oven-dried mounts (Fig. 19).

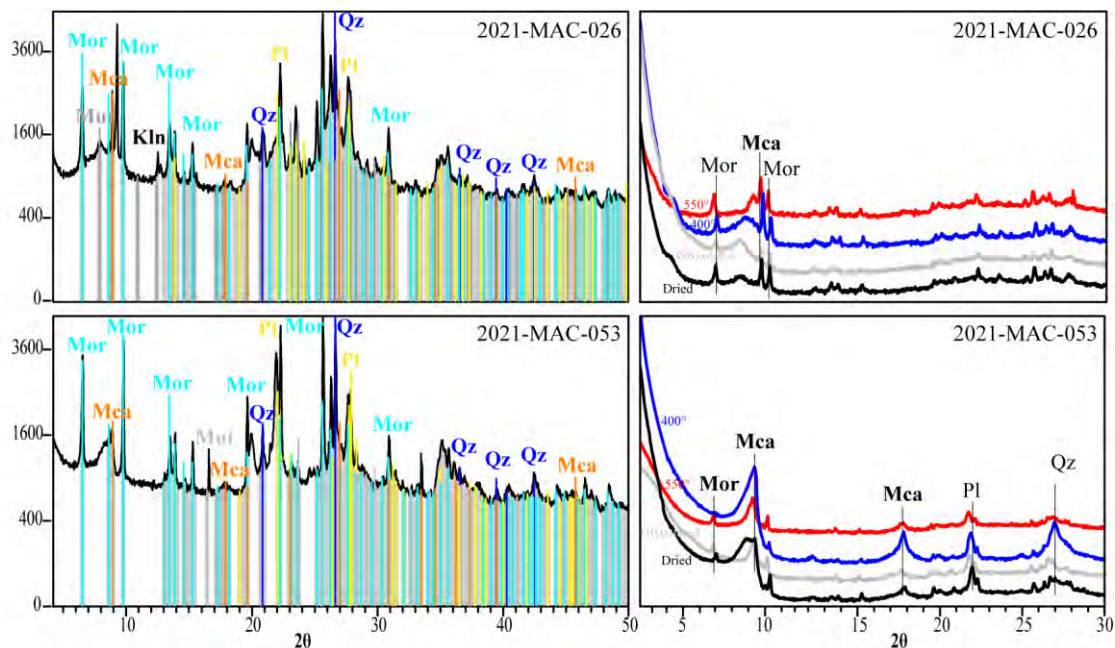


**Figure 19.** Powder XRD patterns of (left) and oriented aggregate XRD patterns (right) of samples 2021-MAC-026 and 2021-MAC-053. The  $d_{001}$  of 9.8 Å ( $2\theta \sim 8.9^\circ$ ) corresponds to mica (Mca). The  $d_{110}$  of 13.5 to 13.7 Å ( $2\theta \sim 6.5^\circ$ ) are interpreted as mordenite (Mor). Other mineral phases identified include plagioclase (Pl), quartz (Qz), and K-feldspar (Kfs)

The systematization of the results obtained allowed the classification of the studied samples into four categories, according to their prevalent mineralogy: i) mica with no zeolite nor clay minerals, ii) mica with kaolinite subgroup minerals, iii) smectite with mica, and iv) zeolite with mica (Fig. 20).

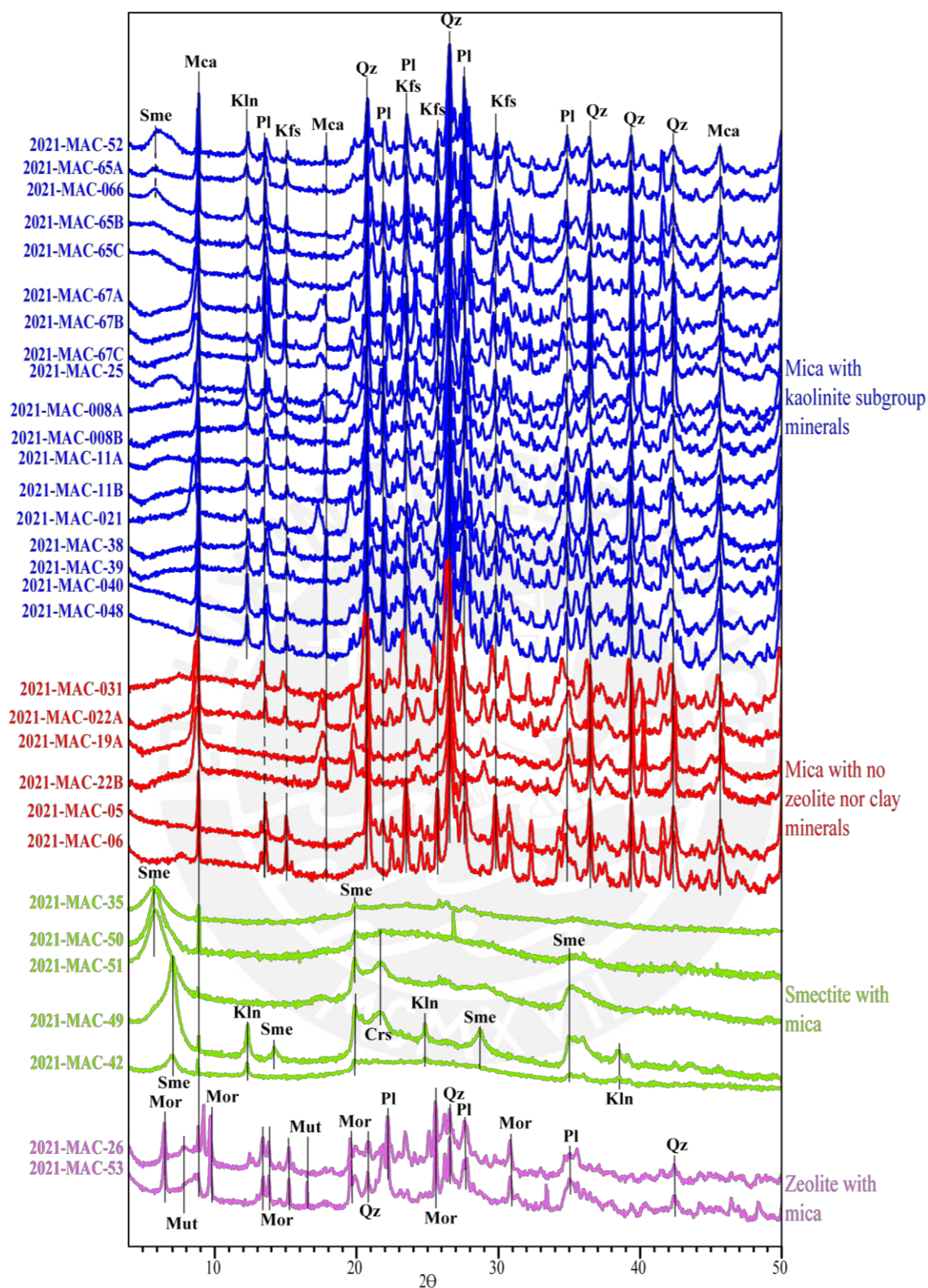


**Figure 20.** Powder XRD patterns showing the interpreted major peaks as black vertical lines with the corresponding mineral labels. Samples are classified according to their prevalent mineralogy. Abbreviations: plagioclase (Pl), mica (Mca), quartz (Qz), K-feldspar (Kfs), kaolinite subgroup minerals (Kln), smectite (Sme), cristobalite (Crs), mordenite (Mor), and mutinaite (Mut)

The powder-XRD patterns of samples from three drill cores (PCHAC-01-TSW, PCHAC-04-TV, and PCHAC-32) are sorted by depth in Figures 21 to 23. Their respective lithium contents, as provided by Macusani Yellowcake-American Lithium for the corresponding 1 m-long segments of the drill cores, are also displayed. In the drill core PCHAC-01-TSW, higher lithium contents were found in samples from the central domain, which are mineralogically dominated by mica and kaolinite subgroup minerals (Fig. 21). The upper and lower domains are characterized by lower lithium contents (~567 to 930 ppm) and the occurrence of smectite.

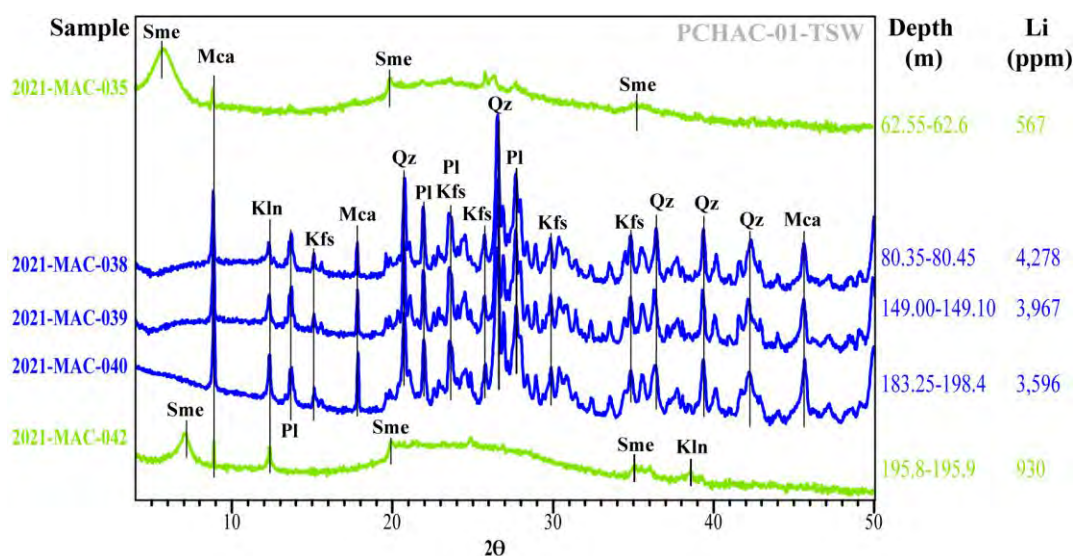


**Figure 21.** Powder XRD patterns of samples from the drill core PCHAC-01-TSW sorted by depth. Lithium values provided by Macusani Yellowcake-American Lithium. Color code as in Fig. 20. Abbreviations: plagioclase (Pl), mica (Mca), quartz (Qz), K-feldspar (Kfs), kaolinite (Kln), and smectite (Sme)

Only two samples from the drill core PCHAC-04-TV were analyzed. The sample collected at a shallower level, which returned a higher lithium content (~3,200 ppm), consists of mica and kaolinite subgroup minerals, whereas the sample taken at a greater depth is characterized by a lower lithium content (~2,000 ppm) and the presence of smectite (Fig. 22).

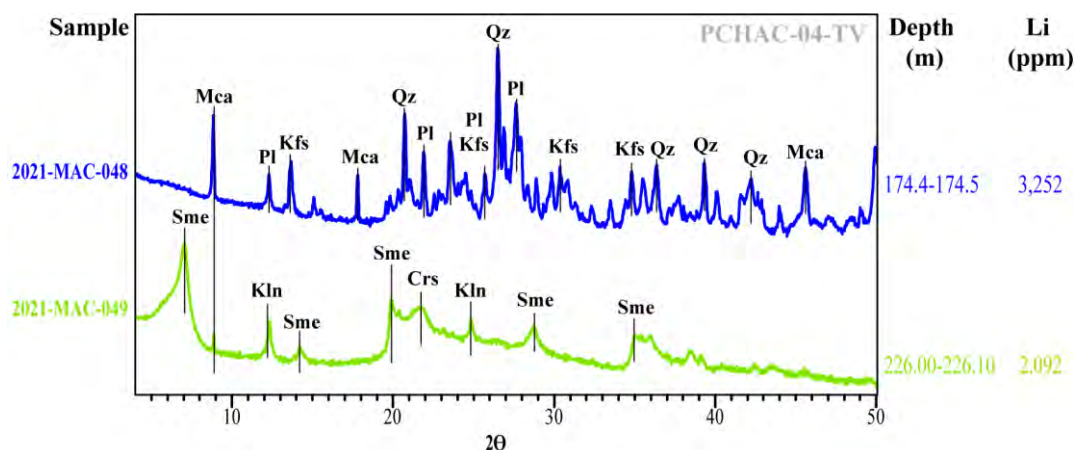


**Figure 22** Powder XRD patterns of samples from the drill core PCHAC-04-TV sorted by depth. Lithium values provided by Macusani Yellowcake-American Lithium. Color code as in Fig. 20. Abbreviations: plagioclase (Pl), mica (Mca), quartz (Qz), K-feldspar (Kfs), kaolinite (Kln), smectite (Sme), and cristobalite (Crs)

Finally, in the drill core PCHAC-32 (Fig. 23), the highest lithium contents were found in samples collected at deeper levels and belonging to the “mica with kaolinite subgroup minerals” (2,800 ppm) and “zeolite with mica” (3,859 ppm) mineralogical types. Shallower samples of the “smectite with mica” type returned lower lithium contents (up to 1,300 ppm).

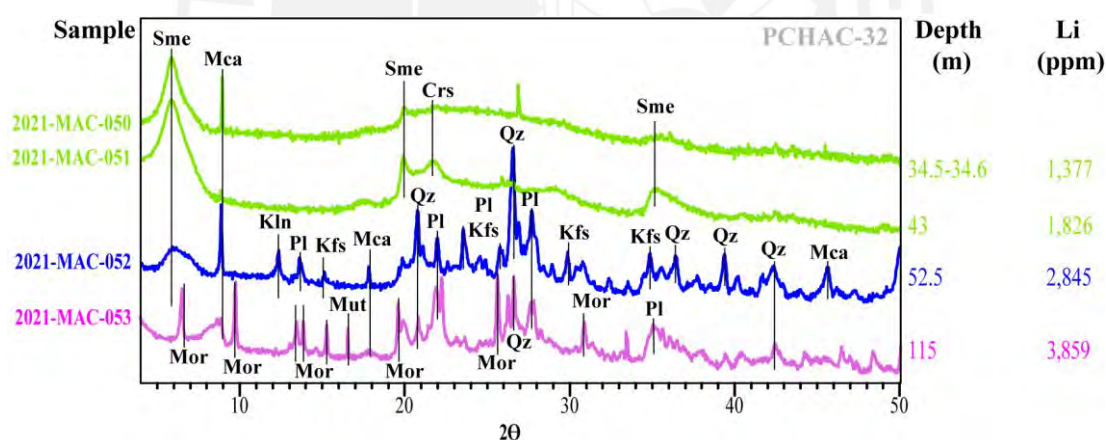


**Figure 23** XRD patterns of samples from the drill core PCHAC-32 sorted by depth. Lithium values provided by Macusani Yellowcake-American Lithium. Color code as in Fig. 20. Abbreviations: albite (Ab), plagioclase (Pl), mica (Mca), quartz (Qz), K-feldspar (Kfs), kaolinite (Kln), smectite (Sme), cristobalite (Crs), mordenite (Mor), and mutinaite (Mut)

In Figure 24, the powder XRD patterns obtained on samples from the three drill cores are sorted according to their relative depth; their respective lithium contents are shown. The following vertical mineral succession comprising three main domains was identified:

- Upper domain, which is characterized by a mineralogical composition dominated by smectites and mica ± cristobalite. The lithium contents are in the range of 567 to 1,826 ppm.

- Central domain, which is mineralogically dominated by kaolinite subgroup minerals and mica, as well as K-feldspar, plagioclase, and quartz. This domain has the highest Li contents, ranging from 2,845 to 4,278 ppm.
- Lower domain, which is mostly composed of smectite ± kaolinite subgroup minerals ± cristobalite and with Li contents between 930 and 2,092 ppm.

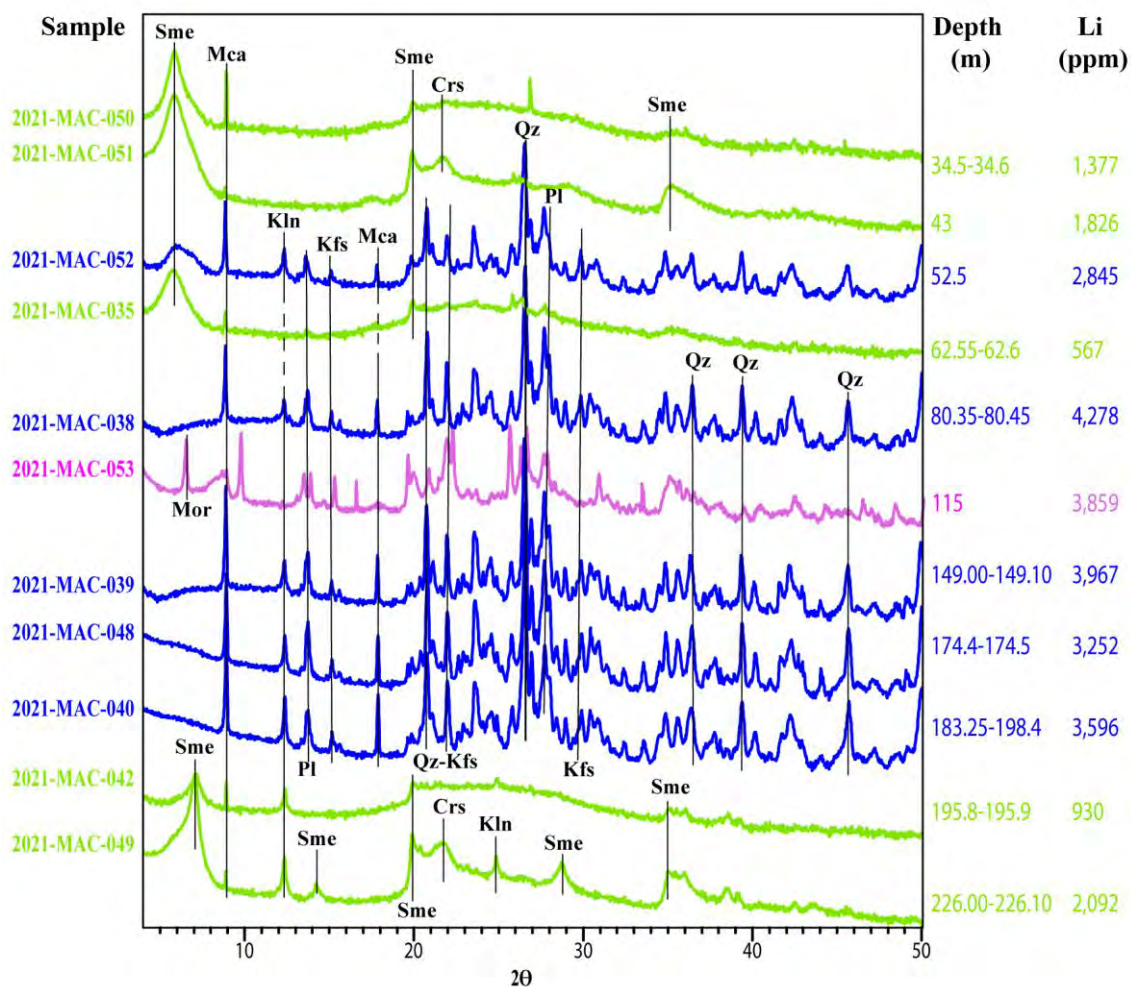


**Figure 24.** Powder XRD patterns of drill core samples (2021-MAC-035 to 2021-MAC-053) classified according to their mineralogy and sorted by depth. Color code as in Fig. 20. Abbreviations: plagioclase (Pl), mica (Mca), quartz (Qz), K-feldspar (Kfs), kaolinite subgroup minerals (Kln), smectite (Sme), cristobalite (Crs), and mordenite (Mor)

#### 4.2. SEM-EDS

In sample 2021-MAC-026, mordenite (identified by powder XRD) is prevalent and occurs as aggregates of subhedral, sheet-like, > 5  $\mu\text{m}$  crystals (Fig. 25A); EDS spectra yielded high contents of Si and O, moderate contents of Al, and low contents of Na and K, which is compatible with the structural formula of mordenite

$[(\text{Na}_2, \text{Ca}, \text{K}_2)_4(\text{Al}_8\text{Si}_{14})\text{O}_{96} \cdot 28\text{H}_2\text{O}]$ . Also, small plates of variable thicknesses are observed, most probably corresponding to kaolinite according to their pseudo-hexagonal morphology (Fig. 25B). Feldspar crystals show rugged surfaces and partial alteration to clays (Figs. 25C-D).

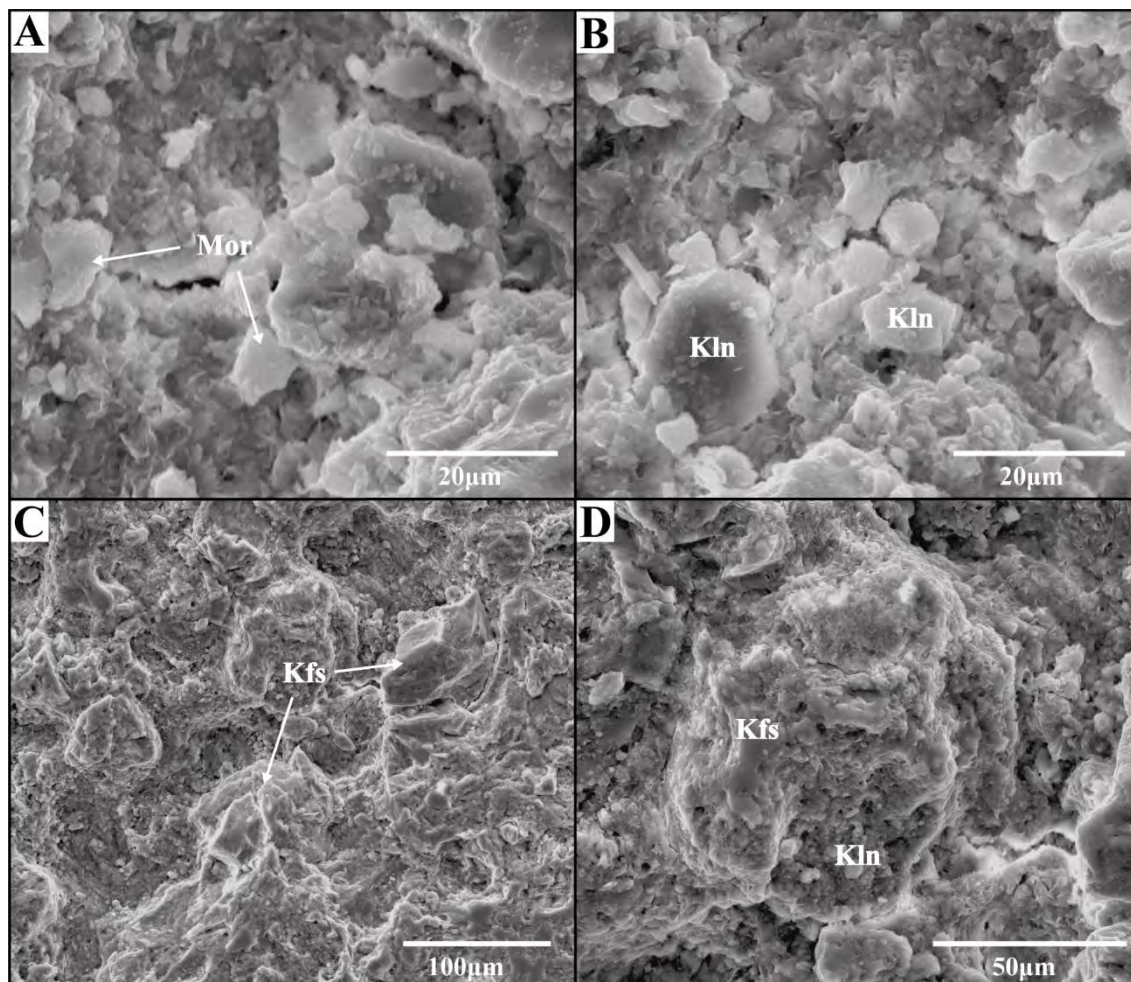


**Figure 25.** Secondary-electron SEM images of sample 2021-MAC-026 (zeolite with mica type). A) Subhedral, sheet-like crystal aggregates, probably of mordenite. B) Pseudo-hexagonal plates of kaolinite with different thicknesses. C-D) Feldspar crystals with rugged and altered surfaces

In samples 2021-MAC-035 and 2021-MAC-050, smectites with different morphologies were observed with SEM. In sample 2021-MAC-035, smectite appears as wavy, flaky masses with curved edges (Figs. 26A-B) and as tightly interwoven flakes (Fig. 26C). In Figure 26D, two different morphologies can be distinguished: one with wavy flakes with curved edges, and the other with irregular, sharper edges. SEM-EDS analyses reveal high Si and Al contents and lower Mg, Ca, and Na contents.

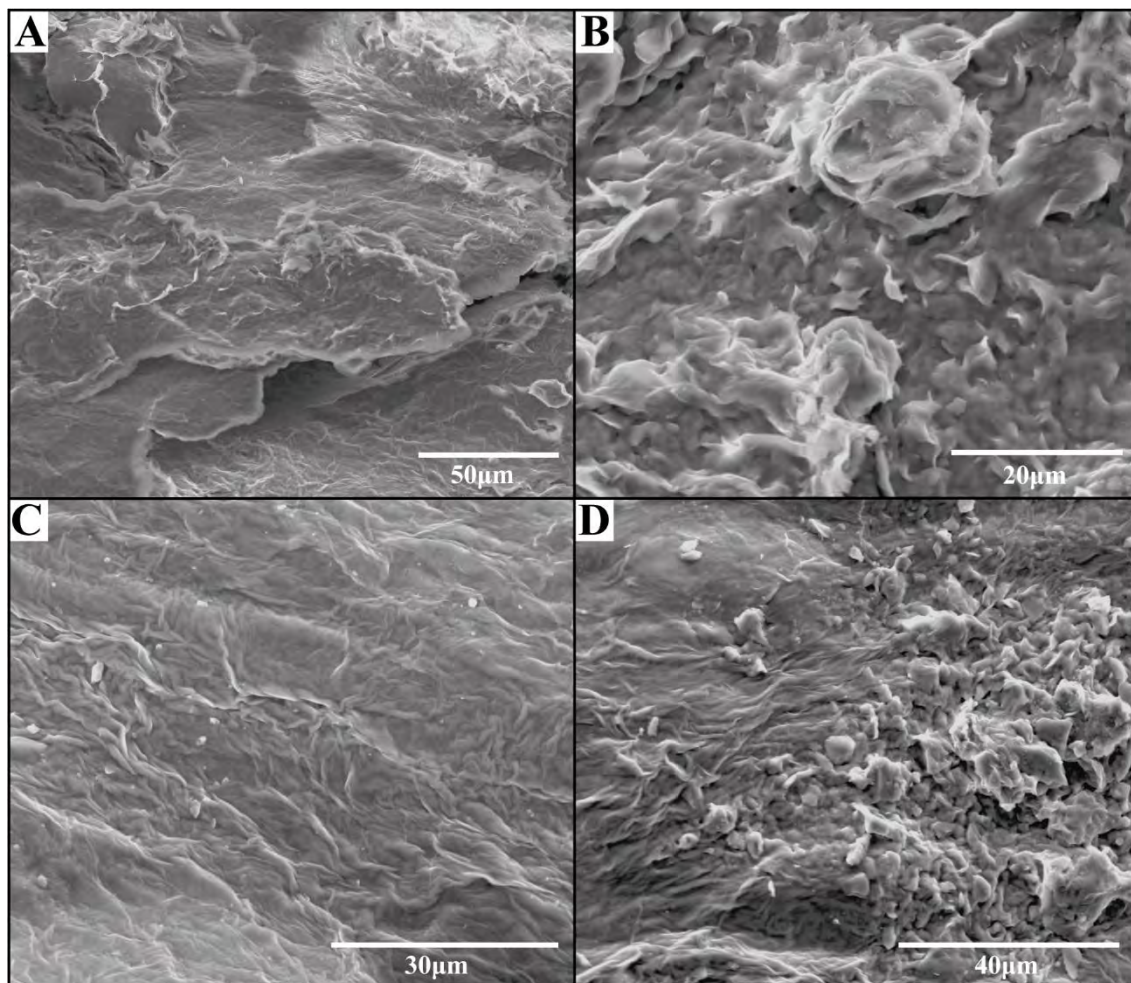


**Figure 26.** Secondary-electron SEM images of smectite in sample 2021-MAC-035 (smectite with mica type). A-B) Wavy, flaky smectite (Sme) masses with curved edges. C) Tightly interwoven, elongated flakes of smectite. D) Wavy flakes with curved edges (left) and irregular and sharp masses (right) of smectite

In sample 2021-MAC-050, angular fragments of feldspar crystals show exposed surfaces altered to smectite (Figs. 27A-B). Both feldspar crystals and local subhedral tabular crystals of mica are cemented by smectite aggregates (Figs. 27C-D).



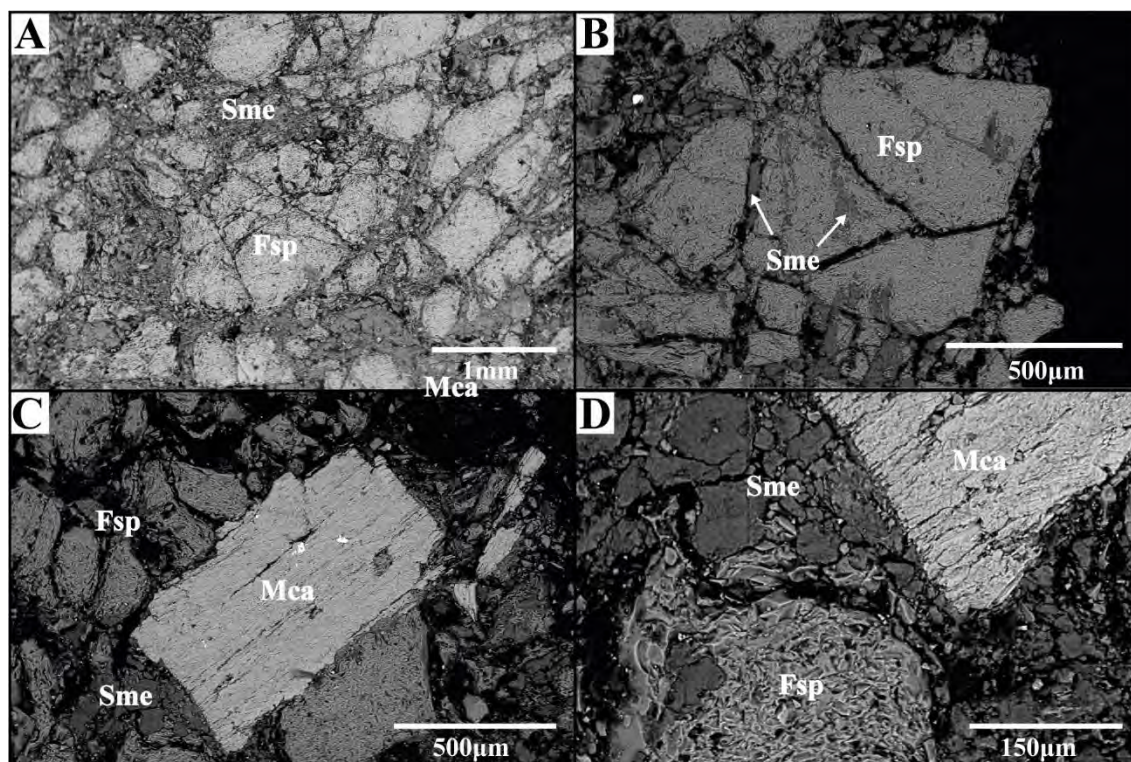


**Figure 27.** Secondary-electron SEM images of sample 2021-MAC-050 (smectite with mica type). A-B) Angular fragments of feldspar (Fsp) altered to smectite (Sme). C) Tabular mica (Mca) crystal (~750 µm) surrounded by crystal fragments of feldspar altered to clay minerals. D) Close-up of C), showing the tabular mica crystal (upper right) in a fragmentary matrix composed of feldspar and cemented by smectite

Finally, in sample 2021-MAC-039, prismatic crystals of K-feldspar, sheets of mica, and euhedral grains of quartz are cemented by an irregular mass of kaolinite (Fig. 28). Tabular grains of feldspar are partially altered to kaolinite (Figs. 28A, C). Subhedral mica sheets in Figure 28B show irregular surfaces and returned high fluorine contents (>10 wt.%) in EDS analyses, which accords well with chemical data in Torr o et al. (2023). Mica crystals also form open booklets partially altered to kaolinite (Figs. 28C-D).

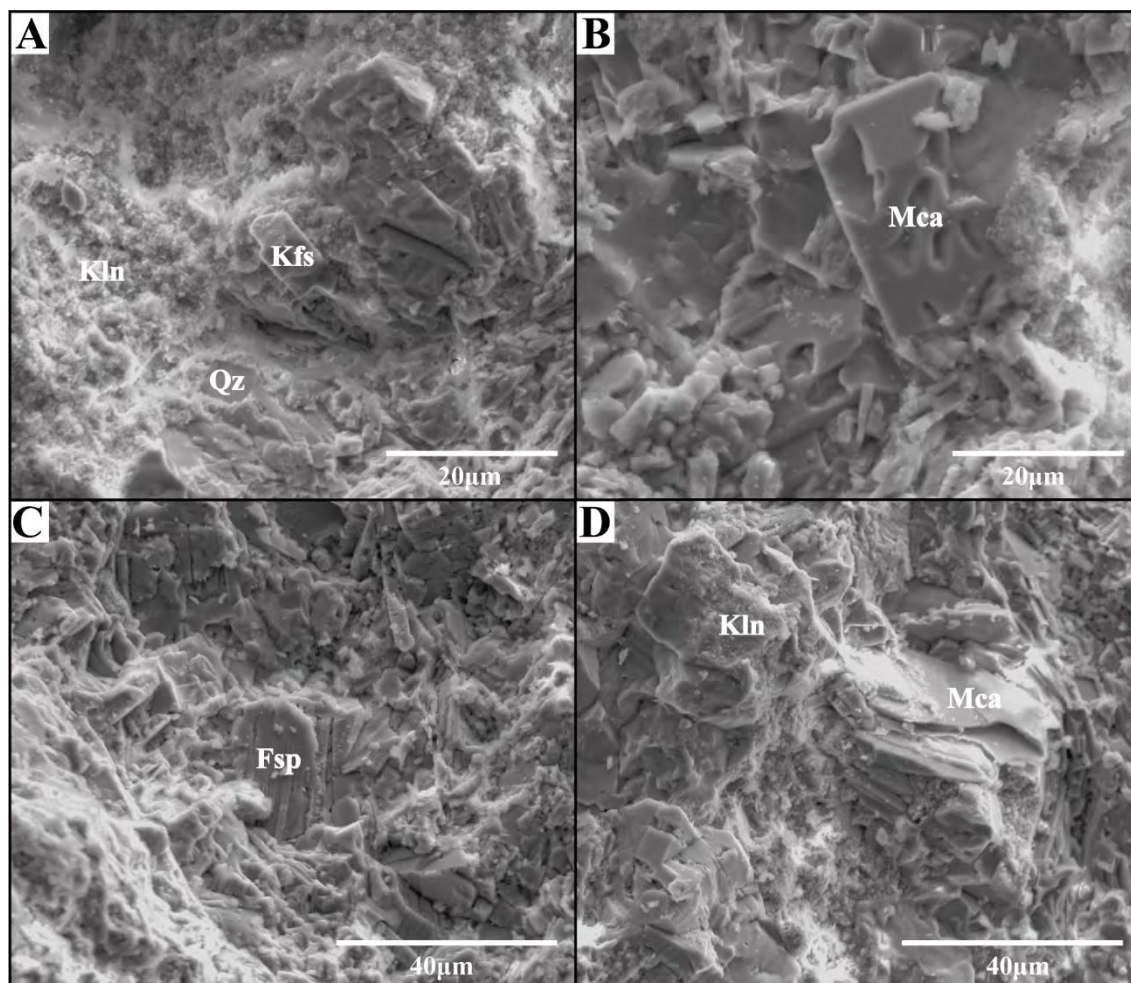


**Figure 28.** Secondary-electron SEM images of sample 2021-MAC-039 (mica with kaolinite subgroup minerals type). A) Tabular crystals of feldspar (Fsp) and euhedral grains of quartz (Qz) embedded in a mass of kaolinite (Kln). B) Detail of a mica (Mca) tabular crystals with an irregular surface. C) Small (<5  $\mu\text{m}$ ), subhedral feldspar crystal, partially altered to and embedded in a mass of kaolinite. D) Flaky, undulated grains of mica embedded in a mass of kaolinite

### 4.3. TEM

TEM observations corroborate the predominance of mica and kaolinite subgroup minerals in sample 2021-MAC-038. Kaolinite crystals form the typical pseudo-hexagonal-shaped platelets with slightly rounded outlines (Figs. 29A-B), and their individual sizes are up to 200 nm. Electron diffraction patterns show a pseudo-hexagonal arrangement and present the crystal parameters  $a = 5.11 \text{ \AA}$  and  $b = 8.88 \text{ \AA}$ , which are coherent with those of kaolinite (Figs. 29 C). TEM-AEM analyses of kaolinite subgroup minerals reflect intense peaks for O, Al, and Si (Fig. 29D). Tubular crystals of halloysite are observed very locally (Fig. 29E).

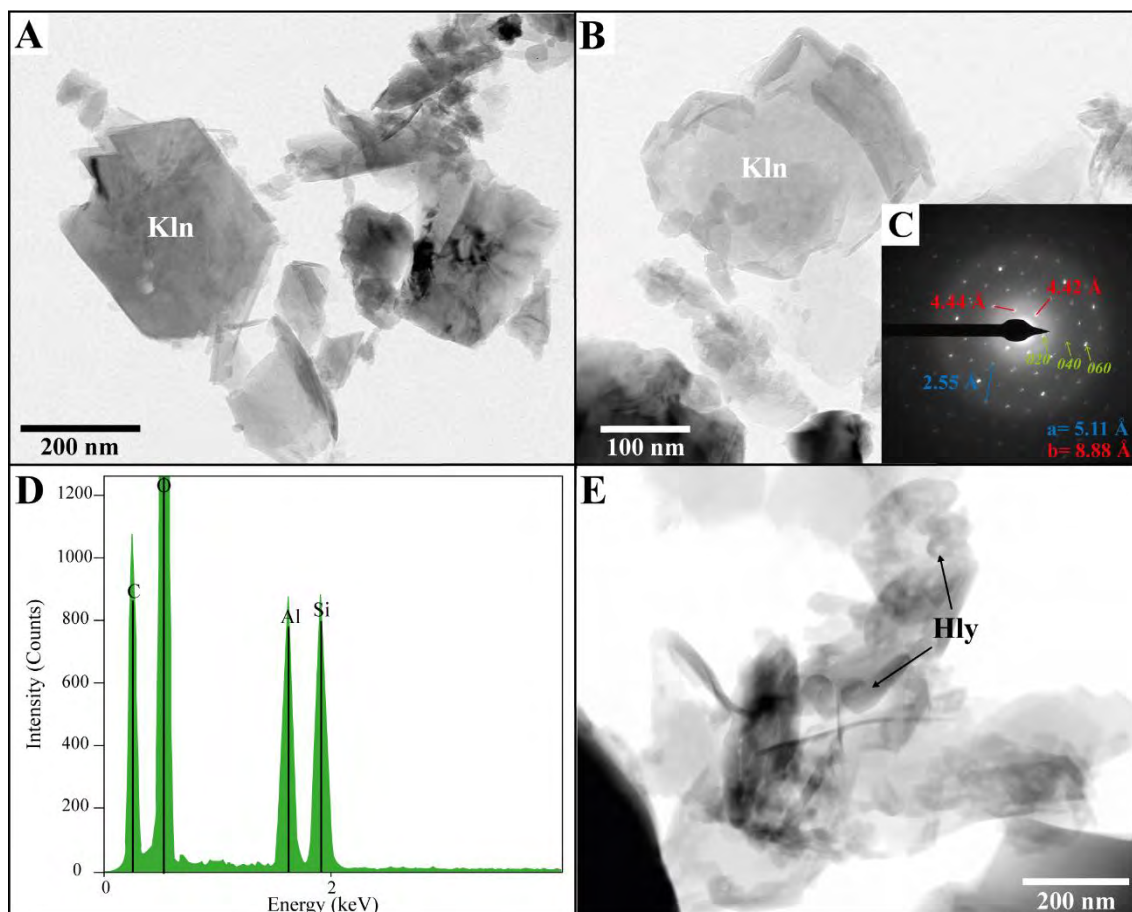


**Figure 29.** TEM data of sample 2021-MAC-038 (mica with kaolinite subgroup minerals type). A-B) Bright-field images of pseudohexagonal-shaped platelets of kaolinite (Kln). C) Electron diffraction of kaolinite showing crystal parameters  $a=5.11 \text{ \AA}$  ( $2 \times 2.55 \text{ \AA}$ ) and  $b=8.88 \text{ \AA}$  ( $2 \times 4.44 \text{ \AA}$ ). D) TEM-AEM spectrum of kaolinite. E) Halloysite (Hly) crystals with hollow tubular morphologies and lengths up to 200 nm

In sample 2021-MAC-049, the fine fraction analyzed with TEM is chiefly composed of smectite (Fig. 30A). TEM-AEM spectra on smectite particles reveal high contents of Si and Al and lower contents of K, Na, and Ca (Fig. 30B). In high-resolution TEM images,  $d_{001}$  of  $10.23 \text{ \AA}$  and  $10.26 \text{ \AA}$  were measured, consistent with those of a collapsed smectite (Fig. 30C). The smooth ring pattern observed in the electron diffraction suggests that the smectite aggregates are randomly oriented and may be poorly crystalline, presenting the crystal parameters  $a=5.12 \text{ \AA}$  and  $b=8.62 \text{ \AA}$  consistent with dioctahedral phyllosilicates (Fig. 30D). Local kaolinite is also observed in this sample (Fig. 30E). The electron diffraction of a kaolinite crystal presents a crystal parameter of  $a=5.14 \text{ \AA}$  and  $b=8.88 \text{ \AA}$ , indicative of dioctahedral phyllosilicates (Fig. 30F) and the TEM-AEM spectrum shows high contents of Si, Al, and O, and much lower contents of Na, Ca, and K (Fig. 30G).

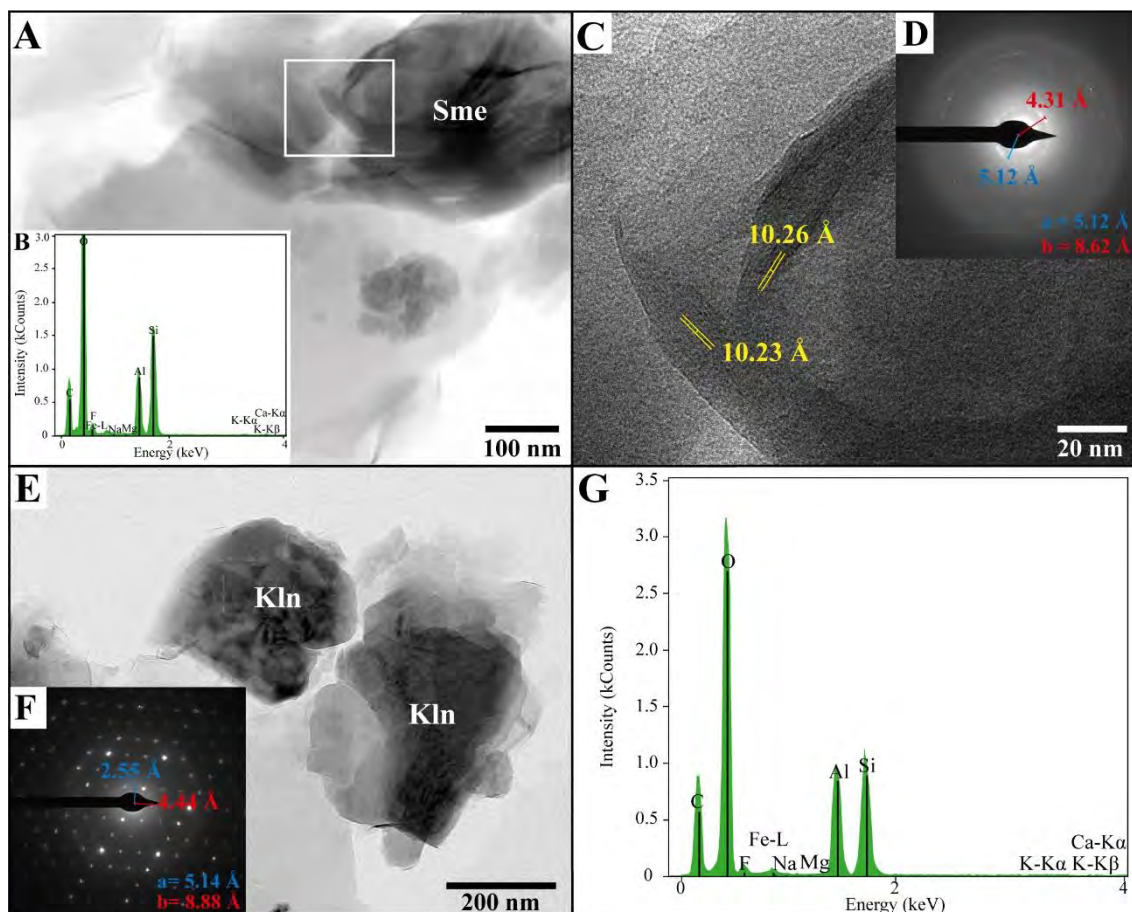


**Figure 30.** TEM data of sample 2021-MAC-049 (smectite with mica type). A) Bright-field image of smectite (Sme) particles (bright and dark) and B) its representative TEM-AEM spectrum. C) High-resolution TEM image of the frame area in A showing  $d_{001}$  of 10.23 Å and 10.26 Å in smectite. D) Electron diffraction pattern of smectite aggregates from which crystal parameters  $a = 5.1$  Å and  $b = 8.9$  Å were calculated. E) Bright-field image, F) electron diffraction with crystal parameters ( $a = 5.14$  Å and  $b = 8.88$  Å), and G) TEM-AEM spectrum of kaolinite (Kln)

In sample 2021-MAC-050, scaly crystals of smectite forming rose-shaped aggregates of around 500  $\mu\text{m}$  in diameter, are ubiquitous (Fig. 31). These aggregates are common on the surface of feldspar crystals, suggesting replacement (Figs. 31A-B). Lattice fringes of a collapsed smectite (montmorillonite–beidellite series) were measured in high-resolution TEM images, revealing a  $d_{001}$  of 11.05 Å (Fig. 31C). Smectite presents little crystallinity to judge from smooth ring-shaped electron diffraction patterns, with a spacing of 10.96 Å, which may correspond to the  $d_{001}$  of a collapsed smectite (Fig. 31D). Finally, the TEM-AEM spectra indicate high contents of Si, Al, and O and much lower contents of K, Na, and Ca contents suggesting that small amounts of these elements occur in the interlayer position (Fig. 31E).

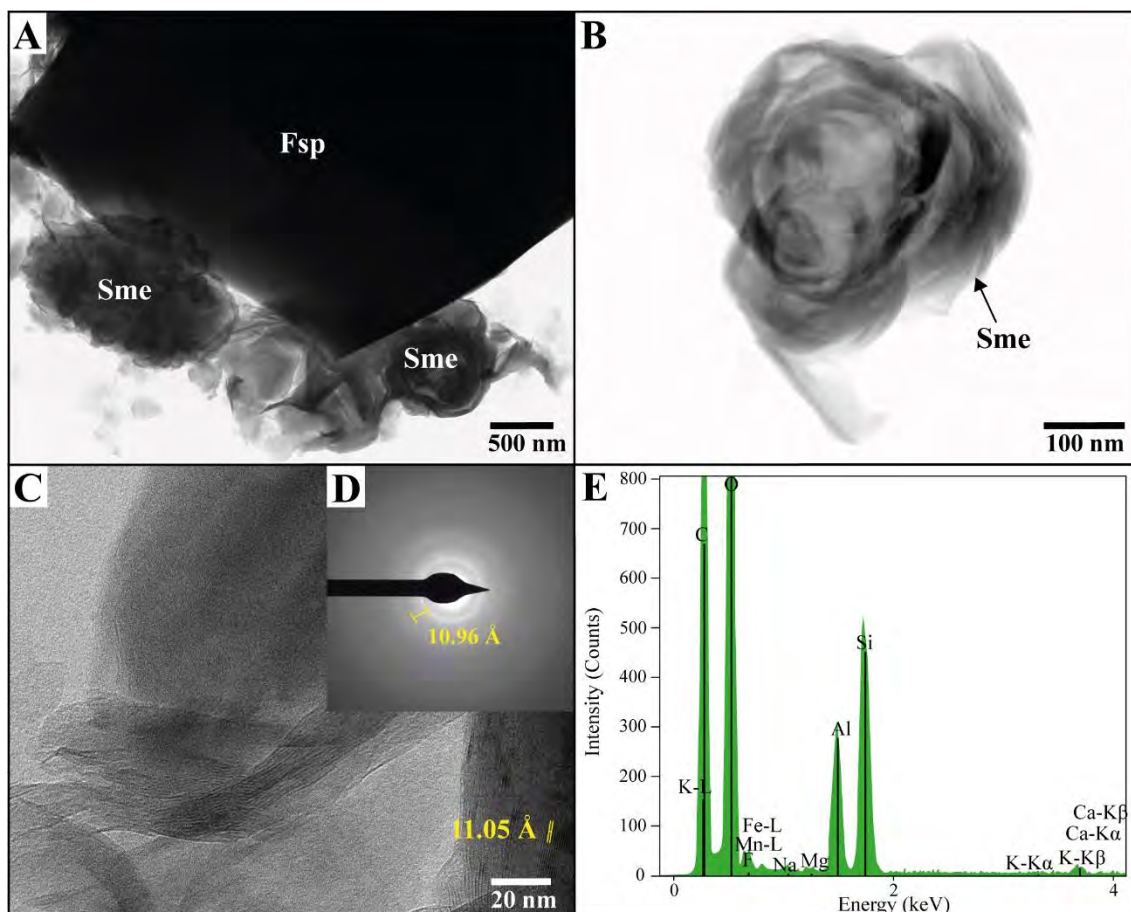


**Figure 31.** TEM data of sample 2021-MAC-050 (smectite with mica type). A) Bright-field image of a feldspar (Fsp) particle with scaly particles of smectite (Sme) forming rose-shaped aggregates on its edges. B) Detail of an isolated rose-shaped smectite aggregate. C) High-resolution TEM image of smectite with a  $d_{001}$  11.05 Å. D) Smooth ring electron diffraction pattern with a spacing of 10.96 Å, it must be noted that the orientation does not allow the measurement of a and b and hence the determination of dioctahedral or trioctahedral character, and E) TEM-AEM spectrum of a smectite particle

## 5. DISCUSSION

### 5.1. Mineralogical expression of lithium in the Lithium-rich Tuff

In volcanogenic lithium deposits, the lithium ore is usually related to secondary minerals formed upon alteration of a pre-enriched rhyolite volcanic rock (Benson et al. 2017; Neukampf et al. 2019; Bowell et al. 2020; Michaud et al. 2021; Ellis et al. 2022; Sarchi et al. 2023). Described secondary lithium-bearing phases in volcanogenic deposits include clay minerals (in which lithium may be structural or occur in interlaminal positions or adsorbed) as well as other phases such as zeolites and jadarite (Starkey 1982; Benson et al. 2017; Bowell et al. 2020; Castor and Henry 2020; Borojević Šoštarić and Brenko 2023). The magnesium-lithium clay mineral hectorite (Table 1), a trioctahedral smectite, is considered by Bowell et al (2020) the main ore in volcanic tuff-hosted deposits and is widely described in volcanogenic lithium (e.g., McDermitt Caldera; see

below) but also in clay (including bentonite) and borate deposits found along western USA ([mindat.org/min-1841.html](http://mindat.org/min-1841.html)), including the type locality Hector Bentonite Mine (Foshag and Woodford 1936). In addition, tainiolite – a mineral of difficult classification identified by some authors as an illite-smectite (e.g., [Bowell et al. 2020](#)) and by others as a trioctahedral mica (e.g., [Toraya et al. 1977](#)) – is also an important lithium ore in this type of deposits.

From a mineralogical point of view, the best studied volcanogenic clay-type lithium deposits are probably those found at the McDermitt Caldera on the Nevada-Oregon border in the United States. In the Thacker Pass deposit in the McDermitt Caldera, [Castor and Henry \(2020\)](#) concluded that lithium occurs in hectorite and an illitic clay chemically similar to tainiolite, as well as in mixed smectite-illite clays. Likewise, in lithium deposits of the Western Balkan lithium-boron metallogenic zone that formed in lacustrine environments, the lithium ore is linked to either the Li-borosilicate jadarite (Jadar basin) or Li clays (Valjevo deposit and Rekovac Li-B project; [Borojević Šoštarić and Brenko 2023](#)). In the latter, Li ore is vaguely described as Li-bearing smectites.

According to the XRD, SEM-EDS, and TEM results presented in this thesis, the Lithium-rich Tuff of the Macusani Volcanic Field is mineralogically composed of quartz, plagioclase, K-feldspar, trioctahedral micas (lepidolite and zinnwaldite; [Torró et al. 2023](#)), and clay minerals (Fig. 20). The clay minerals, which are the main focus of this thesis, include kaolinite subgroup minerals (kaolinite and, very locally, halloysite; Fig. 29) and dioctahedral smectites (montmorillonite-beidellite; Figs. 30-31). In addition, cristobalite and zeolites (e.g., mordenite and mutinaite) were found in a few samples. The absence of hectorite in the studied samples contrasts with the common assumption that it represents the main ore in tuff-hosted volcanogenic deposits ([Bowell et al. 2020](#)). Also, the occurrence of tainiolite is discarded in the studied samples.

Despite micas (lepidolite and zinnwaldite) being the only confirmed lithium minerals, the mineralogical expression of lithium in the Lithium-rich Tuff is probably more complex. Preliminary tests performed by Macusani Yellowcake and reported in [The Mineral Corporation \(2019\)](#) attained high lithium extractions from samples of Lithium-rich Tuff by using acid leaching at low temperatures. For example, leaching with sulfuric acid resulted in a 75-79 % recovery of lithium at 88°C and 90 % at 90-95°C. Also, hydrochloric acid allowed an 88 % extraction of lithium at 92°C. These data strongly

suggest that lithium in the Lithium-rich Tuff also occurs in easily leachable positions such as interlaminar or adsorbed onto clays in addition to structurally bonded in micas. Unfortunately, the reported extraction tests do not indicate the mineralogical composition of the tested samples. Therefore, the contribution of the different potential lithium-bearing phases (i.e., micas, clays – smectite and kaolinite –, zeolites) on the lithium endowment cannot be constrained.

A rough approximation to the contribution of the identified minerals in the Lithium-rich Tuff to the bulk lithium contents is intended here based on the visual comparison of peak intensities in powder XRD patterns, considering the direct proportionality between the intensity of the peaks and the amount of mineral in the sample (Fig. 24). As explained above, the samples with the highest lithium contents (2,500 to 4,300 ppm) in drill cores come from the central portion of the tuff sequence and belong to the “micas with kaolinite subgroup minerals” and “zeolite with mica” mineralogical types defined in this thesis. A first visual approximation would suggest that in samples of the “micas with kaolinite subgroup minerals” type, lithium is hosted primarily in micas to judge from the higher relative intensity of powder XRD mica peaks compared to those of kaolinite. On the other hand, samples of the “zeolite with mica” type show more intense peaks for mordenite than micas, which would agree with the mineralogical association of lithium with this zeolite (see Hoyer et al. 2015).

Samples from the upper and lower portions of the tuff sequence, which belong to the “smectite with mica” mineralogical type, yielded lower Li contents in the range between 500 and 2,500 ppm (Fig. 24). In these samples, the relative intensity of the powder XRD peaks corresponding to smectite are considerably higher than those of micas, suggesting a higher proportion of the former in the analyzed samples. The lower proportion of mica in samples of the “smectite with mica” type might explain the lower values of lithium in these samples when compared with the mica- and lithium-rich samples of the central portion of the tuff sequence. However, the observation of individual diffractograms of samples of the “smectite with mica” type suggest quite the opposite. Samples with lower proportions of micas (e.g., 2021-MAC-49 and 2021-MAC-50 with 1,610 ppm and 2,760 ppm Li, respectively) returned higher Li values relative to those with more intense mica and less intense smectite peaks (e.g., 2021-MAC-42 and 2021-MAC-50 with 880 ppm and 960 ppm Li, respectively). This strongly suggests that smectite may also be an

important lithium scavenger in the Lithium-rich Tuff, which is in good agreement with the preliminary extraction test results performed by Macusani Yellowcake.

Considering the exposed data, lithium in the Lithium-rich Tuff is assumed to occur both in primary (igneous) minerals, namely lepidolite-zinnwaldite (Torró et al., 2023), as well as adsorbed onto or occupying interlaminal positions in secondary clay minerals. In addition, Li might also occur sorbed on zeolites (Hoyer et al. 2015). The performance of laboratory-scale cation-exchange capacity tests on mineralogically well characterized clay- and zeolite-rich samples of the Lithium-rich Tuff is advised to assess the proportions of lithium that occur either bounded in the structure of micas in interlaminal positions in clays or sorbed onto the clay and zeolite minerals identified in this thesis.

## **5.2. Classification of the Falchani Lithium Project**

*Hard-rock* LCT pegmatite and hydromorphic salar deposits are considered conventional lithium sources (Bradley et al. 2017a; Bowell et al. 2020). On the other hand, non-conventional sources of lithium include volcanogenic, bauxite, and Mn oxide deposits (Fig. 32).

According to the geological setting, facies description, and mineralogical characterization reported in this thesis, the Macusani Lithium Project belongs to the volcanogenic type (see also The Mineral Corporation 2019). Volcanogenic lithium deposits are, in turn, subdivided into clay mineral, ion-clay, and jadarite sub-types (Bowell et al. 2020). According to our data, lithium in the Lithium-rich Tuff of the Macusani Lithium Project is hosted by primary (igneous) phases, in this case, zinnwaldite and lepidolite, and also associated with secondary minerals such as clays (particularly smectites, as discussed above) and zeolite. Therefore, an unequivocal classification of the Macusani Lithium Project in one of these predefined types of volcanogenic lithium deposits is not possible. Noteworthy also is the fact that, to our best knowledge, primary lithium micas are not reported as important mineral components in other volcanogenic lithium deposits and, hence, may represent a singularity in the case of the Falchani Lithium Project. The opposite occurs with Li clay minerals, for trioctahedral Li smectites, amply described as the main lithium ore in tuff-hosted volcanogenic lithium deposits (Benson et al. 2017; Castor and Henry 2020; Borojević Šoštarić and Brenko 2023), were not identified in the Lithium-rich Tuff of the Falchani Lithium Project. Pending cation-exchange capacity results on samples from the Lithium-rich Tuff to more precisely assess



the contribution of each Li-bearing mineral to the general Li endowment, we preliminarily propose the classification of the Falchani Lithium Project as a “mixed” primary mica – secondary clay/zeolite volcanogenic deposit type (Fig. 32).

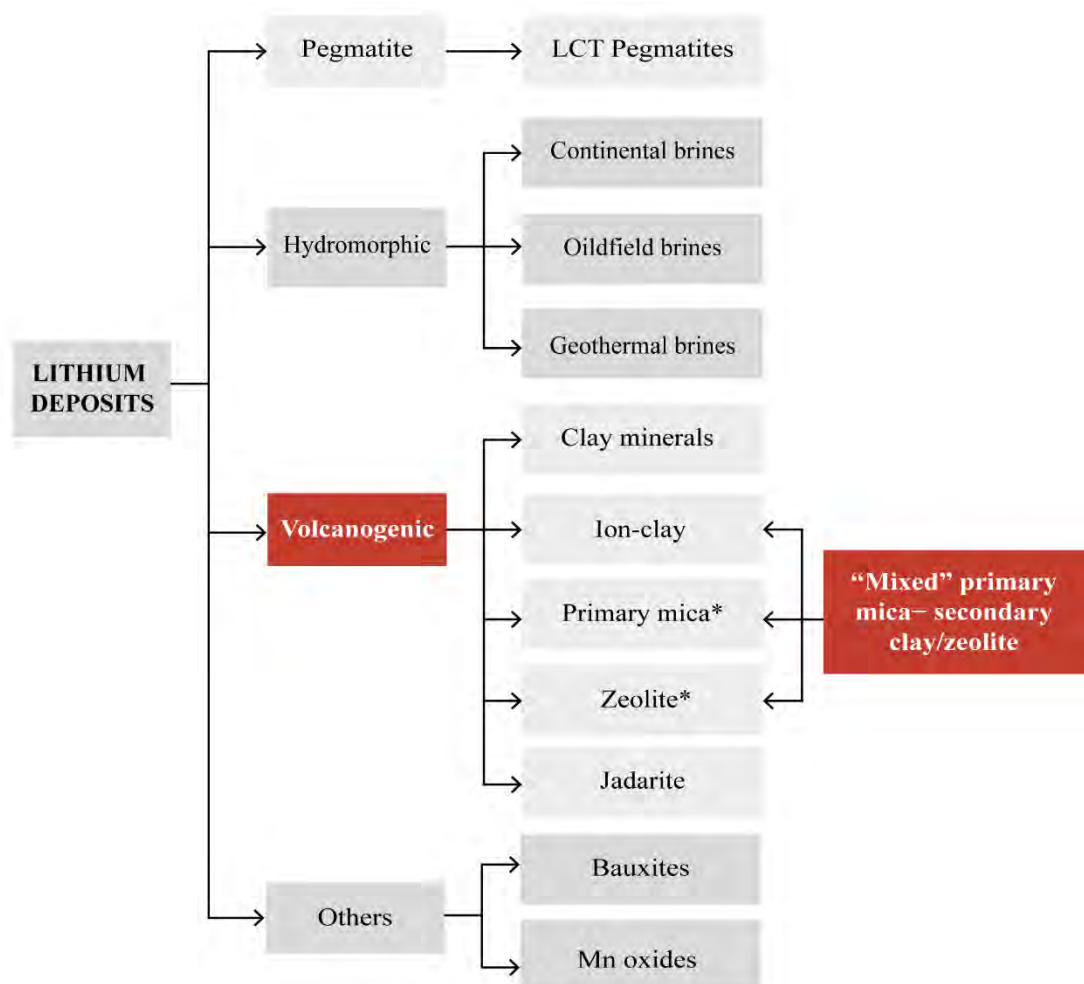


**Figure 32.** Classification of lithium deposits mostly based on Bowell et al. (2020), highlighting the proposed “mixed” primary mica – secondary clay/zeolite volcanogenic deposit type for the Falchani deposit. The zeolite\* and primary-mica\* endmembers within volcanogenic lithium deposits are merely indicative since they have not been described

The lixiviation of lithium that is in interlaminar positions in, or adsorbed onto, clay minerals is energetically favorable regarding the extraction of lithium from lepidolite and zinnwaldite, which typically involves roasting at high temperatures (750 – 1,000°C) with additives (Luong et al. 2013). Despite the fact that extraction of Li from lepidolite is still considered technically challenging, new methods are under development, such as the integration of flotation and leaching with sulfuric acid, to convert Li-micas into usable products (Mulwanda 2021; Lepidico 2023). Therefore, even though mica minerals may be important Li carriers in the Lithium-rich Tuff, the main ore by volume in this deposit

is probably represented by clay and zeolite minerals, in which the extraction is much inexpensive, micas representing and added economic value.

## 6. CONCLUSIONS

In this thesis, samples of the Lithium-rich Tuff, which hosts the main resource in the Falchani Lithium Project, Puno, Peru, have been mineralogically characterized using XRD, SEM-EDS, and TEM. The following conclusions are reached:

- The major mineralogical composition of the Lithium-rich Tuff consists of quartz, plagioclase, K-feldspar, trioctahedral micas (lepidolite and zinnwaldite), and clay minerals (smectite and kaolinite subgroup minerals). In addition, zeolites (mordenite ± mutinaite) and cristobalite are found in a few samples.
- The samples have been grouped into four mineralogical types: i) mica with no zeolite nor clay minerals, ii) mica with kaolinite subgroup minerals, iii) smectite with mica, and iv) zeolite with mica.
- A vertical mineralogical succession has been identified in drill core samples. The identified zones include i) the lower domain ( $\leq \sim 1,850$  ppm Li), which is characterized by the ubiquitous occurrence of smectites and lesser amounts of micas; ii) the central domain, which presents the highest lithium contents ( $\leq \sim 4,200$  ppm Li) and embraces samples of the “micas with kaolinite subgroup minerals” and “zeolite with mica” types; and iii) the upper domain ( $\leq \sim 2,800$  ppm Li), characterized by the presence of smectites with lesser proportions of micas and traces of kaolinite.
- The examination of clay minerals with high-resolution techniques (HRTEM) proved the dioctahedral character of the smectites (montmorillonite-beidellite), with crystal parameters  $a=5.12$  Å and  $b=8.62$  Å. Kaolinite subgroup minerals correspond to kaolinite, with crystal parameters  $a=5.11-5.14$  Å and  $b=8.88$  Å and, very locally, halloysite.
- In addition to lithium micas (zinnwaldite and lepidolite), it is plausible that an important proportion of lithium in the Lithium-rich Tuff is also associated with secondary minerals, chiefly dioctahedral smectites (either adsorbed or occupying

interlaminar positions) and zeolite (probably, as a sorbed cation). Cation-exchange capacity tests on mineralogically well-characterized clay- and zeolite-rich samples are advised to assess the proportions of lithium that occur either bounded in the structure of micas, in interlaminar positions in clays or sorbed onto the clay and zeolite minerals.

- The Falchani Lithium Project is tentatively classified as a ‘mixed’ primary mica – secondary clay/zeolite volcanogenic deposit type.



## 7. REFERENCES

- Agencia Reuters (2020) Plateau Energy Metals recauda US\$ 600 millones para producir litio en Perú, con retraso por pandemia. *Gestión*. <https://gestion.pe/economia/plateau-energy-metals-recauda-us-600-millones-para-producir-litio-en-peru-con-retraso-por-pandemia-nndc-noticia/>. Accessed 10 July 2022
- American Lithium Corp. (2022) American Lithium validates Sulfate of Potash as a strategic by-product of future lithium production at Falchani. American Lithium. <https://americanlithiumcorp.com/american-lithium-validates-sulfate-of-potash-as-a-strategic-by-product-of-future-lithium-production-at-falchani/>. Accessed 10 July 2022
- Aral H, Vecchio-Sadus A (2008) Toxicity of lithium to humans and the environment—A literature review. *Ecotoxicol Environ Saf* 70:349–356.
- Arribas A, Figueroa E (1985) Las mineralizaciones de Uranio en las rocas volcánicas de Macusani, Puno (Peru). *Estudios geológicos* 41:323–342. <https://doi.org/10.3989/egeol.85415-6714>
- Azevedo M, Baczyńska M, Hoffman K, Krauze A (2022) Lithium mining: How new production technologies could fuel the global EV revolution. McKinsey & Company, 10 p
- Bárdossy G (2013) Karst bauxites. Elsevier, pp 1-440
- Barnes VE, Edwards G, Mclaughlin WA, Friedman I, Joensuu O (1970) Macusanite Occurrence, Age, and Composition, Macusani, Peru. *Geol Soc Am Bull* 81:1539–1546. [https://doi.org/10.1130/0016-7606\(1970\)81\[1539:MOAACM\]2.0.CO;2](https://doi.org/10.1130/0016-7606(1970)81[1539:MOAACM]2.0.CO;2)
- Bauer D, Diamond D, Li J, McKittrick M, Sandalow D, Telleen P (2011) Critical Materials Strategy. US Department of Energy, 196 p
- Benson TR, Coble MA, Rytuba JJ, Mahood GA (2017) Lithium enrichment in intracontinental rhyolite magmas leads to Li deposits in caldera basins. *Nat Commun* 8:270. <https://doi.org/10.1038/s41467-017-00234-y>
- Bibienne T, Magnan J, Rupp A, Laroche N (2020) From Mine to Mind and Mobiles: Society's Increasing Dependence on Lithium. *Elements* 16:265–270. <https://doi.org/10.2138/GSELEMENTS.16.4.265>
- Borojević S, Brenko T (2023) The Miocene Western Balkan lithium-boron metallogenic zone. *Miner Deposita* 58:639–658. <https://doi.org/10.1007/s00126-022-01151-x>
- Bowell RJ, Lagos L, de los Hoyos CR, Declercq J (2020) Classification and characteristics of natural lithium resources. *Elements* 16:259–264. <https://doi.org/10.2138/GSELEMENTS.16.4.259>
- Bradley D, Jaskula B (2014) Lithium for harnessing renewable energy. U.S. Geological Survey, Mineral Resources Program Fact Sheet 2014-3035. <https://doi.org/10.3133/fs20143035>
- Bradley DC, Stillings LL, Jaskula BW, Munk L, McCauley AD (2017a) Critical mineral resources of the United States—Economic and environmental geology and prospects for future supply. U.S. Geological Survey, Virginia, pp K1– K21. <https://doi.org/10.3133/pp1802K>
- Bradley DC, McCauley AD, Stillings LM (2017b) Mineral-deposit model for lithium-cesium-tantalum pegmatites. U.S. Geological Survey, Virginia, pp 1-48. <https://doi.org/10.3133/sir201050700>
- Brooks K (2020) Lithium minerals. *Geology Today* 36:192–197. <https://doi.org/10.1111/gto.12326>
- Castor SB, Henry CD (2020) Lithium-Rich Claystone in the McDermitt Caldera, Nevada, USA: Geologic, Mineralogical, and Geochemical Characteristics and Possible Origin. *Minerals* 10:1–39. <https://doi.org/10.3390/min10010068>

- Chávez A, Salas G, Gutiérrez E, Cuadros J (1997) Geología de los cuadrángulos de Corani y Ayapata. Hojas 28-u y 28-v. Instituto Geológico, Minero y Metalúrgico, 128 p
- Cheilletz A, Clark AH, Farrar E, Arroyo Pauca G, Pichavant M, Sandeman HA (1992) Volcano-stratigraphy and  $^{40}\text{Ar}/^{39}\text{Ar}$  geochronology of the Macusani ignimbrite field: monitor of the Miocene geodynamic evolution of the Andes of southeast Peru. *Tectonophysics* 205:307–327. [https://doi.org/10.1016/0040-1951\(92\)90433-7](https://doi.org/10.1016/0040-1951(92)90433-7)
- Chen C, Lee CTA, Tang M, Biddle K, Sun W (2020) Lithium systematics in global arc magmas and the importance of crustal thickening for lithium enrichment. *Nat Commun* 11:5313. <https://doi.org/10.1038/s41467-020-19106-z>
- Clark AH, Farrar E, Kontak DJ, Langridge RJ, Arenas MJ, France LJ, McBride SL, Woodman PL, Wasteneys HA, Sandeman HA, Archibald, DA (1990) Geologic and geochronologic constraints on the metallogenic evolution of the Andes of southeastern Peru. *Economic Geology*, 85: 1520-1583
- Collins AG (1976) Lithium abundance in oilfield waters. In: Vine J (ed). *Lithium resources and requirements by the year 2000*. US Geol Surv Prof Pap 1005, Colorado, pp116–123. <https://doi.org/10.3133/pp1005>
- De la Cruz J, López JC, León W, Lara M (1996) Geología del cuadrángulo de Macusani. Hoja 29-v. Instituto Geológico, Minero y Metalúrgico, 197 p
- Ellis BS, Szymanowski D, Harris C, Tollan PM, Neukampf J, Guillong M, Cortes-Calderon EA, Bachmann O (2022). Evaluating the potential of rhyolitic glass as a lithium source for brine deposits. *Economic Geology*, 117: 91-105
- European Commission (2023) Study on the EU's list of Critical Raw Materials – Final Report. European Commission, Brussels, 158 p
- Evans K (2014) Lithium. In: Gunn G (ed) *Critical Metals Handbook*. John Wiley & Sons, Nottingham, pp 230–260. <https://doi.org/10.1002/9781118755341.ch10>
- Fission 3.0 Corp. (2022) Macusani Project. Fission 3.0. <https://www.fission3corp.com/projects/peru/macusani-peru/>. Accessed 23 June 2022
- Fortier SM, Nassar NT, Lederer GW, Brainard J, Gambogi J, McCullough EA (2018) Draft critical mineral list—Summary of methodology and background information—U.S. Geological Survey technical input document in response to Secretarial Order No. 3359. U.S. Geological Survey, Virginia, 15 p
- Foshag WF, Woodford AO (1936) Bentonitic magnesian clay mineral from California. *Am Min*, 21: 238-244
- Garrett DE (2004) Part 1 - Lithium. In: *Handbook of Lithium and Natural Calcium Chloride*. Elsevier, pp 1–235
- Gestión (2018) ¿Cómo se descubrió en Perú el yacimiento de litio que podría convertirse en el más grande del mundo? Gestión. <https://gestion.pe/peru/descubrio-peru-yacimiento-litio-convertirse-grande-mundo-238710-noticia/>. Accessed 23 June 2022. Accessed 11 Jul 2022
- Gourcerol B, Gloaguen E, Tuduri J, Melleton J (2019) Typology of hard-rock Li-hosted deposits in Europe. In 15th Biennial Meeting SGA 2019.
- Grew ES (2020) The minerals of lithium. *Elements* 16:235–240. <https://doi.org/10.2138/GSELEMENTS.16.4.235>
- Hoyer M, Kummer NA, Merkel B (2015) Sorption of lithium on bentonite, kaolin and zeolite. *Geosciences*, 5:127-140. <https://doi.org/10.3390/geosciences5020127>

- Huh Y, Chan LH, Zhang L, Edmond JM (1998) Lithium and its isotopes in major world rivers: implications for weathering and the oceanic budget. *Geochim Cosmochim Acta* 62:2039–2051. [https://doi.org/10.1016/S0016-7037\(98\)00126-4](https://doi.org/10.1016/S0016-7037(98)00126-4)
- IRENA (2019) *Global Energy Transformation: A Roadmap to 2050*. International Renewable Energy Agency, Abu Dhabi, 52 p
- Jowitt SM, McNulty BA (2021) Battery and Energy Metals: Future Drivers of the Minerals Industry? *SEG Discovery* 127:11–18. <https://doi.org/10.5382/2021-127.fea-01>
- Kay S, Mpodozis C (2020) The Andes. *Encyclopedia of Geology* 80:41–72. <https://doi.org/10.1016/B978-0-08-102908-4.00173-9>
- Karrech A, Azadi MR, Elchalakani M, Shahin MA, Seibi AC (2020) A review on methods for liberating lithium from pegmatites. *Miner Eng* 145:106085. <https://doi.org/10.1016/j.mineng.2019.106085>
- Kesler SE, Gruber PW, Medina PA, Keoleian GA, Everson MP, Wallington, TJ (2012) Global lithium resources: Relative importance of pegmatite, brine, and other deposits. *Ore Geol Rev* 48:55–69. <https://doi.org/10.1016/j.oregeorev.2012.05.006>
- Kontak DJ, Clark AH, Farrar E, Archibald DA, Baadsgaard H (1990) Late Paleozoic-early Mesozoic magmatism in the Cordillera de Carabaya, Puno, southeastern Peru: Geochronology and petrochemistry. *J South Am Earth Sci* 3:213–230.
- Laubacher G (1978) *Estudio geológico de la región norte del lago Titicaca*. Instituto Geológico, Minero y Metalúrgico, 120 p
- Lee J, Bazilian M, Sovacool B, Hund K, Jowitt SM, Nguyen TP, Månberger A, Kah M, Greene S, Galeazzi C, Awuah-Offei K, Moats M, Tilton J, Kukoda S (2020) Reviewing the material and metal security of low-carbon energy transitions. *Renew Sust Energ Rev* 124:24. <https://doi.org/10.1016/j.rser.2020.109789>
- Lepidico (2023) Leading the next lithium cycle. *Lepidico*. <https://lepidico.com/technology> . Accessed 10 August 2023
- Lodders K (2020) The Cosmic Lithium Story. *Elements* 16:241–246. <https://doi.org/10.2138/GSELEMENTS.16.4.241>
- London D (2008) Pegmatites. *The Mineralogical Association*, 347 p
- London D (2017) Reading Pegmatites: Part 3—What Lithium Minerals Say. *Rocks & Minerals* 92:144–157.
- López JC (1996) *Geología del cuadrángulo de Nuñoa*. Hoja 29-u. Instituto Geológico, Minero y Metalúrgico, 171p
- Lorimer GW, Cliff G (1976) Analytical Electron Microscopy of Minerals. In: Wenk HR (ed) *Electron Microscopy in Mineralogy*. Springer, Berlin. [https://doi.org/10.1007/978-3-642-66196-9\\_38](https://doi.org/10.1007/978-3-642-66196-9_38)
- Luong VT, Kang DJ, An JW, Kim MJ, Tran T (2013). Factors affecting the extraction of lithium from lepidolite. *Hydrometallurgy* 134:54-61.
- Marschall HR, Tang M (2020) High-temperature processes: Is it time for lithium isotopes? *Elements* 16:247–252. <https://doi.org/10.2138/gselements.16.4.247>
- Michaud JAS, Pichavant M, Villaros A (2021) Rare elements enrichment in crustal peraluminous magmas: insights from partial melting experiments. *Contrib Mineral Petrol* 176:96. <https://doi.org/10.1007/s00410-021-01855-9>

- Mišković A, Spikings RA, Chew DM, Košler J, Ulianov A, Schaltegger U (2009) Tectonomagmatic evolution of Western Amazonia: Geochemical characterization and zircon U-Pb geochronologic constraints from the Peruvian Eastern Cordilleran granitoids. *Geol Soc Am Bull* 121:1298–1324. <https://doi.org/10.1130/B26488.1>
- Moore DM, Reynolds RCJ (1989) X-Ray Diffraction and the Identification and Analysis of Clay Minerals. Oxford University Press, Oxford
- Mulwanda J (2021). Extraction of lithium from lepidolite and spodumene. Doctoral dissertation, Murdoch University
- Munk LA, Hynek SA, Bradley DC, Boutt D, Labay K, Jochens H (2016) Lithium Brines: A Global Perspective. *Reviews in Economic Geology*, pp 339–365. <https://doi.org/10.5382/rev.18.14>
- National Research Council (2008) Minerals, critical minerals, and the U.S. Economy. National Academies Press, Washington, 245 p. <https://doi.org/10.17226/12034>
- Neukampf J, Ellis BS, Magna T, Laurent O, Bachmann O (2019) Partitioning and isotopic fractionation of lithium in mineral phases of hot, dry rhyolites: the case of the Mesa Falls Tuff, Yellowstone. *Chem Geol*, 506:175–186. <https://doi.org/10.1016/j.chemgeo.2018.12.031>
- Penniston-Dorland S, Liu XM, Rudnick RL (2017) Lithium Isotope Geochemistry. *Rev Mineral Geochem* 82:165–217. <https://doi.org/10.2138/rmg.2017.82.6>
- Perez ND, Horton BK, Carlotto V (2016) Structural inheritance and selective reactivation in the central Andes: Cenozoic deformation guided by pre-Andean structures in southern Peru. *Tectonophysics* 671:264–280
- Perez ND, Horton BK, McQuarrie N, Stübner K, Ehlers TA (2016) Andean shortening, inversion and exhumation associated with thin- and thick-skinned deformation in southern Peru. *Geol Mag* 153:1013–1041. <https://doi.org/10.1017/S0016756816000121>
- Pichavant M, Valencia Herrera J, Boulmier S, Briquieu L, Joron JL, Juteau M, Marin L, Michard A, Sheppard AMF, Treuil M, Vernet M (1987) The Macusani glasses, SE Peru: evidence of chemical fractionation in peraluminous magmas. In: Mysen BO (ed) *Magmatic processes, physicochemical principles*. *Geochem Soc Special Publ* 1: 359–373
- Pichavant M, Kontak DJ, Valencia Herrera J, Clark AH (1988a) The Miocene-Pliocene Macusani Volcanics, SE Peru - I. Mineralogy and magmatic evolution of a two-mica aluminosilicate-bearing ignimbrite suite. *Contrib to Mineral Petrol* 100:300–324.
- Pichavant M, Kontak DJ, Briquieu L, Valencia Herrera J, Clark AH (1988b) The Miocene-Pliocene Macusani Volcanics, SE Peru - II. Geochemistry and origin of a felsic peraluminous magma. *Contrib Mineral Petrol* 100:325–338. <https://doi.org/10.1007/BF00379742>
- Pichavant M, Montel JM (1988) Petrogenesis of a two-mica ignimbrite suite: The Macusani Volcanics, SE Peru. *Earth Environ Sci Trans R Soc Edinb* 79:197–207. <https://doi.org/10.1017/S0263593300014218>
- Pogge von Strandmann PAE, Kasemann SA, Wimpenny JB (2020) Lithium and Lithium Isotopes in Earth's Surface Cycles. *Elements* 16:253–258. <https://doi.org/10.2138/GSELEMENTS.16.4.253>
- Ramos VA (1999) Plate tectonic setting of the Andean Cordillera. *Episodes* 22:183–190. <https://doi.org/10.18814/epiiugs/1999/v22i3/005>
- Redacción RPP (2018) El Perú podría llegar a ser el país con más reservas de litio en el mundo. RPP Noticias. <https://rpp.pe/economia/economia/peru-tendria-la-primera-mina-de-litio-del-mundo-si-explota-yacimiento-puno-noticia-1137200>. Accessed 23 June 2022

- Redacción RPP (2022) El mundo mira al litio, el “oro blanco” con grandes reservas en Latinoamérica. In: RPP Noticias. <https://rpp.pe/mundo/latinoamerica/el-mundo-mira-al-litio-el-oro-blanco-con-grandes-reservas-en-latinoamerica-noticia-1406957?ref=rpp>. Accessed 11 Jul 2022
- Rodríguez R, Choquehuanca S, Sánchez E, Fabián C, Del Castillo B (2021) Geología de los cuadrángulos de Macusani (hojas 29v1, 29v2, 29v3, 29v4) y Limbani (hojas 29x1, 29x2, 29x3, 29x4). Instituto Geológico, Minero y Metalúrgico, 82 p.
- Ronquillo MC, Torre Antay J, Fuentes Palomino J, Minaya Encarnación I (2019) Informe preliminar de prospección de litio en el sur del Perú. Instituto Geológico, Minero y Metalúrgico, Lima
- Rosas S, Fontboté L, Tankard A (2007) Tectonic evolution and paleogeography of the Mesozoic Pucará Basin, central Peru. *J South Am Earth Sci* 24:1–24. <https://doi.org/10.1016/j.jsames.2007.03.002>
- Saldarriaga J (2021) Minem advierte que la explotación de litio generará “serio problema de radiación” en Puno. ¿Tiene razón? In: El Comercio. [https://elcomercio.pe/economia/litio-minem-advierte-que-la-explotacion-de-litio-generara-serio-problema-de-radiacion-en-puno-tiene-razon-noticia/#google\\_vignette](https://elcomercio.pe/economia/litio-minem-advierte-que-la-explotacion-de-litio-generara-serio-problema-de-radiacion-en-puno-tiene-razon-noticia/#google_vignette). Accessed 11 Jul 2022
- Sánchez AW, Zapata AA (2003) Memoria descriptiva de la revisión y actualización de los cuadrángulos de Río Picha (25-p), Timpia (25-q), Chuanquiri (26-p), Quillabamba (26-q), Quebrada Honda (26-r), Parobamba (26-s), Pacaypata (27-p), Machupicchu (27-q), Urubamba (27-r), Calca (27-s), Chotachaca (27-t), Quincemil (27-u), Ocongate (28-t), Corani (28-u) y Ayapata (28-v). Instituto Geológico, Minero y Metalúrgico, Lima, 51 p. <https://hdl.handle.net/20.500.12544/2073>
- Sandeman HA, Clark AH (2003) Glass-rich, Cordierite–Biotite Rhyodacite, Valle Ninahuisa, Puno, SE Peru: Petrological Evidence for Hybridization of ‘Lachlan S-type’ and Potassic Mafic Magmas. *J Petrol* 44:355–385. <https://doi.org/10.1093/petrology/44.2.355>
- Sandeman HA, Clark AH (2004) Commingling and mixing of S-type peraluminous, ultrapotassic and basaltic magmas in the Cayconi volcanic field, Cordillera de Carabaya, SE Peru. *Lithos* 73:187–213. <https://doi.org/10.1016/j.lithos.2003.12.005>
- Sandeman HA, Clark AH, Farrar E, Arroyo-Pauca G (1996) A critical appraisal of the Cayconi Formation, Crucero Basin, southeastern Peru. *J South Am Earth Sci* 9:381–392. [https://doi.org/10.1016/S0895-9811\(96\)00021-1](https://doi.org/10.1016/S0895-9811(96)00021-1)
- Sandeman HA, Clark AH, Farrar E, Arroyo-Pauca G (1997) Lithostratigraphy, petrology and  $^{40}\text{Ar}$ - $^{39}\text{Ar}$  geochronology of the Crucero Supergroup, Puno Department, SE Peru. *J South Am Earth Sci* 10:223–245. [https://doi.org/10.1016/S0895-9811\(97\)00023-0](https://doi.org/10.1016/S0895-9811(97)00023-0)
- Sarchi C, Lucassen F, Meixner A, Caffè PJ, Becchio R, Kasemann SA (2023) Lithium enrichment in the Salar de Diablillos, Argentina, and the influence of Cenozoic volcanism in a basin dominated by Paleozoic basement. *Miner Deposita*, pp 1-20
- Sempere T, Carlier G, Soler P, Fornari M, Carlotto V, Jacay J, Arispe O, Néraudeau D, Cárdenas J, Rosas S, Jiménez N (2002) Late Permian-Middle Jurassic lithospheric thinning in Peru and Bolivia, and its bearing on Andean-age tectonics. *Tectonophysics* 345:153–181. [https://doi.org/10.1016/S0040-1951\(01\)00211-6](https://doi.org/10.1016/S0040-1951(01)00211-6)
- Sempere T, Jacay J (2008) Anatomy of the Central Andes: Distinguishing between western, magmatic Andes and eastern, tectonic Andes. 7th International Symposium on Andean Geodynamics 504–507
- SIDEMCAT (2022) Consulta al Sistema de Derechos Mineros y Catastro. In: INGEMMET. <https://portal.ingemmet.gob.pe/web/guest/sidemcat>. Accessed 10 Jul 2022
- Spikings R, Reitsma MJ, Boekhout F, Mišković A, Ulianov A, Chiaradia M, Gerde A, Schaltegger U (2016) Characterization of Triassic rifting in Peru and implications for the early disassembly of western Pangaea. *Gondwana Res* 35:124–143. <https://doi.org/10.1016/j.gr.2016.02.008>



- Starkey HC (1982) The role of clays in fixing lithium. US Gov, Virginia
- Sterba J, Krzemień A, Fernández PR, García-Miranda C E, Valverde GF (2019) Lithium mining: Accelerating the transition to sustainable energy. *Resour Policy* 62:416–426. <https://doi.org/10.1016/j.resourpol.2019.05.002>
- Stewart DB (1978) Petrogenesis of lithium-rich pegmatites. *Am Mineral* 63:970–980
- Tang B, Fu Y, Yan S, Chen P, Cao C, Guo C, Wu P, Long Z, Long K, Wang T, Liu Y, Yang Y (2022) The source, host minerals, and enrichment mechanism of lithium in the Xinmin bauxite deposit, northern Guizhou, China: Constraints from lithium isotopes. *Ore Geol Rev* 141:104653. <https://doi.org/10.1016/j.oregeorev.2021.104653>
- The Mineral Corporation (2019) Mineral Resource Estimates for the Falchani Lithium Project in the Puno District of Peru. Bryanston, pp 1–72.
- Thompson JM, Fournier RO (1988) Chemistry and geothermometry of brine produced from the Salton Sea scientific drill hole, Imperial Valley, California. *J Geophys Res Earth Surf* 93: 13165-13173. <https://doi.org/10.1029/JB093iB11p13165>
- Toba AL, Nguyen RT, Cole C, Neupane G, Paranthaman MP (2021) U.S. lithium resources from geothermal and extraction feasibility. *Resour Conserv Recycl* 169:105514. <https://doi.org/10.1016/j.resconrec.2021.105514>
- Toraya H, Iwai S, Marumo F, Hirao M (1977) The crystal structure of taeniolite,  $\text{KLiMg}_2\text{Si}_4\text{O}_{10}\text{F}_2$ . *Zeitschrift für Kristallographie* 146:73-83
- Torró L, Villanova-de-Benavent C, Monnier L, Laurent O, Segovia-More MK, Sanandres-Flores M, Ramírez-Briones J, Vallance J, Salvi S, Baby P, Proenza JA, Nieto F (2023) Lithium-bearing micas in the ‘lithium-rich tuff’ from the Macusani Volcanic Field, Puno, Peru. *Proceedings of the 17th SGA Biennial Meeting*, in press.
- Trading Economics (2023) Lithium. <https://tradingeconomics.com/commodity/lithium>. Accessed 15 Jul 2023
- United States Geological Survey (2023) Mineral Commodity Summaries 2023. <https://doi.org/10.3133/mcs2023>
- Vilca Arpasi PC (2020) El Proyecto de Explotación de Litio en Puno. Asociación Servicios Educativos Rurales, Lima
- Wörner G, Schildgen TF, Reich M (2018) The Central Andes: Elements of an extreme land. *Elements* 14:225–230. <https://doi.org/10.2138/gselements.14.4.225>



**APPENDIX A.** List of studied samples from the Macusani Volcanic Field

Sample	Coordinates		Drill core	Depth (m)	Concession	Description
	UTM E	UTM N				
2021-MAC-005	317,768	8,451,301	-	-	Huarituña 3	Oriented oligomictic cemented floatbreccia with dark matrix and sub-rounded to angular light clasts.
2021-MAC-006	317,759	8,451,260	-	-	Huarituña 3	Oriented oligomictic cemented floatbreccia with dark matrix and sub-rounded to angular light clasts.
2021-MAC-008 A	317,880	8,451,590	-	-	Falchani	Finely laminated (alternating white/gray laminae), non-foliated volcanic mudstone with concretions relicts.
2021-MAC-008 B	318,893	8,451,535	-	-	Falchani	Finely laminated (alternating white/gray laminae), non-foliated volcanic mudstones with pseudo-stromatolytic texture and concretion relicts.
2021-MAC-011 A	319,446	8,451,382	-	-	Falchani	Finely laminated (alternating orange-beige/white laminae), non-foliated volcanic mudstone with a convoluted level and concretion relicts.
2021-MAC-011 B	319,564	8,451,884	-	-	Falchani	Finely laminated (alternating orange-beige/white laminae), non-foliated volcanic mudstone with a convoluted level and concretion relicts.
2021-MAC-019A	308,594	8,451,082	-	-	Sapanuta 3	Massive, grayish white volcanic mudstone with ash-size mica crystals and surface-impregnate ferric oxides and hydroxides.
2021-MAC-021	308,601	8,450,888	-	-	Sapanuta 3	Massive, cohesive, grayish white volcanic mudstone. Matrix-supported scarce medium ash-size mica crystals.
2021-MAC-022A	308,738	8,450,791	-	-	Sapanuta 3	Massive, grayish white volcanic mudstone. Matrix-supported medium ash-size mica crystals and surface-impregnate ferric oxides and hydroxides.

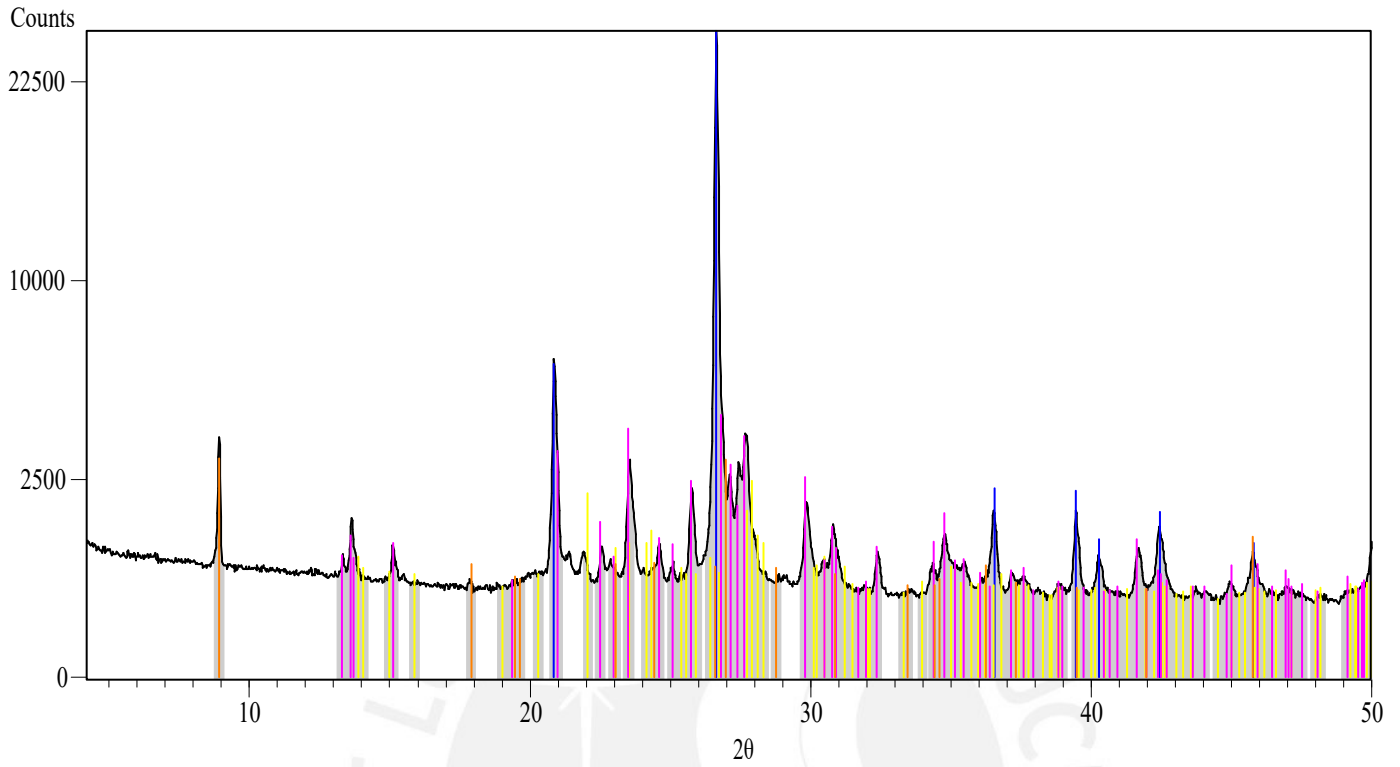
Sample	Coordinates		Drill core	Depth (m)	Concession	Description
	UTM E	UTM N				
2021-MAC-022B	308,738	8,450,791	-	-	Sapanuta 3	Massive, grayish white volcanic mudstone. Matrix-supported scarce medium ash-size mica crystals. Dissemination of very fine crystals of realgar/orpiment/cinnabar and radiating acicular crystals of stibnite.
2021-MAC-025	318,397	8,451,249	-	-	Falchani	Massive, white grayish white volcanic mudstone. Matrix-supported scarce medium ash-size mica crystals.
2021-MAC-026	318,247	8,451,169	-	-	Falchani	Finely undulated laminated (alternating white/light gray laminae), non-foliated mud-size grained rock with dark-gray aggregates.
2021-MAC-031	318,003	8,451,079	-	-	Falchani	Slumped volcanic mudstone with dark matrix, sub-rounded to angular light clasts, and sporadic medium ash-size mica crystals.
2021-MAC-035	319,729	845,1374	PCHAC 01-TSW (1)	62.55-62.60	Falchani	Strongly altered massive, mud-size grained volcanoclastic rock with low hardness and cream color. Scarce medium ash-size matrix-supported mica crystals and/or crystal-fragments are evenly distributed.
2021-MAC-038	319,729	8,451,374	PCHAC 01-TSW (1)	80.35-80.45	Falchani	Finely curved laminated (alternating white/gray laminae), foliated mud-size grained rock with medium ash-grained mica crystals.
2021-MAC-039	319,729	8,451,374	PCHAC 01-TSW (1)	149.00-149.10	Falchani	Finely laminated (alternating white/gray laminae), non-foliated mud-size grained rock with medium ash-grained mica crystals.
2021-MAC-040	319,729	8,451,374	PCHAC 01-TSW (1)	183.25-183.35	Falchani	Cohesive, finely beige-white/gray laminated, non-foliated, mud-size grained rock with white nodules and fine ash- to medium ash-size mica crystals

Sample	Coordinates		Drill core	Depth (m)	Concession	Description
	UTM E	UTM N				
2021-MAC-042	319,729	8,451,374	PCHAC 01-TSW (1)	195.80-195.90	Falchani	Breccia with strongly altered, massive, mud-size grained volcanoclastic rock. Scarce medium ash-size matrix-supported mica crystals and/or crystal-fragments are evenly distributed
2021-MAC-048	319,748	8,451,643	PCHAC 04-TV	174.40-174.50	Ocacasa 4	Finely laminated (alternating white/gray laminae), slightly foliated mud-size grained rock with medium ash-grained mica crystals.
2021-MAC-049	319,748	8,451,643	PCHAC 04-TV	226.00-226.10	Ocacasa 4	Strongly altered, massive mud-size grained volcanoclastic rock with black material distributed along two-structural-orientations lineaments.
2021-MAC-050	318,576	8,451,429	PCHAC 32-TNW	34.50-34.60	Falchani	Strongly altered, massive, mud-size grained volcanoclastic rock. Matrix-supported scarce medium ash-size mica crystals.
2021-MAC-051	318,576	8,451,429	PCHAC 32-TNW	~43.00	Falchani	Strongly altered, massive volcanic mudstone. Medium ash- to coarse ash-size mica, K-feldspar and smoky quartz crystal fragments are matrix-supported.
2021-MAC-052	318,576	8,451,429	PCHAC 32-TNW	~ 52.50	Falchani	Strongly altered, massive, mud-size grained grayish white volcanoclastic rock. Very fine- to medium-grained K-feldspar and quartz crystal fragments, and very fine- to medium-grained mica fragments.
2021-MAC-053	318,576	8,451,429	PCHAC 32-TNW	~115.00	Falchani	Strongly altered, massive, mud-size grained and light cream volcanoclastic rock. Medium ash-size matrix-supported mica, quartz, feldspar crystals and/or crystal-fragments are unevenly distributed.

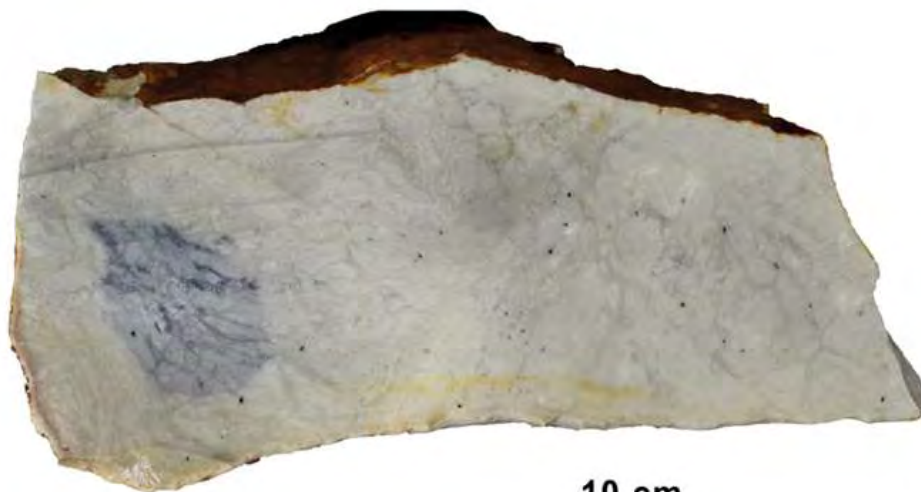
Sample	Coordinates		Drill core	Depth (m)	Concession	Description
	UTM E	UTM N				
2021-MAC-065 A	316,951	8,440,039			Antacora seis	Finely laminated (alternating dark gray/white laminae), non-foliated, volcanic mudstone with concretions relicts, quartz, feldspar, and mica crystals.
2021-MAC-065 B	316,951	8,440,039	-	-	Antacora seis	Finely laminated (alternating dark gray/white laminae), non-foliated, volcanic mudstone with concretions relicts, quartz, feldspar, and mica crystals.
2021-MAC-065 C	316,951	8,440,039	-	-	Antacora seis	Finely laminated (alternating dark gray/white laminae), non-foliated, volcanic mudstone with concretions relicts, quartz, feldspar, and mica crystals.
2021-MAC-066	316,910	8,439,957			Antacora seis	Massive pale orange volcanic mudstone. Matrix-supported crystals and/or crystal fragments include quartz, feldspar, and “books” of micas.
2021-MAC-067A	319,344	8,437,743			San Vicente white	Massive, white/pale orange, crystal-rich volcanic mudstone with smoky quartz, feldspar, and mica crystals.
2021-MAC-067B	319,344	8,437,743	-	-	San Vicente white	Massive, white/pale orange, crystal-rich volcanic mudstone with smoky quartz, feldspar, and mica crystals.
2021-MAC-067C	319,344	8,437,743	-	-	San Vicente white	Massive, white/pale orange, crystal-rich volcanic mudstone with smoky quartz, feldspar, and mica crystals.

# Appendix B. XRD results

2021-MAC-005

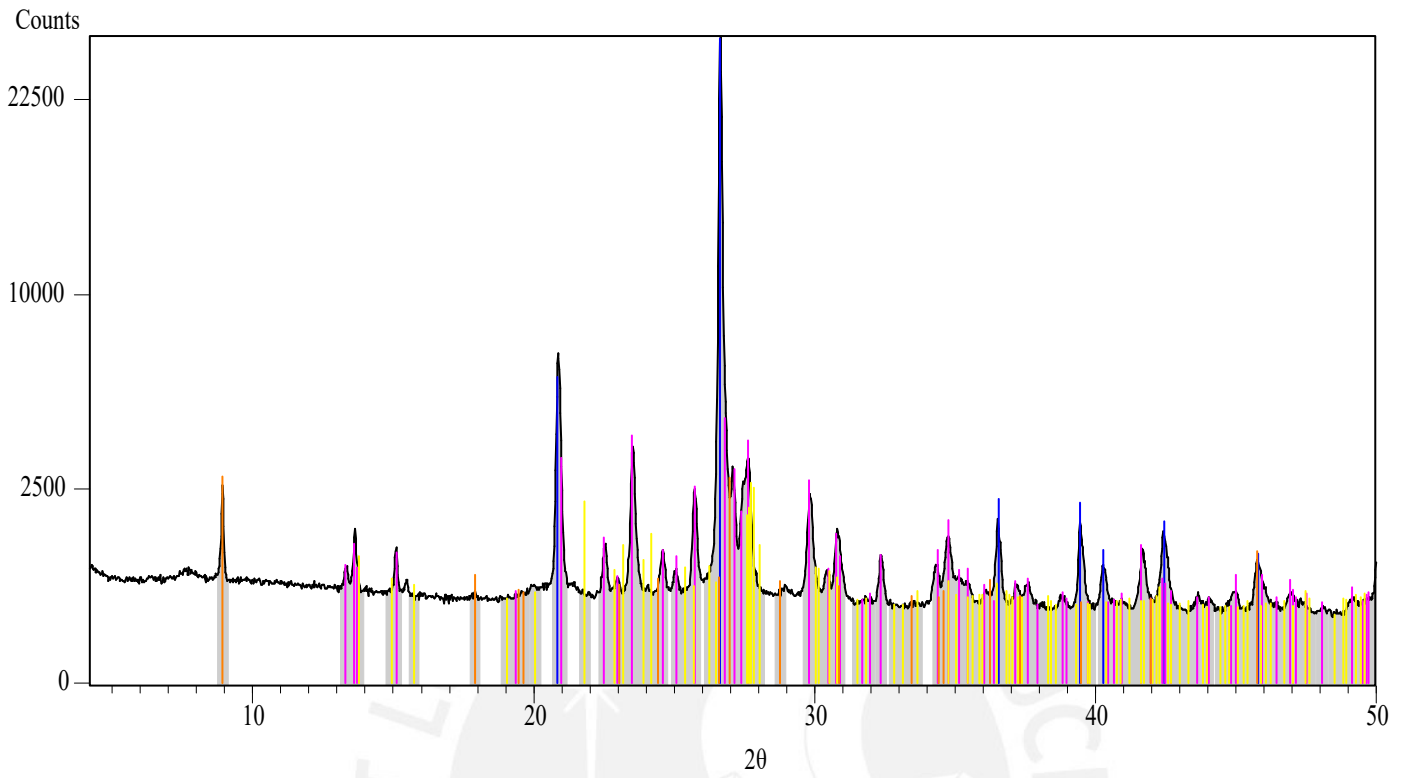


Peak List
Quartz
Plagioclase
K-Feldspar
Mica



10 cm

2021-MAC-006

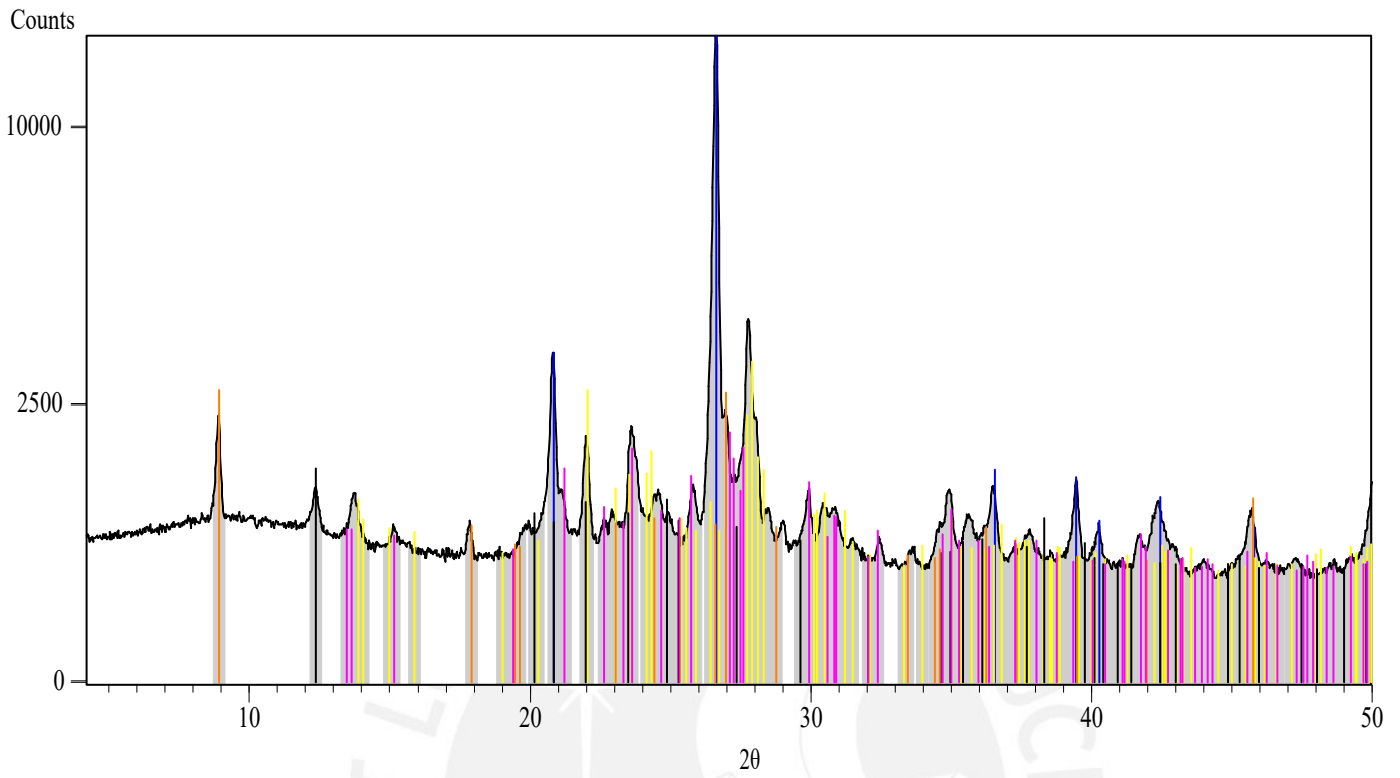


Peak List	Intensity
Quartz	Low
K-Feldspar	High
Plagioclase	Medium
Mica	Low

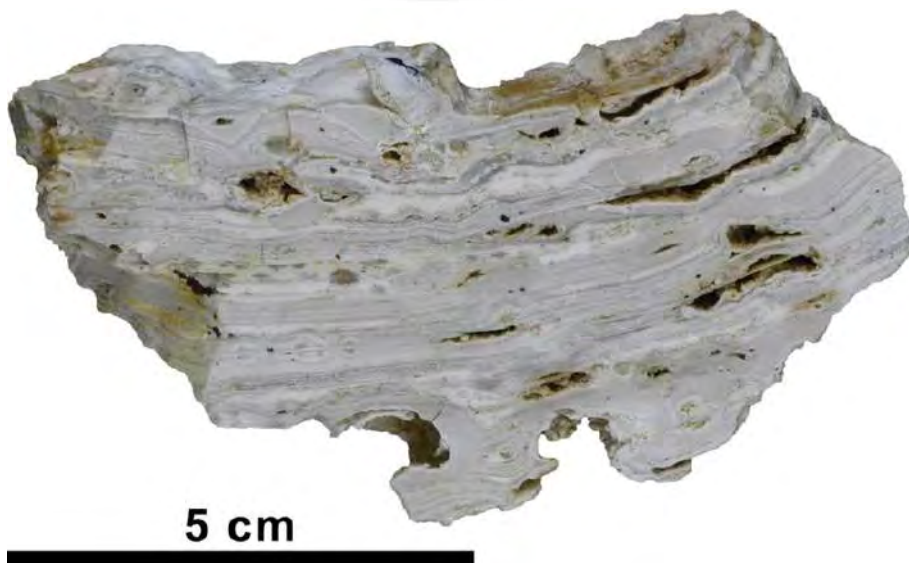




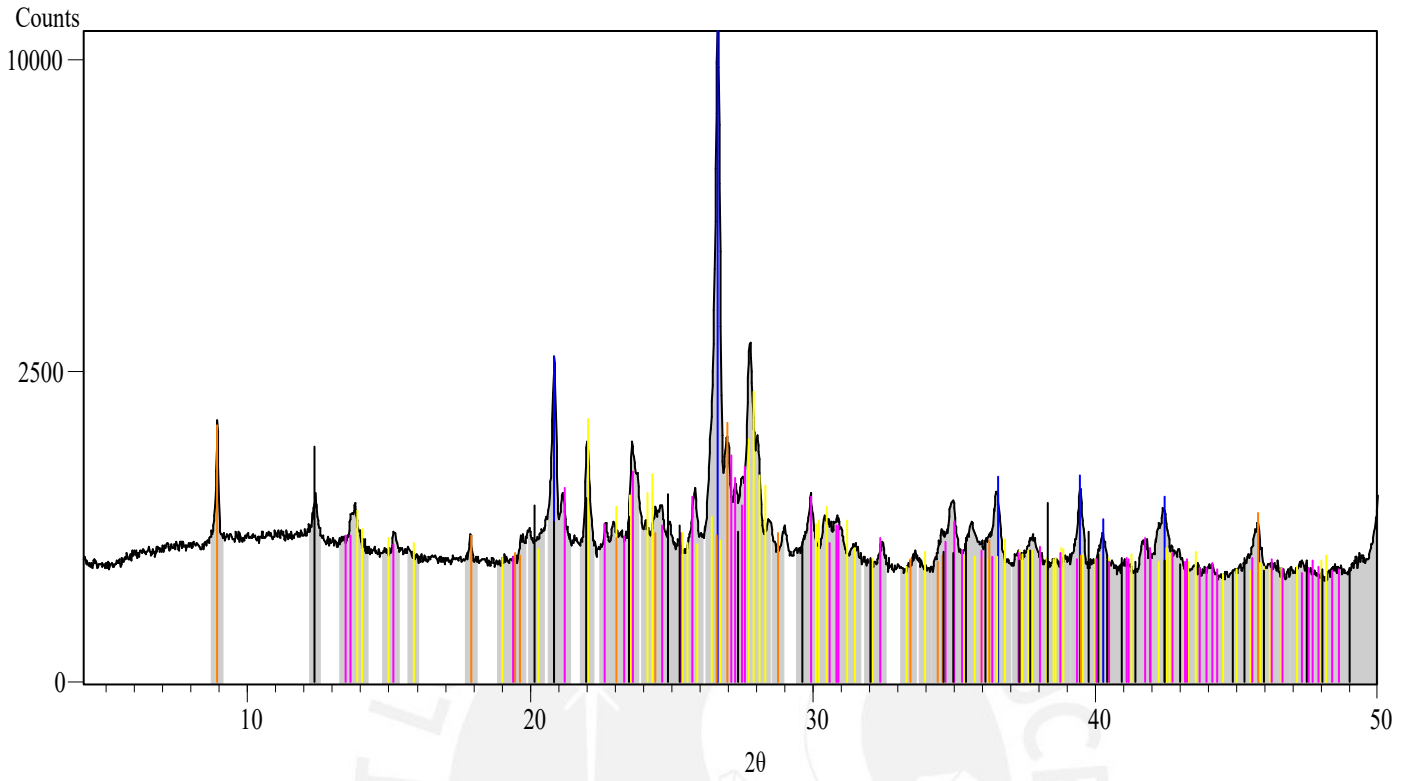
2021-MAC-008A



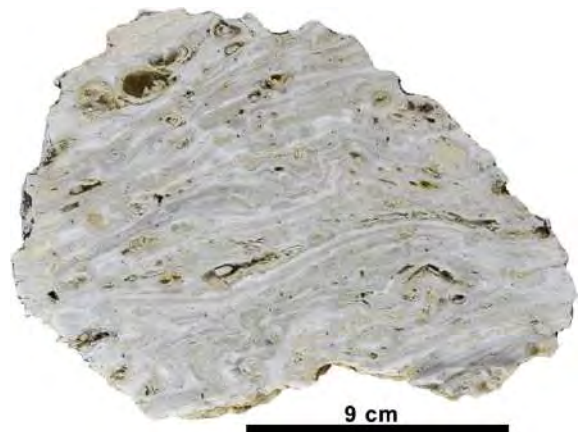
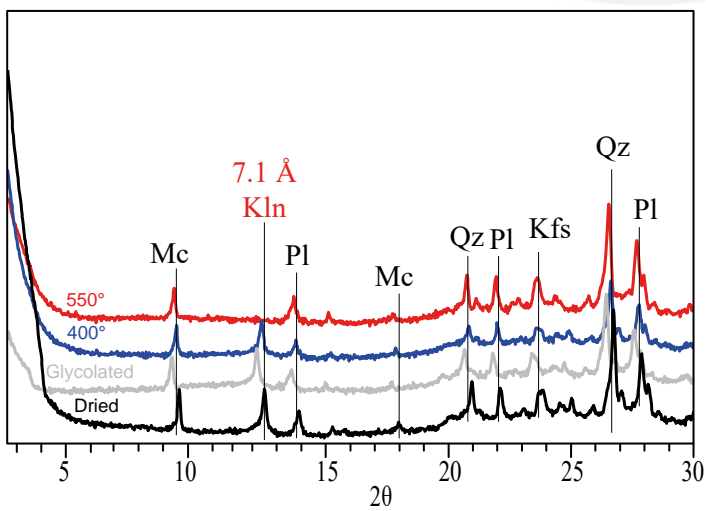
Peak List
Quartz
Plagioclase
Kaolinite
Mica
K-Feldspar



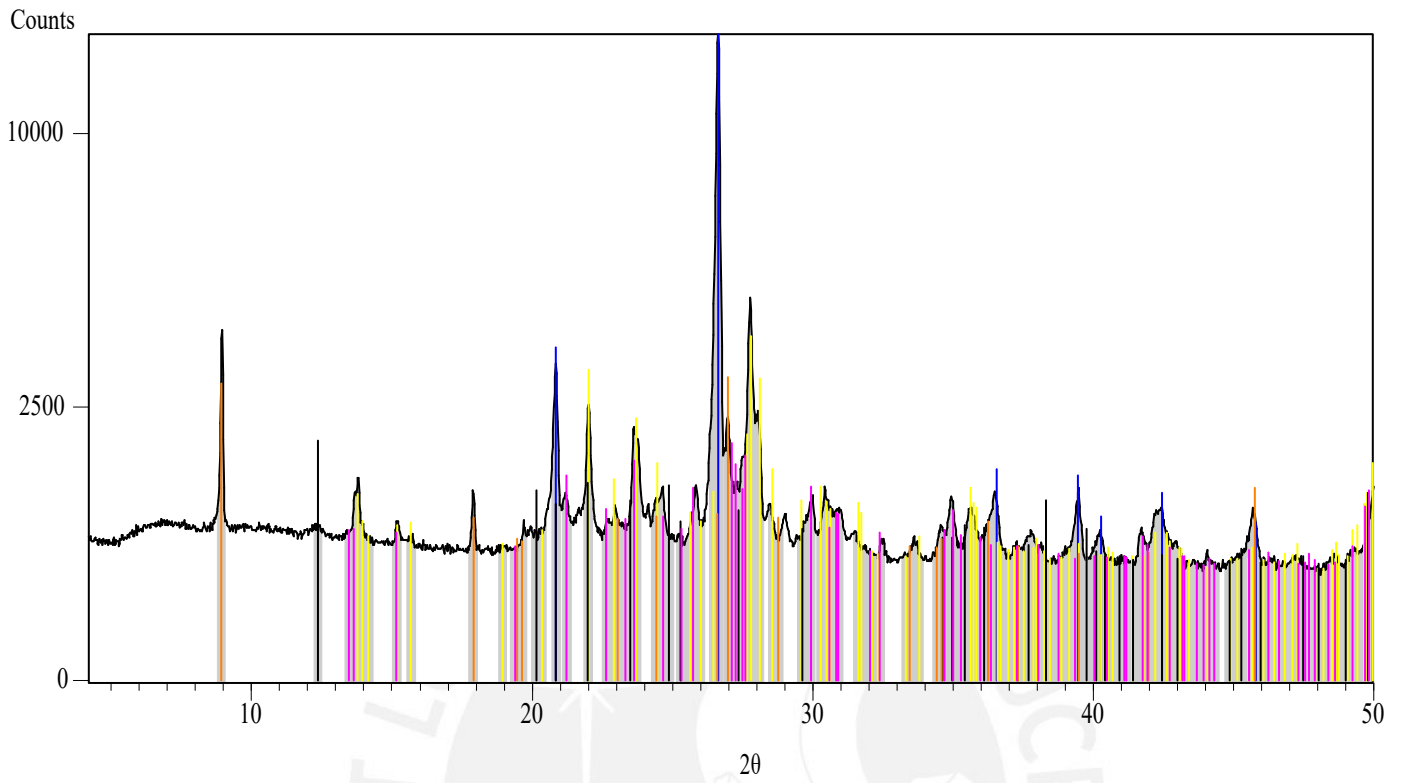
2021-MAC-008B



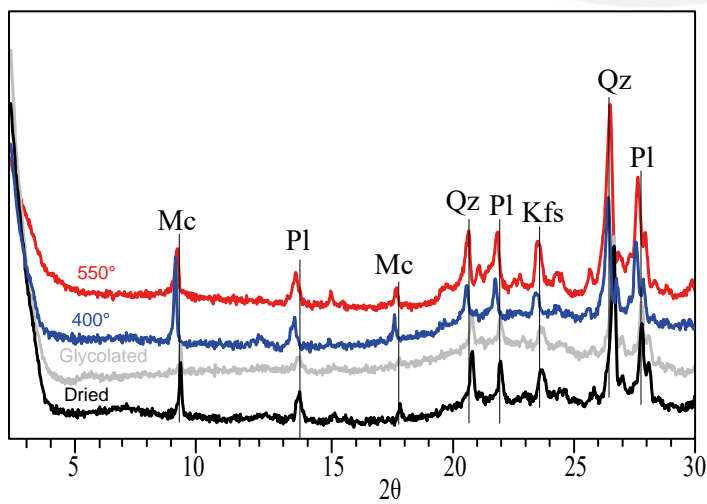
Phase	Approximate 2θ (degrees)
Quartz	10, 20, 26.5, 38, 40, 42, 44, 46, 48
Plagioclase	10, 12, 14, 16, 18, 20, 22, 24, 26, 28, 30, 32, 34, 36, 38, 40, 42, 44, 46, 48
Mica	10, 12, 14, 16, 18, 20, 22, 24, 26, 28, 30, 32, 34, 36, 38, 40, 42, 44, 46, 48
K-Feldspar	10, 12, 14, 16, 18, 20, 22, 24, 26, 28, 30, 32, 34, 36, 38, 40, 42, 44, 46, 48
Kaolinite	10, 12, 14, 16, 18, 20, 22, 24, 26, 28, 30, 32, 34, 36, 38, 40, 42, 44, 46, 48



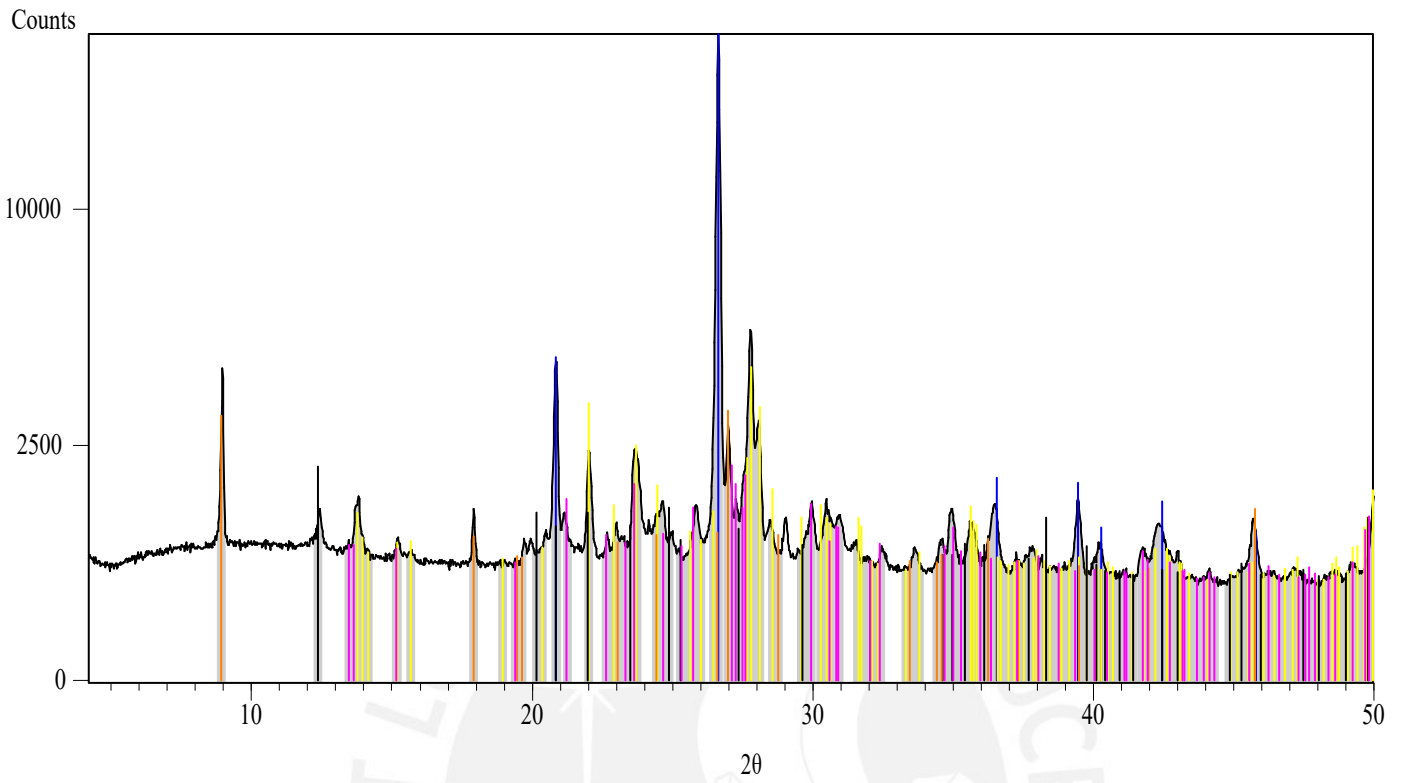
2021-MAC-011A



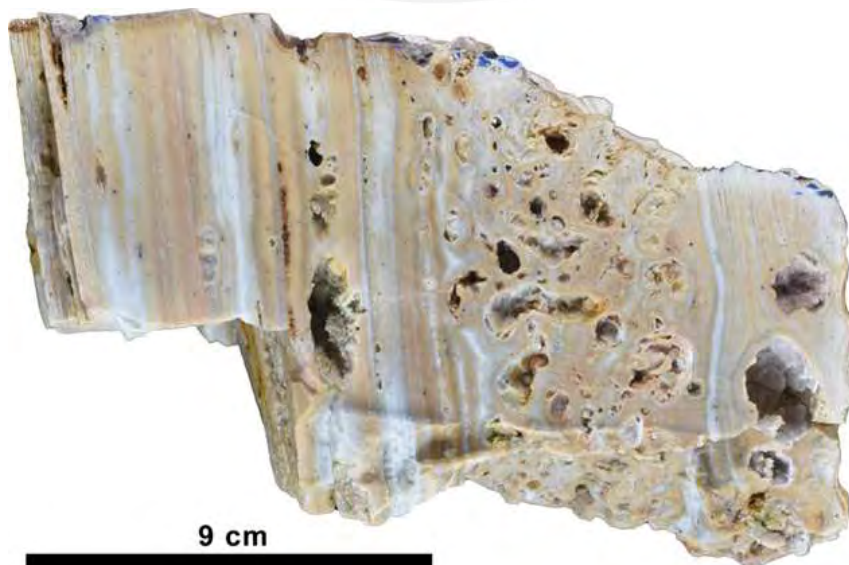
Peak List
Quartz
Plagioclase
Kaolinite
Mica
K-Feldspar



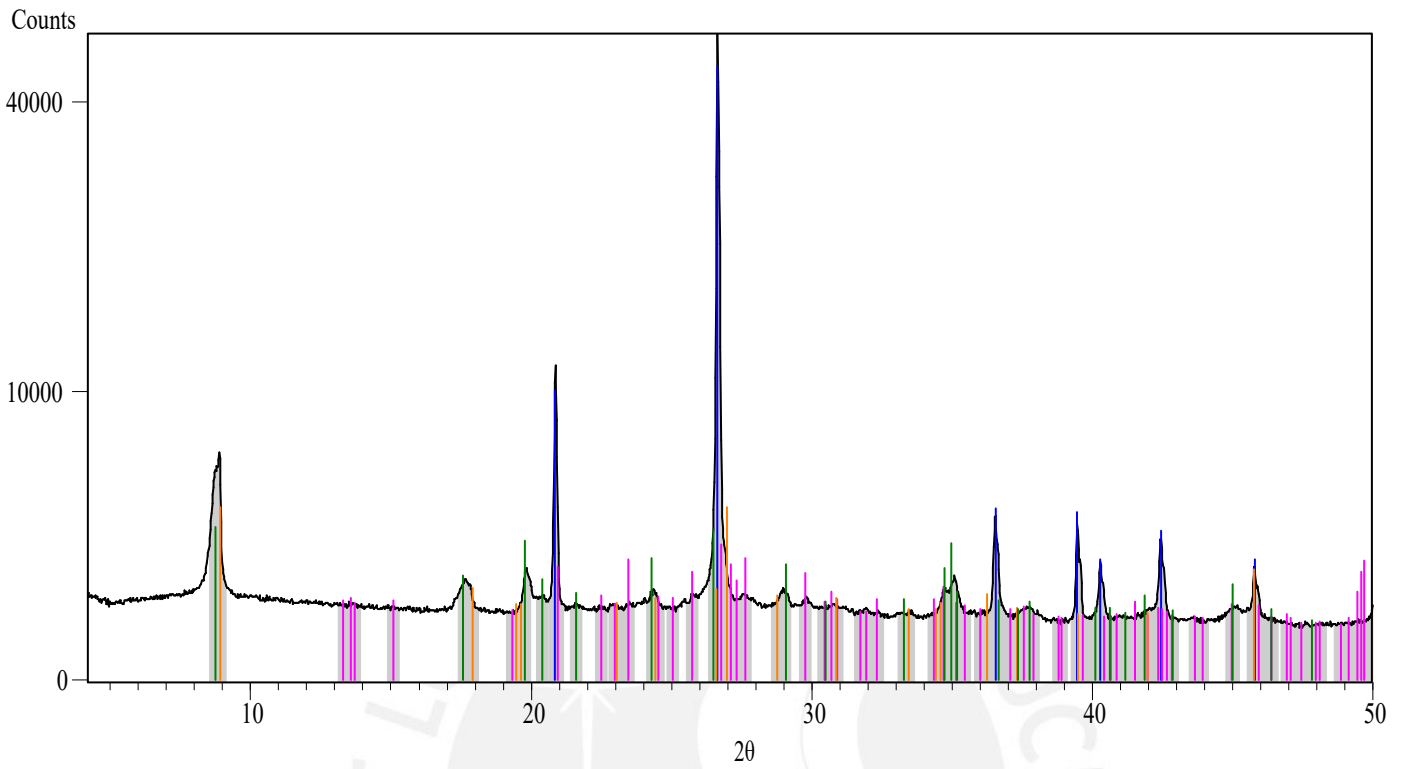
2021-MAC-011B



Peak List
Quartz
Plagioclase
Kaolinite
Mica
K-Feldspar

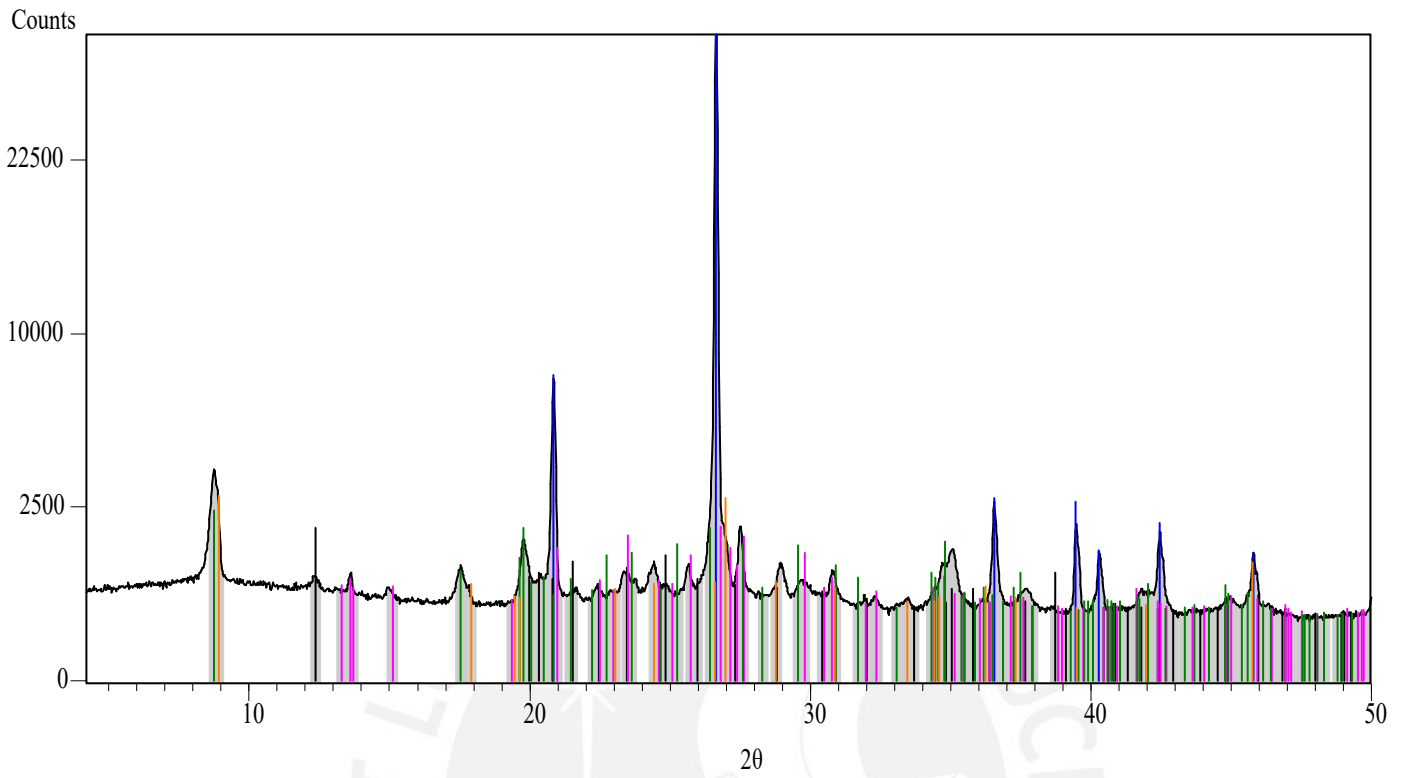


2021-MAC-019A

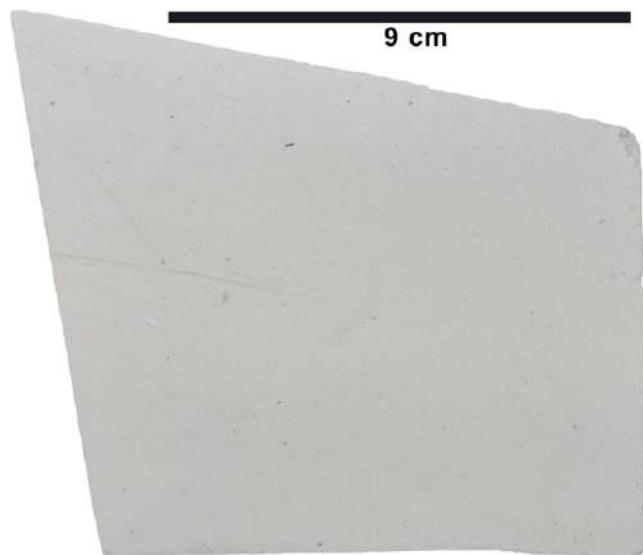


Peak List	Reference
Quartz	Blue vertical lines
K-Feldspar	Magenta vertical lines
Mica	Orange vertical lines
Mica	Green vertical lines

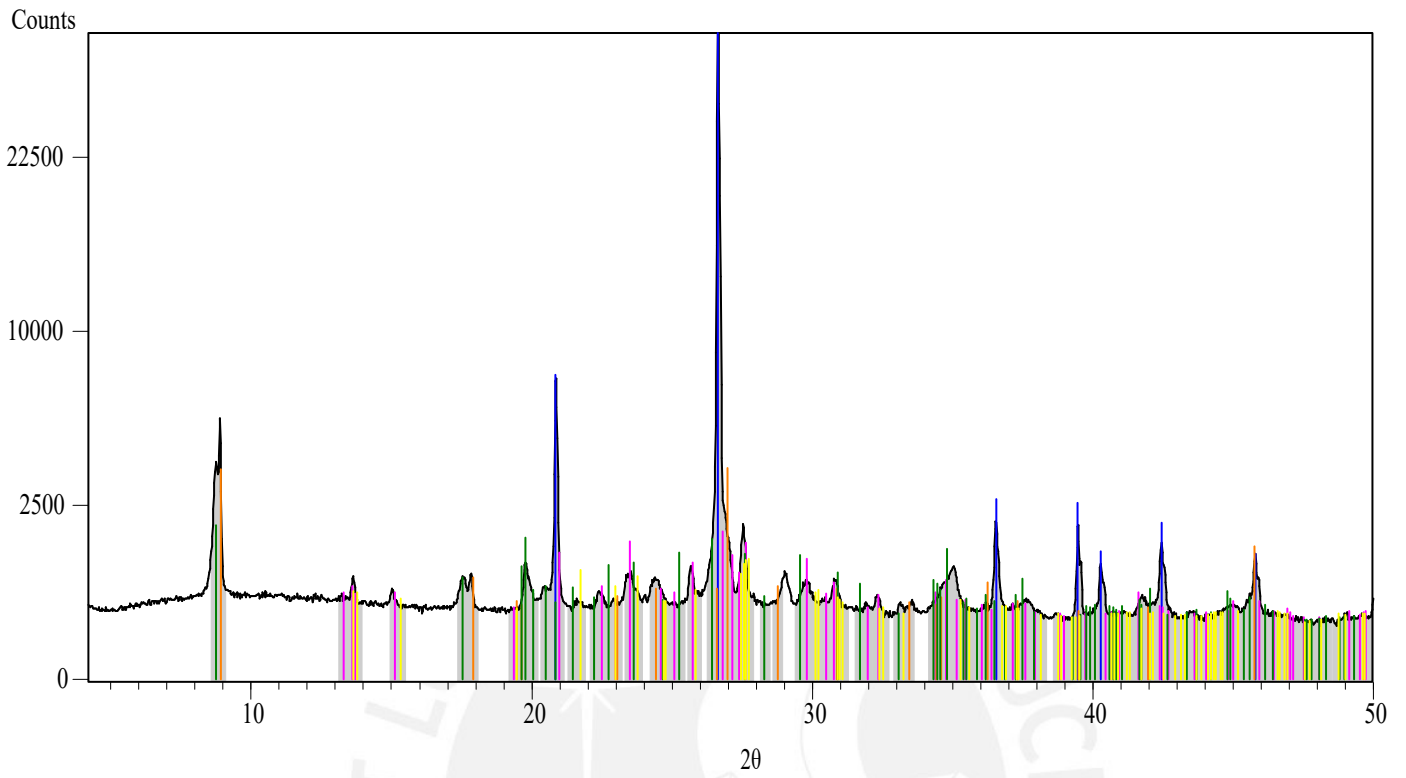




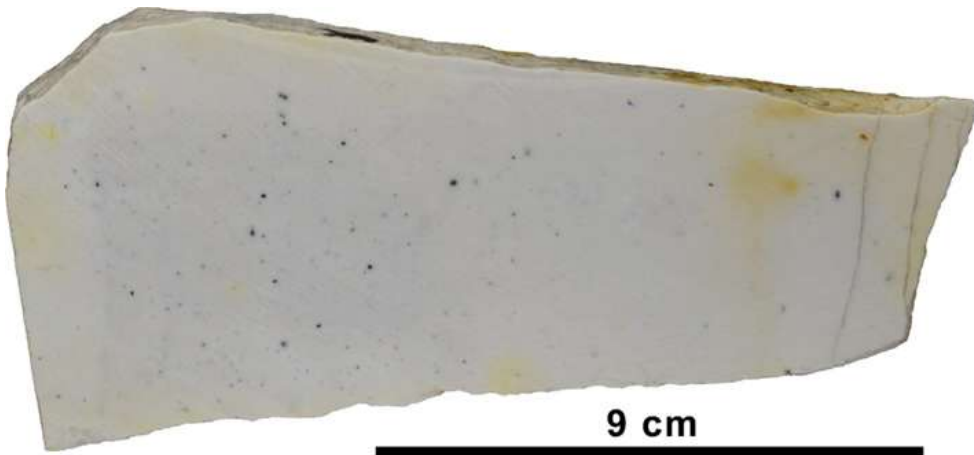
Peak List	Quartz	Kaolinite	K-Feldspar	Mica	Mica
Peak 1					
Peak 2					
Peak 3					
Peak 4					
Peak 5					
Peak 6					
Peak 7					
Peak 8					
Peak 9					
Peak 10					
Peak 11					
Peak 12					
Peak 13					
Peak 14					
Peak 15					
Peak 16					
Peak 17					
Peak 18					
Peak 19					
Peak 20					
Peak 21					
Peak 22					
Peak 23					
Peak 24					
Peak 25					
Peak 26					
Peak 27					
Peak 28					
Peak 29					
Peak 30					
Peak 31					
Peak 32					
Peak 33					
Peak 34					
Peak 35					
Peak 36					
Peak 37					
Peak 38					
Peak 39					
Peak 40					
Peak 41					
Peak 42					
Peak 43					
Peak 44					
Peak 45					
Peak 46					
Peak 47					
Peak 48					
Peak 49					
Peak 50					



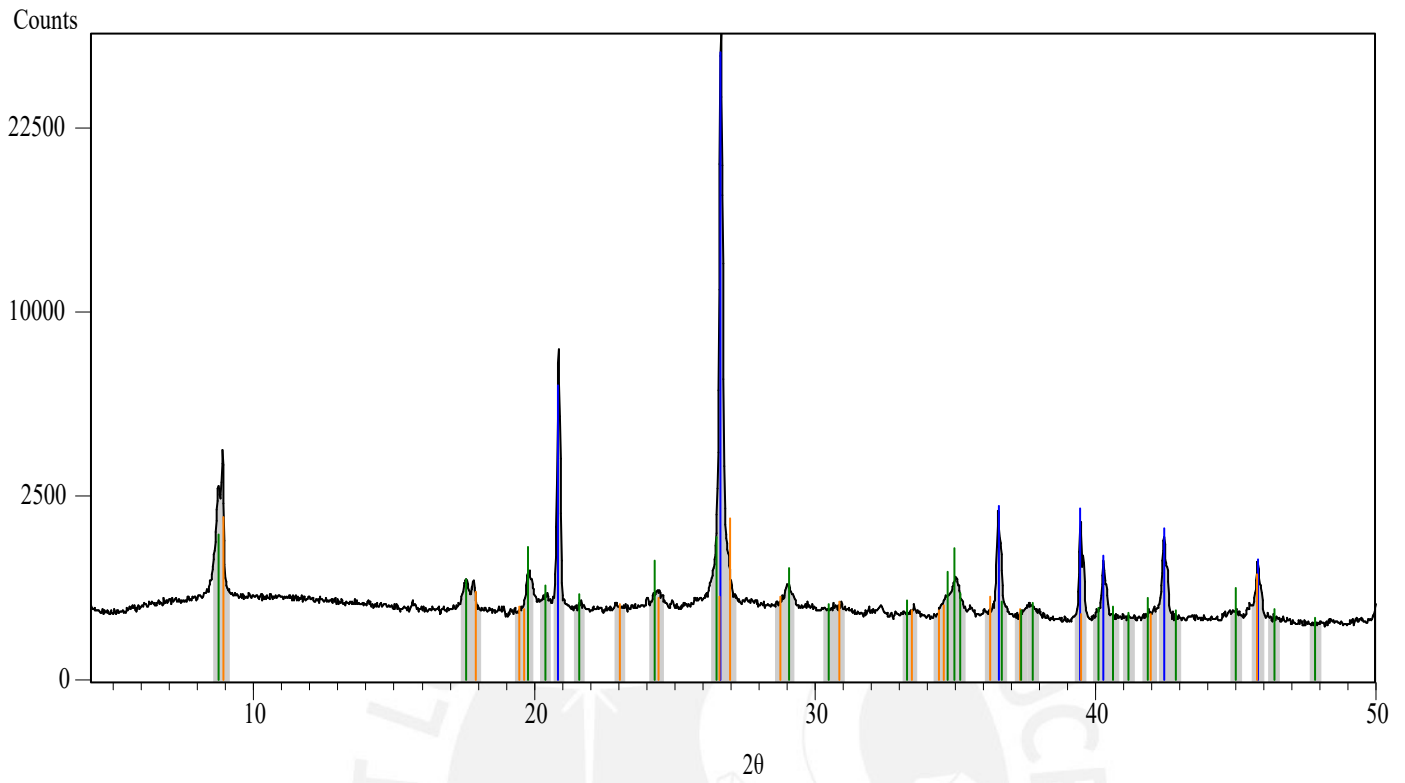
2021-MAC-022A



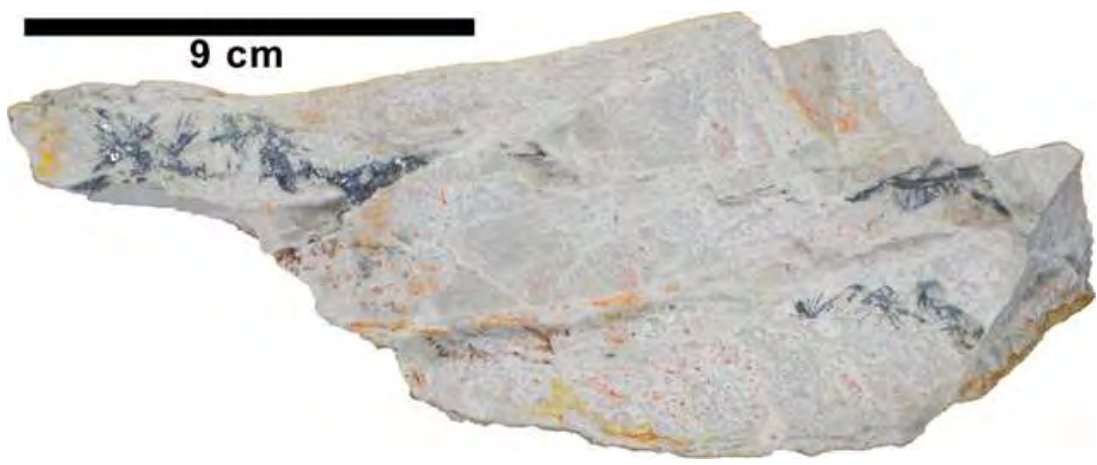
Peak List
Quartz
K-Feldspar
Mica
Mica
Plagioclase



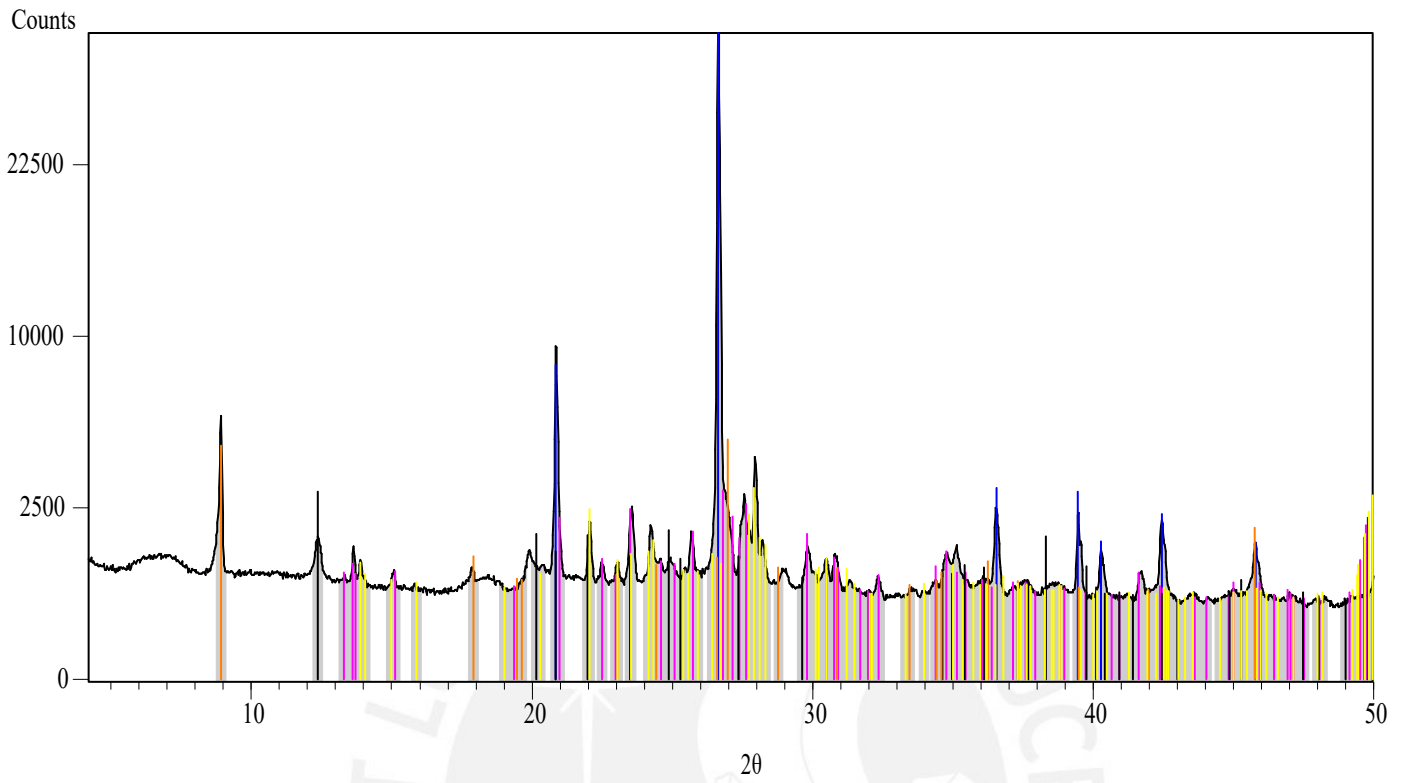
2021-MAC-022B



Peak List	Reference
Quartz	Blue vertical bars
Mica	Orange vertical bars
Mica	Green vertical bars

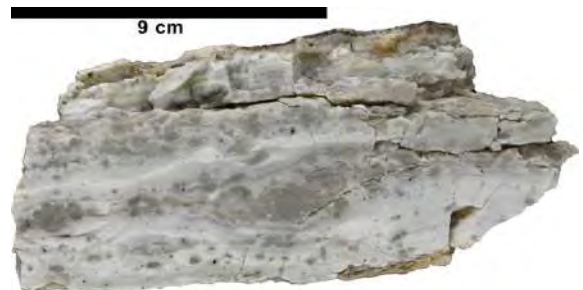
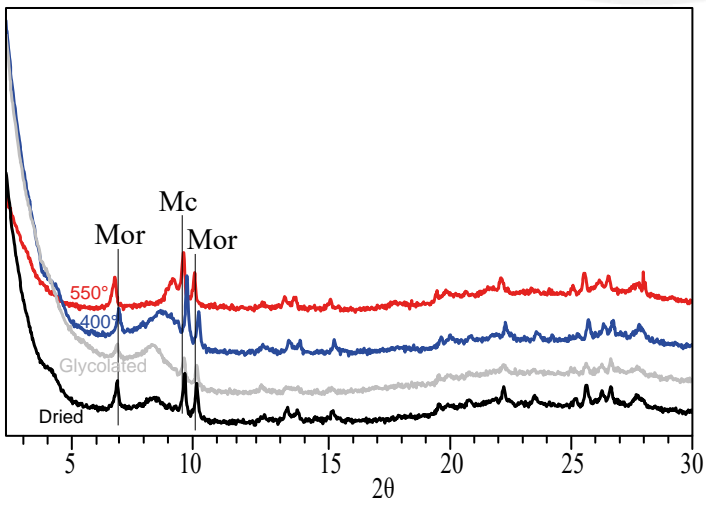
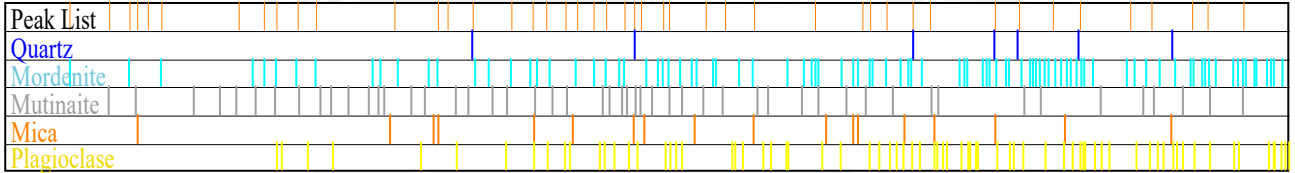
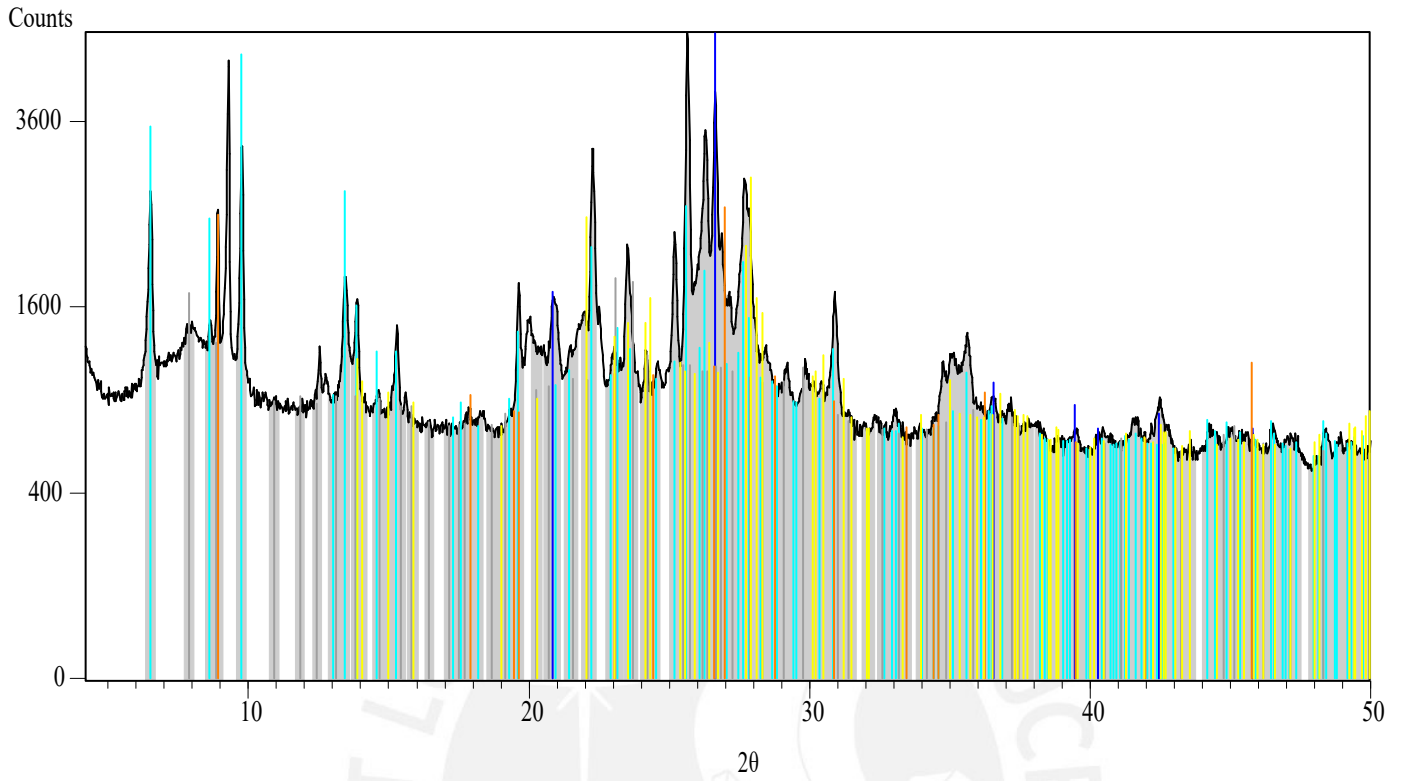




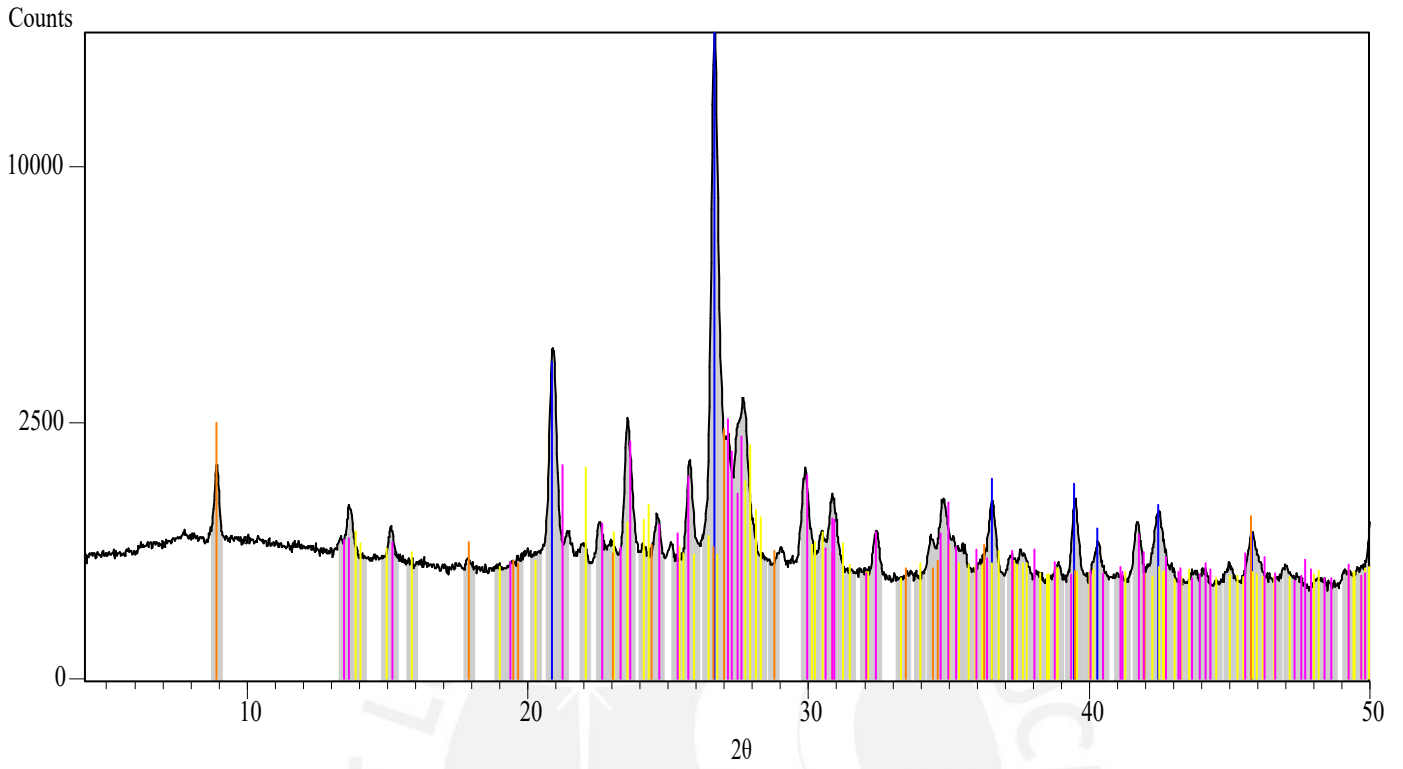


Peak List
Quartz
K-Feldspar
Kaolinite
Mica
Plagioclase

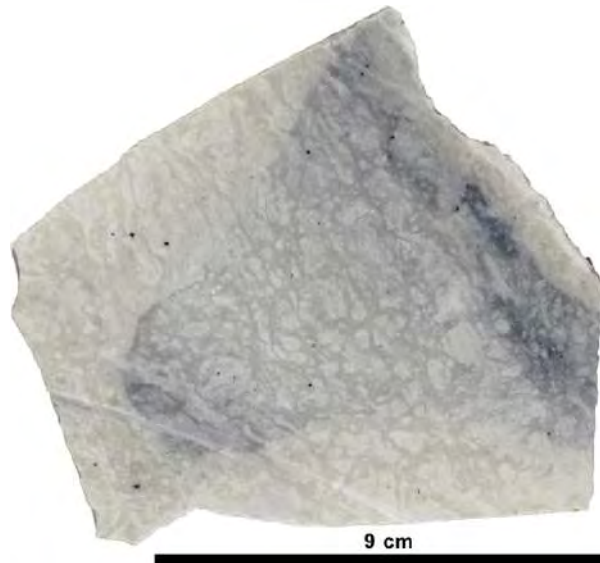


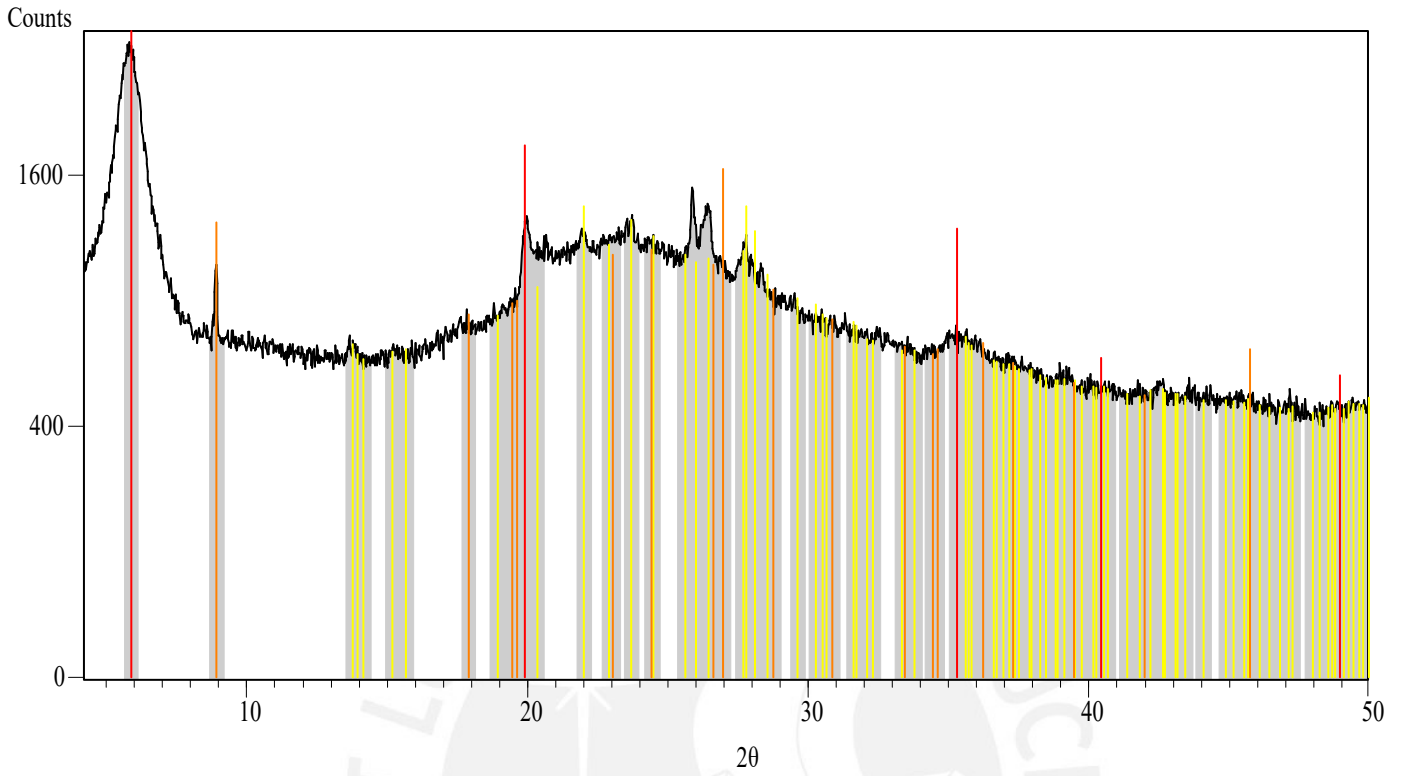


2021-MAC-031

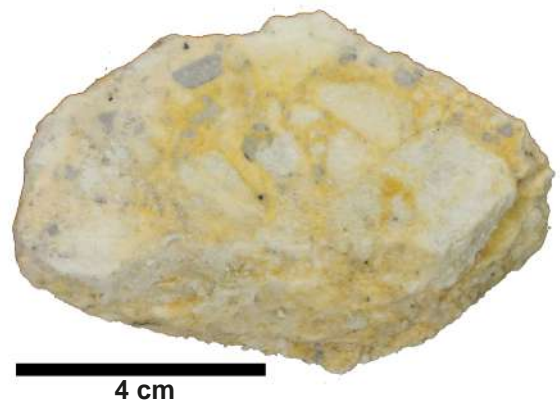
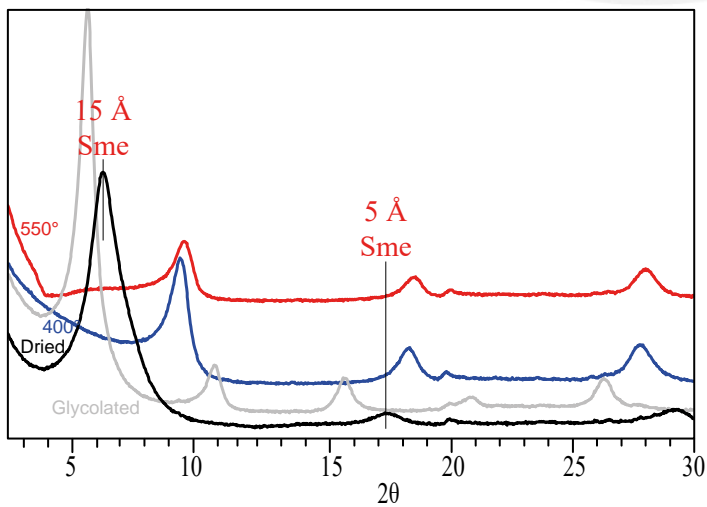


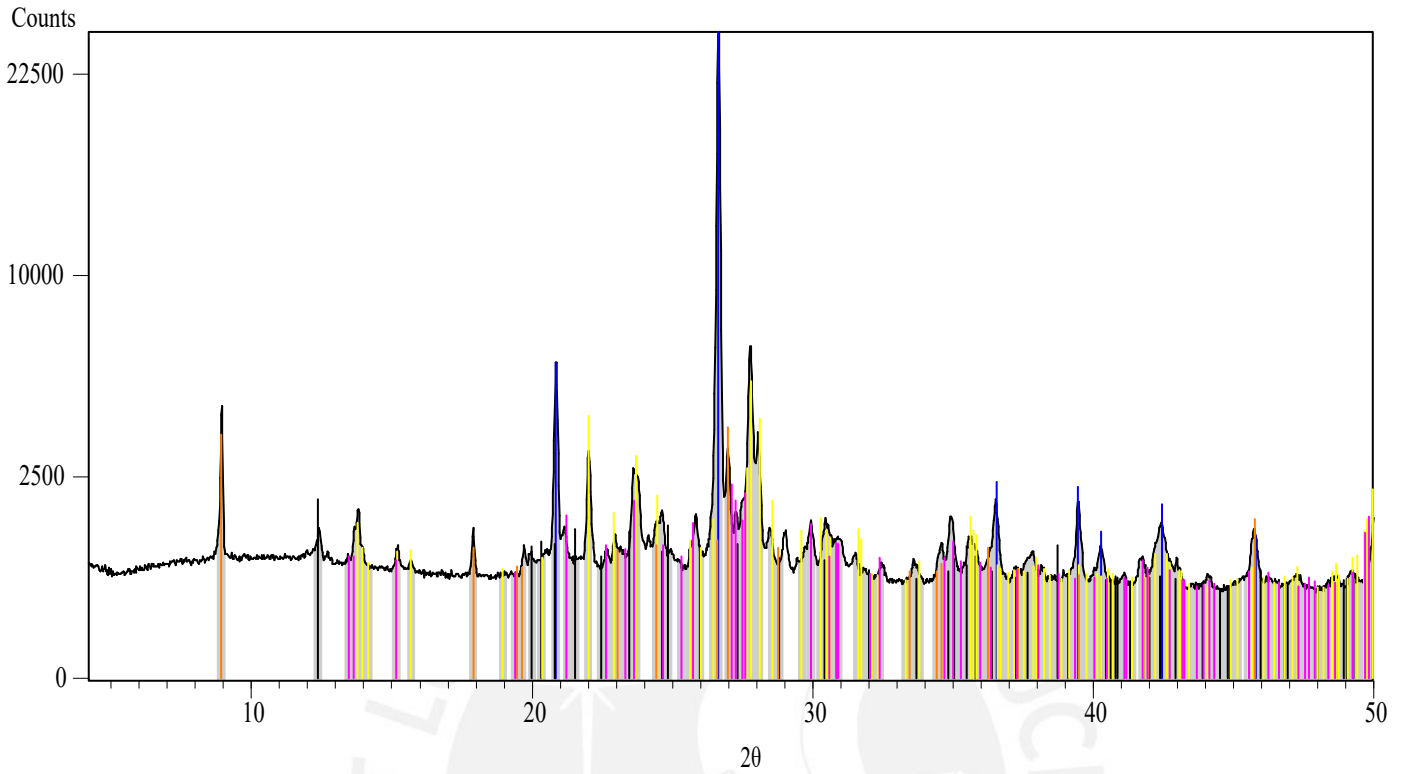
Peak List	Reference
Quartz	Blue vertical lines
Plagioclase	Yellow vertical lines
Mica	Orange vertical lines
K-Feldspar	Magenta vertical lines



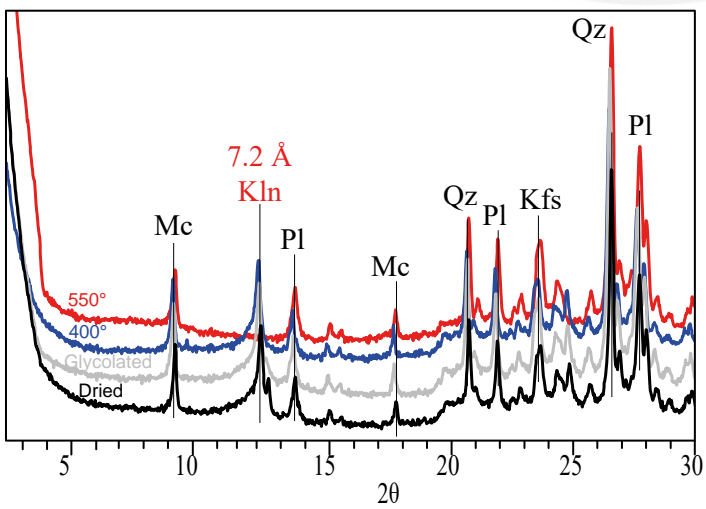


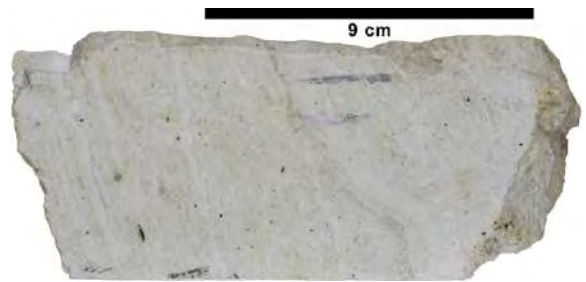
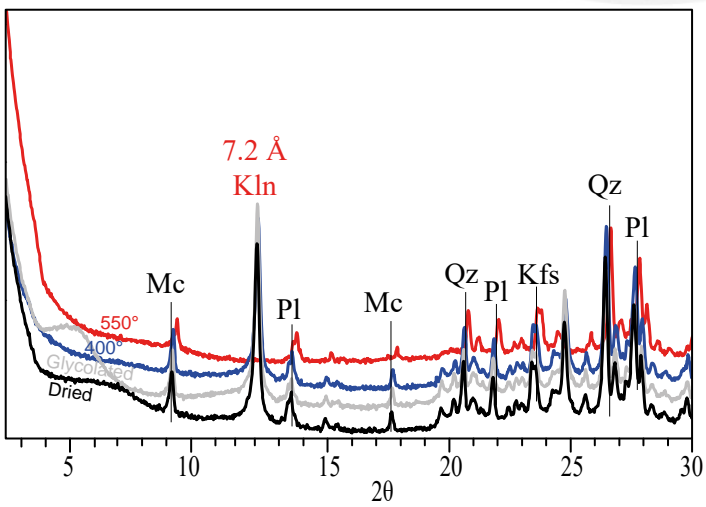
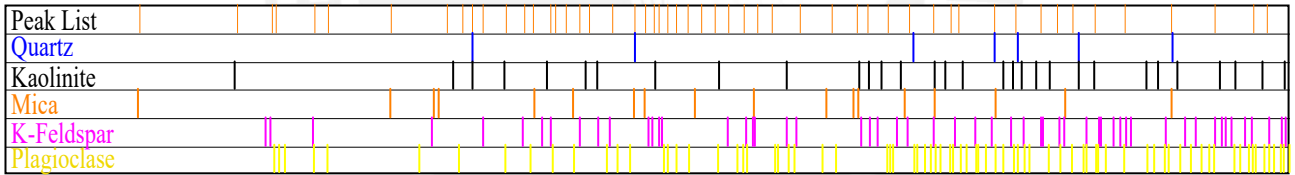
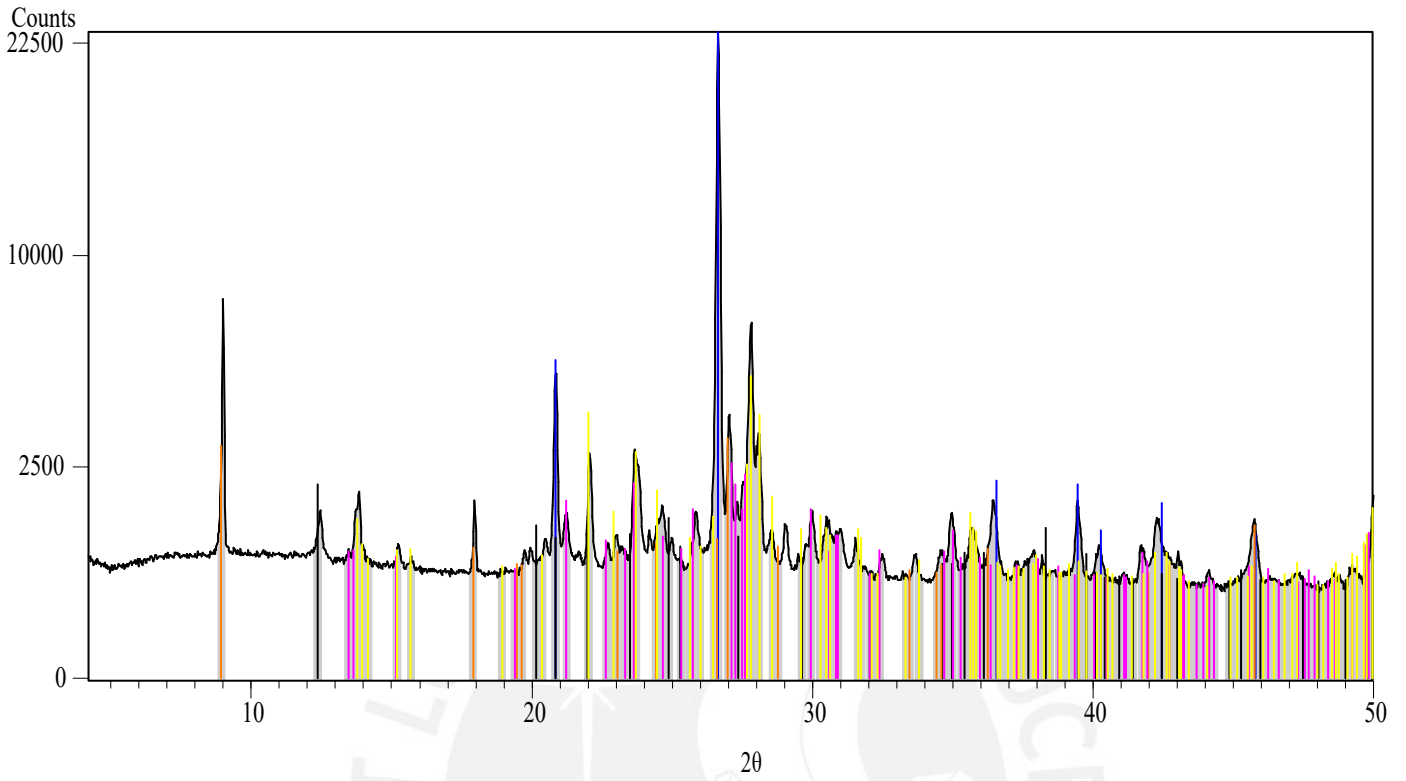
Peak List
Smectite
Plagioclase
Mica

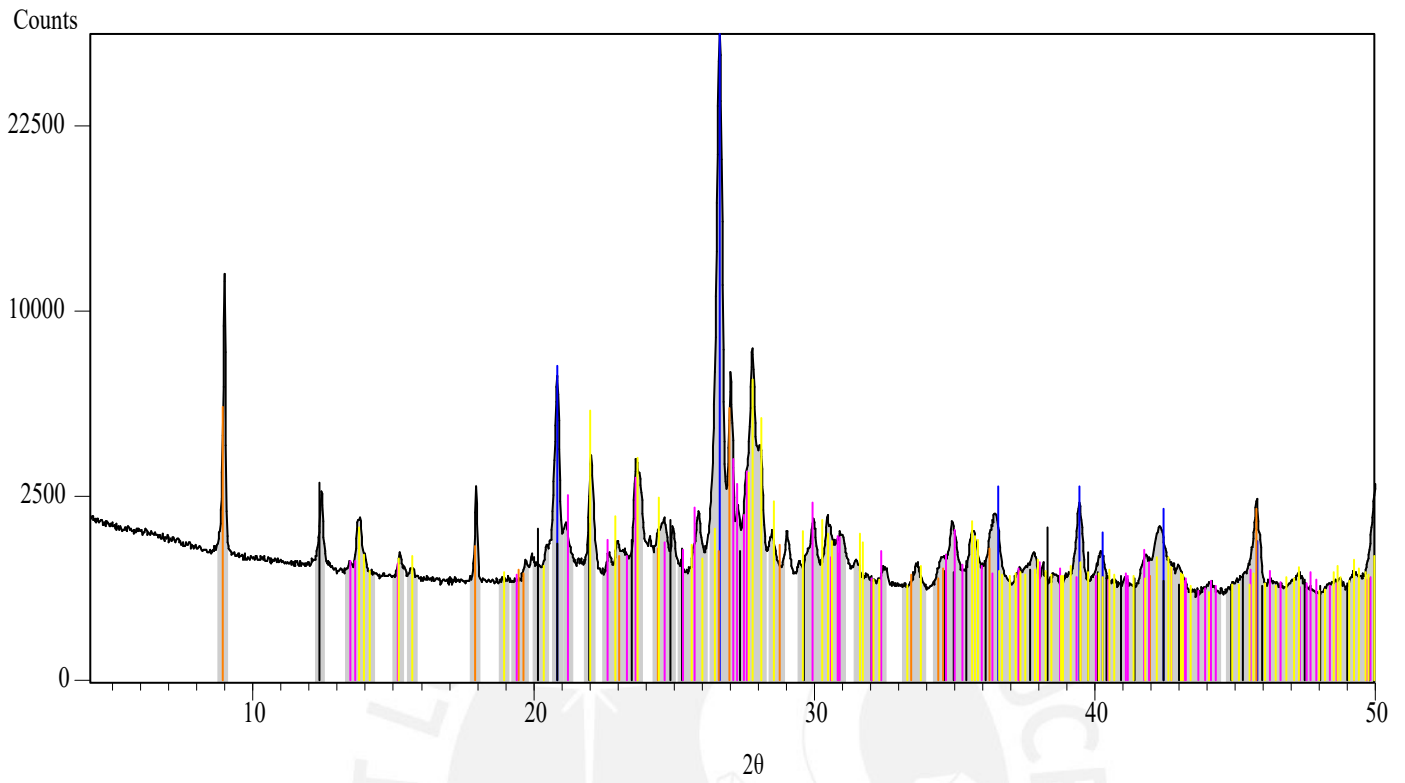




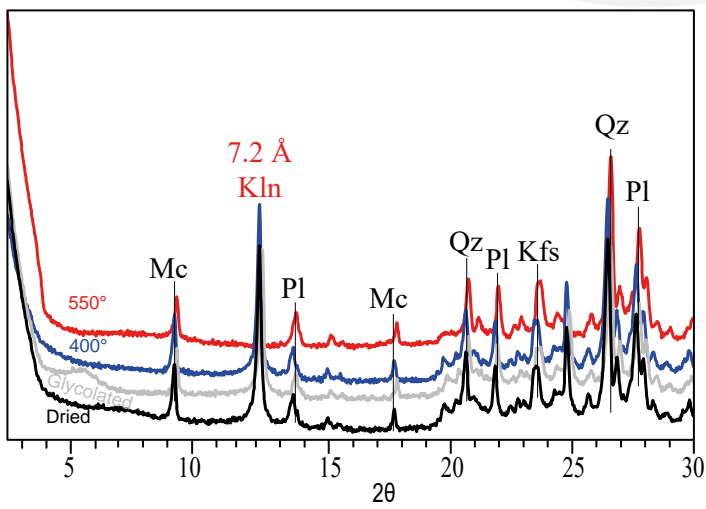
Peak List
Quartz
Kaolinite
Plagioclase
Mica
K-Feldspar

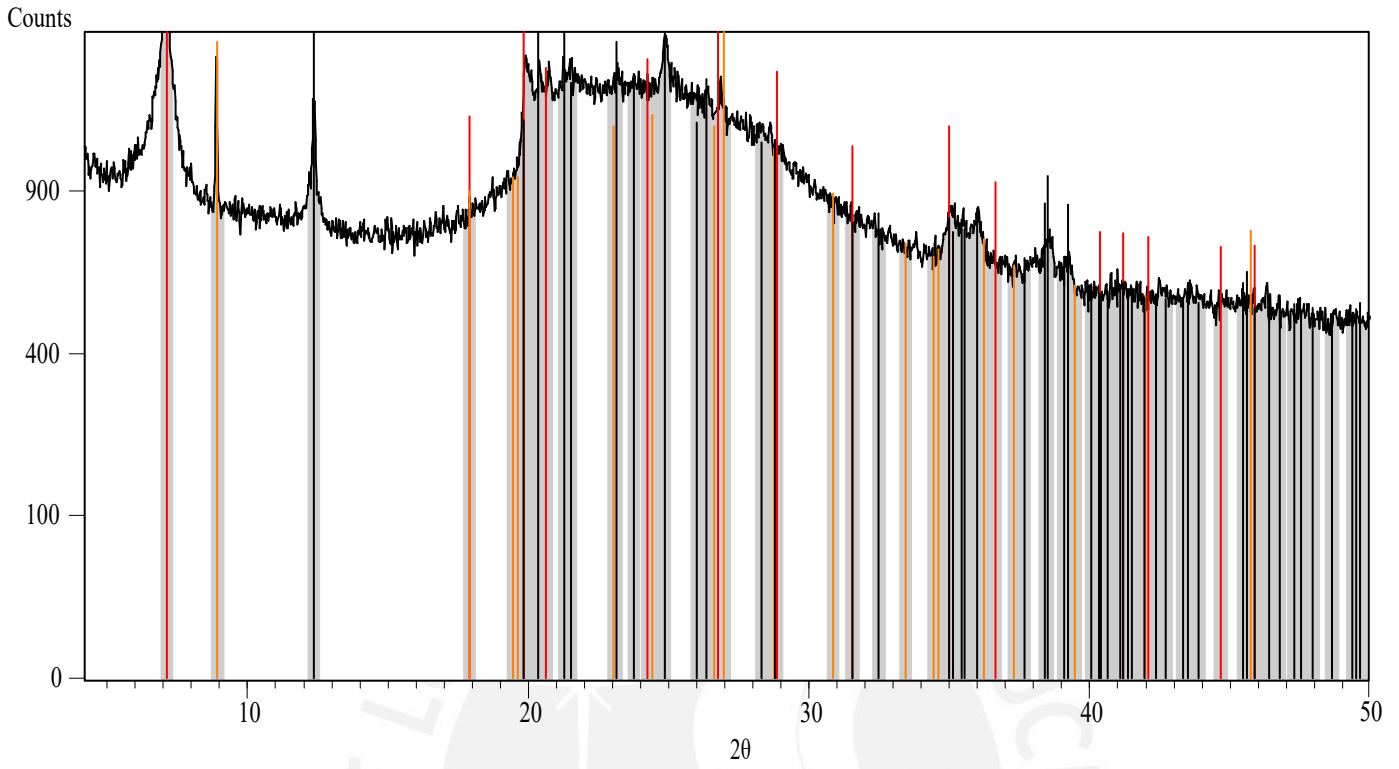




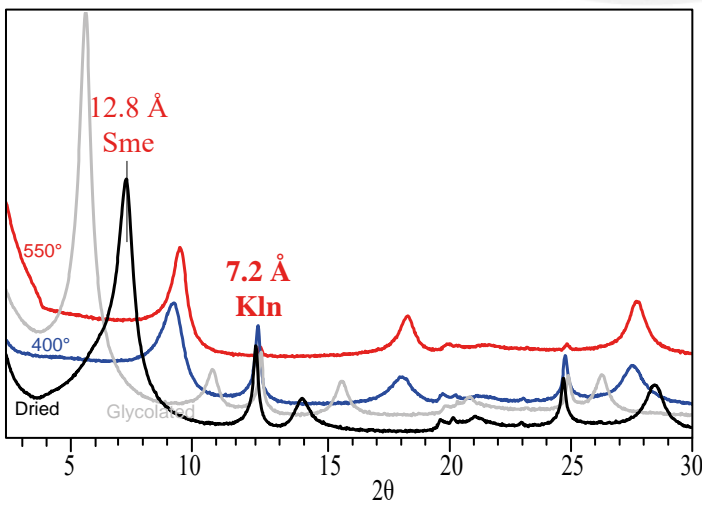


Peak List
Quartz
Kaolinite
Mica
K-Feldspar
Plagioclase



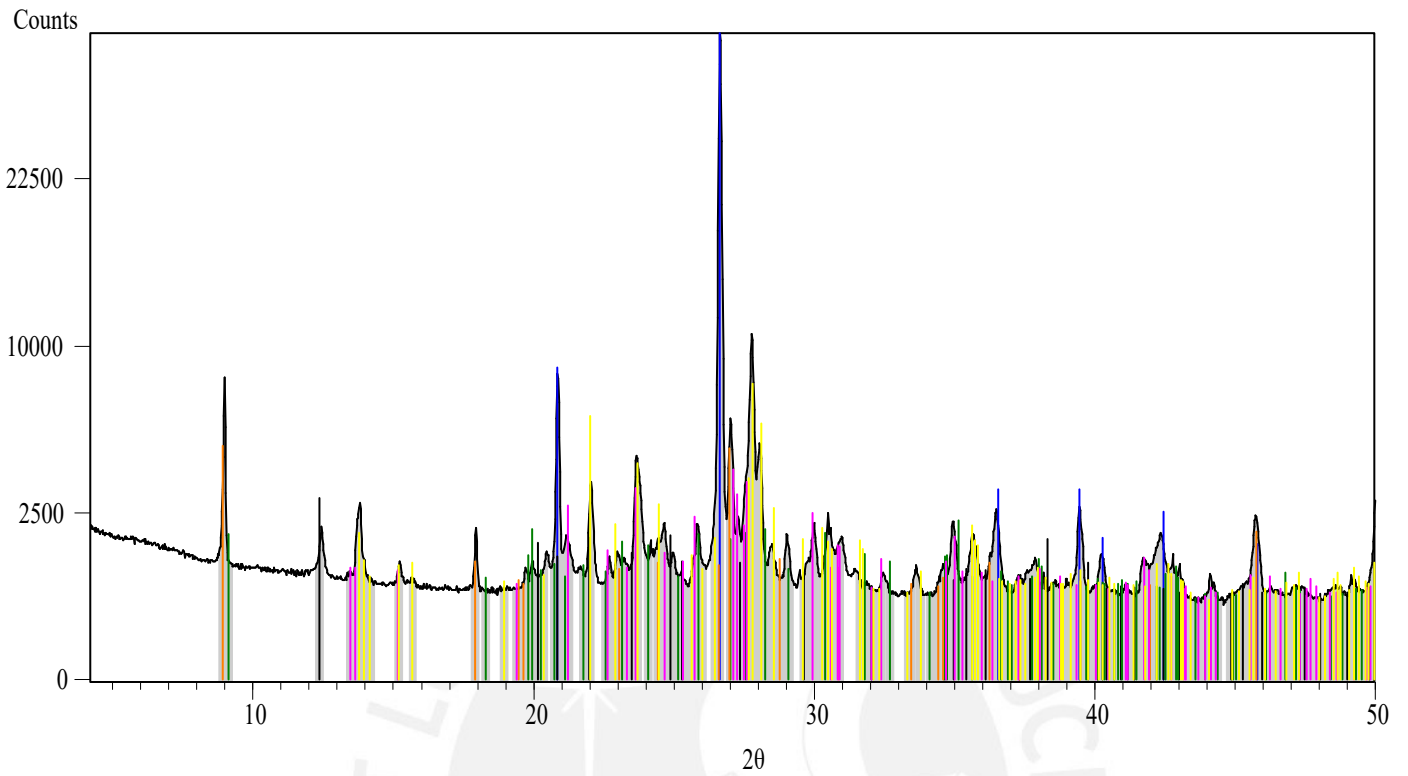


Peak List
Smectite
Mica
Kaolinite

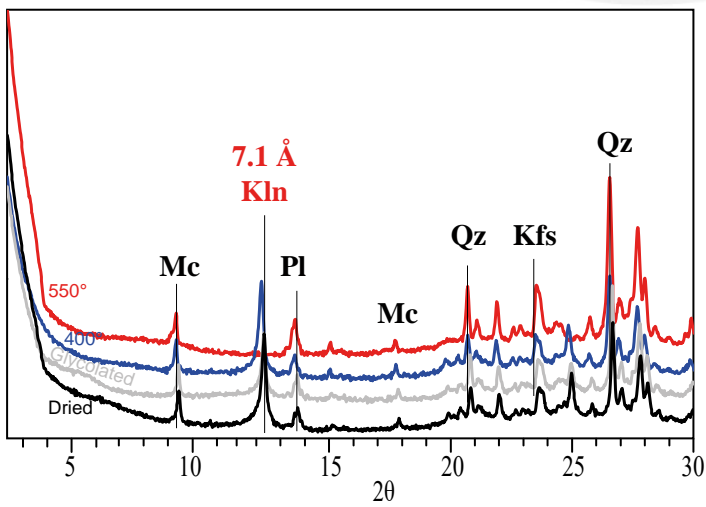


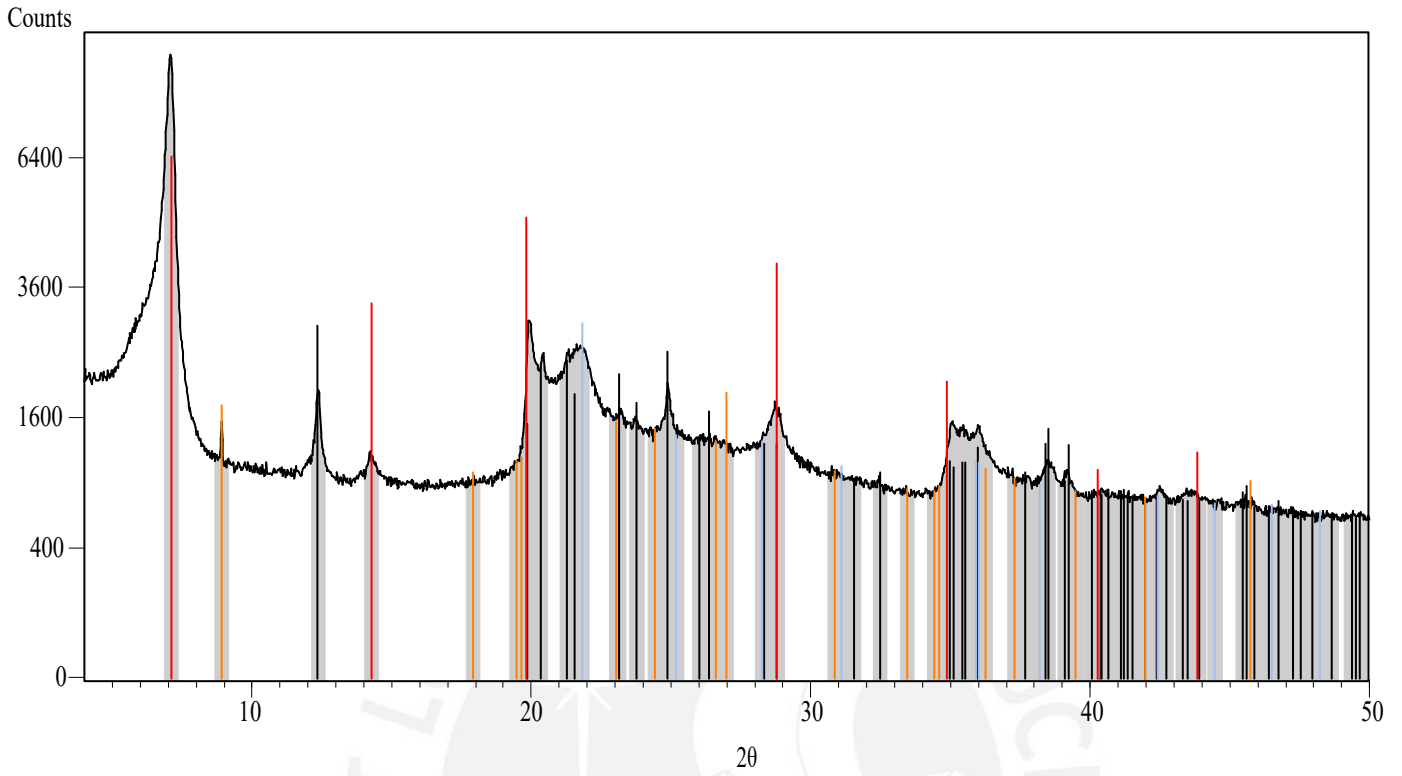
3 cm



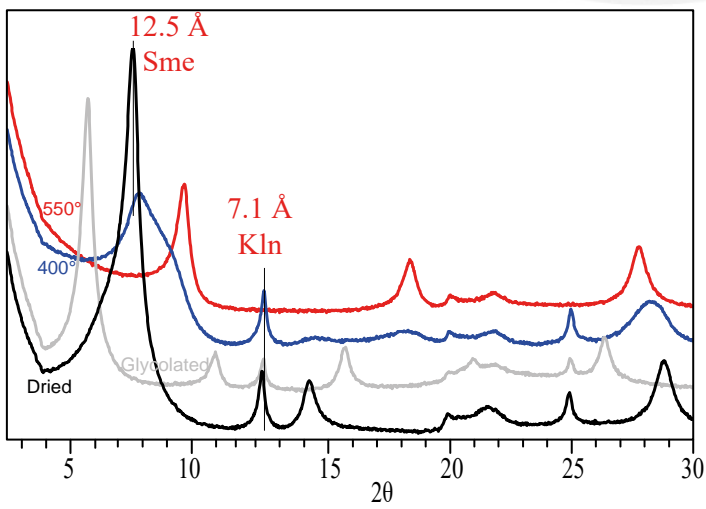


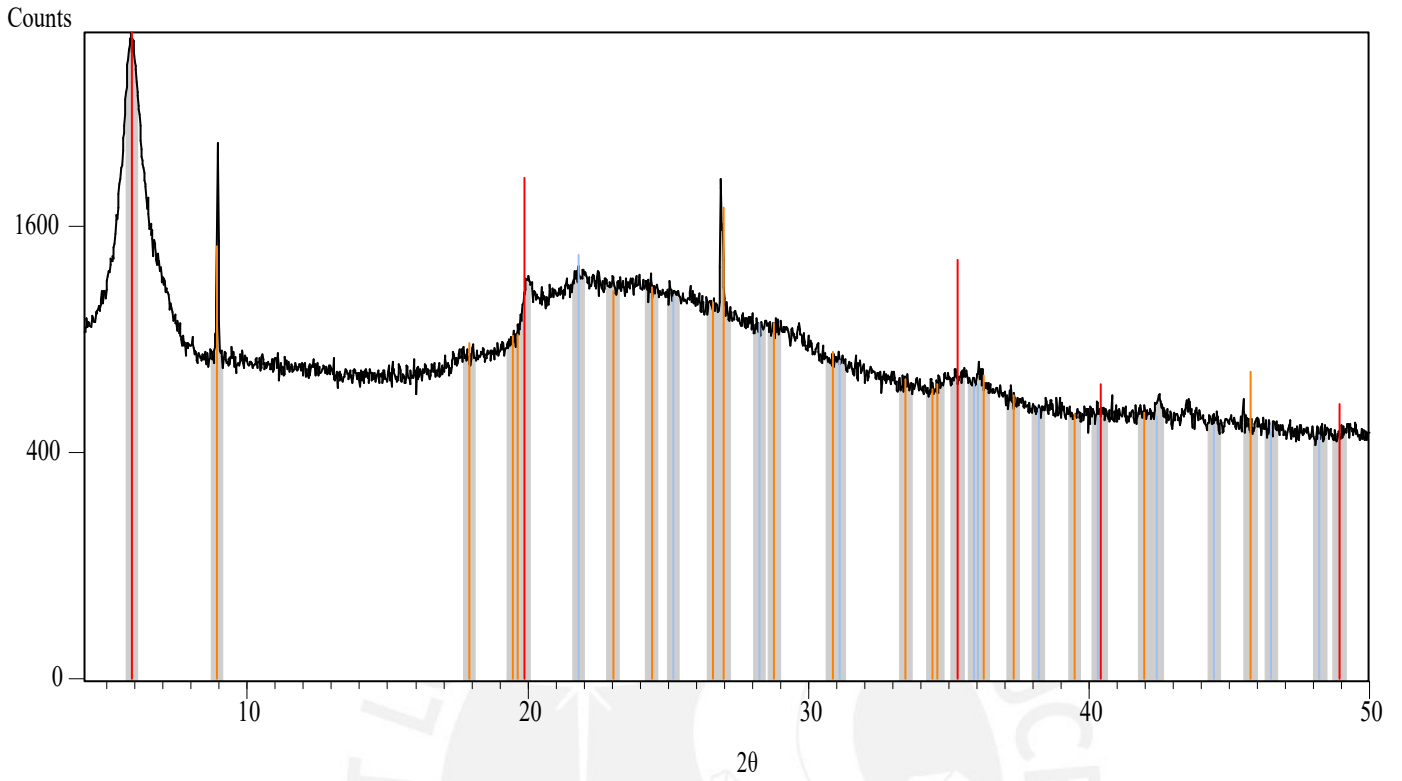
Phase	Approximate 2θ (degrees)
Quartz	12.2, 14.7, 16.3, 17.8, 20.8, 21.3, 26.6, 28.4, 34.5, 39.6, 40.1, 45.7, 47.5
Kaolinite	10.1, 12.5, 14.7, 16.3, 17.8, 20.8, 21.3, 26.6, 28.4, 34.5, 39.6, 40.1, 45.7, 47.5
Mica	10.1, 12.5, 14.7, 16.3, 17.8, 20.8, 21.3, 26.6, 28.4, 34.5, 39.6, 40.1, 45.7, 47.5
Mica	10.1, 12.5, 14.7, 16.3, 17.8, 20.8, 21.3, 26.6, 28.4, 34.5, 39.6, 40.1, 45.7, 47.5
K-Feldspar	10.1, 12.5, 14.7, 16.3, 17.8, 20.8, 21.3, 26.6, 28.4, 34.5, 39.6, 40.1, 45.7, 47.5
Plagioclase	10.1, 12.5, 14.7, 16.3, 17.8, 20.8, 21.3, 26.6, 28.4, 34.5, 39.6, 40.1, 45.7, 47.5



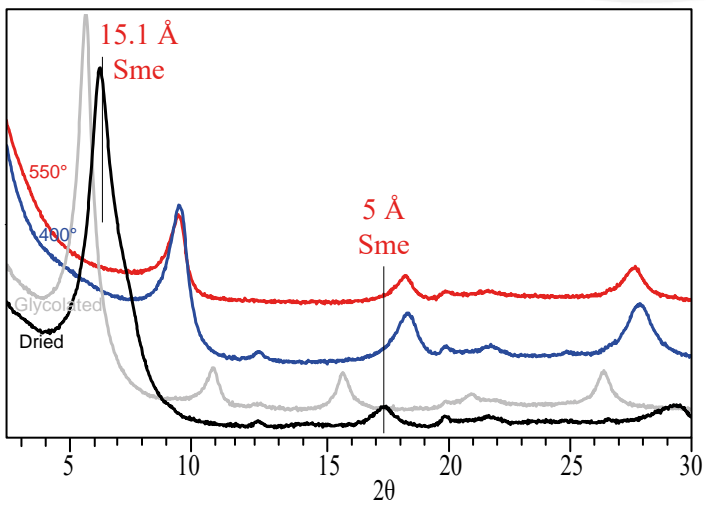


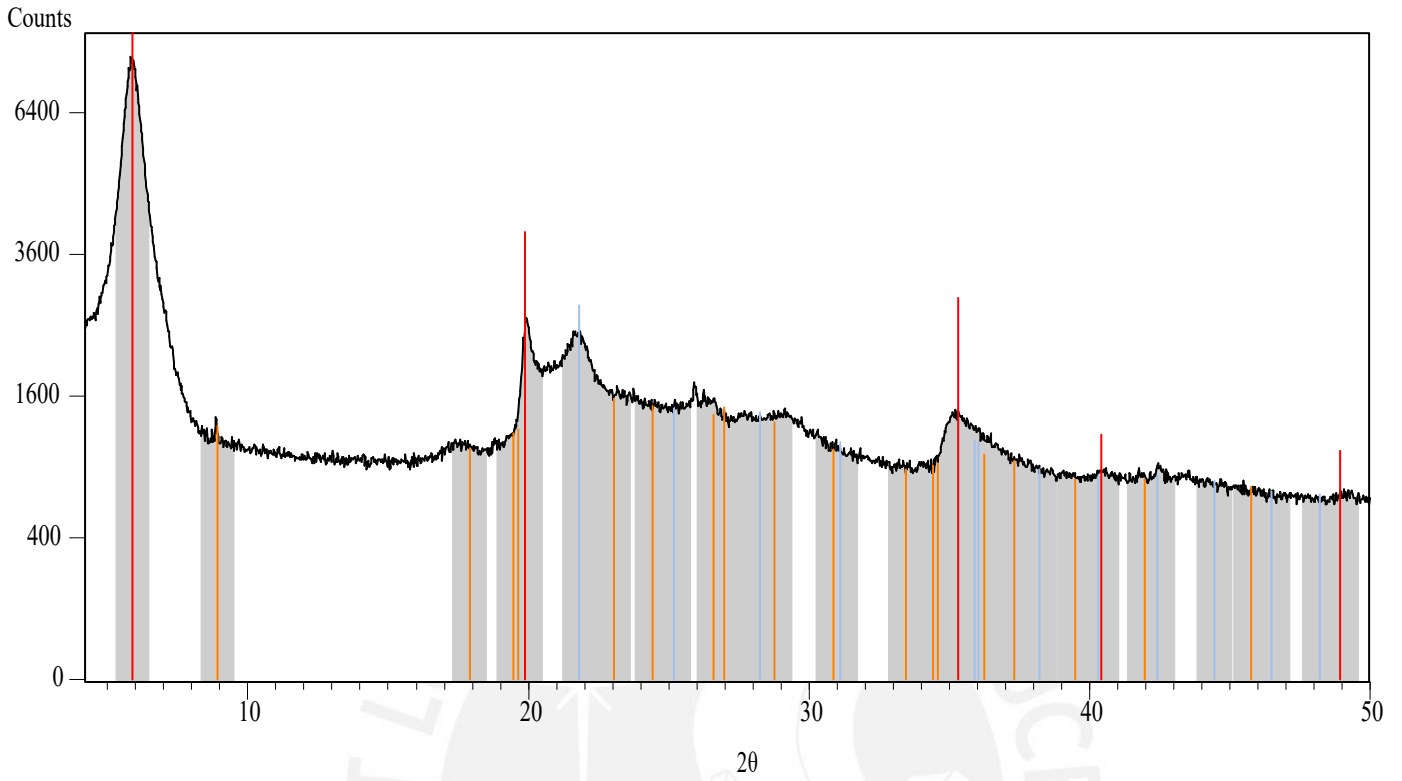
Peak List	Reference
Kaolinite	Black vertical lines
Cristobalite	Blue vertical lines
Mica	Orange vertical lines
Smectite	Red vertical lines



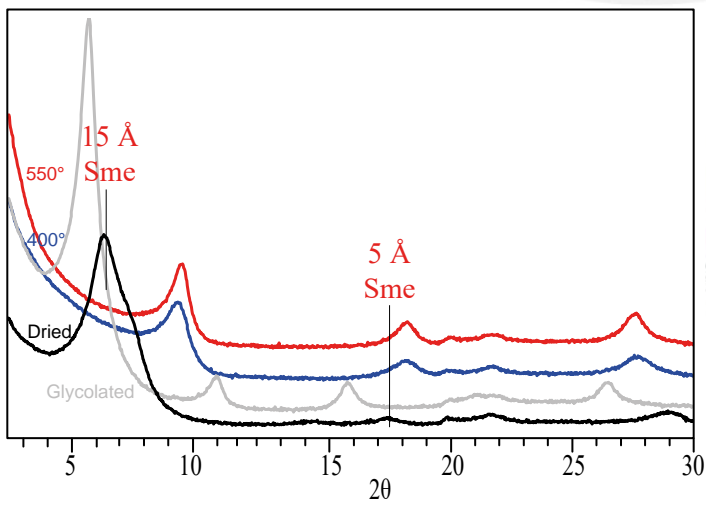


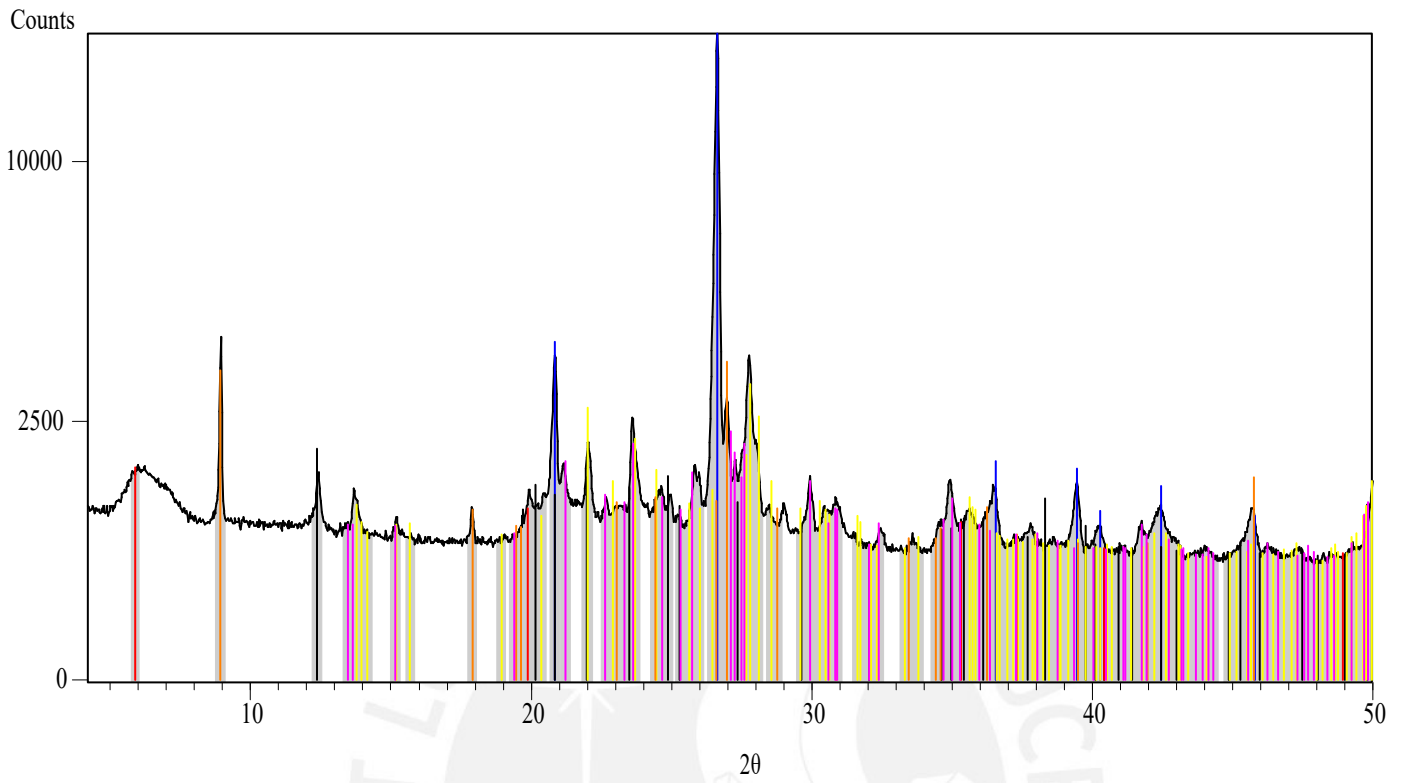
Peak List
Cristobalite
Smectite
Mica



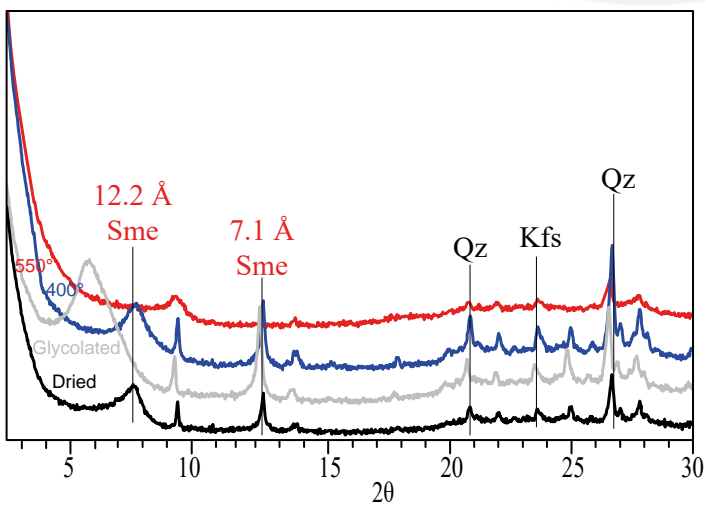


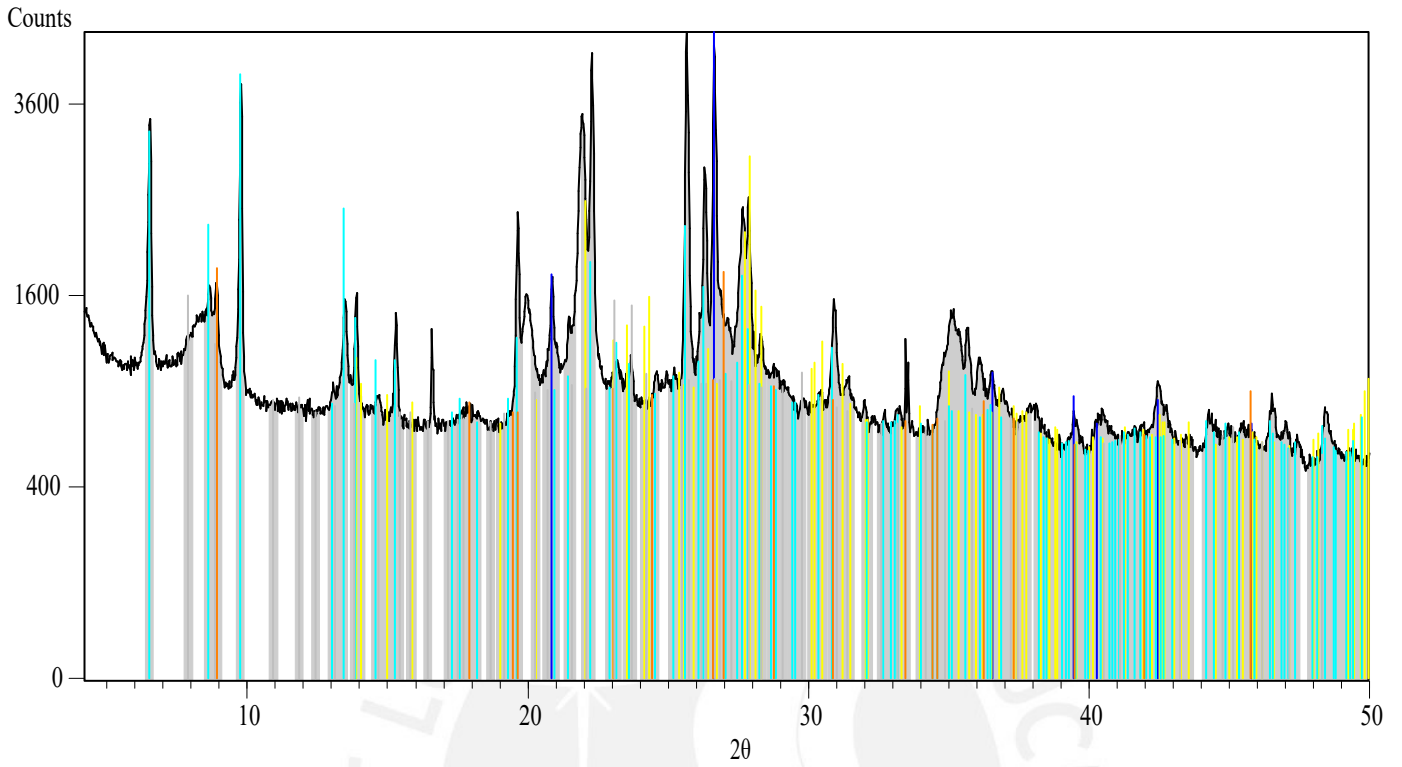
Peak List
Smeectite
Cristobalite
Mica



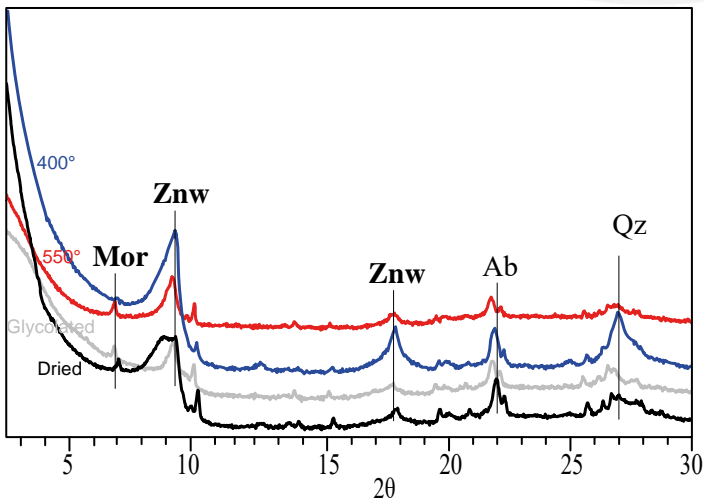


Phase	Peak Position (2θ)
Quartz	~26.6
Kaolinite	~10.0, 14.6, 17.6, 20.1, 21.4, 22.8, 24.2, 25.6, 27.0, 28.4, 29.8, 31.2, 32.6, 34.0, 35.4, 36.8, 38.2, 39.6, 41.0, 42.4, 43.8, 45.2, 46.6, 48.0, 49.4
Smeectite	~7.1, 14.2, 21.3, 28.4, 35.5, 42.6, 49.7
Plagioclase	~10.0, 14.6, 17.6, 20.1, 21.4, 22.8, 24.2, 25.6, 27.0, 28.4, 29.8, 31.2, 32.6, 34.0, 35.4, 36.8, 38.2, 39.6, 41.0, 42.4, 43.8, 45.2, 46.6, 48.0, 49.4
Mica	~10.0, 14.6, 17.6, 20.1, 21.4, 22.8, 24.2, 25.6, 27.0, 28.4, 29.8, 31.2, 32.6, 34.0, 35.4, 36.8, 38.2, 39.6, 41.0, 42.4, 43.8, 45.2, 46.6, 48.0, 49.4
K-Feldspar	~10.0, 14.6, 17.6, 20.1, 21.4, 22.8, 24.2, 25.6, 27.0, 28.4, 29.8, 31.2, 32.6, 34.0, 35.4, 36.8, 38.2, 39.6, 41.0, 42.4, 43.8, 45.2, 46.6, 48.0, 49.4

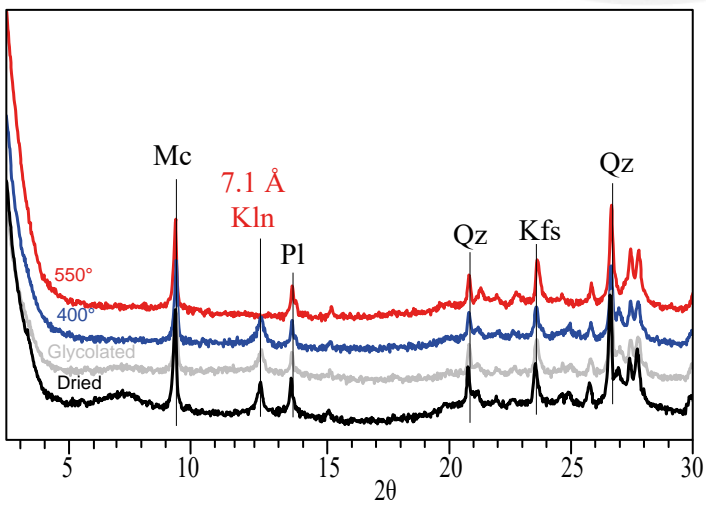
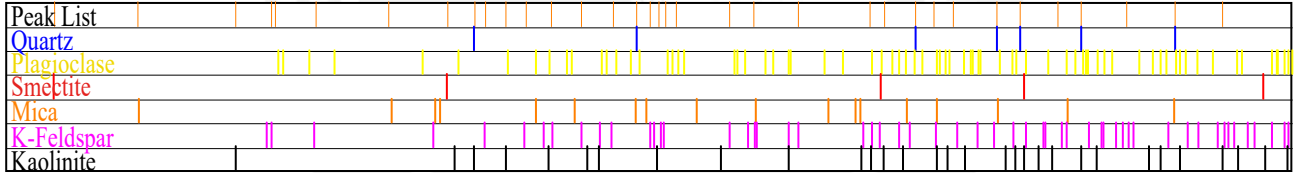
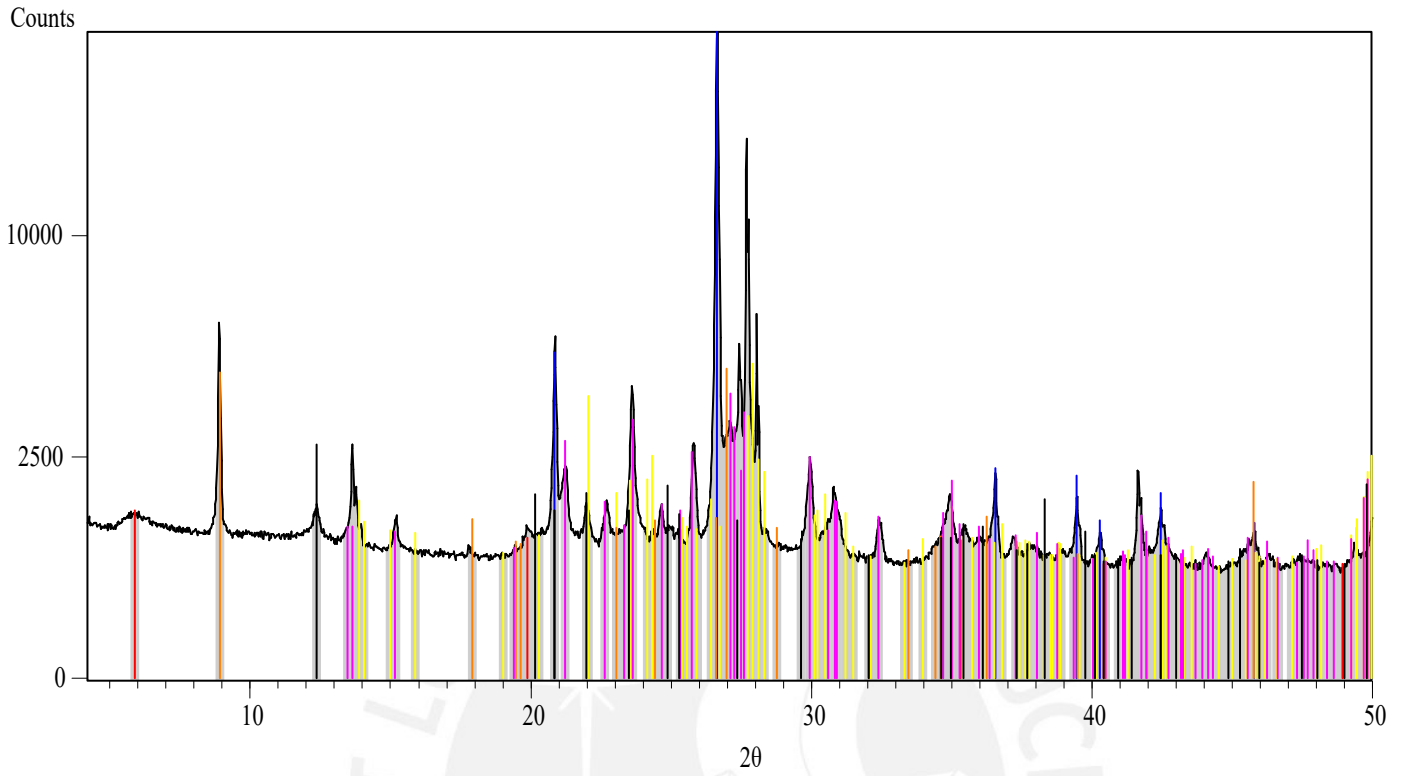




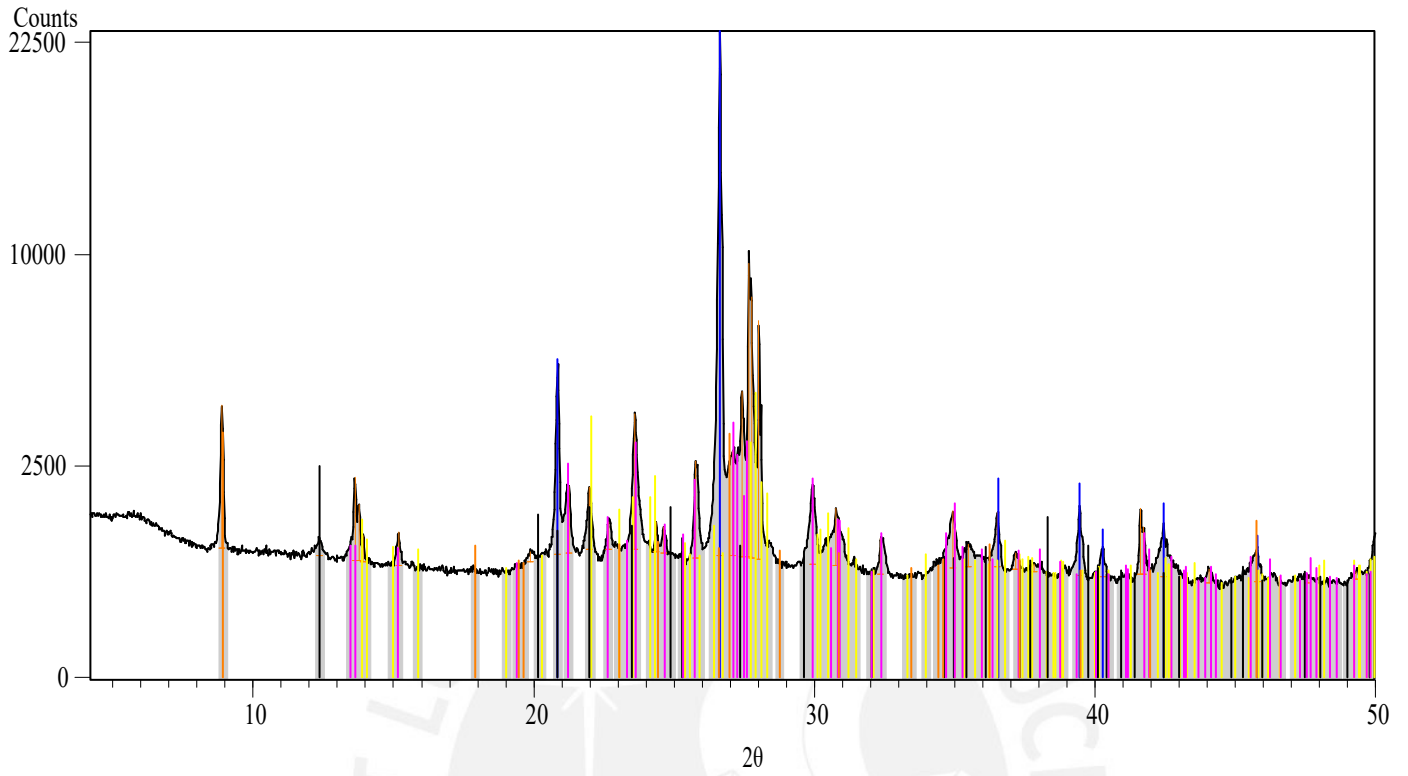
Phase	Approximate 2θ (degrees)
Quartz	10, 20, 26.5, 35, 40, 45
Plagioclase	10, 15, 20, 25, 30, 35, 40, 45
Mordenite	10, 15, 20, 25, 30, 35, 40, 45
Mica	10, 15, 20, 25, 30, 35, 40, 45
Mutinaite	10, 15, 20, 25, 30, 35, 40, 45



2021-MAC-065A



2021-MAC-065B

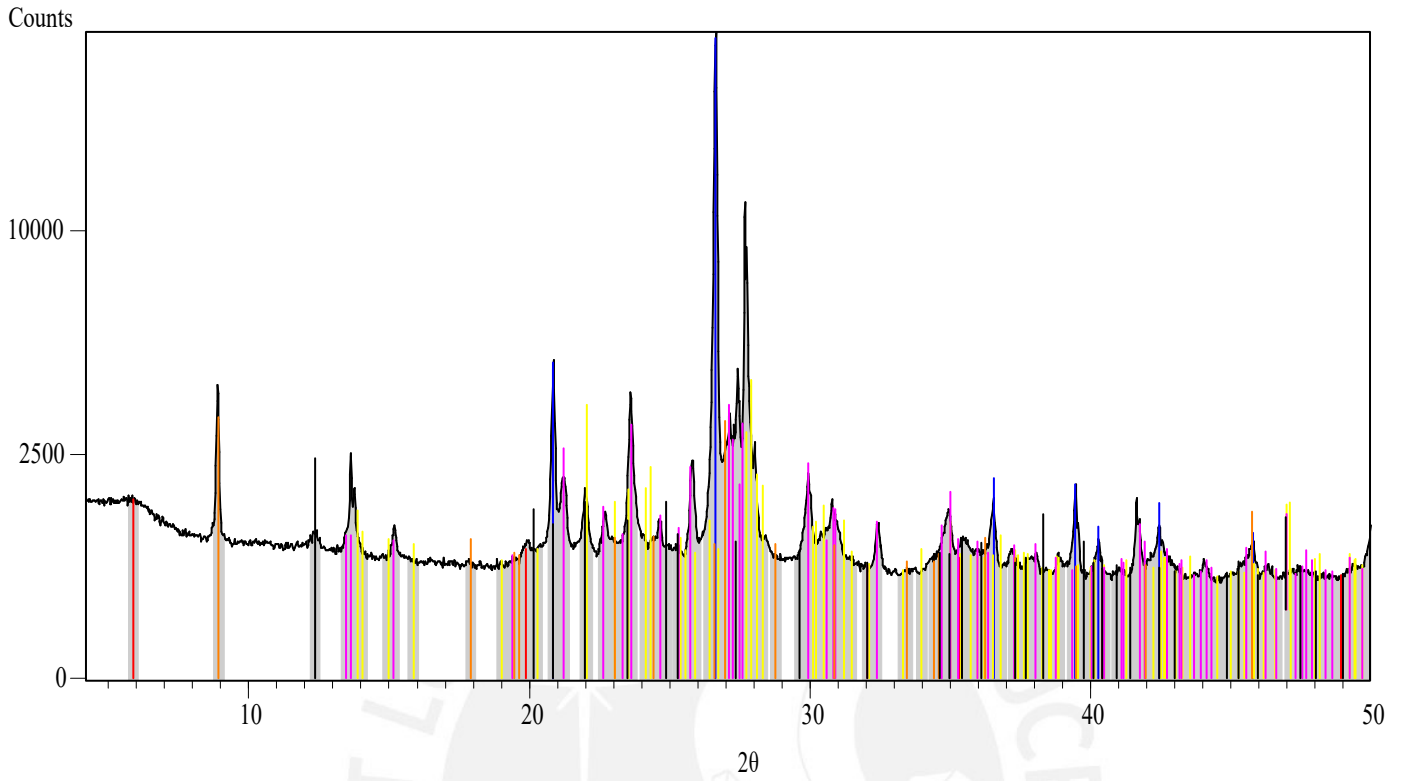


Peak List	Reference
Quartz	Blue vertical lines
Plagioclase	Yellow vertical lines
Kaolinite	Black vertical lines
K-Feldspar	Magenta vertical lines
Mica	Orange vertical lines





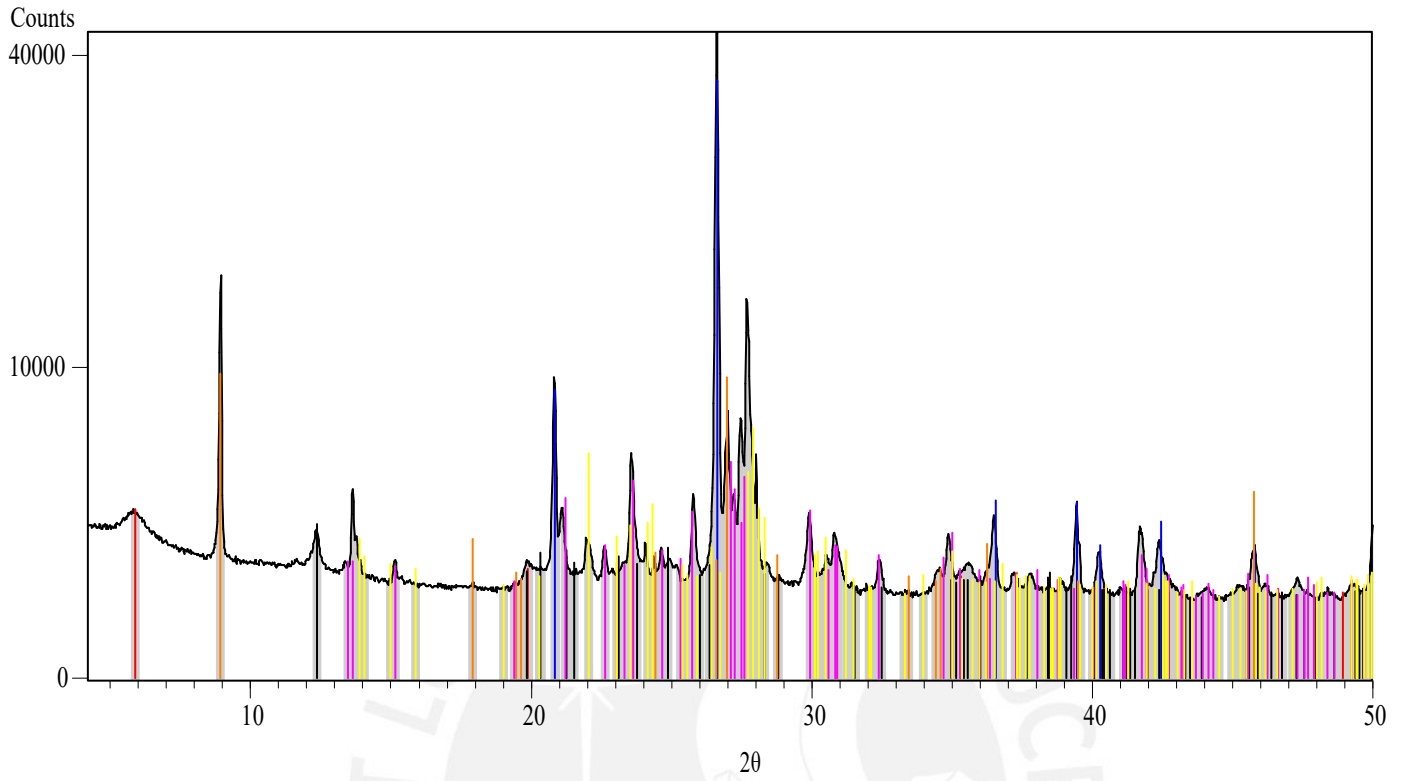
2021-MAC-065C



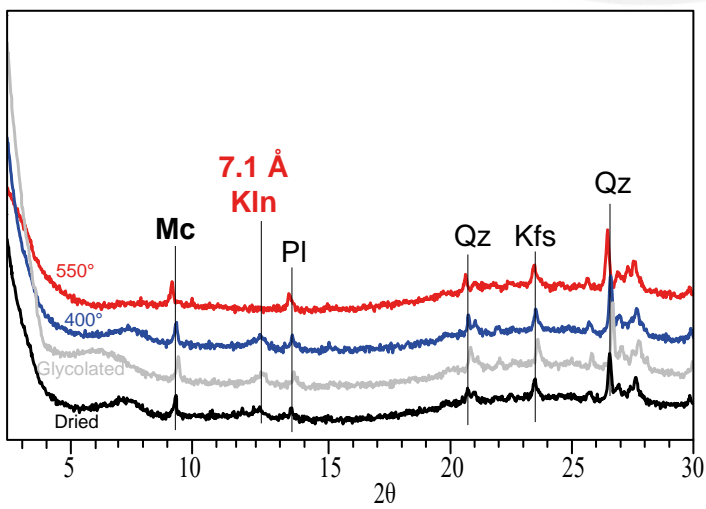
Peak List	Quartz	Plagioclase	Smetite	K-Feldspar	Mica	Kaolinite
1						
2						
3						
4						
5						
6						
7						
8						
9						
10						
11						
12						
13						
14						
15						
16						
17						
18						
19						
20						
21						
22						
23						
24						
25						
26						
27						
28						
29						
30						
31						
32						
33						
34						
35						
36						
37						
38						
39						
40						
41						
42						
43						
44						
45						
46						
47						
48						
49						
50						



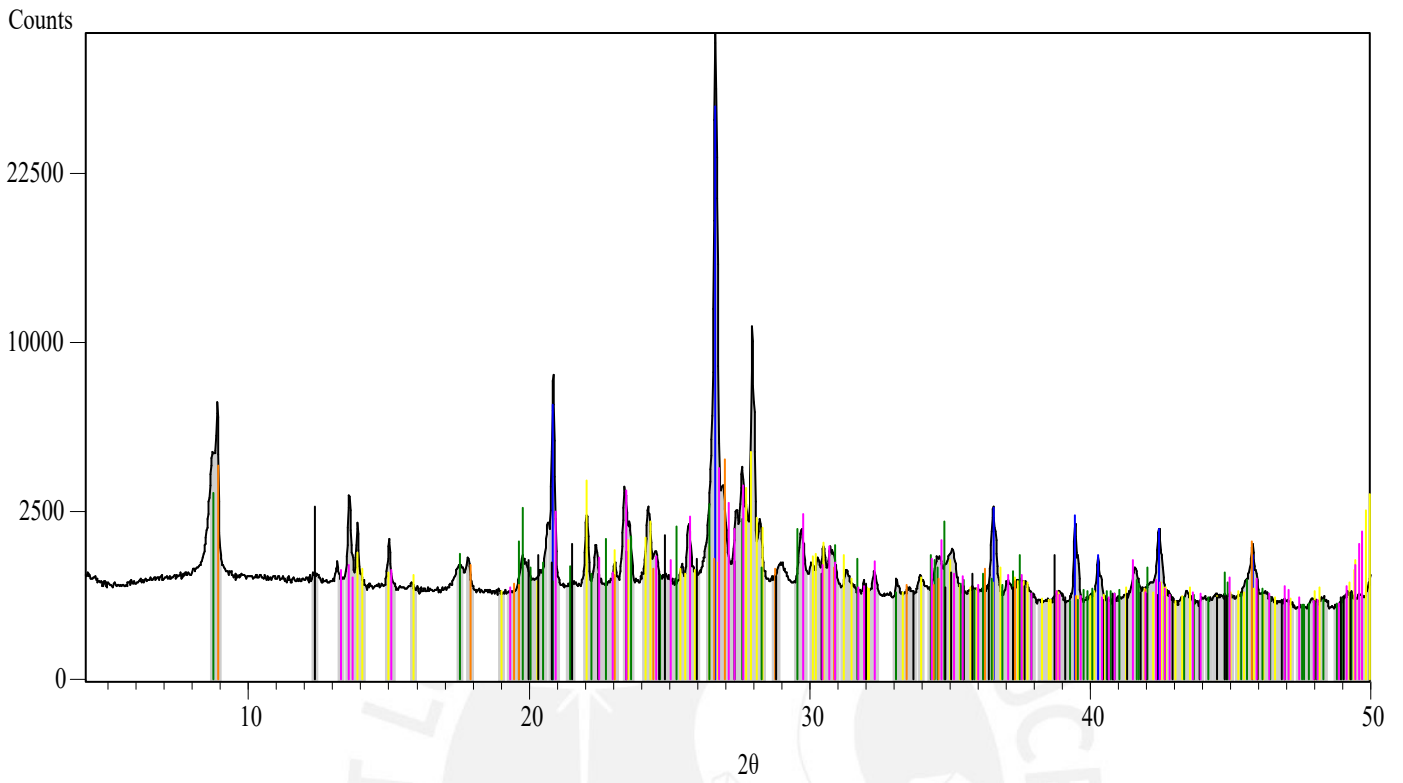
2021-MAC-066



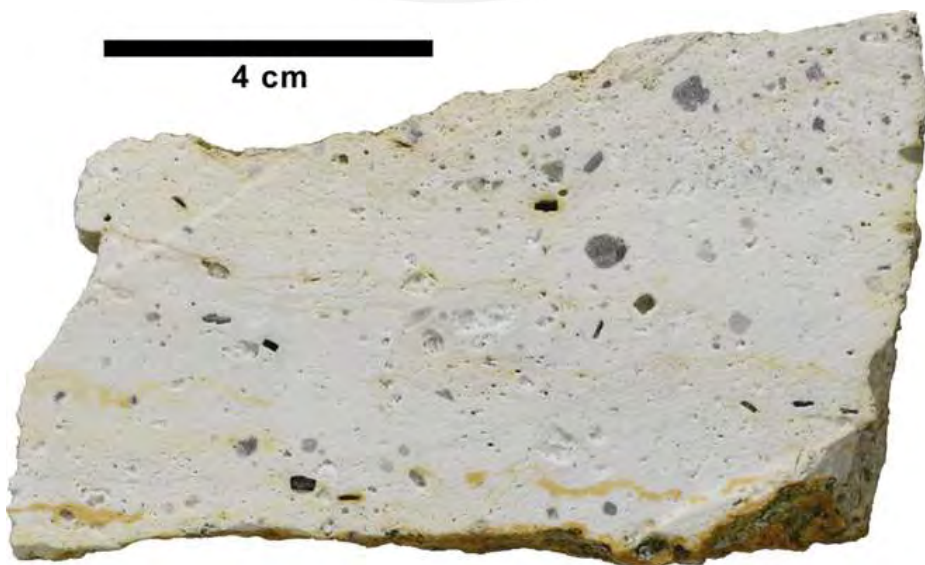
Peak List
Quartz
Smectite
Kaolinite
Mica
K-Feldspar
Plagioclase



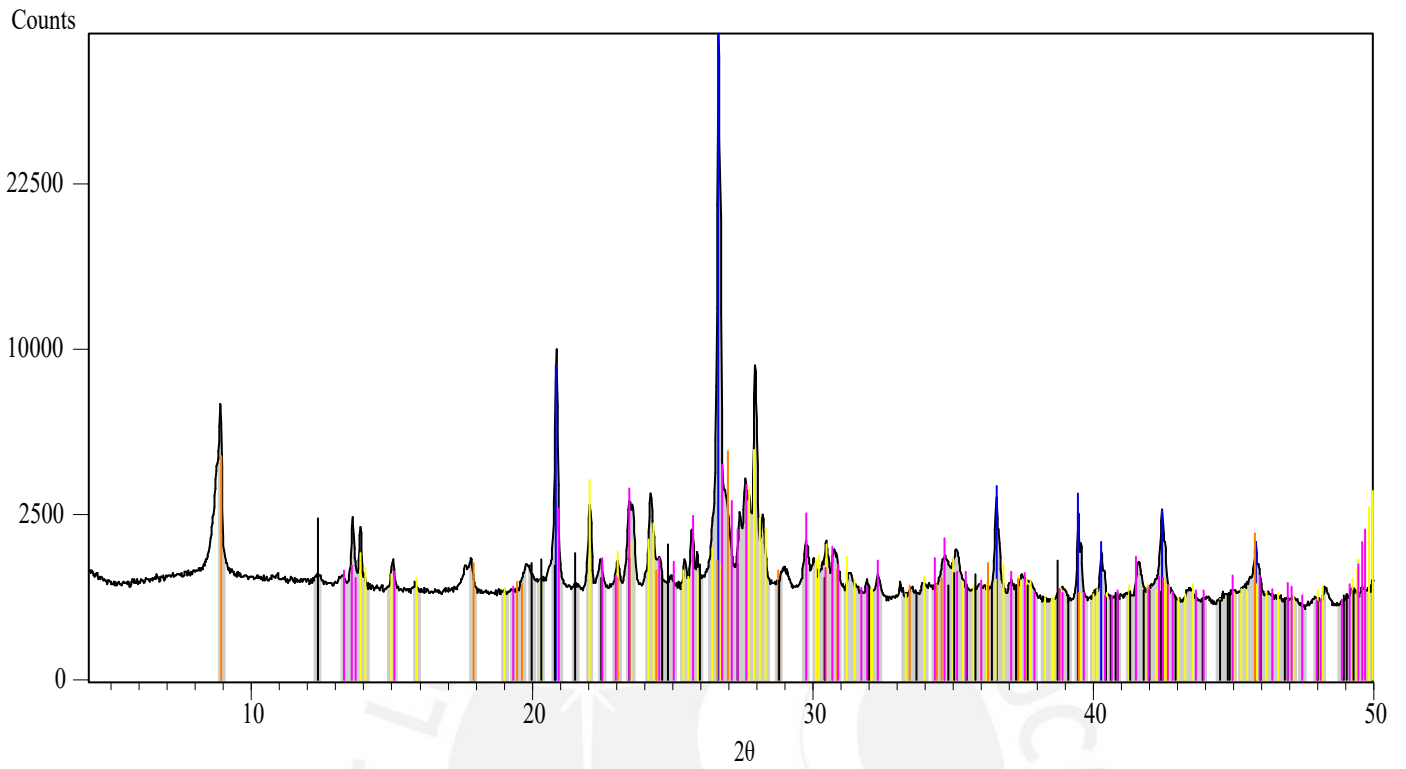
2021-MAC-067A



Peak List	Reference
Quartz	Blue vertical lines
Plagioclase	Yellow vertical lines
Mica	Green vertical lines
Mica	Orange vertical lines
Kaolinite	Black vertical lines
K-Feldspar	Pink vertical lines



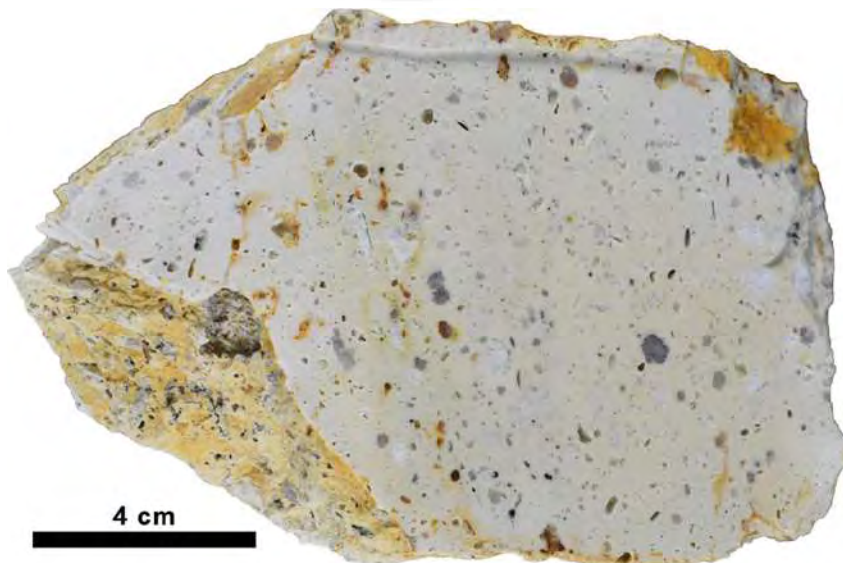
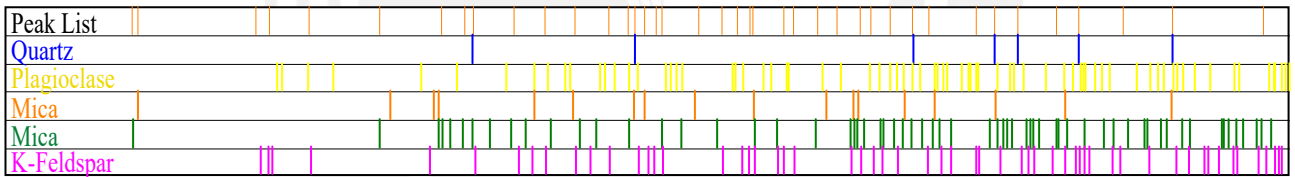
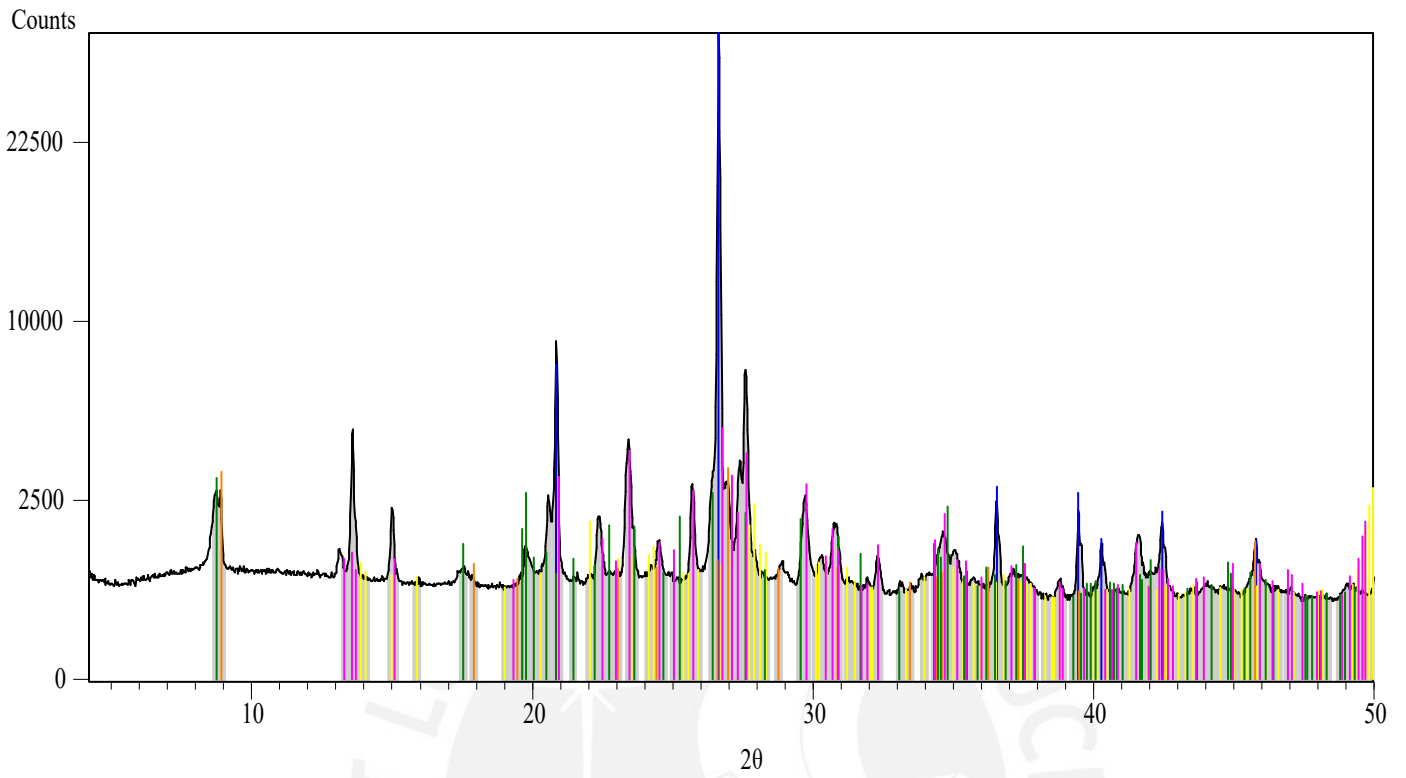
2021-MAC-067B



Peak List
Quartz
Plagioclase
Mica
Kaolinite
K-Feldspar

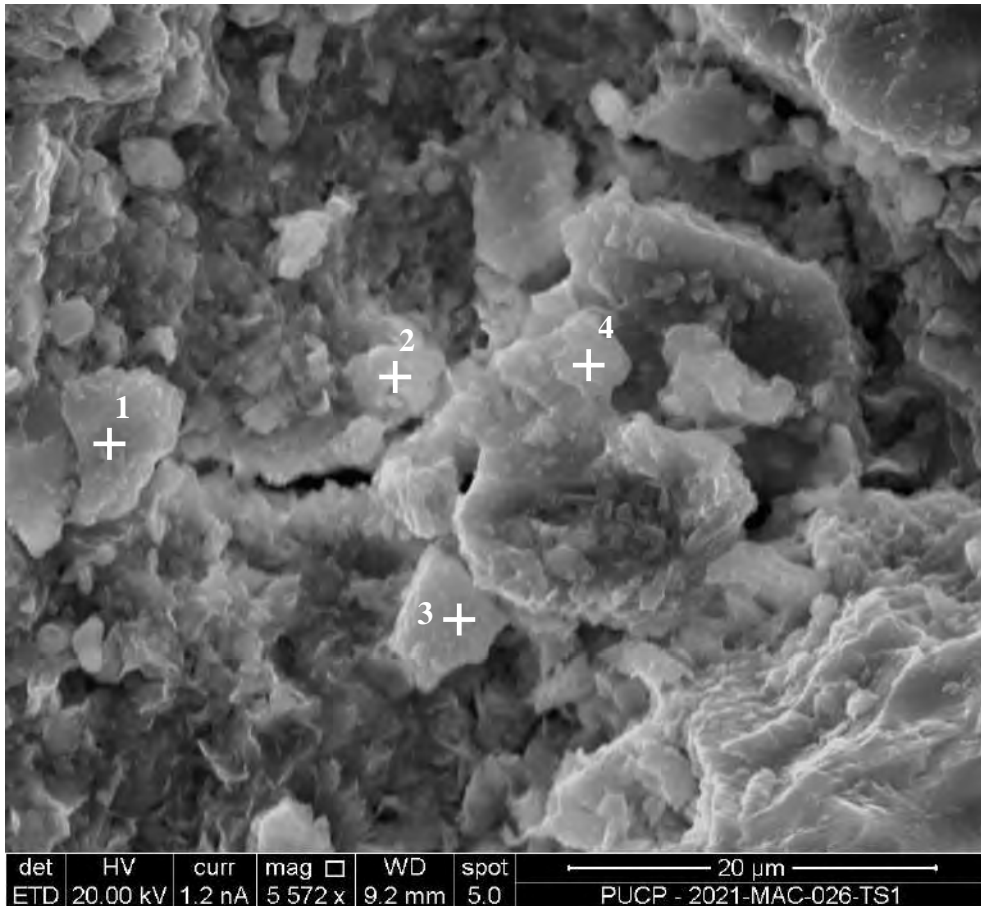


2021-MAC-067C

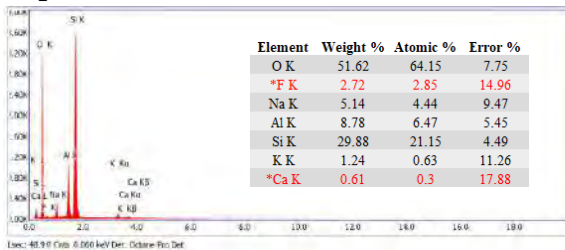


# APPENDIX C. SEM - EDS

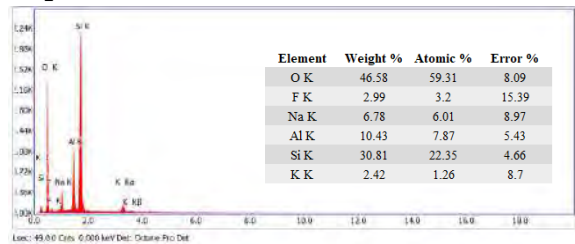
## 2021-MAC-026 : 'Zeolite with mica'



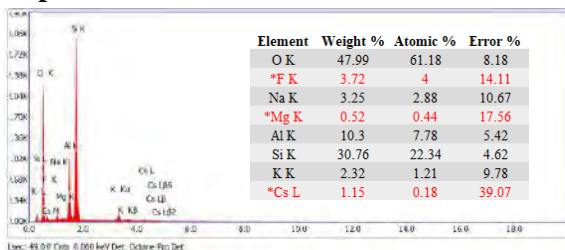
Spot 1:



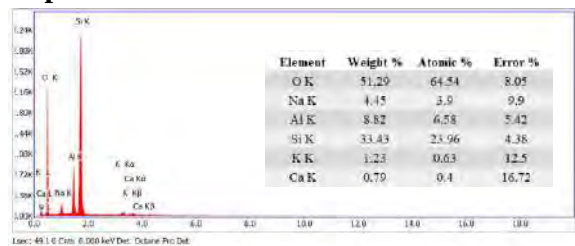
Spot 3:



Spot 2:

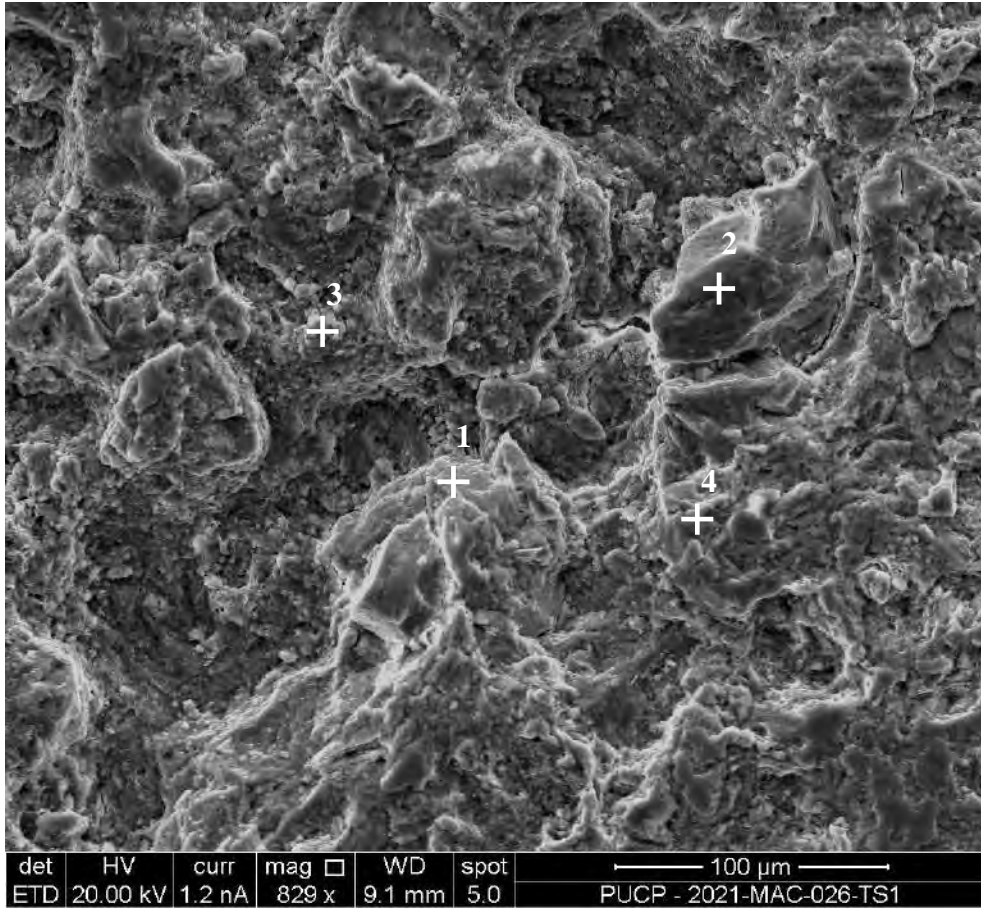


Spot 4:

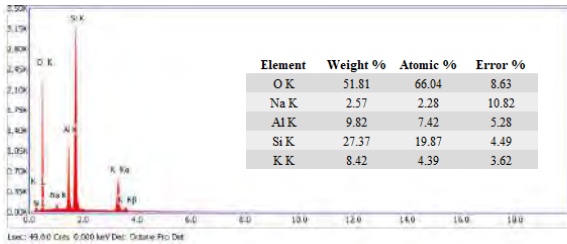


The elements and values presented in \*red can be considered erroneous

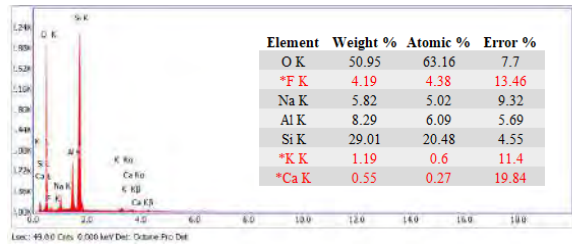
2021-MAC-026 : 'Zeolite with mica'



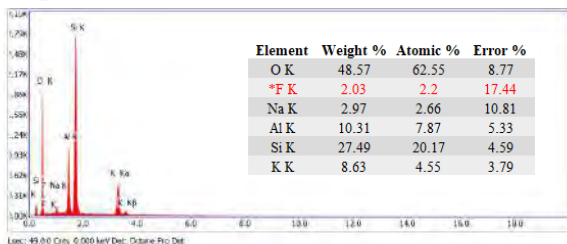
Spot 1:



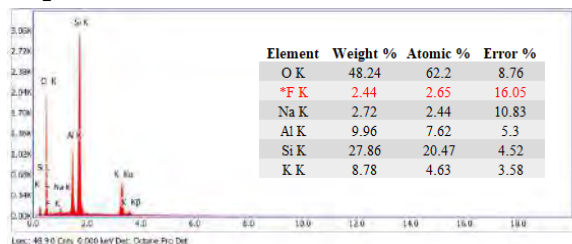
Spot 3:



Spot 2:

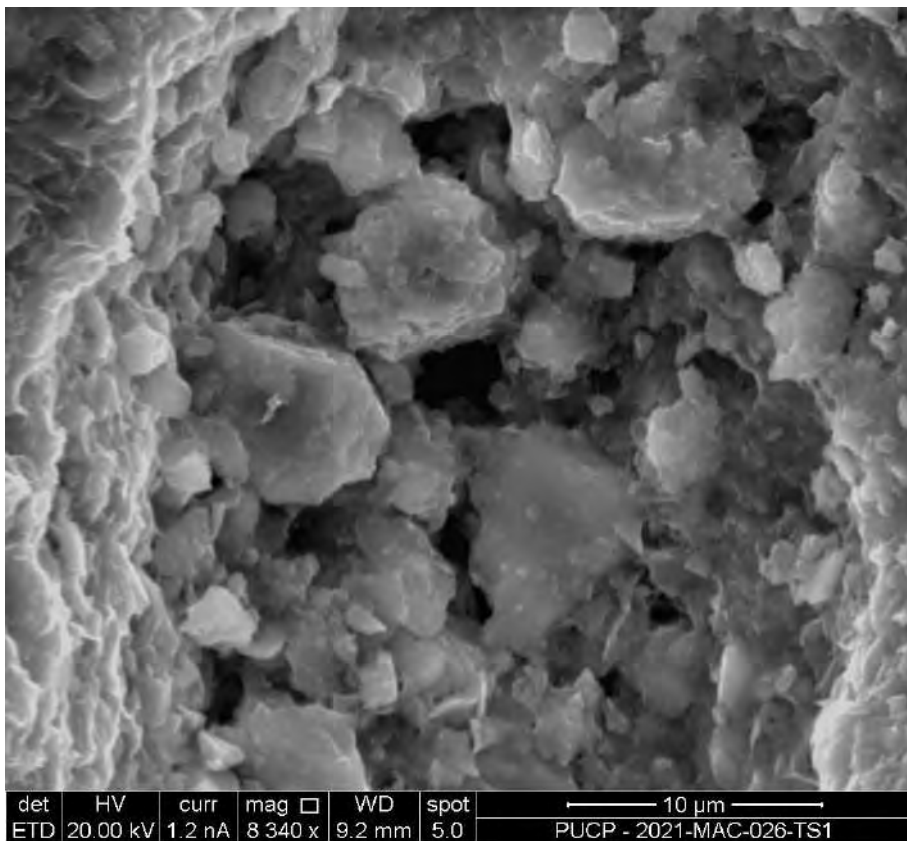
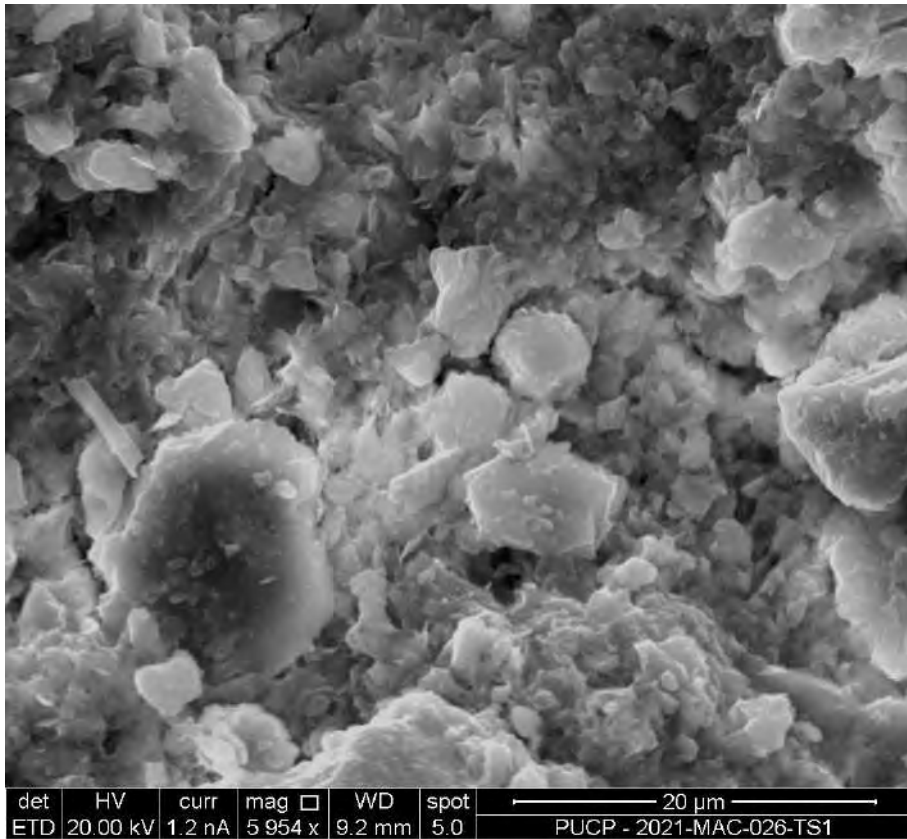


Spot 4:



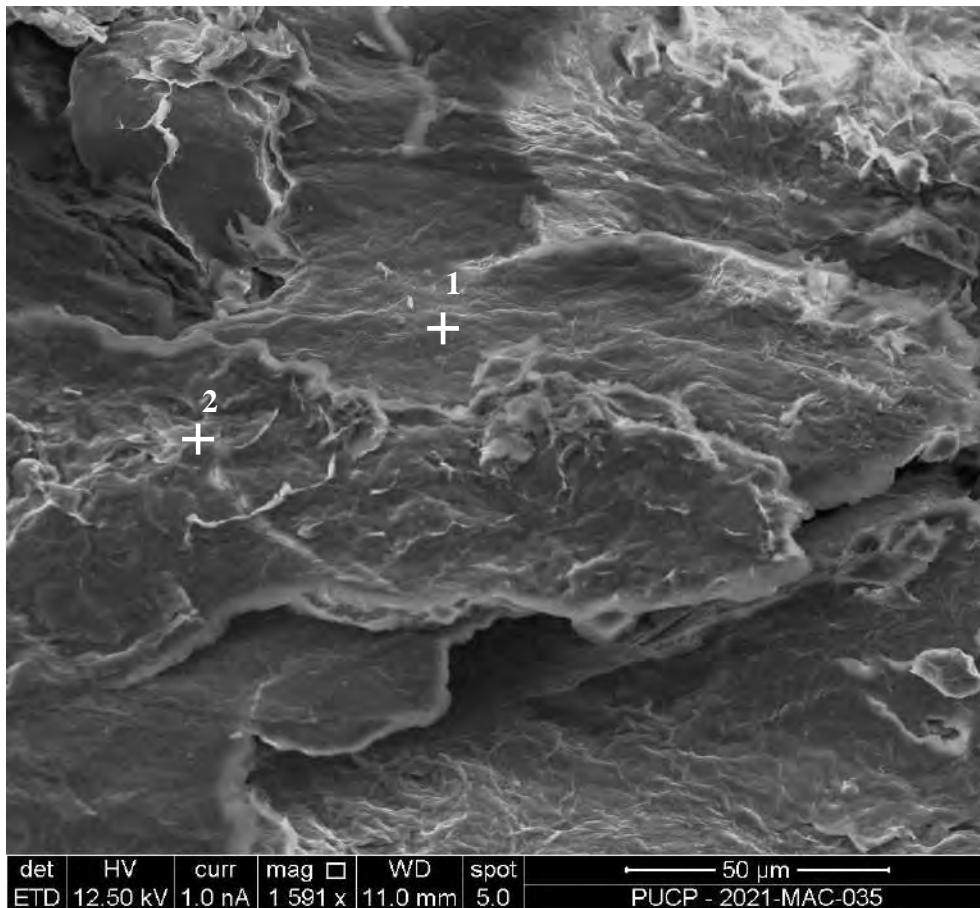
The elements and values presented in \*red can be considered erroneous

2021-MAC-026 : 'Zeolite with mica'

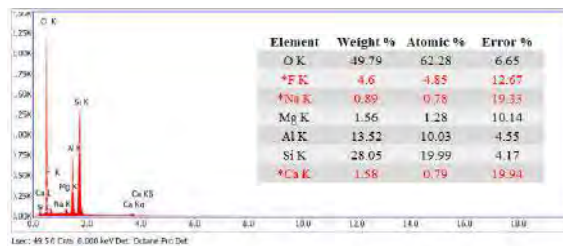




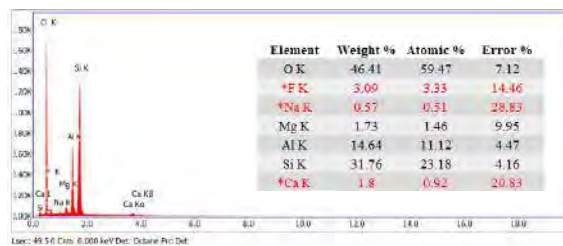
2021-MAC-035 : 'Smectite with mica'



Spot 1:

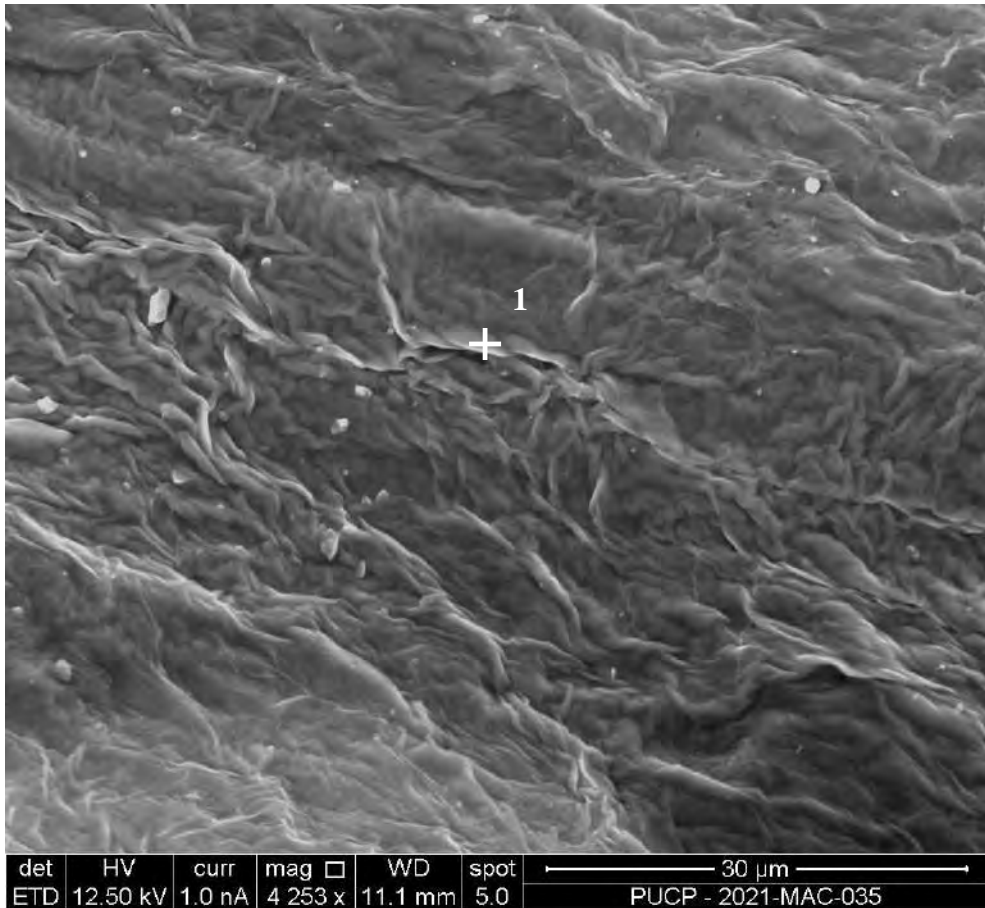


Spot 2:

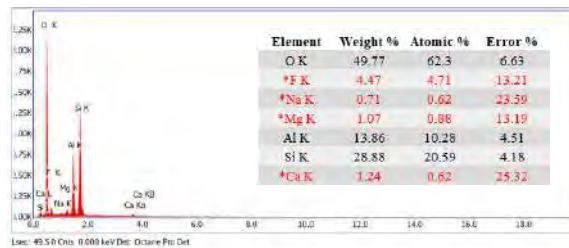


The elements and values presented in \*red can be considered erroneous

2021-MAC-035 : 'Smectite with mica'

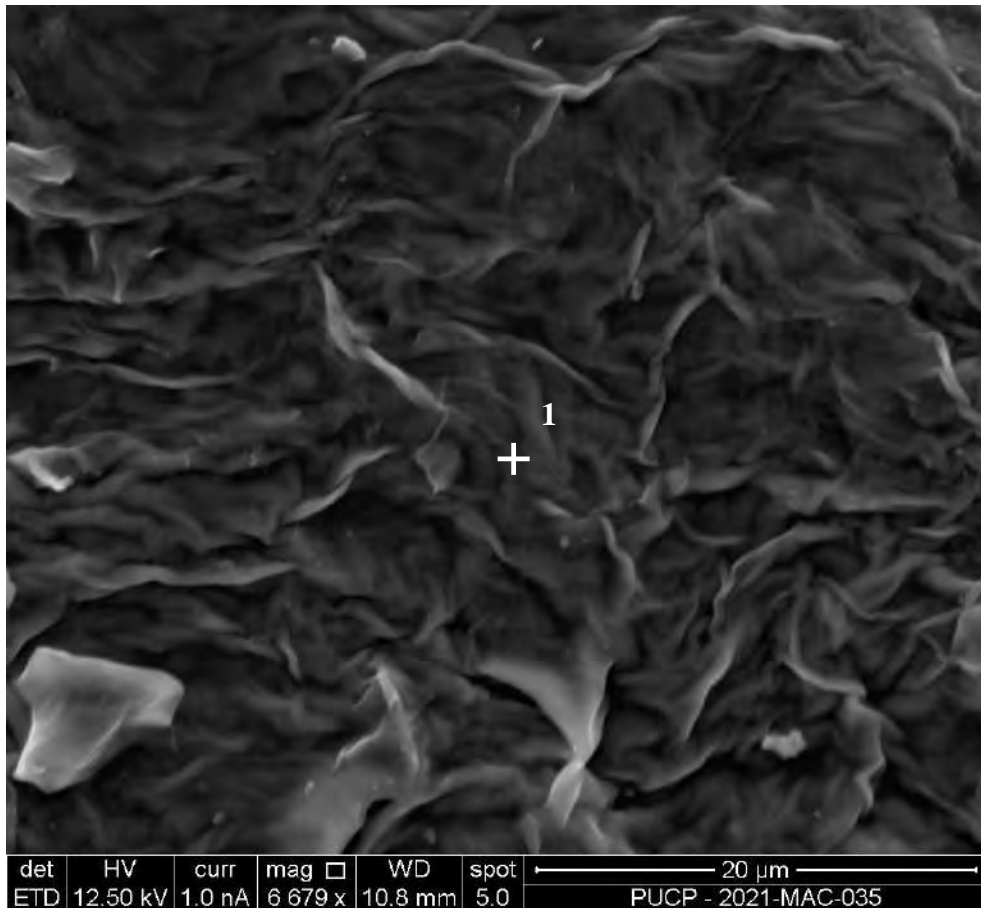


Spot 1:

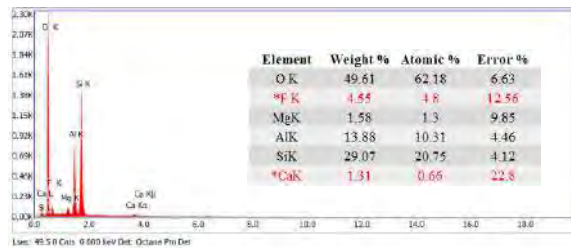


The elements and values presented in \*red can be considered erroneous

2021-MAC-035 : 'Smectite with mica'

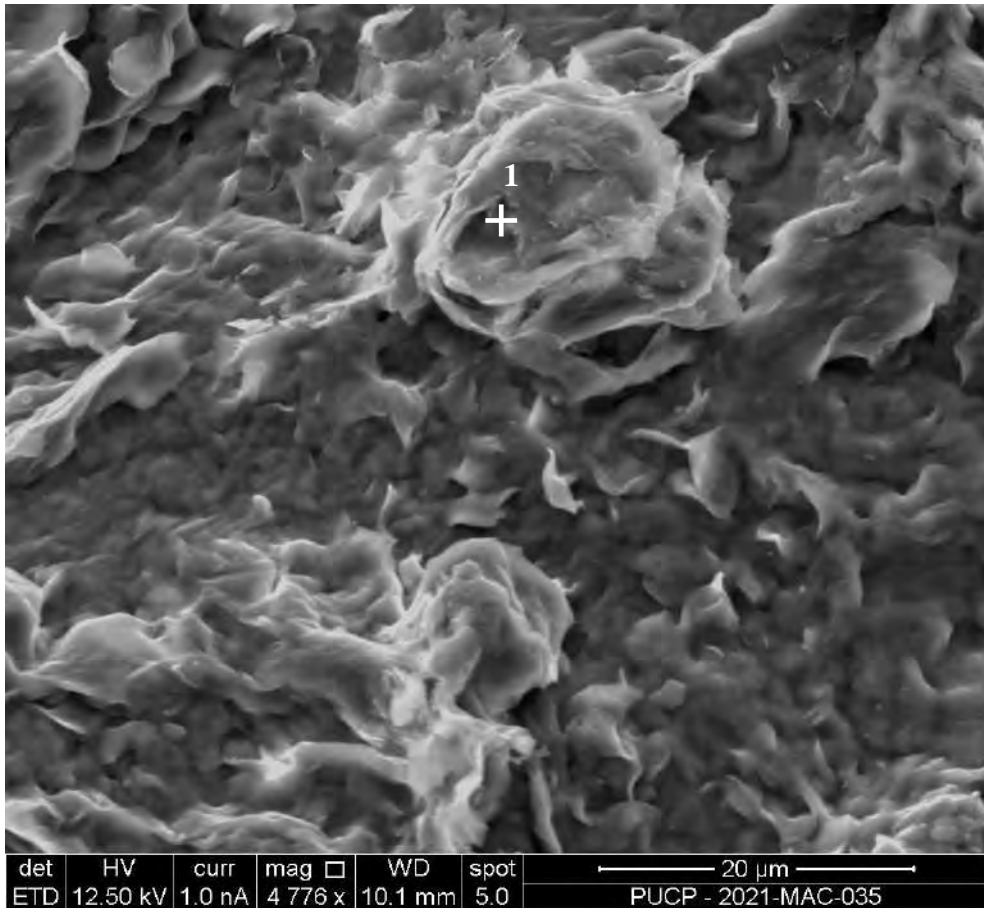


Spot 1:

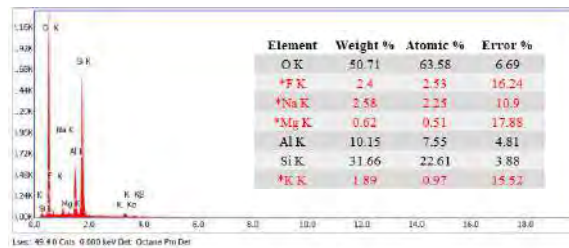


The elements and values presented in \*red can be considered erroneous

2021-MAC-035 : 'Smectite with mica'

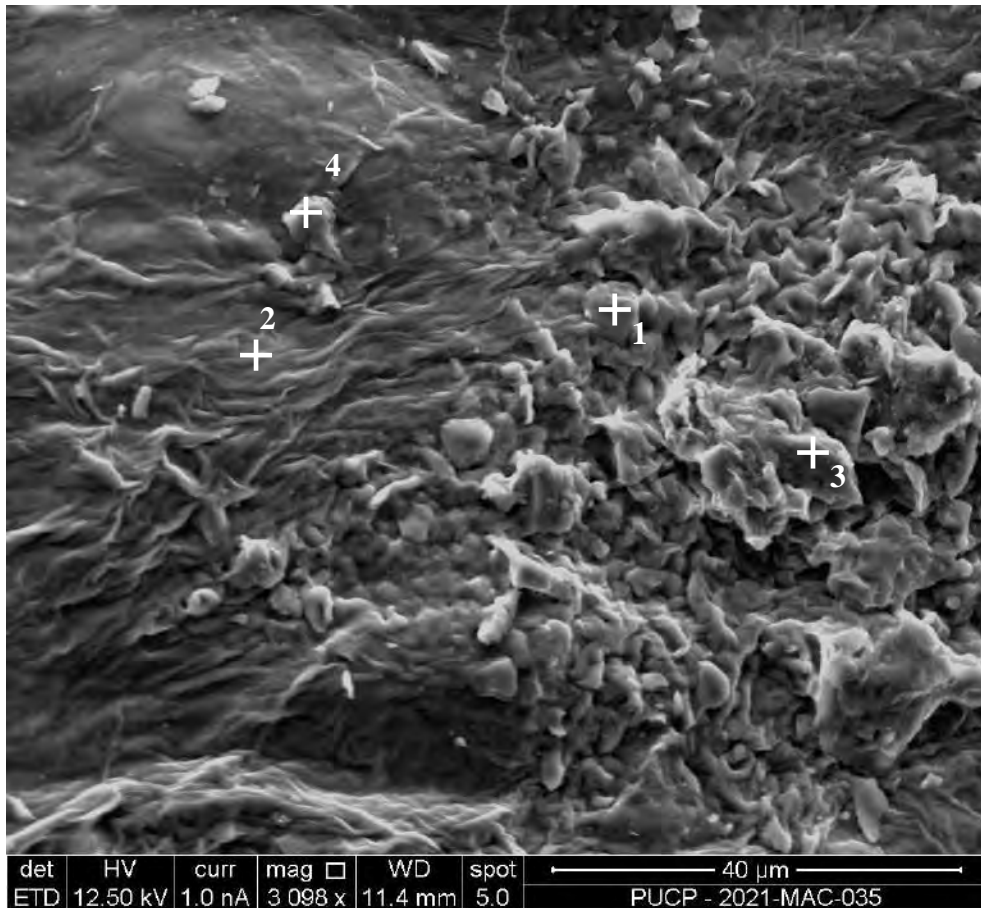


Spot 1:

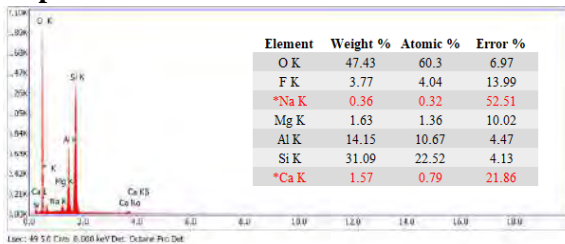


The elements and values presented in \*red can be considered erroneous

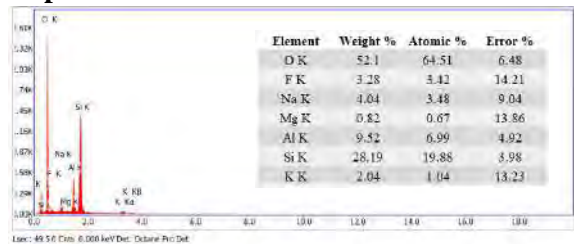
2021-MAC-035 : 'Smectite with mica'



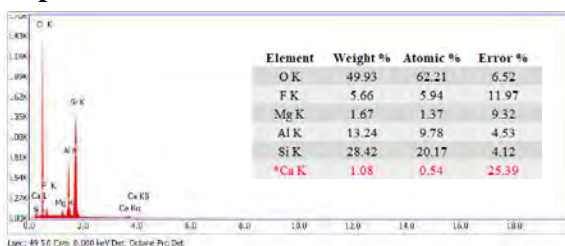
Spot 1:



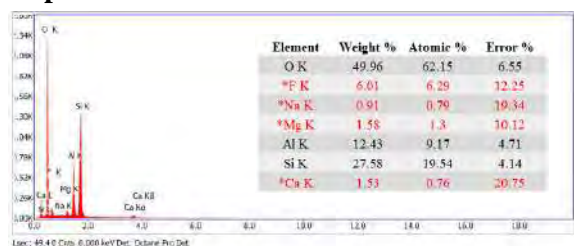
Spot 3:



Spot 2:

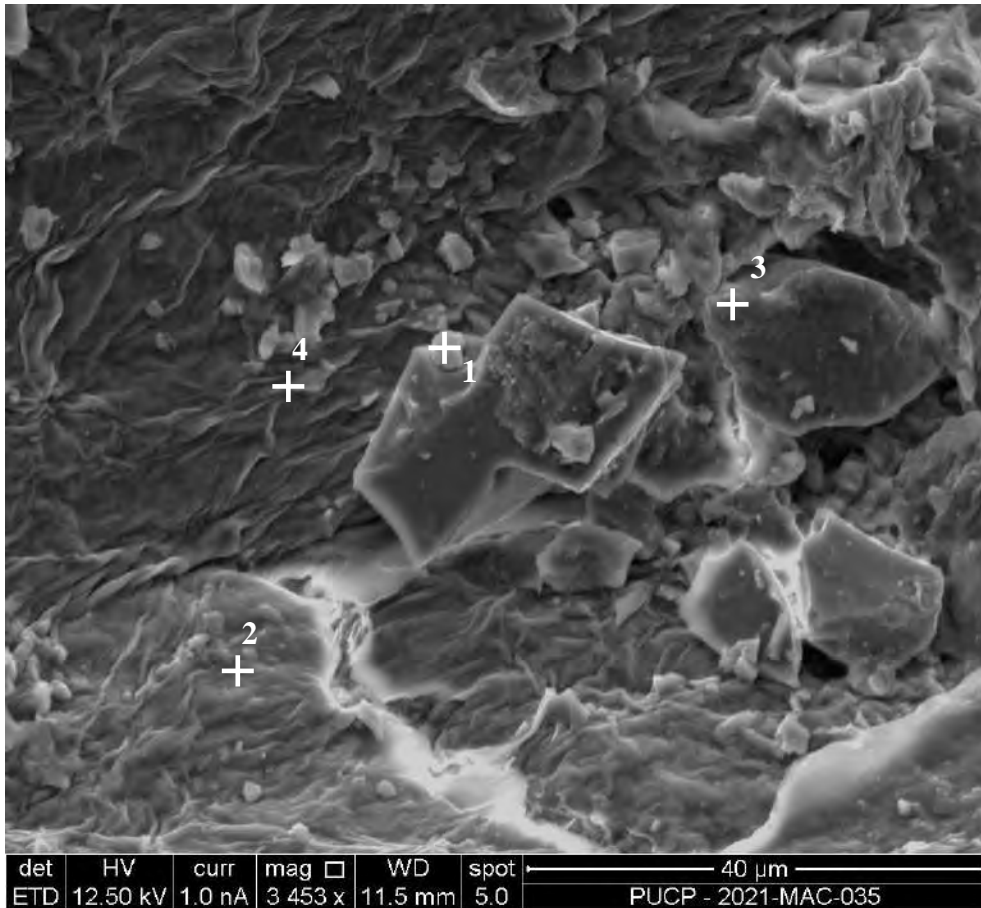


Spot 4:



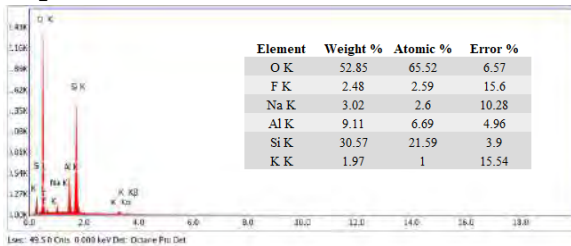
The elements and values presented in \*red can be considered erroneous

2021-MAC-035 : 'Smectite with mica'

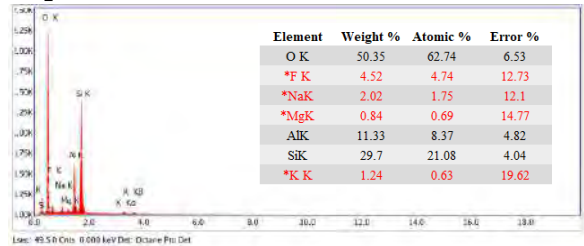


det HV curr mag WD spot 40 µm  
 ETD 12.50 kV 1.0 nA 3 453 x 11.5 mm 5.0 PUCP - 2021-MAC-035

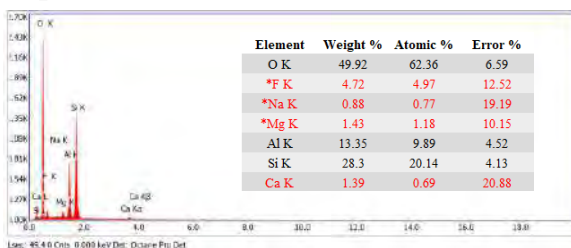
Spot 1:



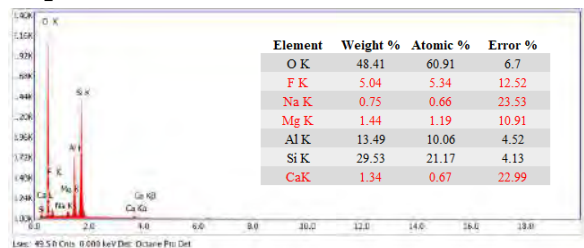
Spot 3:



Spot 2:

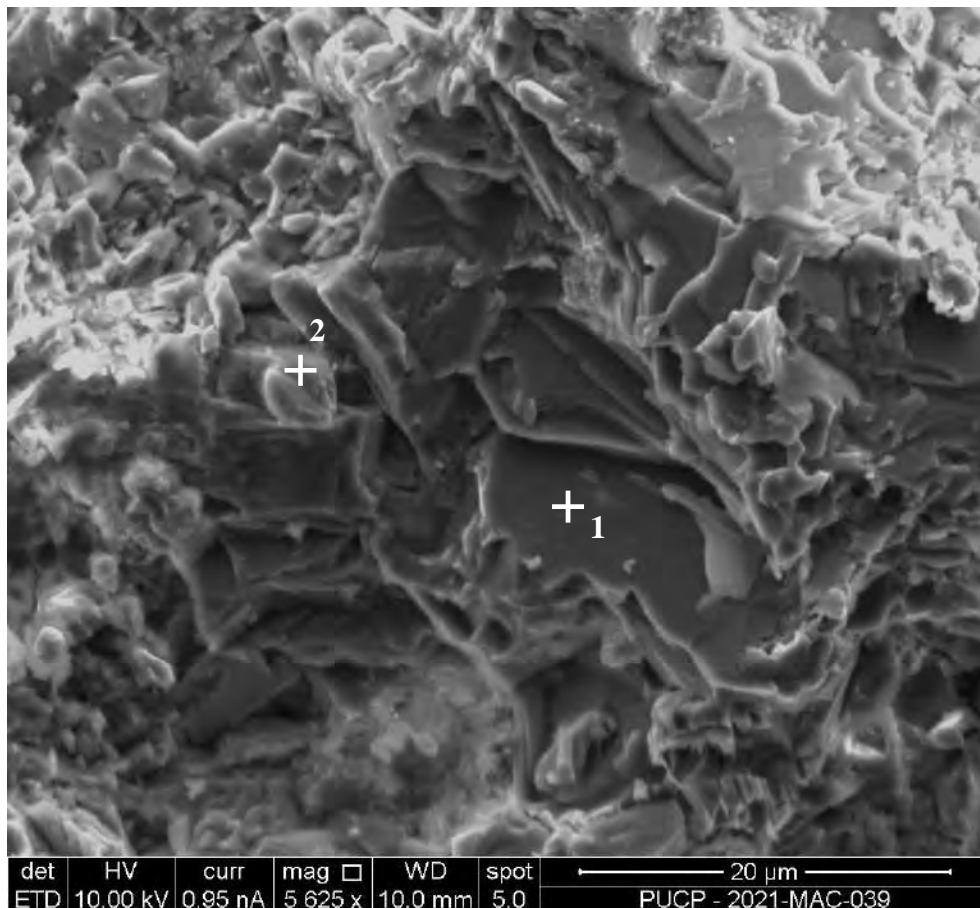


Spot 4:



The elements and values presented in \*red can be considered erroneous

2021-MAC-039 : 'Mica with kaolinite subgroup minerals'



Spot 1:

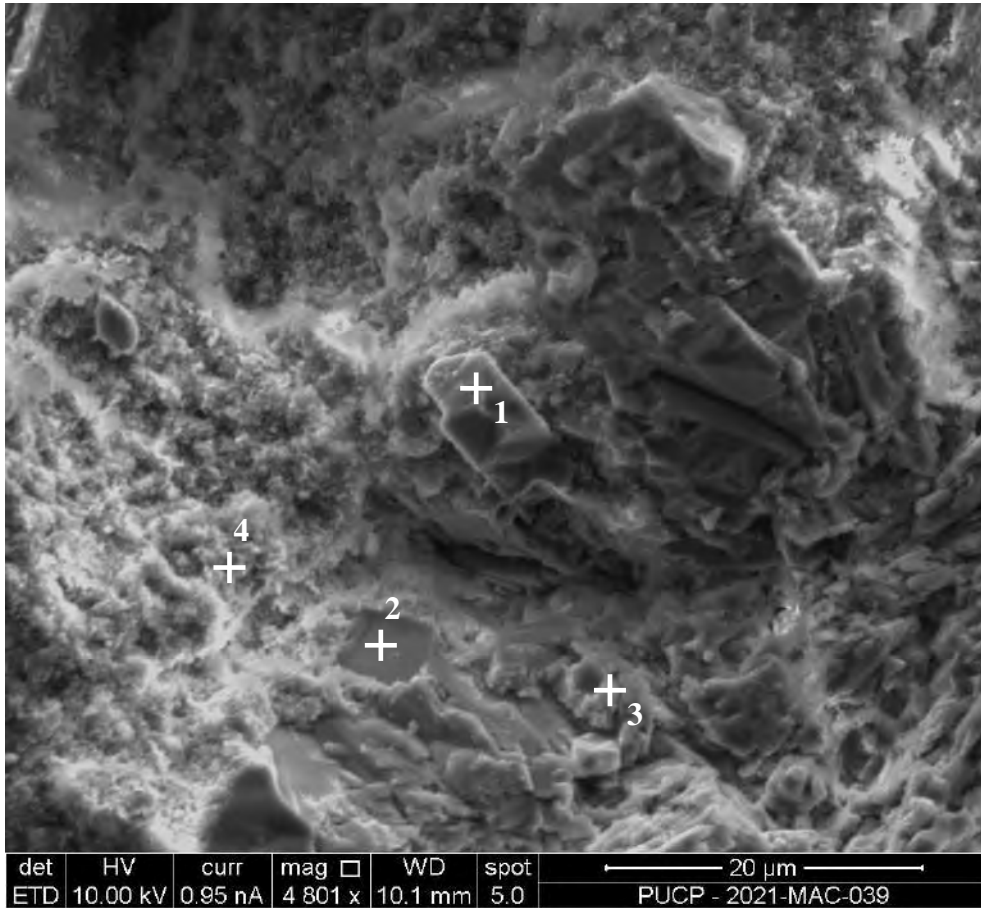


Spot 2:



The elements and values presented in \*red can be considered erroneous

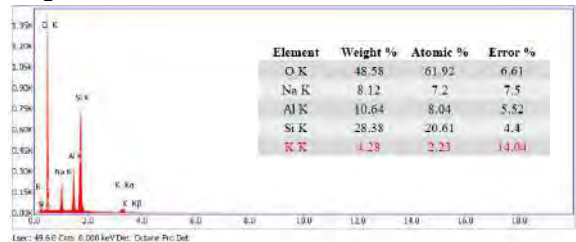
2021-MAC-039 : 'Mica with kaolinite subgroup minerals'



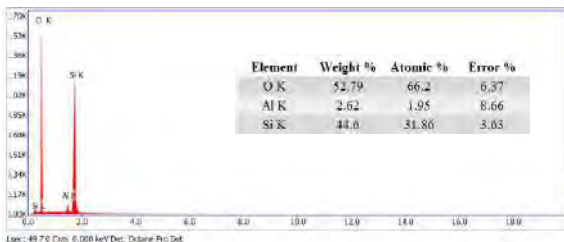
Spot 1:



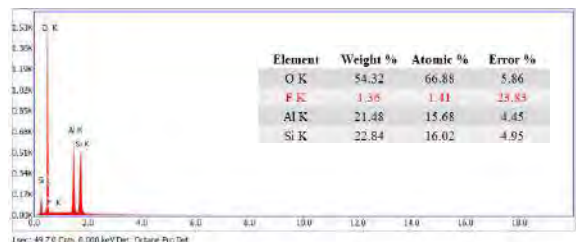
Spot 3:



Spot 2:



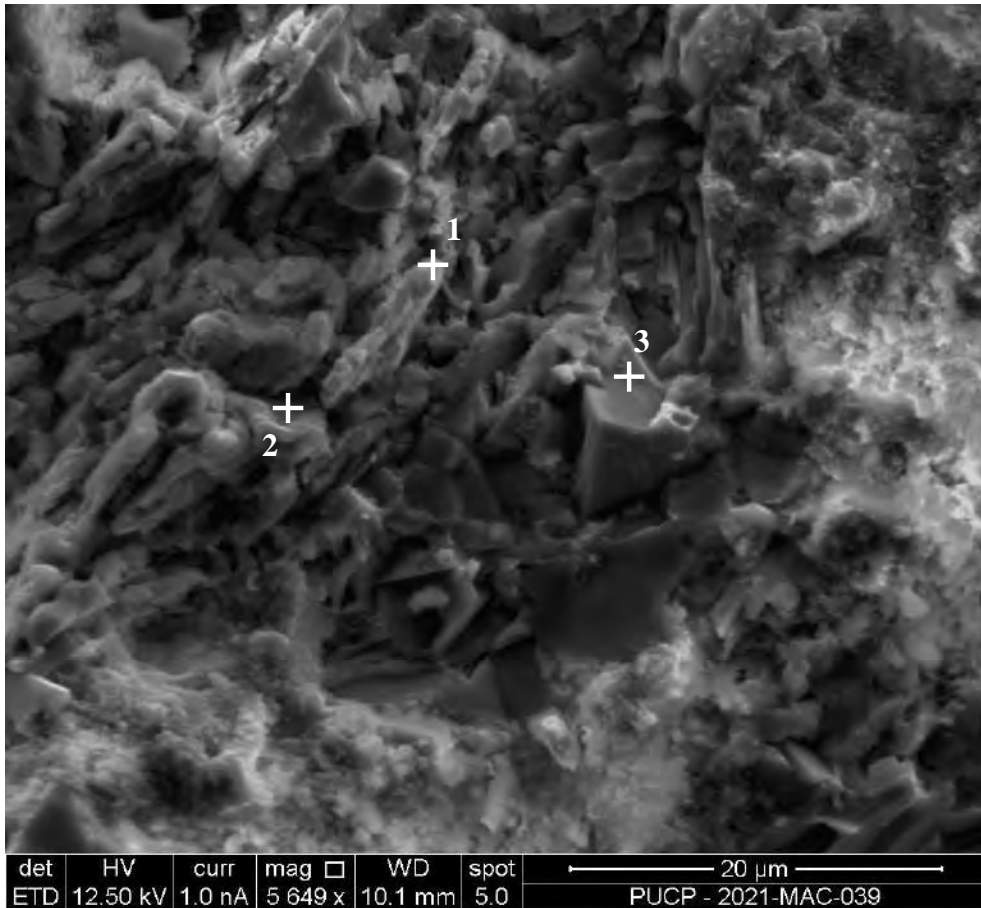
Spot 4:



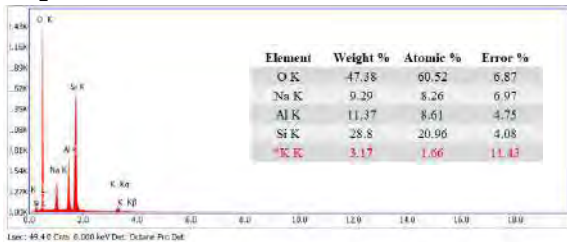
The elements and values presented in \*red can be considered erroneous



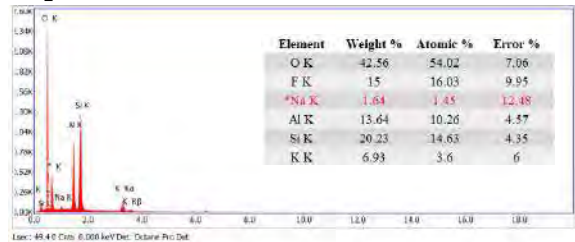
2021-MAC-039 : 'Mica with kaolinite subgroup minerals'



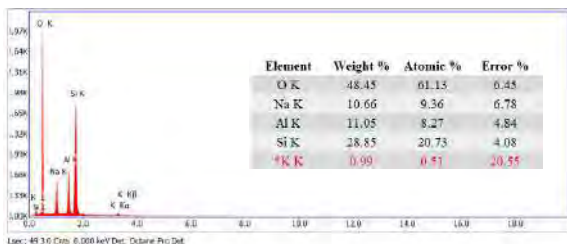
Spot 1:



Spot 3:

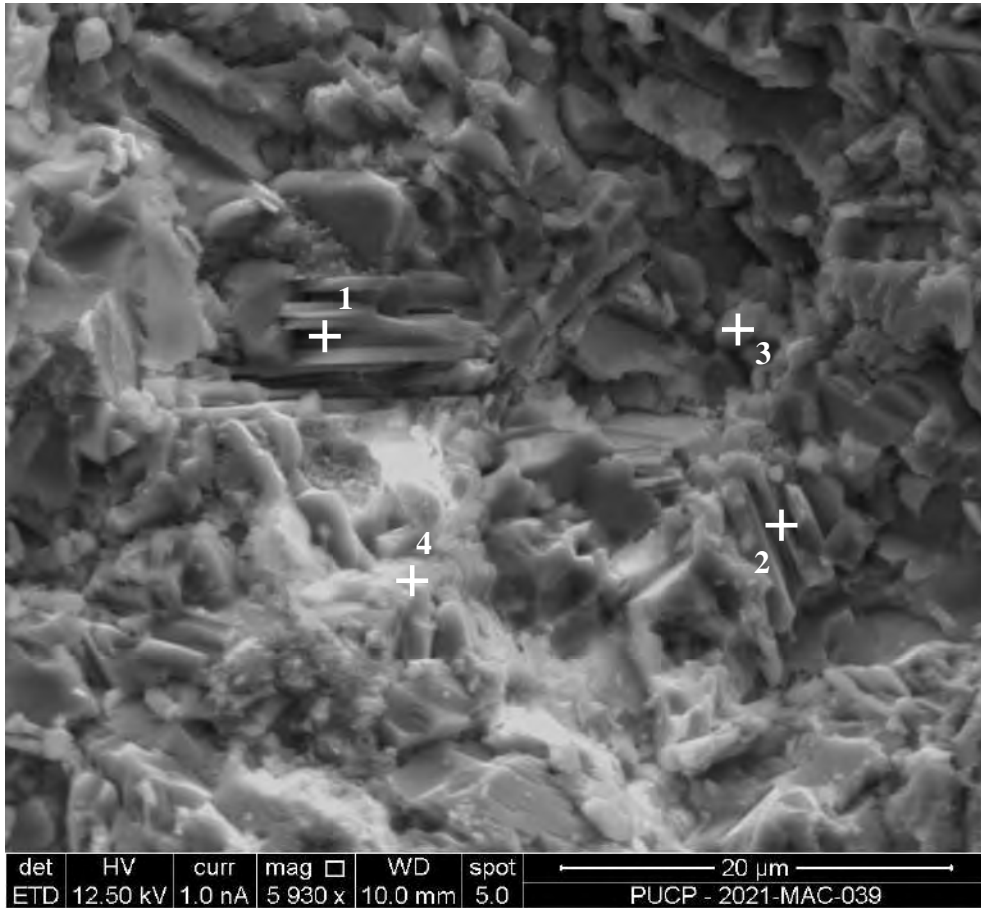


Spot 2:

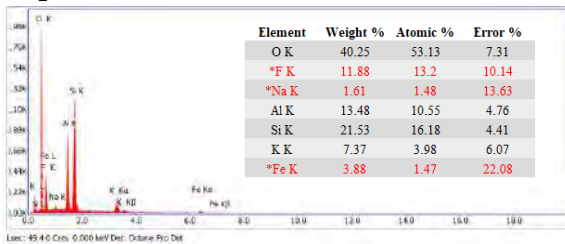


The elements and values presented in \*red can be considered erroneous

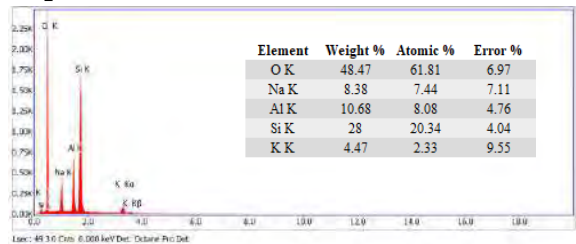
2021-MAC-039 : 'Mica with kaolinite subgroup minerals'



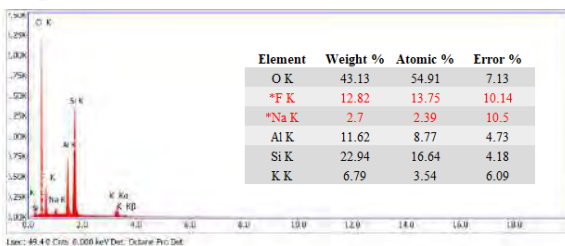
Spot 1:



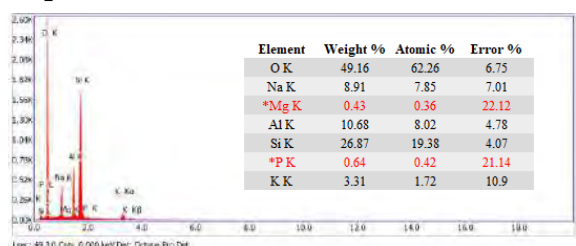
Spot 3:



Spot 2:

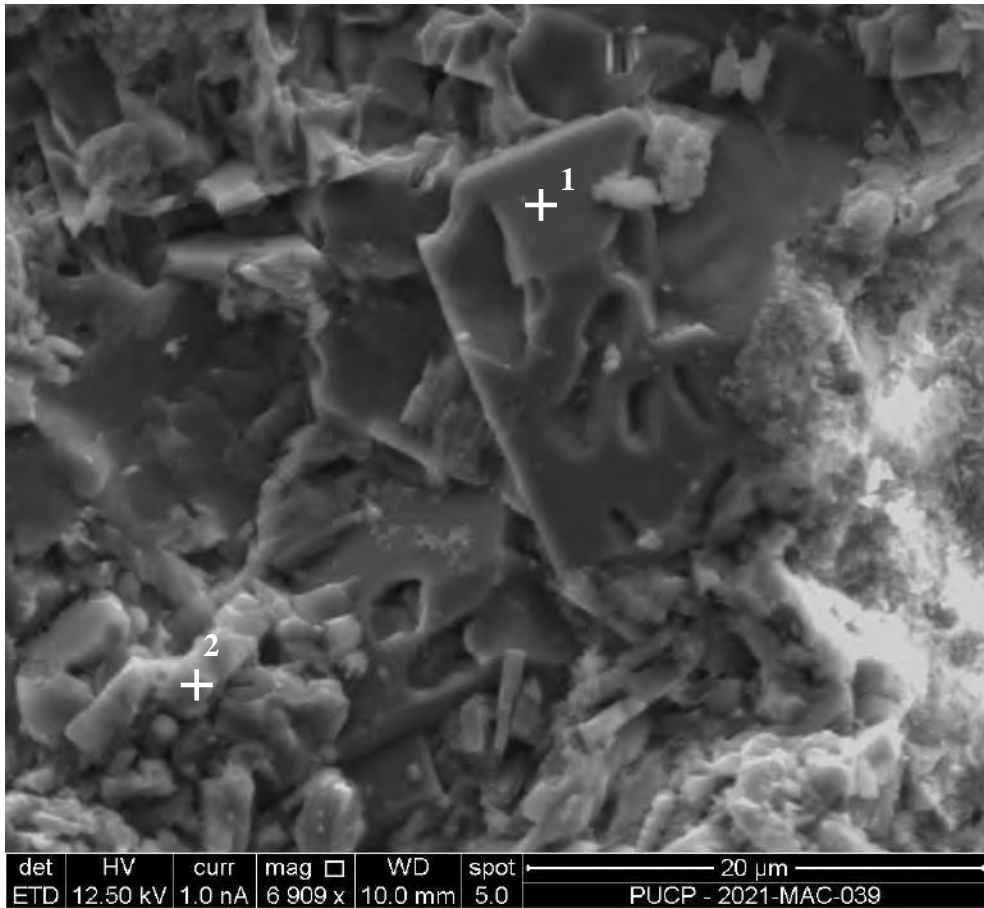


Spot 4:

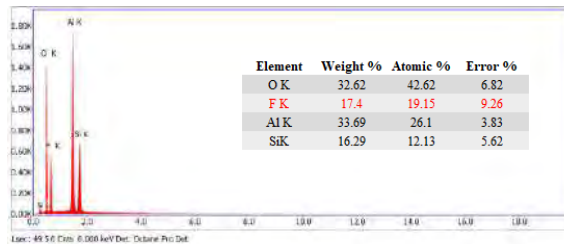


The elements and values presented in \*red can be considered erroneous

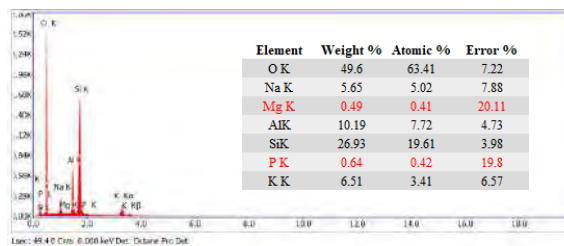
2021-MAC-039 : 'Mica with kaolinite subgroup minerals'



Spot 1:

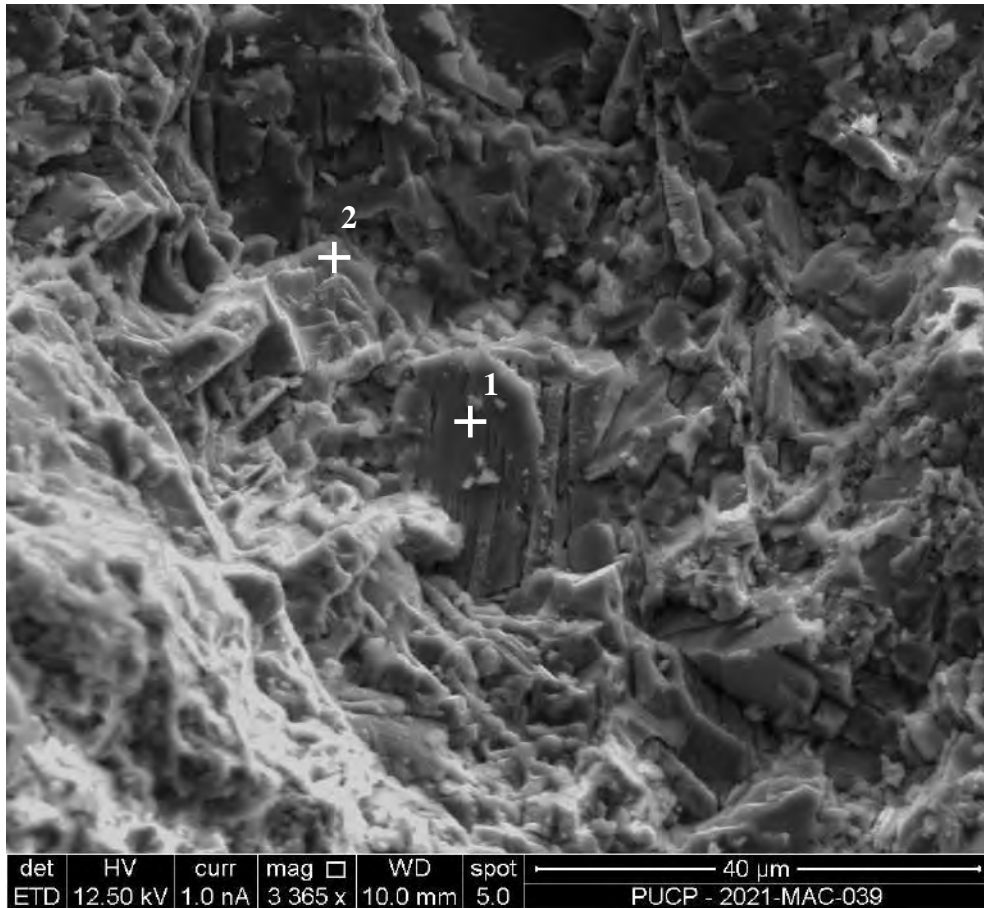


Spot 2:

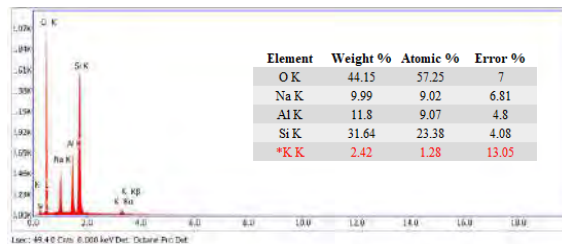


The elements and values presented in \*red can be considered erroneous

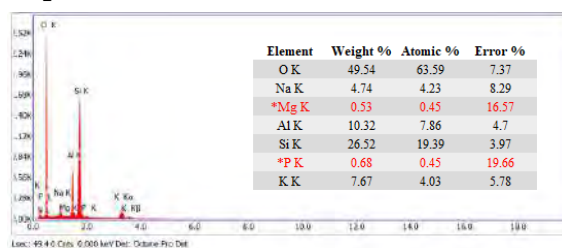
2021-MAC-039 : 'Mica with kaolinite subgroup minerals'



Spot 1:

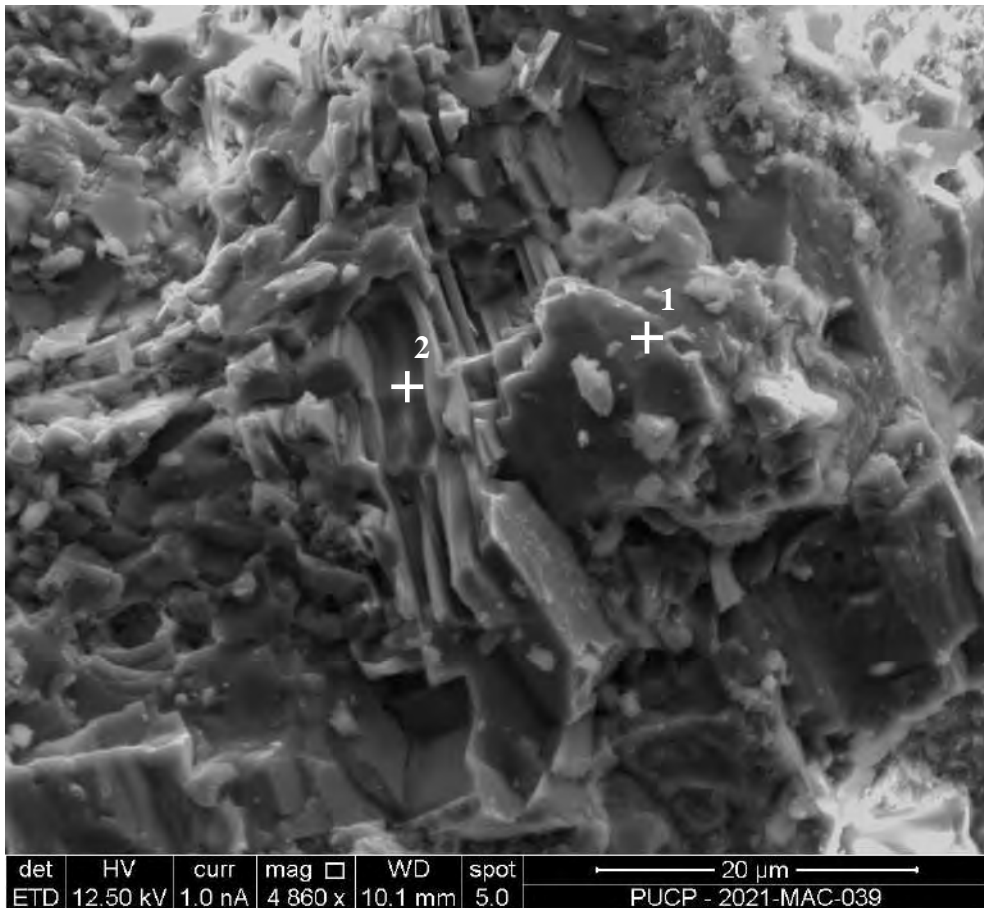


Spot 2:

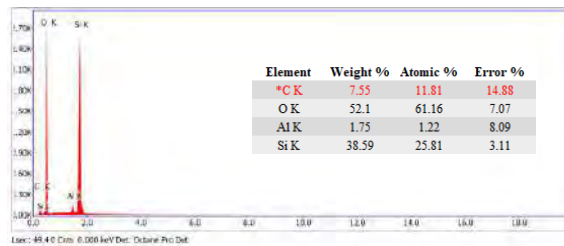


The elements and values presented in \*red can be considered erroneous

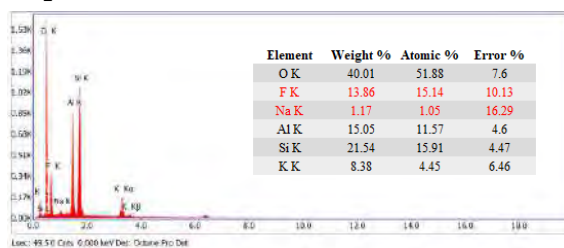
2021-MAC-039 : 'Mica with kaolinite subgroup minerals'



Spot 1:

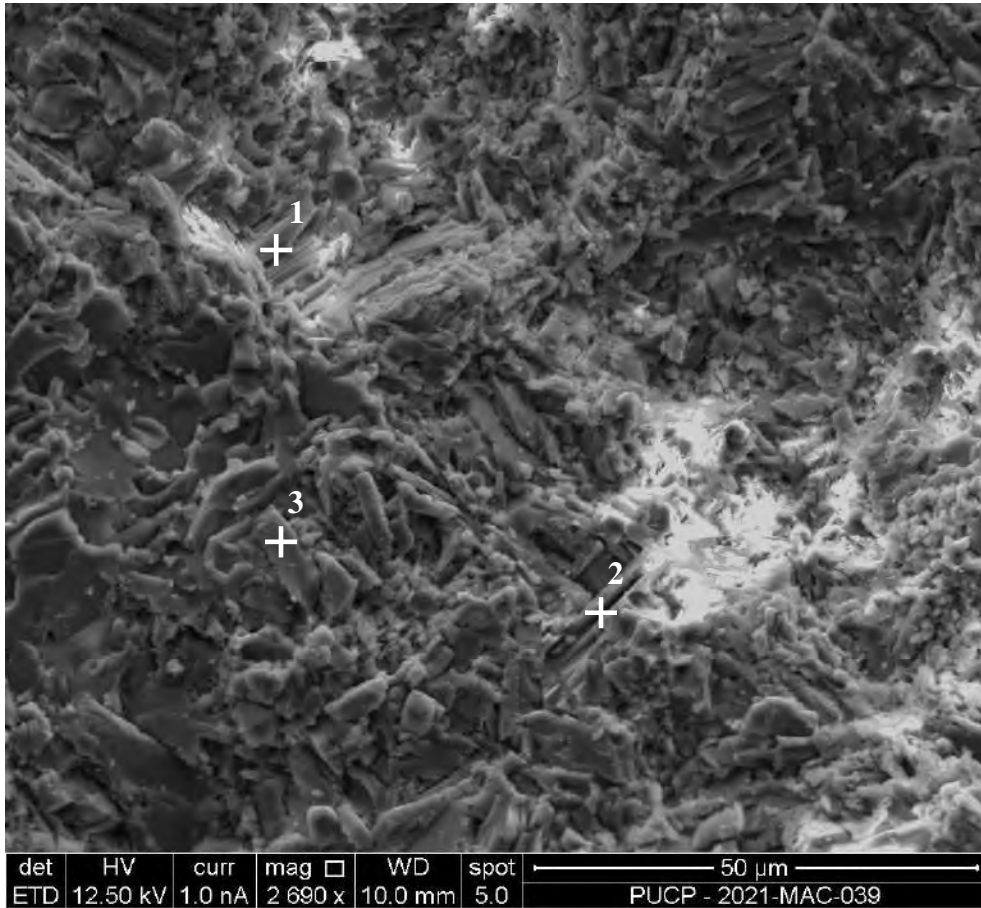


Spot 2:

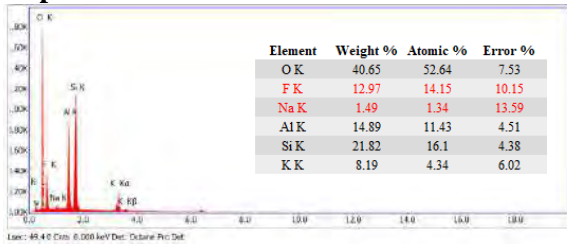


The elements and values presented in \*red can be considered erroneous

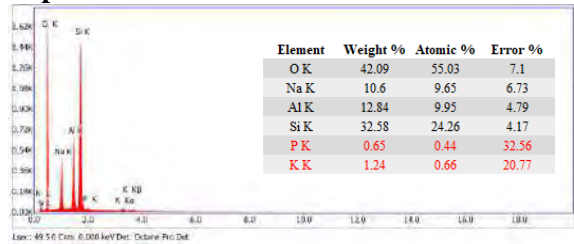
2021-MAC-039 : 'Mica with kaolinite subgroup minerals'



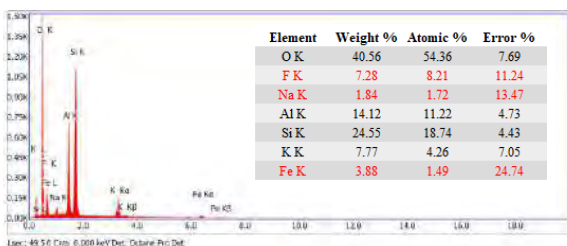
Spot 1:



Spot 3:

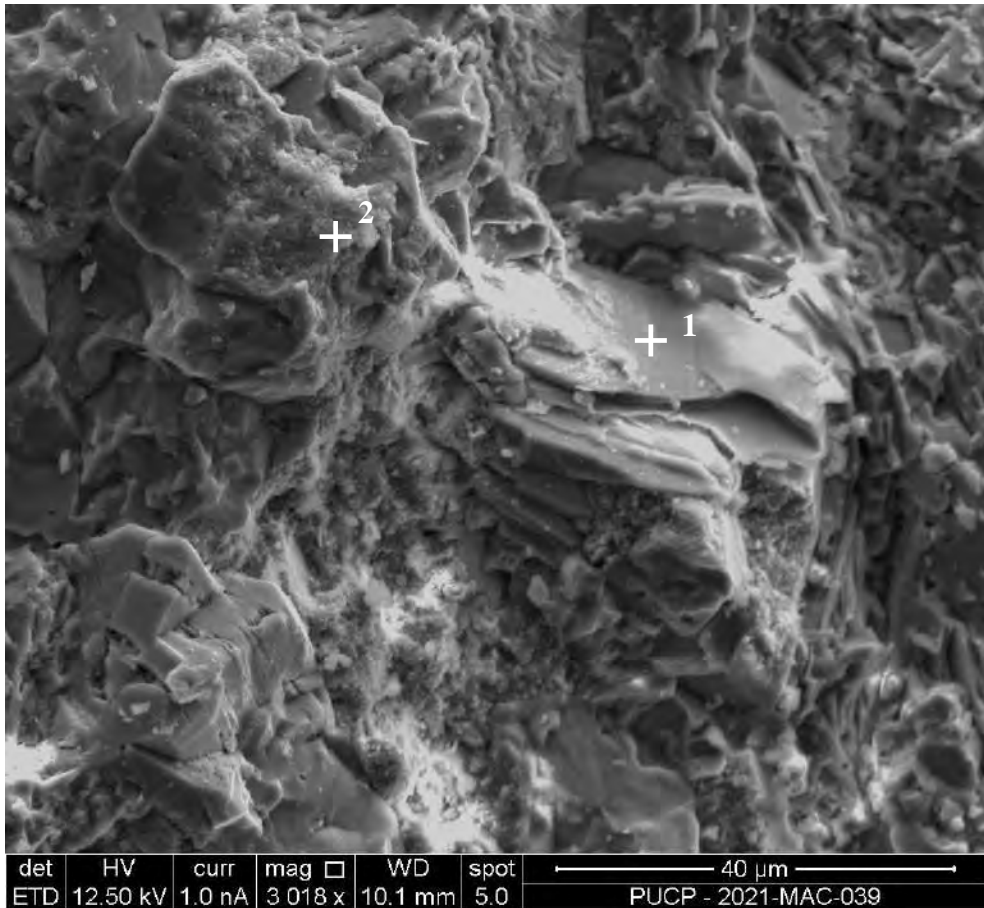


Spot 2:

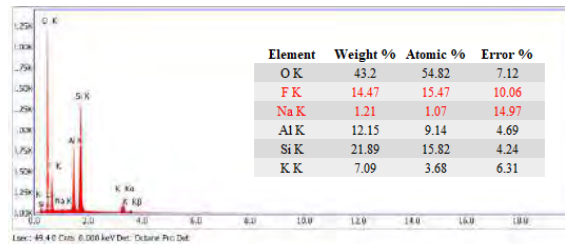


The elements and values presented in \*red can be considered erroneous

2021-MAC-039 : 'Mica with kaolinite subgroup minerals'



Spot 1:



Spot 2:



The elements and values presented in \*red can be considered erroneous